Laser modification for the increased lifetime of a commercial Stainless-Steel Alloys

Mark Swayne B.Sc. (Hons.) Chemistry

A thesis submitted in fulfilment of the requirements for the degree of

Doctor of Philosophy (PhD)

from

Dublin City University

School of Mechanical and Manufacturing Engineering

Supervisors

Prof. Dermot Brabazon

Dr. Jennifer Gaughran

July 2025

Declaration

I hereby certify that this material, which I now submit for assessment on the programme of study leading to the award of PhD, is entirely my own work, and that I have exercised reasonable care to ensure that the work is original, and does not to the best of my knowledge breach any law of copyright, and has not been taken from the work of others save and to the extent that such work has been cited and acknowledged within the text of my work.

Signed: Mark Swayne Date: 24th July 25. ID: 20214548

Mark Swayne

Advanced Metallic System Centre for Doctoral Training,

School of Mechanical and Manufacturing, Dublin City University,

Glasnevin, Dublin 9, Ireland.

Acknowledgements

Thank you all.

Funding Acknowledgements

This work is supported by I-Form, the Science Foundation Ireland Research Centre for Advanced Manufacturing. This work is also supported by Advanced Metallic Systems Centre of Doctorial Training (AMSCDT), which incorporates four universities namely Dublin City University (DCU), University College Dublin, The University of Sheffield and The University of Manchester. This work is in partnership PRO Stainless Design Ltd, a company based in Ireland. Science Foundation Ireland (18/EPSRC-CDT/3584) and the Engineering and Physical Sciences Research Council (EP/S022635/1) supported this work.

Contents

Table of figures

Table of Tables

List of Publications

1. Mark Swayne, Gopinath Perumal, Dermot Brabazon, **Mechanism for Control of Laser-Induced Stainless-Steel Oxidation,** Advanced Materials Interfaces. **DOI:10.1002/admi.202300991**
2. Mark Swayne, Gopinath Perumal, Dilli Babu Padmanaban, Davide Mariotti, Dermot Brabazon, **Exploring the impact of laser surface oxidation parameters on surface chemistry and corrosion behaviour of AISI 316L stainless steel**, Applied surface science advances (2024). DOI:10.1016/j.apsadv.2024.100622
3. Mark Swayne, Gopinath Perumal, Dilli Babu Padmanaban, Davide Mariotti, Dermot Brabazon, **Improved lifetime of a Pulsed Electric Field (PEF) system-using laser induced surface oxidation,** Innovative Food Science and Emerging Technologies (2024). DOI:10.1016/j.ifset.2024.103789
4. Abhijit Cholkar, Ronan McCann, Gopinath Perumal , Suman Chatterjee, Mark Swayne , David Kinahan, Dermot Brabazon, **Advances in laser-based surface texturing for developing antifouling surfaces: A comprehensive review,** Applied surface science advances (2023), DOI:10.1016/j.apsadv.2023.100513

List of Presentations

1. Mark Swayne, Gopinath Perumal, Dermot Brabazon, **Effect of laser surface modification on the metal released during pulsed electric field processing**, AMSCDST International Student Conference in Metallic Materials, July 2022, Dublin City University, Ireland.
2. Mark Swayne, Dermot Brabazon, **Laser Based Surface Modification of Stainless Steel for Improvement in Corrosion Properties**, AMSCDT International Student Conference in Metallic Materials, July 2021, Online.
3. Mark Swayne, Gopinath Perumal, Dermot Brabazon, **Influence of laser induced oxidation on corrosion and compositional characteristics of stainless steel,** AMPT2023 - 24th International Conference on Advances In Materials And Processing Technologies, September 2023, Universiti Putra Malaysia, MALAYSIA,
4. Mark Swayne, Gopinath Perumal, Dermot Brabazon, **Use of laser surface oxidation for the reduction of electrode corrosion seen inside a PEF system**, I-Form Gathering, December 2022, Athlone, Ireland

Awards

1. Best poster award at the 2021 AMSCDT International Student Conference in Metallic Materials
2. Best presentation award at the 2023 AMPT2023 - 24th International Conference on Advances In Materials And Processing Technologies,
3. Best environmental poster award at the 2022 I-Form Gathering,
4. Won the DCU Commercialisation Award won in 2022

List of Acronyms

Acronym	Full Term
AMAs	antimicrobial agents
AMSCDT	Advanced Metallic Systems Centre for Doctoral Training
ANOVA	Analysis of Variance
BCC	body centre cubic designs
Cdl	double-layer capacitance
CP	cyclic polarization
CPE	constant phase element
cps	counts per second
Cr	Chromium
CW	Continuous Wave Mode
DAQ	Data Acquisition
DLW	Direct laser writing
DOE	Design of Experiments
Ecorr	corrosion potential
EEC	Equivalent Electrical Circuit
EECs	Equivalent Electrical Circuits
EIS	Electrochemical Impedance Spectroscopy
Epit	pitting potential
Fe	Iron
fs	Femtosecond
FWHM	full width half max
HSFL	high spatial frequency LIPSS
Icorr	corrosion current
ICP-QMS	Inductively Coupled Plasma - Quadrupole Mass Spectrometry
KED	Kinetic Discriminator
kHz	Kilohertz
LC	Laser cladding
LSFL	low spatial frequency LIPSS
LSP	Laser Shock Peening
mm/s	Millimetres per second
Mn	Manganese
Mo	Molybdenum
Nd:YAG	Neodymium-doped Yttrium Aluminium Garnet
Ni	Nickel

Acronym	Full Term
O1s	Oxygen 1s orbital (XPS spectral peak)
OCP	open circuit potential
PEF	Pulsed Electric Field
PSS	period surface structures
PVD	physical vapor deposition
PW	Pulsed Wave Mode
ROS	reactive oxygen species
Rp	charge transfer resistance
Ru	solution resistance
SCC	stress corrosion cracking
SCL	Space Charge Layer
SEM	Scanning Electron Microscopy
SFI	Science Foundation Ireland
SS316L	Stainless Steel grade 316L
UV	Ultraviolet
W	Watt
WCA	water contact angle
XPS	X-ray Photoelectron Spectroscopy
µm	Micrometer (micron)

Abstract

Mark Swayne

Laser Modification for the Increased Lifetime of a Commercial Stainless-Steel Alloys

This research explores laser-induced surface processing to modify surface properties, enhancing the durability and performance of Pulsed Electric Field (PEF) systems. PEF systems use electromagnetic pulses to lyse bacterial cell walls for food pasteurization. However, electrode corrosion and biofouling pose challenges. This study investigates laser-induced oxidation to mitigate metal ion release during PEF operations.

The research focuses on three core areas: (1) expanding a thermokinetic model to predict oxide layer composition and color, (2) optimizing laser oxidation to improve corrosion resistance, and (3) integrating the modified surface into a PEF system.

A model for Nd:YAG laser oxidation of 316L stainless steel was developed using a factorial Design of Experiments (DoE). X-ray photoelectron spectroscopy (XPS) and optical reflectance spectroscopy determined elemental composition and color variations. Oxide layers exhibited a Cr/Fe ratio from 0.13 to 4.5, with controlled color changes via single-pass laser processing.

Further, corrosion resistance was analyzed through laser processing, examining surface chemistry, morphology, and electrochemical properties. Factorial DoE analysis showed lower areal energy samples had superior corrosion resistance and minimal defects, confirmed by cyclic polarization and electrochemical impedance spectroscopy (EIS).

Finally, PEF trials integrated DoE, morphological analysis, metal ion release (via ICP-QMS), waveform capture (DAQ system), and impedance spectroscopy. Pulse waveform variations demonstrated a three-fold reduction in metal ion release in laser-treated samples.

This study offers key insights into optimizing laser parameters to enhance corrosion resistance and surface chemistry, improving metal performance in PEF systems. These advancements contribute to sustainable food processing by extending PEF system lifespan while maintaining efficiency and product quality.

Chapter 1 - Introduction

1.1 Motivation

Stainless steel alloys are widely used in various industrial applications due to their durability, corrosion resistance, and cost-effectiveness. However, in demanding environments—such as those found in the food and pharmaceutical industries —these alloys can suffer from wear, fatigue, and corrosion over time, leading to costly replacements and repairs. Improving the lifetime and performance of these materials is essential for reducing maintenance costs, decrease down time and increasing the reliability of critical components.

Laser modification techniques offer a promising solution by enabling precise control over surface properties. Through processes such as laser cladding, laser hardening, and laser surface alloying, it is possible to enhance the wear resistance, corrosion resistance, and mechanical properties of stainless-steel alloys without compromising their bulk characteristics. These techniques not only provide an efficient, localized treatment but also minimize thermal distortion, making them suitable for complex geometries and high-performance applications.

Automated Process

Laser modification techniques offer a high degree of automation, which is essential for industrial applications requiring precision and consistency. Automated laser processes ensure repeatability in modifying stainless-steel surfaces, making it easier to achieve desired properties across large production volumes. This automation not only reduces the risk of human error but also allows for the precise control of laser parameters to meet specific performance requirements for various alloy compositions, meeting various performance needs in industrial applications.

Contamination-Free

One of the significant advantages of laser modification is its ability to create a contamination-

free surface, which is crucial for stainless-steel alloys used in sensitive industries such as food processing, pharmaceuticals, and medical devices. Unlike traditional coating or painting methods that may introduce new compounds that are unknown to the biological environment, laser treatment minimizes contamination, enhancing the alloy's corrosion resistance and making it suitable for applications where cleanliness and surface integrity are paramount

Fine Tune Parameters

The ability to fine-tune laser parameters provides exceptional control over the depth and quality of the modified layer, allowing targeted improvements in hardness, wear resistance, and corrosion resistance. This precision enables adjustments that optimize stainless steel for specific operating conditions, extending service life without altering the material's bulk properties. Such fine control offers a significant advantage over conventional modification methods, allowing for a flexible approach to material performance enhancement.

Environmentally Friendly

Laser modification is an environmentally friendly process that uses minimal resources and produces little to no hazardous waste. Compared to traditional methods like electroplating or chemical coating, laser treatment reduces the need for toxic chemicals such as high VOC content paints or PTFE, lowers energy consumption, and limits waste generation. This eco-friendly approach aligns with the growing demand for sustainable manufacturing practices, contributing to a reduced environmental footprint while enhancing material performance.

This research aims to explore the potential of laser modification to extend the lifespan of commercial stainless-steel alloys, thereby contributing to sustainable manufacturing and advancing material engineering practices. By optimizing laser parameters and evaluating their effects on the alloy's surface properties, this study seeks to develop a scalable method for improving stainless steel performance in harsh operating conditions, ultimately supporting industries that rely on these materials to maintain high standards of safety and durability.

1.2 Research Thesis and Objectives

The main objective of this thesis was to examine how laser processing parameters influence laser-induced oxidation and the corrosion resistance of 316L stainless steel. This research aimed to advance scientific understanding of laser processing by analysing the material's properties, metallurgical structure, and processing characteristics needed for achieving enhanced and reproduceable performance.

Specifically, the research focused on understanding the impact of different laser settings on oxidation, identifying metallurgical changes due to thermal effects, and evaluating the corrosion resistance under various conditions. By defining optimal laser processing parameters, this work provides valuable insights into achieving improved corrosion resistance and mechanical properties in 316L stainless steel, which is widely used in industries that demand durability and corrosion resilience. This goal was pursued through the following specific objectives

1. Explore the fundamental mechanisms of laser-induced oxidation in stainless steel.
2. Examine how nanosecond laser processing parameters (such as laser power, frequency, scan speed, and hatching distance) influence corrosion, color, surface chemical composition, and surface morphology.
3. Assess the impact of modifying processing parameters on metal release in a commercially used pulsed electric field (PEF) system.
4. Study the effects of laser-induced oxidation on metal release during PEF processing.

1.3 Overview of work and thesis structure

This thesis is structured as a collection of published research papers, each featuring original contributions. The candidate's specific contributions to these publications are detailed as follows.

Chapter	Publication Title	Status	Candidate Contribution
3	Mechanism for control of laser induced stainless steel oxidation	Published, Advanced Materials Interfaces 2024	First author, Corresponding author, project administration Conceptualization, Methodology, Software, Data curation, writing – original draft, Visualization, Investigation, Formal analysis, Writing – review & editing.
4	Exploring the Impact of Laser Surface Oxidation Process Parameters on XPS Elemental Depth Profiling and the Related Corrosion Resistance of 316L Stainless Steel	Published, Applied surface science advances 2024	First author, Corresponding author, project administration Conceptualization, Methodology, Software, Data curation, writing – original draft, Visualization, Investigation, Formal analysis, Writing – review & editing.
5	Improved lifetime of a Pulsed Electric Field (PEF) system-using laser induced surface oxidation	Published, Innovative food science and emerging technologies 2024	First author, Corresponding author, project administration Conceptualization, Methodology, Software, Data curation, writing – original draft, Visualization, Investigation, Formal analysis, Writing – review & editing.

This thesis consists of six chapters, organized in a progressive manner. Below is a brief description of the work completed and the content covered in each chapter.

Chapter 1: The chapter introduces various topics covered in the thesis, outlines the thesis structure, and summarizes its aims and objectives.

Chapter 2: The text thoroughly reviews the foundational information relevant to the topic and examines previous research in the field. It highlights the challenges, limitations, and gaps in current studies, emphasizing the need for further research efforts.

Chapter 3: Presents the investigation into the mechanism for control of laser induced stainless steel oxidation, where a full factorial DOE was used to investigate the effect of processing parameter on the optical and chemical aspects of laser induced oxidation. From this work an expansion of the current thermokenetic model was developed.

Chapter 4: Shows an in-depth investigation into the Impact of Laser Surface Oxidation Process Parameters on XPS Elemental Depth Profiling and the Related Corrosion Resistance of 316L Stainless Steel. In this work 2 full factor DOEs where used to optimise the corrosion resistance of laser surface oxidised samples. This was then investigated using depth profiling XPS and high-end corrosion analysis such as impedance spectroscopy

Chapter 5: Presents the work from the paper 'Improved lifetime of a Pulsed Electric Field (PEF) system-using laser induced surface oxidation'. This paper shows the first practical example of the modification of the electrode surface inside a PEF system to improve the corrosion resistance. This work also investigated the reason behind the extremely high corrosion rates seen and illustrates a way of reduction using process optimisation

Chapter 6: This chapter summarizes the main findings of the research and offers recommendations for future studies.

Chapter 2 – Literature Review

2.0 Introduction

This chapter provides a comprehensive overview of the existing literature relevant to laser surface modification and its application in improving the corrosion resistance of stainless steel. It begins with the fundamental principles of laser operation, including the mechanisms of light production, beam absorption, and the influence of various laser parameters such as pulse duration and frequency. The review then explores state-of-the-art anticorrosion techniques, particularly those suitable for food-grade stainless steel, with a focus on laser-based approaches. Additionally, emerging methods such as laser colouration and antifouling surface treatments are examined for their potential contributions to enhancing material performance. Finally, the chapter addresses the use of pulsed electric field (PEF) systems and their associated challenges, establishing a foundation for the subsequent experimental investigations.

2.1 Laser operation principles

Laser is an acronym from 'Light Amplification by the Stimulated Emission of Radiation'. Lasers have some unique properties that distinguish them from other light sources; these are that they are Directional, Monochromatic, and Coherent. This allows for direct interaction between multiple laser beams [1].

The principal components of a laser are:

1. Gain medium
2. Laser Pumping Energy
3. High Reflector
4. Output Coupler
5. Laser Beam

2.1.1 Light Production in Lasers

The quantization of energy at molecular level means that molecules are to be found in discrete electronic, vibrational and rotational energy levels. Molecules can make transitions from one state to another; these states are specified by the quantum numbers and term symbols [2].

For this, transitions to occur the system must absorb and emit energy/ light. The three most important transitions are A) Induced absorption, B) Spontaneous emission, C) Induced emission. Which can be seen in Figure 2-1 below.

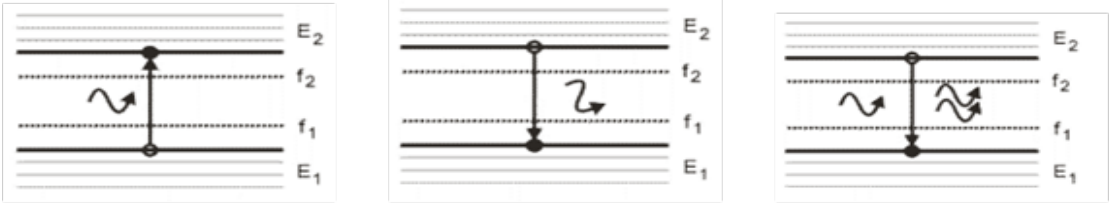

A) Induced Absorption B) Spontaneous emission C) Induced emission

Figure 2-1: Atomic orbital Recombination processes (a) induced absorption, (b) spontaneous emission, (c) induced emission [2]

The probability of each of these processes occurring is determined by the energy level they occupy, and the spectral density applied to the gain medium. The rate relationship between the absorption and emission processes is giving by equation (2-1).

$$R(abs) = R(spon) + R(ind) \qquad \textbf{(2-1)}$$

The rates can be expressed by the Einstein coefficients, which are defined in the following way:

- $B_{(12)}$ transition probability of induced absorption
- $A_{(21)}$ transition probability of spontaneous emission
- $B_{(21)}$ transition probability of induced emission.

$$\frac{A_{(21)}}{B_{(21)}} = \rho(\hbar\omega)\exp\left[\frac{\hbar\omega}{k_B T}\right] - 1 \qquad \textbf{(2-2)}$$

Photon amplification only occurs when induced emission is dominant compared to spontaneous emission, with the produced photon having the same frequency, phases, and direction as the original photon. From equation 2-2, we can see that induced emission is

dominant when $hw << k_bT$. This condition is meet and the lasing process can occur when there is a population inversion inside the system. This arises when the system is out of thermal equilibrium and the number of photons in the higher energy (E_k) level exceeds the number of photons in the lower energy level (E_i) or for a diode laser the number of electrons in the conductions band is grater then the valence band. Pumping is the initial energy required to cause population inversion of the gain medium, and it can occur optically or electrically, this can be seen in Figure 2-2 [1].

For amplification to occur, photons must selectively feedback into the cavity after they are produced. This is accomplished by forming an optical cavity with two or more mirrors. Photons travelling on the axis between the mirrors are reflected through the gain medium by the cavity mirrors. These photons are trapped within the cavity and preferentially amplified over photons travelling in opposite directions.

For semiconductor lasers the band structure is also taken into consideration during the recombination process. For both direct and indirect band gaps the energy of recombination is carried off by a photon, but to conserve momentum one or more phonons must be products for an indirect band gap recombination. This multiparticle interaction is improbable and the recombination efficiency in the indirect band gap material is lower than in the direct band gap material. Direct bandgap structures maximize the tendency of electrons and holes to recombine by stimulated emission, thus increasing the laser efficiency [3].

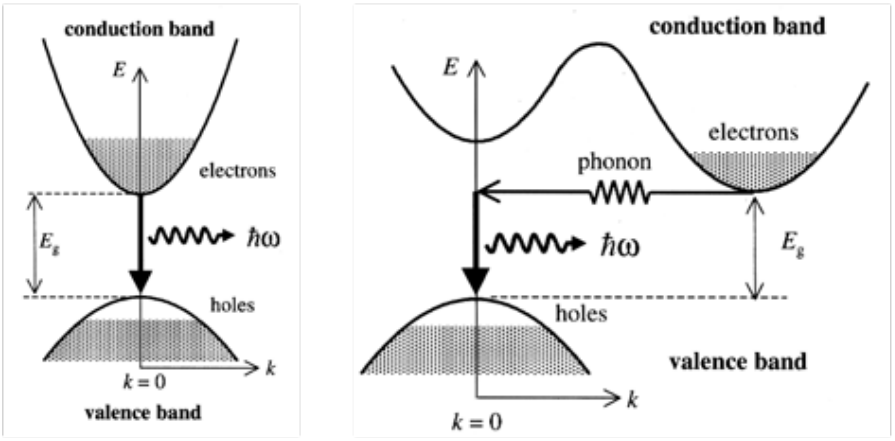

(a) direct-band-gap structure

(b) indirect-band-gap structure

Figure 2-2: Recombination processes of (a) Direct band gap structure (b) indirect band gap structure [3].

2.1.2 Types of lasers

Lasers are divided into 4 different categories depending on the gain medium.

A. Gas Laser
B. Liquid Laser
C. Solid Laser
D. Semiconductor laser

Dahotre et.al [4] added a fourth type the semiconductor lasers even though they are based on solid material, the pumping and lasing mechanisms are different. All these types can work in two modes: the continuous wave mode (CW) in which laser beam can be emitted without interruption and the pulsed wave mode (PW) in which the beam is interrupted periodically. Many materials have been tested for laser action. However, suitable materials for commercial lasers are still limited. In the review below, only the solid-state type of lasers would be discussed, as they are the main laser utilized in this work.

2.1.2.1 Properties of Nd:YAG

Nd^{3+}:YAG is a four-level gain medium, offering substantial laser gain even for moderate excitation levels and pump intensities. The gain bandwidth (allowed pumping band) is relatively small, but this allows for a high gain efficiency and thus low threshold pump power. Nd:YAG lasers can be diode pumped or lamp pumped. Lamp pumping is possible due to the broadband pump absorption mainly in the 800-nm region and the four-level characteristics seem in Figure 2-3.

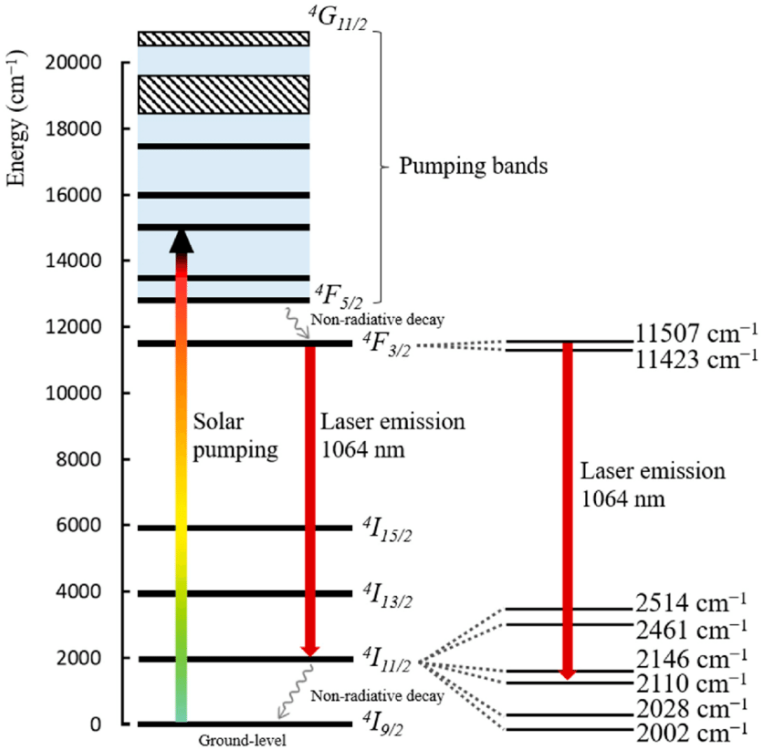

Figure 2-3: Energy level structure and common pump and laser transitions of the trivalent neodymium ion in Nd^{3+}:YAG [5].

The most common Nd:YAG emission wavelength is 1064 nm. The second, third and fourth harmonics at 532, 355 and 266 nm can also be generated by frequency multiplying. Other emission lines are also possible. The transitions are all four-level transitions. Some of these, such as the one at 1123 nm, are extremely weak, making efficient laser operation at these wavelengths difficult.

Nd:YAG is usually used in monocrystalline form, fabricated with the Czochralski growth method. For monocrystalline Nd:YAG, absorption and scattering losses within the length of a laser crystal are normally negligible, even for relatively long crystals.

Typical neodymium doping concentrations are of the order of one atomic percent. High doping concentrations can be advantageous e.g. they reduce the pump absorption length, but too high concentrations leads to quenching of the upper-state lifetime e.g. via up conversion processes. Also, the density of dissipated power can become too high in high-power lasers. Note that the neodymium doping density does not necessarily have to be the

same in all parts; there are composite laser crystals with doped and undoped parts, or with parts having different doping densities [5].

2.1.2.2 Properties of Diode Laser

In a semiconductor If the valence bands are partly filled, this material is p-type, if the conductive bands are partly filled, this material is n-type. Here Fermi level is used to label the occupation conditions of electrons in the semiconductor, it is the energy level to which electrons occupy. Fermi level *(E_{FP})* on p-type is near the valence band and E_{FN} on the n-type is near the conductive band.

A heterojunction is generated when two semiconductors with distinct band structures are joined; a p-n heterojunction is known as a diode. Due to their distinct Fermi levels, electrons and holes transfer to the other side. They mix, leaving the p-side with negative charge and the n-side with positive charge; this region is referred to as the space charge layer (SCL). Because of charge transport and recombination, an inherent voltage V is produced. As seen in Figure **2-4**(a), the Fermi level is continuous across the diode when there is no applied voltage. The inherent voltage prohibits electrons in the conduction band on the n-side from diffusing into the conduction band on the p-side. The same holds true for holes in the valence band, preventing majority carriers from entering the space charge layer. An applied voltage *V can* separate E_{FP} and E_{FN} by eV, and the Fermi level becomes discontinuous across the diode [1].

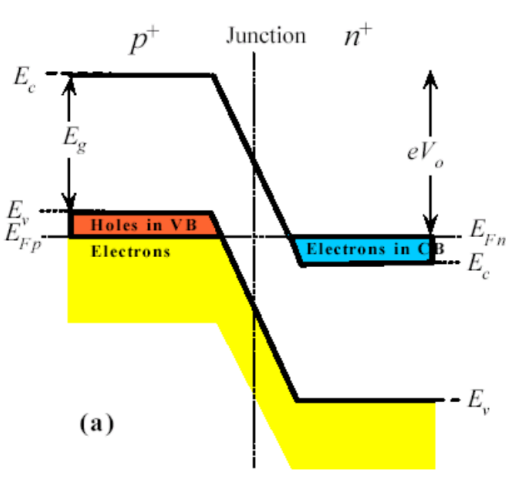

(a) p-n junction without bias

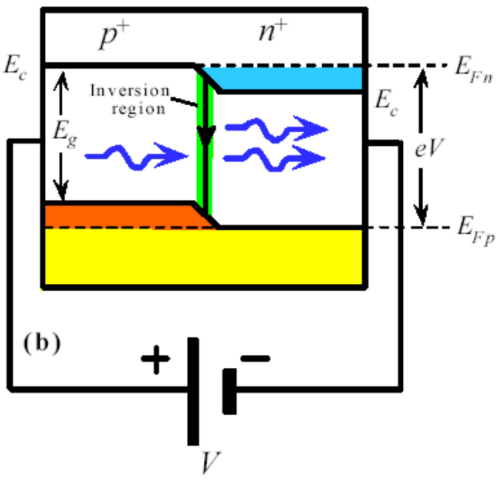

(b) p-n junction after forward bias

Figure 2-4: p-n junction (a) without bias, (b) with bias [1].

As a result of the applied voltage, recombination occurs and the diode current is established. The space charge layer is no longer depleted when the applied voltage exceeds the inherent voltage. Now, at the junction, more electrons with energies near Ec are injected into the conductive band than electrons with energies near Ev into the valence band. This is the population inversion, and the region depicted in Figure 2-4(b) is known as the active region.

2.1.2.3 Optical Feedback Mechanism

A high-efficiency laser requires a resonator that can not only magnify the electromagnetic wave, but also provide feedback to it. Typically, a laser resonator is composed of two parallel mirrors that are perpendicular to the optical axis. A portion of the space between the mirrors is occupied by the amplifying substance. In a laser diode, this structure, known as a Fabry-Perot Resonator. Due to the change in refractive index at the interface between the crystal and other material, the mirror facet functions as a reflective surface. Photons generated by spontaneous emission are amplified and continually reflected by the front and rear facets when the resonator is brought to a condition of population inversion. The electromagnetic wave is then magnified as it goes through the semiconductor material due to stimulated emission [2].

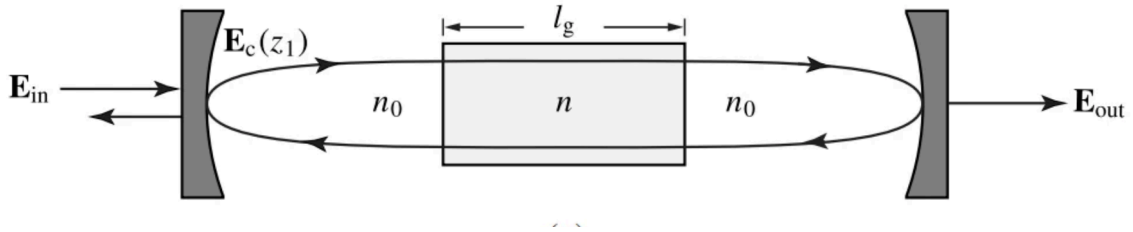

Figure 2-5**:** Schematic of an optical feedback resonator [2].

2.1.3 Oxide growth kinetics

Before the availability of laser assisted processes, furnace techniques were used to grow oxide layers in a strictly isothermal condition. During laser oxide growth the processes is not seen

as a strictly isothermal processes due to the photolytic process occurred by the laser matter interaction. Due to this effect the oxidation kinetic, vary drastically compared to traditional processes with the oxidation constant having a dependence on the temperature, wavelength and other laser processing properties [6].

The metal oxidation processes are a multi-sequence process that considers the transport of oxide molecules to the oxide/gas interface, adsorption, dissociation and diffusion to and through the oxide layer, and the chemical reaction that occur such as photolytic or pyrolytic.

Isothermal metal oxidation occurs as a heterogeneous process between the metal surface and the surrounding atmosphere. Two theories, namely the Cabrera-Mott theory for thin films (>100 nm) and the Wagner theory for thick films (<100 nm), describe oxide growth kinetics. These theories are based on the diffusion of electrically charged species, where fluxes are determined by gradients in chemical potential and electric fields [7] . However, laser-induced oxidation, due to its more complex nature, isn't fully explained by these theories.

For laser processing below the ablation threshold, whether using continuous wave (CW) or pulsed lasers, the growth of laser-induced oxide layers involves several steps: absorption of laser energy, adhesion and dissociation of oxide molecules, nucleation of subatomic layers, transportation of metal and oxide particles through the oxide layer, and growth of the oxide interface.

Understanding the kinetics of oxide growth requires knowledge of the critical temperature of the metal-oxide phase transition, which determines the activation time. Depending on conditions, light-material interactions can lead to photolytic and/or pyrolytic processes, where the material's absorptivity (A) serves as a key parameter [6].

The absorptivity is influenced by optical and thermal parameters such as refractive index (n) and extinction coefficient (k). In the general case, absorptivity varies with optical parameters and oxide thickness, exhibiting interference changes. The sign of the feedback, determined by the derivative of absorptivity (dA/dx), influences system dynamics. Negative feedback ($dA/dx < 0$) leads to self-stability, while positive feedback ($dA/dx > 0$) may result in various instabilities.

Due to the interplay between thermal and optical parameters and laser beam characteristics, self-sustained oscillations, chaotic flows, and temperature changes can occur [8]. The oxidation activation energy remains relatively constant with temperature, while the oxidation constant varies significantly, leading to higher oxide growth rates compared to isothermal oxidation processes [9].

Distinctive characteristics of laser-induced oxidation processes include non-linearity, non-equilibrium circumstances, and temperature-dependent chemical reaction rate constants of Arrhenius type, influenced by laser process parameters [6].

2.1.4 Laser Beam Absorption

The material's absorptivity is influenced by its optical properties, which are primarily determined by free (valence) electrons, as inner electrons have minimal interaction with the applied electric field [10]. As the beam strikes the surface of a non-transparent material it will be reflected and absorbed in a distinct ratio. This absorbed energy will excite the electrons to higher energy levels. Using the Drude model, the material's absorptivity, α, and reflectivity, Ro, can be calculated based on its extinction coefficient, κ, and refractive index, n, through the equation (2-1) [11]

$$\alpha = 2\omega\kappa c = 4\pi\kappa\lambda \tag{2-1}$$

$$R_O = (n-1)^2 + \kappa^2\,(n+1)^2 + \kappa^2 \tag{2-2}$$

$$R_0 + \alpha = 1 \tag{2-3}$$

where λ is the wavelength, ω is the angular frequency, C is the speed of light.

The inverse of absorptivity, α^{-1}, is referred to as the optical penetration depth or absorption length. According to the equation, for metallic materials, reflectivity typically ranges between 90% and 99%, with an optical penetration depth of approximately 10 nm [12]

2.1.4.1 Temperature effect

The absorptivity of materials depends on other factors as well including wavelength, laser beam incidence angle, Surface films, surface roughness and temperature of the material.

The absorptivity of metal surfaces increases with a rise in surface temperature. This phenomenon can be attributed to an increase in energy exchange between phonons and electrons [13,14]. Higher energy levels cause electrons to interact more with the metal structure rather than reradiate. This effect can be intensified by the cumulative impact of multiple laser pulse interactions [15]

2.1.4.2 Effect of surface roughness

Surface roughness plays a significant role in radiation absorptivity [16,17]. High-roughness surfaces can cause multiple reflections of the laser beam and may also lead to enhanced absorption due to interference with sideways-reflected beams as illustrated in Figure 2-6. Techniques like sandblasting can increase laser absorptivity in various materials by creating a rougher surface texture[18]. However, when surface roughness is smaller than the laser beam's wavelength, the surface appears smooth to the beam.

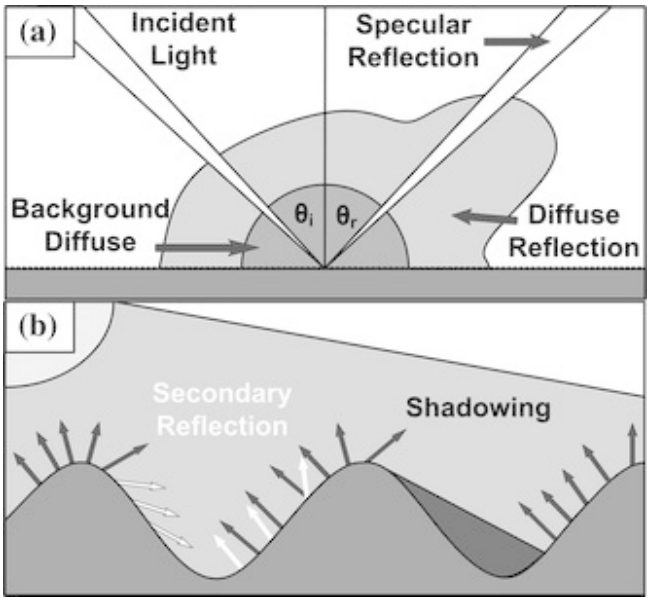

Figure 2-6: Schematic illustrating the effect of surface roughness on absorption of laser light.

2.1.4.3 Effect Laser Beam Wavelength

The wavelength of a laser beam influences the laser ablation process, as it is directly linked to the photon energy of the laser according to the equation (2-4):

$$E = \frac{hc}{\lambda} \tag{2-4}$$

where E is the photon energy, h is the Planck constant, c is the speed of light, λ is the wavelength

According to equation (2-4), increasing the laser beam wavelength results in lower photon energy. For example, a 1064 nm Nd:YAG laser has a photon energy of 1.17 eV, while a 167 nm UV laser has a photon energy of 7.9 eV. Photon energy absorption by the material occurs through either single-photon or multi-photon absorption processes. In the lower wavelength ranges, the photon energy can only be absorbed or interact with the electrons rather than the ions as the ions are too heavy to follow the high frequency field. This higher photon energy enables chemical breakdown of the material, as opposed to the thermal breakdown caused by longer-wavelength lasers [19].

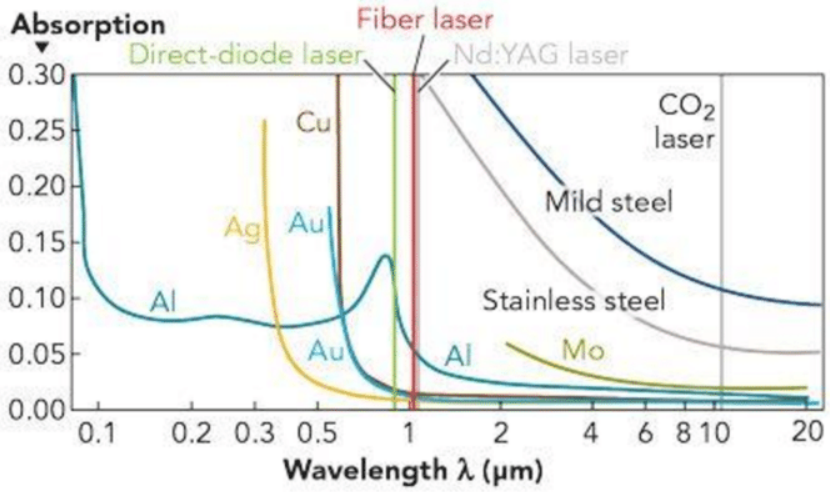

Figure 2-7: Graph of absorption percentage Vs wavelength for a variety of materials

2.1.5 Pulse Frequency

In pulsed wave mode, pulse frequency denotes the number of laser pulses directed at the sample surface per second. Results indicates that higher pulse frequencies lead to better surface quality and significantly reduce thermal stresses. Shorter 'off times' between pulses

limit heat dissipation, increasing the ablation rate as the process shifts from non-thermal to thermal ablation. This shift notably impacts the morphology and scale of the ablated area [20] . Schaffer et al. compared the material's thermal diffusion time with the interval between successive laser pulses and found that shorter intervals cause heat to build up in the focal zone, resulting in material heating through a process known as thermal incubation [21]. This thermal incubation lowers the ablation threshold as the number of pulses increases, with the threshold decreasing exponentially until it approaches an asymptotic limit, as illustrated in Figure 2-8. This phenomenon is observed in both metals and polymers [22,23].

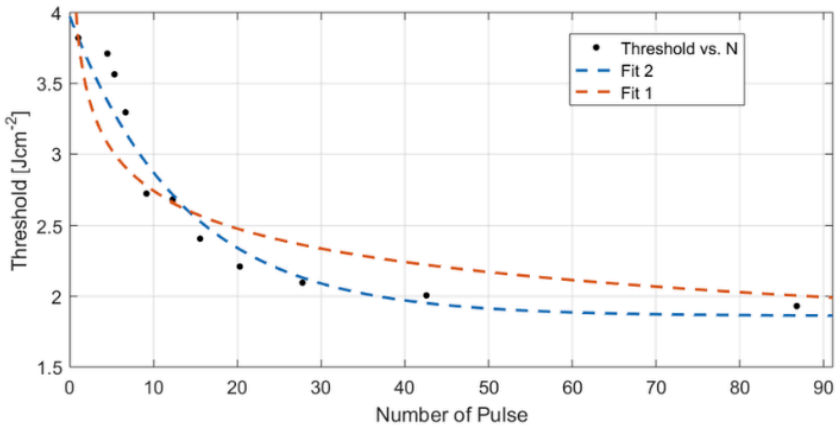

Figure 2-8: Ablation threshold versus number of pulses**.**

Since pulse energy is inversely proportional to Pulse reptation frequency (PRF), lower PRF values correspond to higher pulse energy, which can induce thermal stresses that cause microcracks and flaking [21]. For this reason, using a high PRF with lower energy levels is generally preferred to promote uniform heat distribution and accumulation of heat.

2.1.6 Effect of different pulse lengths on properties long, short and ultra-short

Laser surface modification can be conducted using either continuous wave (CW) or pulsed wave (PW) modes, as illustrated in Figure 2-9. CW modes are characterised by the average power and peak power being almost identical leading to higher energy input, while PW mode discharges energy in rapid, periodic bursts. In PW mode, energy is stored until it reaches a threshold, then released in a short, high-density pulse. As shown in Figure 2-9, PW mode is

characterized by initial spikes in peak laser power, typically with lower average power then CW mode [24,25]

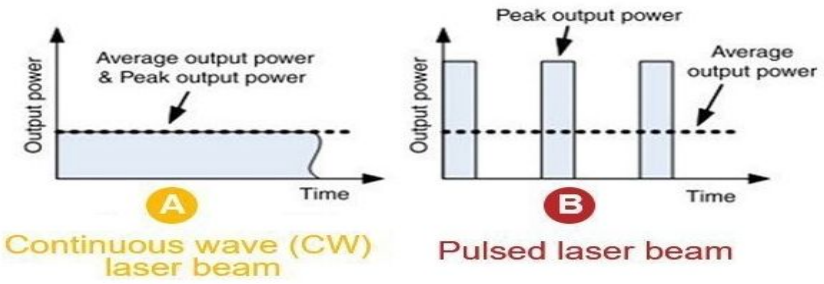

Figure 2-9: Differentiation of lasers based on temporal outputs in continuous wave and pulsed wave modes

In this work PW laser modes are used, whose ablation mechanism are heavily influenced by the pulse width of the laser. A three-step process can describe laser this ablation mechanism. 1) Absorption of light due to inverse Bremsstrahlung in the outer layer. 2) Electron thermal wave by fast energy relaxation within the electron subsystem, 3) Electron- lattice relaxation owing to electron- phonon coupling. [26]

Since the time scale of stage 3 is in the picosecond range, the effect of laser pulse duration above or below this causes a large impact on the results seen. This leads to the two main models of ablation, thermal and a-thermal [27]. Long and short laser pulses in the range of micro to Nano lengths are described by thermal ablation, which is dominated by heat conduction, melting, evaporation, and plasma formation. As the pulse length is longer than the relaxation time the energy absorbed by the material is conducted away from the source as heat, this will produce a temperature field in the work piece known as the heat-affected zone (HAZ). This will cause a melt pool to occur around the source. [28]

Ultra short laser pulses in the picosecond and femtosecond range are described by a-thermal ablation. This causes the electrons and lattice to not be in thermal equilibrium. Since the timescale is too short, there is insufficient time for the exchange of energy from the electrons to lattice. This causes all the energy to be concentrated on the electrons. This produces an extreme thermal gradient as the electrons are heated to hundreds of degrees while the lattice maintains it original temperature [26]. This cause a HAZ of less than 10nm while the thermal ablation HAZ can surpasses 100nm [29]. As the laser pulse length decreases the peak power

of each pulse increases e.g. for a 1mJ average power pulse the peak power for a 1ms pulse is 1 W while the peak power for a 1ps pulse is 1GW [28]. The extreme pressure and temperatures caused by the ultra-short pulse build up and accelerate the ionized material to extremely high velocities. Due to the short timescale continuous evaporation of the material does not occur, instead the material is transferred into an overheated liquid state. This high pressure overheated liquid merges into a mixture of vapor and liquid droplets causing a rapid expansion of the material removing it from the ablated area. This process is known as phase explosion [30]. The lack of a HAZ and the efficient removal of material makes this method have a higher dimensional accuracy allow it to produce finer textures allowing for decrease in surface tension ultimately leading to an increase in antifouling properties of the material [31].

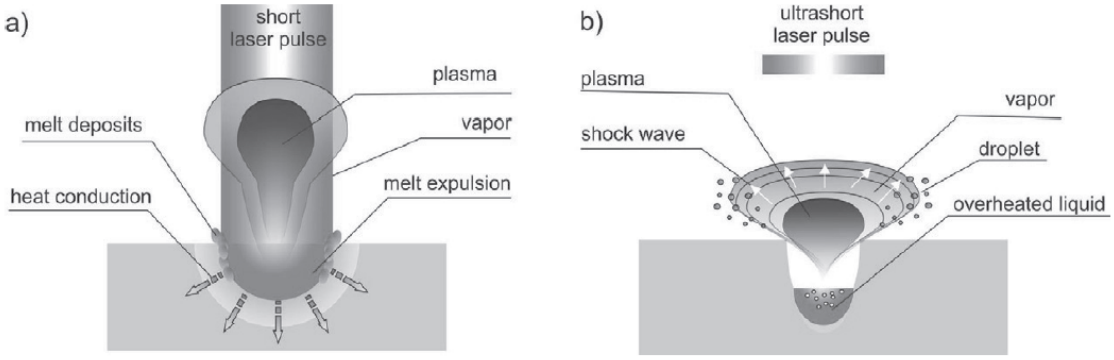

Figure 2-10: a) Model of thermal ablation; b) Model of a-thermal ablation [32].

In the paper by Karl- Heinz Leitz *et.al* he analysed the formation of a bore hole produced by different laser pulse lengths from micro to femtosecond as different laser systems were used in the experiment, they were normalized by peak fluence and not number of passes (N) [32] Figure 2-11 shows the laser ablation of microsecond pulses it can be seen for lower N that the process is mainly produced by thermal effects which is dominated by local melting and heat conduction into the substrate and very little evaporation by ablation. The HAZ increases steadily as the number of pulses increase to N = 100, due to a process called the incubation effect which is where the heat produced does not have sufficient time to diffusion between pulses. This causes a steady increase in temperature of the zone. This effect decreases the ablation threshold of the piece allowing ablation by evaporation to take place easier. As the pulses increase toward N = 1000 the process becomes more dominated by melt expulsion which accumulates around the bore hole producing a large burr. [32]

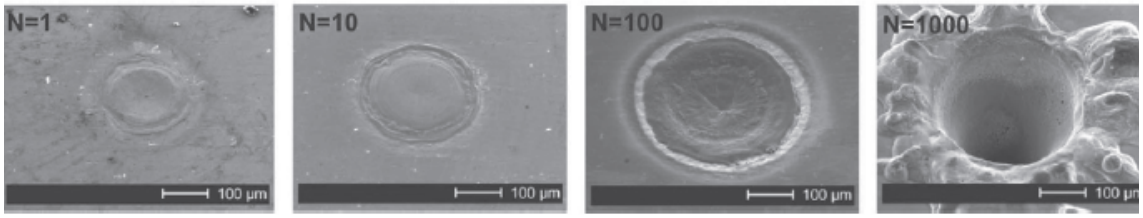

Figure 2-11: Microsecond laser ablation at different numbers of pulses [32].

Figure 2-12 shows the picosecond laser ablation. The main model that describes this is the a-thermal ablation method this is indicates by the little to no increase in the hole diameter as N increases this show that very little HAZ is produced during this method. At N = 500 the formation of a cleft structure is seen at the center of the ablated spot this indicates the presence of a phase explosion. As N increases, the formation of a soft burr on the outside of the hole and a ripple structure inside the hole can be seen. These two structure are both show that the ablation process is dominated by phase explosion [32].

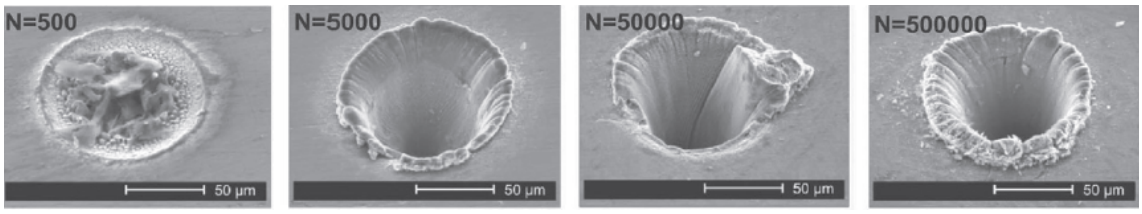

Figure 2-12: Picosecond laser ablation at different numbers number of pulses [32].

This reduced burr compared to the microsecond pulse is beneficial to surface texturing as it will reduce the Ra and Sa (measures of roughness) values the material has allowing for less friction to occur and a potential increase in antifouling properties. [31]

2.1.7 Laser beam profile and transverse modes

The laser beam's cross-section has a distinct energy distribution, defined by spatial patterns formed by light confined within an optical resonator, known as transverse modes. These modes, referred to as TEM_{nm} for transverse electric and magnetic, vary in field pattern across different transverse planes within the resonator, changing shape along the resonator axis. The intensity profile of these patterns follows a Gaussian distribution. In the TEM_{nm}

designation, *n* and m represent the number of intensity nodes along the x and y axes, respectively.[33]

Figure 2-13 illustrates various TEM modes, including the TEM_{00} mode, which is the fundamental Gaussian spatial energy distribution commonly used in laser machining processes. TEM_{00} is the lowest-order transverse mode, with the lowest threshold, smallest beam spot size, and divergence, and contains no nodes in its transverse intensity profile. All experiments in this study were conducted using a focusing lens with a Gaussian TEM_{00} distribution mode [33].

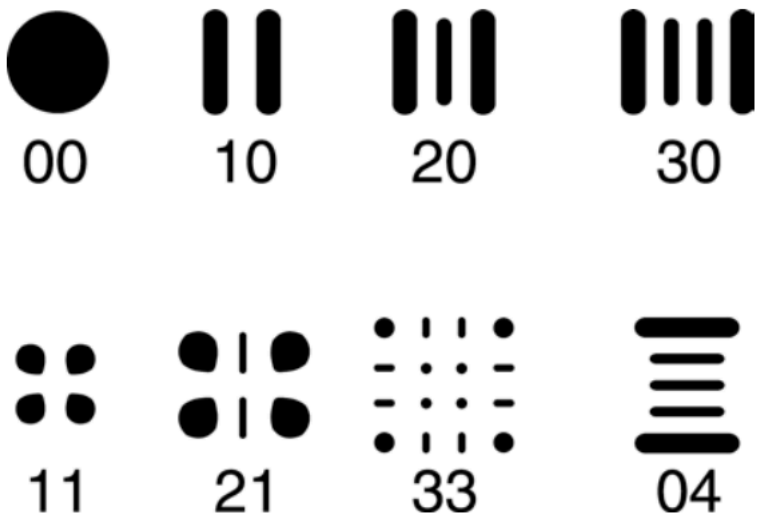

Figure 2-13: Transverse gaussian mode patterns with n,m indicated

The power intensity in a Gaussian distribution profile can be determined using equation (2-6) [34]:

$$I = I_o \exp[\frac{-2r^2}{w^2}] \quad (2\text{-}6)$$

where, r is the radius of the beam, Io Is the beam intensity at the centre of the beam (r=0) and w is the beam radius when.

$$I = I_o/e^2 \tag{2-7}$$

For certain applications, a uniform beam intensity is required. This can be achieved using beam-shaping optics. The resulting intensity profile is illustrated in Figure 2-14, which shows the transformation of a Gaussian beam profile into a "top-hat" beam [35]

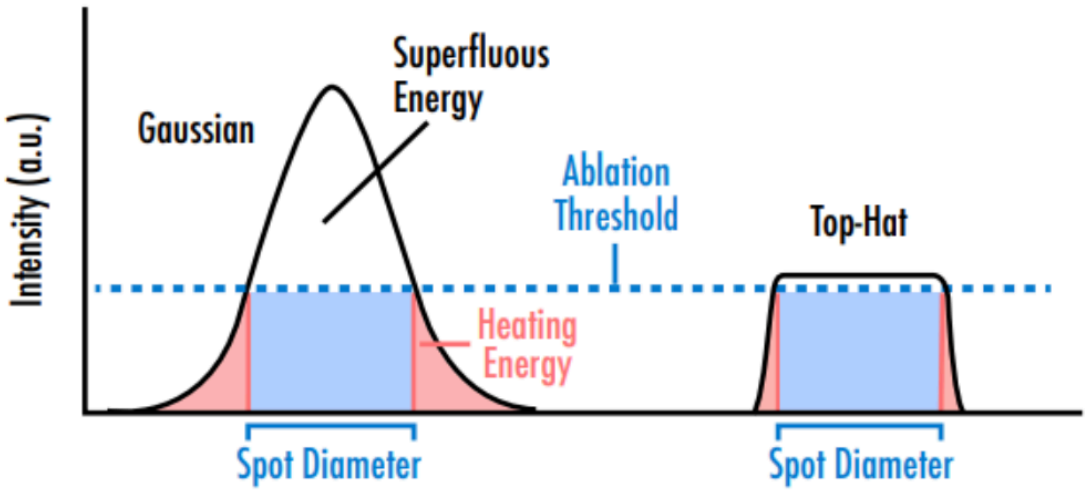

Figure 2-14: Beam profile laser profile of gaussian and top hat forms

2.2 Anticorrosion methods

2.2.1 Food safe coatings/ techniques for stainless steel

Laser surface modification was used in this work to produce an anticorrosive/ antifouling surface for a PEF system. Due to the electrode, being in direct contact with the food surface/ media while under operation, the surface modification method must retain food safety and not produce or release any contaminants into the media. Food safety coatings that have been used to reduce corrosion and fouling inside the food industry are presented here. These are separated into chemical, mechanical and antimicrobial coatings.

2.2.1.1 Chemical coatings

Polytetrafluoroethylene (Teflon) is a well-known anti-fouling coating used in the food industry and for cookware. PTFE has highly energetic and polarized bonds [36], but its structure makes it behave like a non-polar polymer. It has a high melting point about 330 C^0, compared to other traditional polymers [37], making it stable during heating. Chemical inertness and mechanical resistance prevent organic molecules from sticking to PTFE's surface, making it a popular food-processing material. Due to the fact that PTFE coatings can be damaged by mechanical surface-cleaning processes, they are formulated with fillers to increase their wear resistance [38]. Carbon, glass fibers, minerals, or bronze are common PTFE fillers [38,39]TFE coatings' service life depends on the environment [40]. Such coatings have a 2- to 4-week lifespan [41], but cyclic mechanical, thermal, and chemical stresses can degrade them even fast. In one example, it has been found that Ni-PTFE-modified SS surfaces in milk processing plants significantly reduce milk and bacterial fouling by more than 96% [42]. Due to the short life span, expensive coating process, and the possibility of leaching of the monomer into the food product PTFE coating inside commercial food processing vessels are quite limited in their application [43].

2.2.1.2 Mechanical protection

Passivation: The primary and most common passivation treatment for stainless steel is simply exposure to air. The alloy will quickly form a thin, durable Chromia oxide film due to this exposure. This passivating film formation is accelerated when the surface is subjected to water or other oxidising environments [44]. Light surface contamination from shop dirt, iron particles from cutting tools, and machining lubricants can be removed from machined stainless-steel parts through additional passivation [44]. When performed as a mild cleaning operation following machining, passivation treatments with nitric or mild organic acids improve the protective nature of the naturally formed, air-formed film on stainless steel. By treating stainless steel with nitric acid, the chromium content of the film's protective layer can be increased [45].

Electro polishing: An effective substitute for pickling processes which acid paste used for passivation is electro polishing. After fabrication, it is commonly used to remove imperfections from the stainless steel's surface. It removes embedded iron particles and other film defects in a similar fashion of pickling paste [44]. This process is performed by corroding the surface's protective film and smoothing the surface profile. A copper cathode and an electrolyte, typically phosphoric acid, are used in a controlled manner with adjusting of the current and dwell time [45]. Alongside the increased corrosion resistance, electro polishing will also decrease the surface roughness. EU regulation 852/2004 on the hygiene of foodstuffs requires the surface to be of low roughness with $Ra \leq 0.8$ µm and free of pits, folds, crevices, cracks and misalignments [46]. Smoother topology decreases bacterial adhesion, minimising the risk of biofilm formation which also further increases the corrosion resistance [47].

2.2.1.3 Antimicrobial coatings

Release-based antimicrobial coatings: the incorporation of antimicrobial agents (AMAs) into a coating that gradually releases its payload with time is one of the most common methods for modifying food contact surfaces to control bacterial growth. These surfaces facilitate the inactivation of microorganisms when in close contact. One advantage of such systems is that, unlike antifouling or super hydrophobic surfaces, released-based surfaces do not only retard bacterial deposition and growth, but also inactivate bacterial cells. The short duration of their usefulness is a significant drawback of these coatings. The coating stops being effective once

all the AMA that was built into it during production has been released. Imbedding matrices with AMAs for slow release is one technique to extend this duration. Various antibacterial agents might be explored for this purpose, ranging from phenolic to heavy metals, [48,49]. The majority of these compounds function by denaturing proteins vital to bacterial action and/or by disrupting the plasma membrane of bacteria.

Silver nanoparticles and ions, have seen lots of interest as AMAs [50]. The key mechanisms of antimicrobial action of silver ions and NPs is reported to include interaction of the silver with thiol group of l-cysteine that disrupts enzymatic activity vital to cell function, the alteration of cell membrane permeability via electrostatic interactions, and DNA damage induced by reactive oxygen species (ROS) generation [51,52]. In a particularly intriguing work, stainless steel was coated with a porous, crystalline aluminosilicate zeolite. The coating was then impregnated with silver ions and inoculated with *L. innocua* and *E. coli* bacteria. The coatings minimized biofilm development by lowering *E. coli* populations by four log cycles over 8 hours and *L. innocua* populations by two log cycles over the same time period [53].

2.2.2 Laser anticorrosion methods

Stainless steel, renowned for its corrosion resistance and mechanical properties, is a crucial material in various industrial applications, including aerospace, biomedical, and chemical processing. Enhancing its corrosion resistance further can significantly extend the lifespan and reliability of stainless steel components. Laser processing has emerged as a promising technique to achieve this improvement. The key mechanisms by which laser processing can enhance corrosion resistance include.

1. Surface Modification: Laser treatment can alter the microstructure and composition of the surface layer, leading to improved passivation properties [54].
2. Grain Refinement: High cooling rates associated with laser processing can result in finer grain structures, which enhance the material's overall corrosion resistance.
3. Oxide Layer Formation: Controlled oxidation during laser treatment can form protective oxide layers that improve corrosion resistance [55].
4. Surface Smoothing: Lasers can reduce surface roughness, which minimizes sites for corrosion initiation [56].

Several different laser based methods have incorporated these mechanisms to increase the corrosion resistance of stainless steel, these include. Laser surface melting, Laser Cladding, Laser shock peening, Laser surface alloying and Laser surface oxidation

2.2.2.1 Laser cladding

Laser cladding (LC) is an advanced surface modification technique, widely used in industrial applications like rapid manufacturing, parts repair, surface coating, and alloy development[57]. This process typically involves using a laser beam to melt and deposit a wear- or corrosion-resistant alloy onto a substrate, forming a thin bonding layer with minimal dilution. The powder injection technique allows for mixing multiple powders with controlled feed rates, making laser cladding a flexible method for producing heterogeneous components and functionally graded materials. The high precision of laser cladding enables control over the material's microstructure, allowing tailored properties for specific applications. Laser cladding focuses on preserving the solid properties of the addition material. Additionally, the rapid heating and cooling rates of laser cladding can create extended solid solubility in metastable phases, opening possibilities for new materials with advanced properties[58,59].

A large area of interest is the laser cladding of high entropy alloys for anticorrosion. This is due to the huge flexibility of the composition of HEA coatings. By optimising LC process parameter, you can achieve a defect free macrostructure and uniform microstructure with exceptional anticorrosion properties. Two main HEA systems that are used for anticorrosion coatings are Fe-Co-Ni-Cr and Ti-Nb-Zr-Mo [59,60]. These surfaces have been looked at in equal molar and unequal molar ratios. Mg-Zr and Mg-Al systems for corrosion-resistant materials were studied as well [61,62]

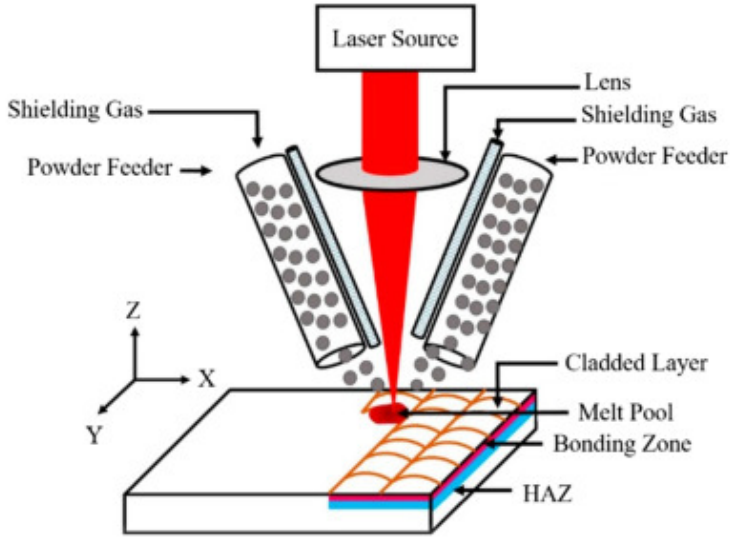

Figure 2-15: Schematic illustration of the laser cladding process [57]

2.2.2.2 Laser shock peening

Laser Shock Peening (LSP) is an advanced surface enhancement technique that uses high-energy laser pulses to induce compressive residual stresses on the surface of metallic materials, significantly improving their mechanical properties and fatigue resistance. The process involves applying short-duration laser pulses to a material's surface, generating high-pressure plasma that creates shock waves, leading to plastic deformation and beneficial compressive stresses [63–65]. These stresses counteract tensile stresses, preventing crack initiation and growth, thereby enhancing fatigue life and resistance to stress corrosion cracking. LSP enhances the durability and reliability of critical components without introducing mechanical damage or contamination. By refining the grain structure and increasing surface hardness [66,67]. LSP has been used in many industrial applications to reduce corrosion, such as pressurized heavy water and boiling water reactors in the nuclear industry, which experience severe stress corrosion cracking.

LSP is mainly used for materials that experience stress corrosion cracking (SCC) and intergranular corrosion cracking. SSC occurs in an event where a material experiences a tensile stress above the threshold value while simultaneously being inside a corrosive environment [68] .

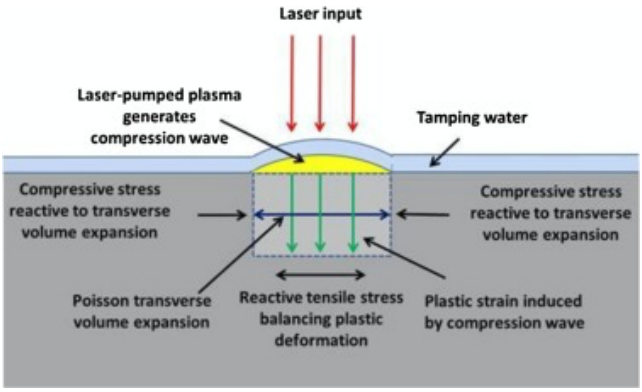

Figure 2-16: Schematic illustration of the laser peening process [69]

2.2.2.3 Laser surface oxidation:

Laser surface oxidation is a sophisticated technique in which a laser is directed across the metal surface at a power density below the ablation threshold. This controlled exposure allows the metal to react with ambient oxygen, resulting in a deliberate expansion of the oxide layer. This method enables precise refinement of the surface oxide composition and is adaptable to a range of materials, including titanium, steel, and aluminium alloys [70–72]. In this work, laser surface oxidation serves as the principal method employed for surface modification.

In a study by Cui, the production of the oxide film on AISI 304 stainless steel was examined using a 1064nm Nd:YAG pulsed laser and derived a thermokinetic model to describe the composition of the film produced [73]. A systematic illustration of the model can be seen in Figure 2-17 below. The energy distribution of a single laser pulse is uneven with the peak power being located at the center of the pulse and the energy decaying radial outwards following a Gaussian distribution this causes an uneven heating effect throughout the laser spot producing a non-homogenous morphology [74].

From XRD and XPS it shows that the composition of the center of the laser spot is mainly consisted of small grain Fe_2O_3 with small amounts of Cr_2O_3, while the edges consist of larger hexagonal grains of Cr_2O_3 with small amounts of MnO2. This data also shows that the concentration of Cr on the surface is twice that of the original sample going from 16.68 to 32.16% [73]. This will have a huge effect on the surface properties of the stainless stain, especially corrosion resistance.

The reason for this distribution Is due to the relationship between the thermodynamic and kinetic reaction occurring in the process. Initial the formation of Cr_2O_3 oxide is preferred over the formation of Fe_2O_3 as Chromium has a lot higher affinity for the chemisorbed oxygen then iron does so is thermodynamically favorable. This causes an initial increase of chromium at the surface of the stainless steel. But due to the higher temperature at the center of the laser spot and the higher diffusion rate of Fe inside the oxide layer, Fe_2O_3 becomes present at the surface of the stainless steel. This produces a duplex oxide at the center of the laser spot. Secondary compounds also become present in the surface layer such as spinel $FeFe_2$-$xCrxO_4$ [73].

This model becomes the explanation behind all the laser processing seen with in this

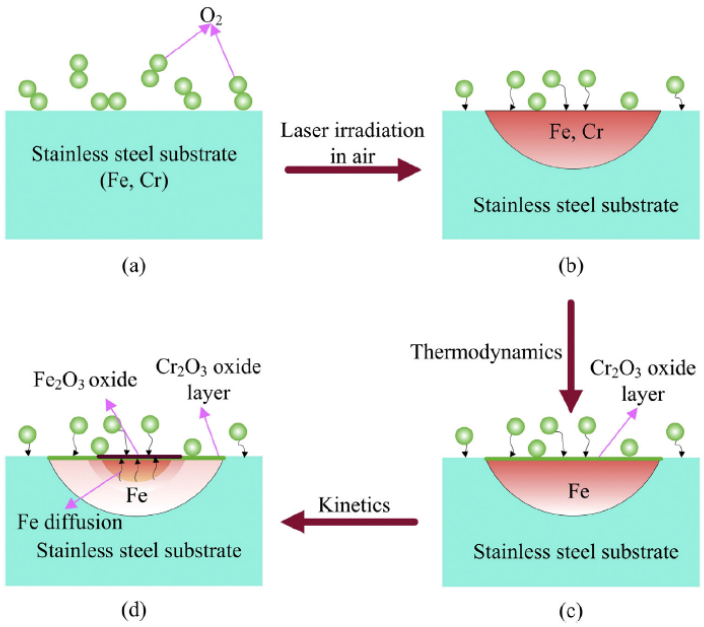

Figure 2-17: Thermokinetic model for the formation of the oxide layer by a single laser pulse [73].

These results were consistent with Li and Lu's studies [75,76]. Changing the laser intensity, focal offset, and scanning direction allowed Li to produce different colors on stainless steel. Figure 2-18 shows the colors produced. Each scanning run investigated the oxide laser's composition. The first run almost exactly matched Cui's results. However, further scans revealed a second oxide layer. The layer thickness grows from 140 nm in run 1 to 302 nm in run 6, changing the surface color due to thin layer interference effects [76]. The inner oxide

layer had a much greater concentration of Cr_2O_3, possibly due to the longer diffusion time allowing the Fe_2O_3 to build at the surface [76].

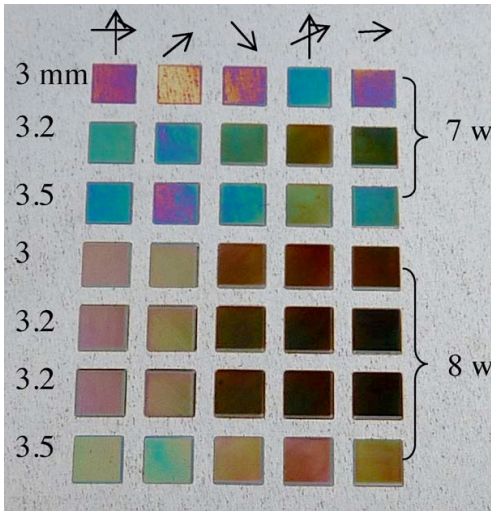

Figure 2-18: Colour map produced by different scanning directions [76].

In a study by Lecka et al., the corrosion resistance of the laser induced oxides produced on the AISI 304 stainless steel was investigated [77]. The results showed colour induced on the surface is dependent on the fluence input used which is described by the equation:

$$F_{Amax} = {2\sqrt{2}\,P}/{\pi\omega V} \qquad (2\text{-}8)$$

P = Laser power: ω = Radius of laser beam: V = scanning speed

The samples were electrochemically corroded in 3 percent sodium chloride solution and 3.5 pH sulphuric acid. The test used three electrodes: oxidised steels as the working electrode, SCE as the reference electrode, and a platinum wire counter electrode in the -1.0V to 0.8V. both environment showed similar results With lower fluencies of 50-70 J/cm2, there was an initial substantial rise in corrosion resistance, followed by a fast decline back down to a minimum with a smaller secondary local maximum at around 250 J/cm^2 fluence. These results can be seen in Figure 2-19 [77].

These results almost exactly match Z.L. Li and C.Y. Cui's surface chromium to iron ratio studies[73,76]. With higher fluence, the surface temperature rises, giving more time for iron

diffusion through the oxide layer. This reduces the Cr/Fe ratio on the metal surface, reducing the effect of the passivation layer and lowering corrosion resistance.[78] The cause of the secondary maxima is due to the formation of CrO3 caused by the higher temperatures seen. The greater fluence employed causes micro-cracks in the oxide layer Lawrence et al [79]. Due to the increased surface area and decreased impact of the passivation layer, these fissures allow electrolyte and oxygen into the oxide layer. Fluences under 100J/cm2 showed a well-sealed morphology with few to no fissures [80]. These factors combined to indicate that smaller fluences showed no corrosion after 6 hours in a brine chamber. [77]

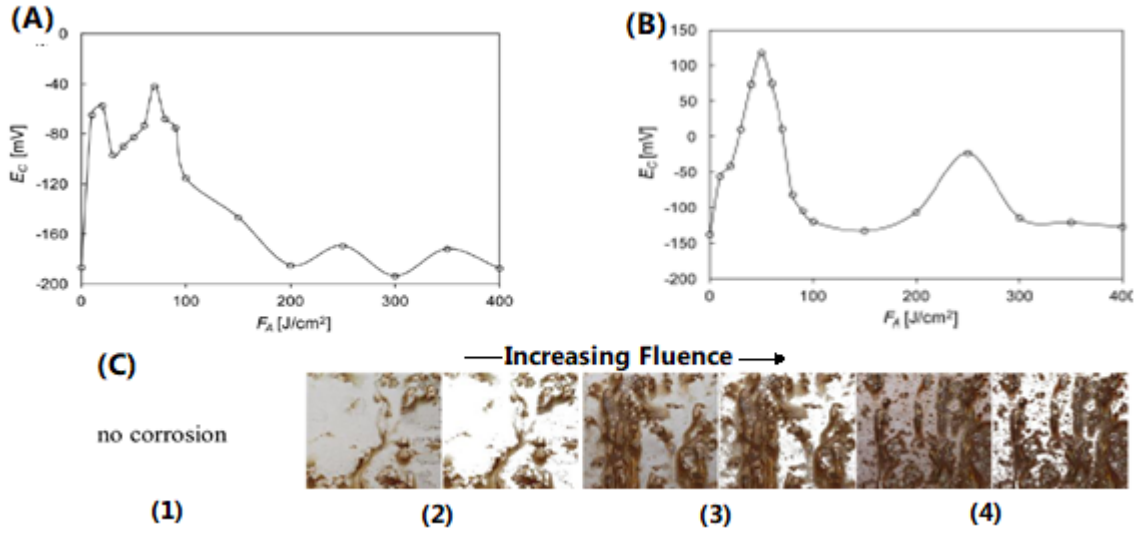

Figure 2-19: A) Corrosion potential vs fluence in NaCl. B) Corrosion potential vs fluence in H_2S0_4. C) Images of corrosion of 4 different fluences at 6 hours in a brine bath [77]**.**

2.2.3 Laser colouration methods.

Laser coloration of metals has been performed using three different methods. These are thin film oxidation, metal nanoparticle formation and period surface structures (PSS). These all change the optical properties of the surface causing a change of color. Metal nanoparticle formation by laser irradiation is mainly used on precious metals such as silver as they have a poor reactivity with oxygen.[81–84] Laser coloration is preferable to other coloration

methods such as chemical oxidation as it as it is a nondestructive/noninvasive method so will keep the intrinsic properties of the material. [85,86].

Coloration of stainless steel surface using periodic nano structures. This method uses a femtosecond laser with high scan speed and high repetition rate to produce periodic structures with a size smaller than the wavelength visible light. This will change the optical properties of the surface in the visible range causing a range of colors to be seen depending on the perimeter used. As the colour obtained is based on the interference of light seen so by changing the angle of incidence difference colors can be obtained [87,88]. Normally the periodic structure can only be produced in the micron size using a microscope objective lens [89]. But Yoshiki tamamura *et al*. proposed a method incorporating Low numerical aperture lens which allow grid spacing in the nanoscale which produced homogenous 'nanograting' on the surface. This method allows for a higher degree of freedom in the properties and widened the range of colours that can be obtained. [87]

A Ti:sapphire 800 nm, 100-fs and 10 Hz laser was used in for the creation of the nanograting on the stainless steel. The method was optimised to a fluence of 350 mJ/cm^2 a scan velocity of 17µm/s with a vertical scanning direction. This method produced a homogenous nanograting with a uniform period of d = 467nm which is approximately Λ/2. [87] This can be seen in Figure 2-20.

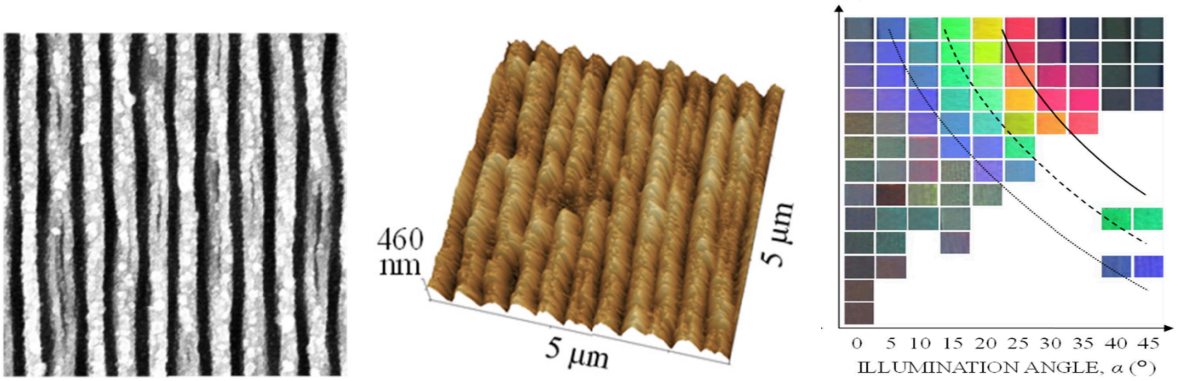

(A) (B) (C)

Figure 2-20: A) Nanograting at F = 350 mj/cm^2 for v = 17µm/s. B) Optical profilometry of the surface, C) Colour map produced by this process. [87].

A colour map was produced from this nanograting using the simplified equation

$$\boldsymbol{A} = (\boldsymbol{sin\alpha} + \boldsymbol{sin\beta}) \qquad (2\text{-}9)$$

where α is the incident angle and β is the observation angle. It shows that if A is constant the same wavelength/colour is produced. This can be seen by the 3 curved line in Figure 2-20 showing A = 1.05 for green, A = 1.20 for blue and A = 1.35 for red. Representing 490, 560 and 630nm wavelength respectively [87].

The main method of laser coloration is by the production of a surface oxides on the stainless steel this will produce a thin film on the surface which can cause thin film interference to occur causing a variation in colour to be seen. [90,91] Thin film interference is a phenomenon where a film on the surface cause light to be reflected twice. Once at the film air interface and a second at the film surface interface these reflected beams will either constructively or destructively interfere with each other producing different colours. The colour obtained is dependent on the phase shift of the light seen this is proportional to the thickness and the refractive index of the thin film produced [71,92]. This method can be performed on any material that can produce a passive layer, with stainless steel and titanium being able to produce a full colour spectrum range due to their mostly transparent oxide [93,94]. This method is most clearly seen on in the work by Antończak et. Al. where he illustrated the mechanism behind laser induced oxidation and shows the full range of colors present[95]. In this case the color is directly related to the thickness of the oxide later due to the colorless nature of the TiO_2 oxide present [96]. This can be seen in Figure **2-21**. For non-transparent oxide films such as Al compounds the color markers present are all dark color with color variation from dark to dark black [97].

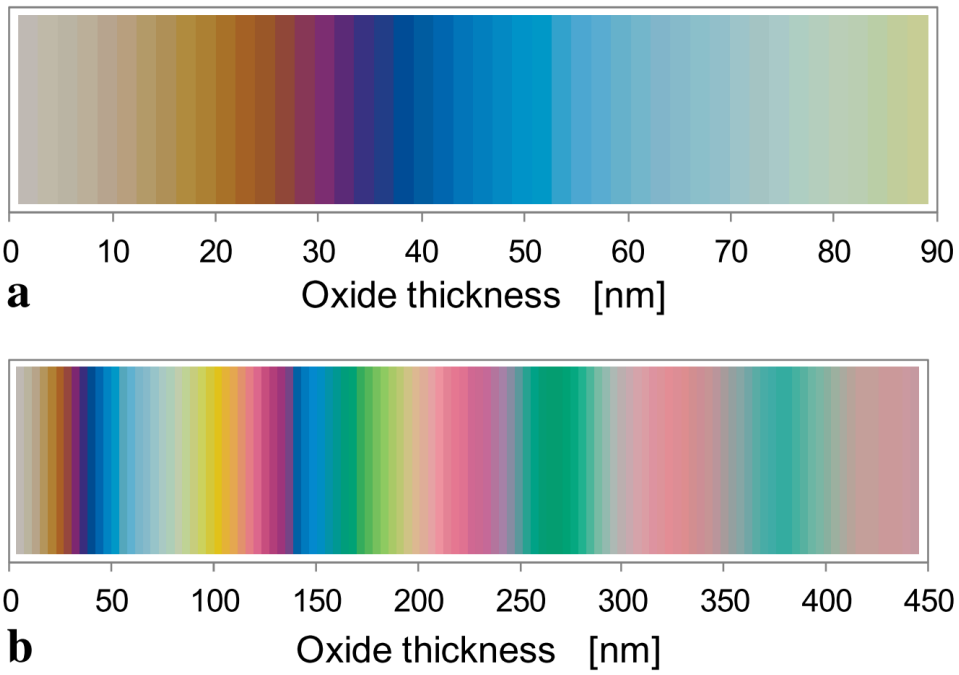

Figure 2-21: The analysis of oxide film thickness: (a) and (b) show the color sequences corresponding to oxide layer thicknesses in the ranges of 0–90 nm and 0–450 nm, respectively [95]

2.2.4 Laser Antifouling methods

Various methods for producing antifouling coatings have been previously investigated. Such techniques described below include direct laser writing, laser induced periodic structuring, and direct laser interference patterning.

2.2.4.1 Direct laser Writing

Direct laser writing (DLW) is one of the most common laser texturing methods due to its ease of processing and simpler equipment [98]. DLW has been used to produce a plethora of different 3D micro structure on a large variety of materials [99,100]. Even with its excellent texturing ability DLW is hindered by it low through-put processing minimizing its efficiency in large scale processing. To combat this issue DLW has more recently be combined with the other laser texturing method such as LIPSS (laser induced periodic surface structures) or DLIP (Direct laser interference patterns). A nanosecond pulse width DLW was used to produce a microcell pattern with a width of 50µm on TiAL6V4 followed by the use of a picosecond DLIP to create micropillars within the larger microcells at a width of 2.6 µm [101]. This was found to produce a hierarchical micro-nano structures on the surface of the material which in turn

increased the water contact angle (WCA) to a value over 110^{o}. DLW was also developed in work by Avik et al. [102] where the authors produced a method to fabricating super hydrophobic steel surfaces using a two-step process of water confined nanosecond laser texturing in combination with an immersion in cholosilane solution to hydrophobized the textured surface. The submerging of the steel specimen in deionized water confines the laser pulse induced plasma thereby increasing the texturing effect of the laser allowing for a higher throughput. This process produces a super hydrophobic micro-nano scale textures on the surface of the steel. The effect of different laser power on the final WSCA was investigate and showed a sharp increase in WSCA from 0 to 0.2GW/cm2 where the WSCA leveled off at 155 degrees.

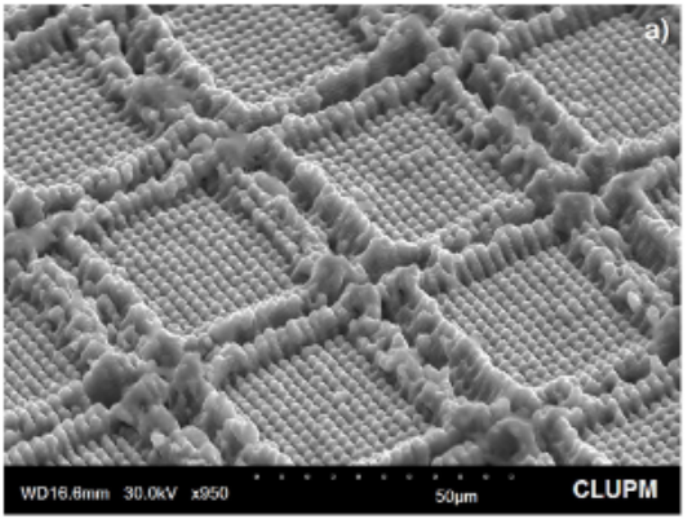

Figure 2-22: Antifouling stainless-steel surface containing a combination of Direct laser writing and Direct laser interference patterns [102].

2.2.4.2 Laser induced periodic structures.

Laser induced periodic structures also known as LIPSS are the self-organized structures produced by the laser irradiation of a material surface. LIPSS produces periodic ripple textures on the surface of the material with a spatial period (Λ). LIPSS are then broken down into two further categories based on the spatial period these are low spatial frequency LIPSS (LSFL) where the spatial period is roughly equal to the wavelength of the incident laser sources $\Lambda \sim \lambda$ and high spatial frequency LIPSS (HSFL) where $\Lambda \sim \lambda/3$ [103]. Due to the larger HAZ and less precise nature of short laser pulses only HSFL has being successfully synthesised using

ultrashort pulse lasers [104]. The mechanism for the formation of LIPSS is still under consideration but the most widely accepted being Sipes theory which is based on the interference of the incident laser radiation with surface electromagnetic waves that are generated by scattering on the surface roughness [105]. The wavelength scale of the LIPSS texture makes it an ideal chose for the creation of ordered micro-nano structures which increase antifouling and hydrophobic behaviour [106].

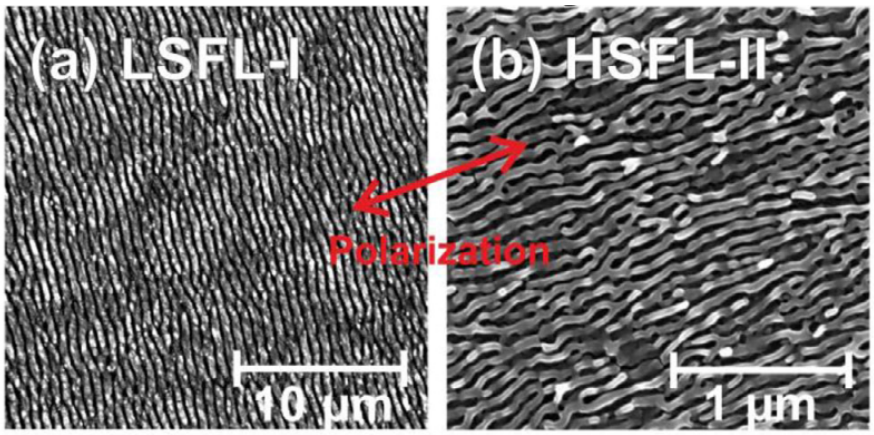

Figure 2-23: Lipss produced on TI_6AL_4V (a) Low spectral frequecny (b) High spectral frequency [104].

2.2.4.3 Direct laser interference patterning

Direct Laser Interference Patterning (DLIP) incorporates the uses of multiply coherent laser beams whose overlapping signals produces an interference pattern. This process produces periodic micro-nano structures on the surface of the material. The periodic structures/ removal of material corresponds to the amplitude distribution of the interference pattern [107]1]. The polarization, number of beams and laser fluence all contribute to the distribution and size of the final texture produced. [108] [109]. DLIP is the most suitable laser texturing process for high through put processing due to its ability to process sub-milliscale areas with a single pulse and fast processing speed of 0.9m2/min [110]. The spatial period (Λ) for a 2-laser beam system is described by equation 2-10.

$$\boldsymbol{\Lambda = \lambda / 2 sin(\theta)} \qquad (2\text{-}10)$$

With λ being the incidence wavelength of both beams and θ being the incident angle between the 2 beams. LIPSS is also commonly formed during the DLIP process producing

higher order structures on the surface [111]. In the work done by [108] the effect of altering process parameter on the homogeneity of DLIP on Ti6Al4V using a nanosecond Nd:YLF laser was investigated. This worked showed that the hatching distance is the most significant parameter for the surface homogeneity with a relevant importance on the large periodic modulation it shows that the hatching distance must be a multiple of the interference spatial period and must be smaller than the laser beam diameter. Higher pulse-to-pulse overlaps also showed the highest texture homogeneity with the overlap having a strong influence on the structural depth of the line pattern. The lowest Surf Err% values of 21% was obtained using a spatial period of 5.82µm and a hatch distance of 29.10 µm. This increase homogeneity has been seen to increase the water contact angle and antifouling properties

2.3 Pulsed electric Field Systems

2.3.1 What is it

Pulsed electric field (PEF) is a non-thermal method of preserving food that incorporates the use of high voltage short electric pulses, usually in the millisecond range. Theses pulses cause microbial inactivation while not negatively affecting food quality. Due to this beneficial effect compared to tradition thermal pasteurization, PEF has gained increased interest since the late 1960s [112]. A full transition from thermal to PEF has not occurred in industry electrode issues are discussed in section 2.3.3 below which are an application focus of the investigated laser surface modification process.

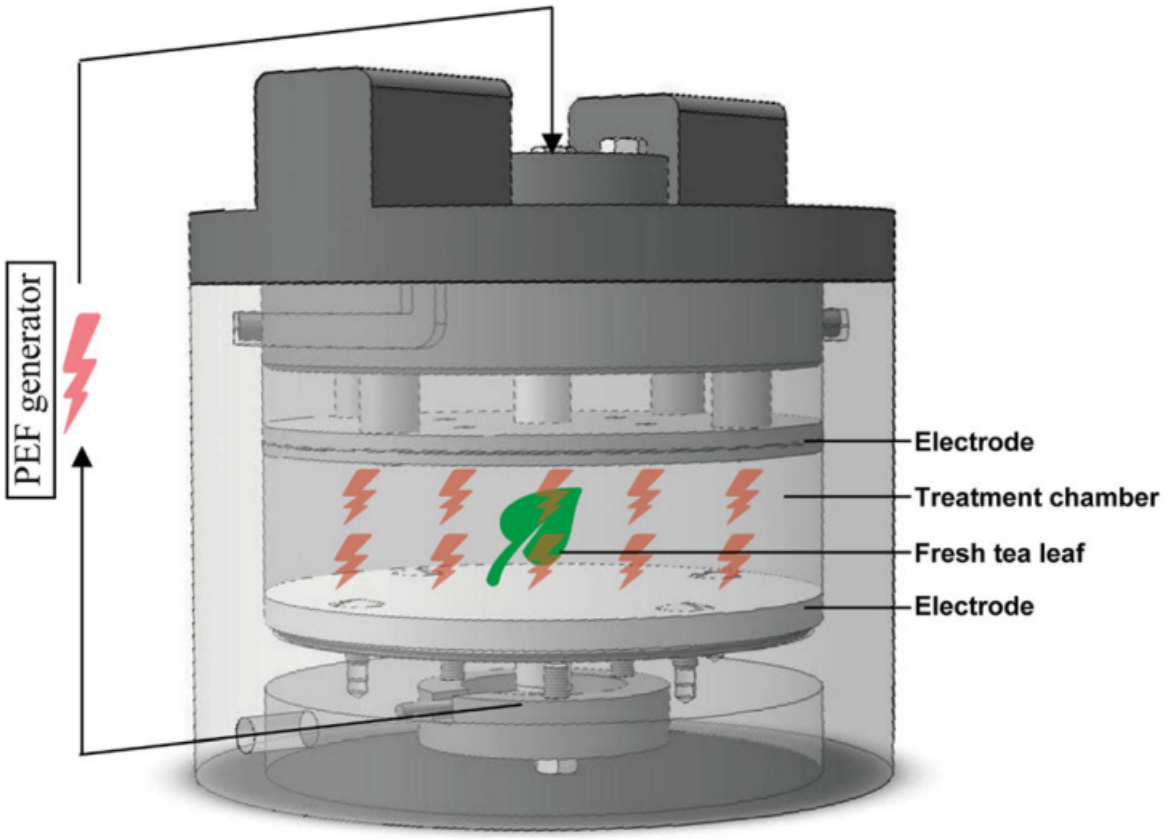

Figure 2-24: Schematic of a Pulsed electric field system [113].

2.3.2 How Pulsed Electric Field system works

PEF systems deliver short pulse of high electric fields with durations in the millisecond range and pulse strengths ranging from 1 to 100 kV/cm^2 to the target area. Upon subjecting the bacteria to the pulse, polarization of the dipoles and separation of the ions occurs, resulting in the generation of a resistive and capacitive current across the PEF cell seen in Figure 2-24. A simple parallel plate RC circuit can then be used to describe the behavior of this system. Based on the assumption that the food has uniform dielectric and electrical properties, the capacitance and effective resistance can be calculated as

$$C = \frac{\varepsilon_0 \varepsilon_{rA}}{d} \quad R = \frac{\rho d}{A} \tag{2-11}$$

where ε_0 is the permittivity of free space, ε_r, is the relative permittivity, i.e. dielectric constant of the food material, A is the electrode area, d is the gap between the two parallel electrodes, and ρ is the resistivity of the food [114].

The PEF Pulse induces dielectric breakdown of the bacteria cell membrane, resulting in pores in the membrane, which causes cell impairment and eventually cell death, as shown Figure 2-25. To ensure that dielectric, breakdown of only the bacteria cells and not the food itself, the applied field strength (E) needs to be lower than the dielectric strength of the food being processed (E_b) [114]. When the food undergoes dielectric breakdown, this is referred to as spark-over, and it can result in reduced lifetimes inside the PEF chamber due to increased electrical current, the evolution of gas bubbles, an increase in pressure, and the possibility of arcing [115].

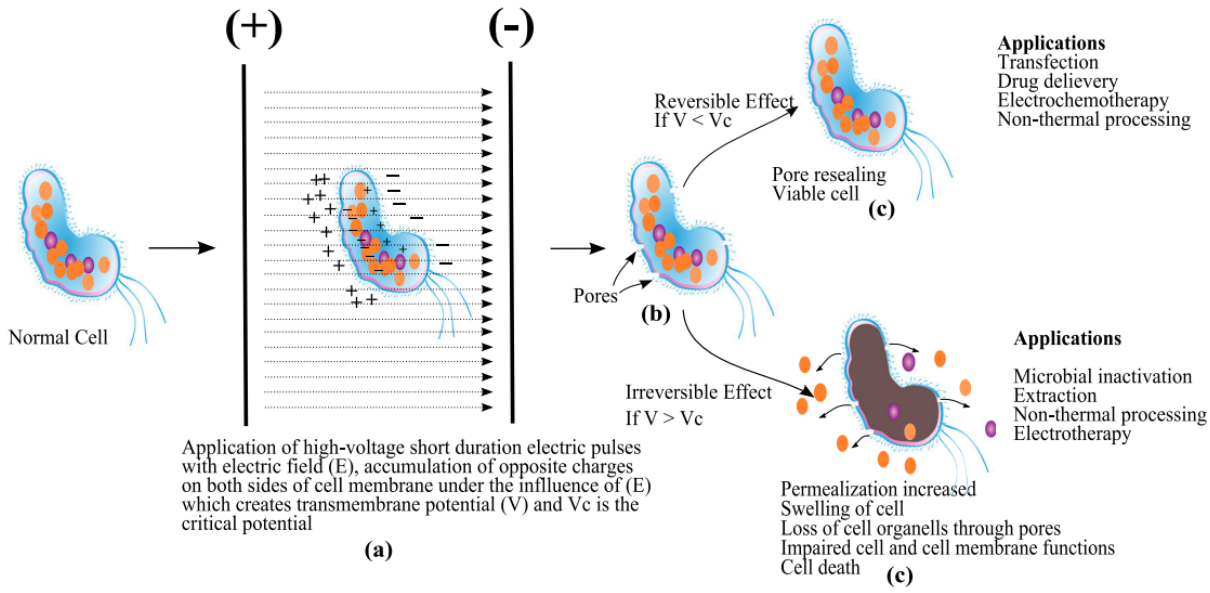

Figure 2-25: Schematic diagram of the mechanism of pulsed electric filed pasteurization [116].

2.3.3 Current issues

Currently, two main electrode challenges are sought to be overcome for the Pulse Electric Field system. First, a short life span of the electrodes themselves, which must be replaced frequently due to the high corrosion that occurs; and second, biofouling caused by the food product inside the system, which results in arcing and reduced flow inside the system, further reducing the system's lifetime [117].

During the treatment of the food produce, the two electrodes of the PEF system are in direct contact with the liquid media. The charged particles serve as current carriers in the liquid medium, whereas the current carriers in the electrodes are made up entirely of free electrons. In order to preserve charge conservation at the electrode-food interface electrochemical reactions must occur. These reactions result in corrosion of the electrode, which reduces the electrode's lifetime and increases the possibility of contamination of the food product.

2.3.4 Electrode Chemical Reactions

The PEF system can be simply described as a two-electrode system connected with an electrolyte. At the electrode-electrolyte interface an electrical double layer is formed where electrochemical reactions can occur, this layer behaves similar to a capacitor. The voltage across this double layer increases as an external voltage is applied to the electrode; once this voltage reaches a certain level (referred to as the threshold voltage U_{th}), two independent electrochemical half-cell redox reactions begin to take place. After charging of the double layer, the solution is decomposed due to the current which passes through [118].

The equivalent circuit depicted in Figure 2-26 can be used to represent the processes described above with C_{DL}, R_S, R_f representing the double layer capacitance, the resistance of the solution and the decomposition current respectively. As most PEF systems use the same material for both electrodes, this allows two equivalent values to be used for the metal electrolyte interface. This simplifies the circuit further as shown in Figure 2-26b , (i.e. $C'_{dl} = ½ C_{dl}$ and $U'_{th} = 2.U_{th}$) [118].

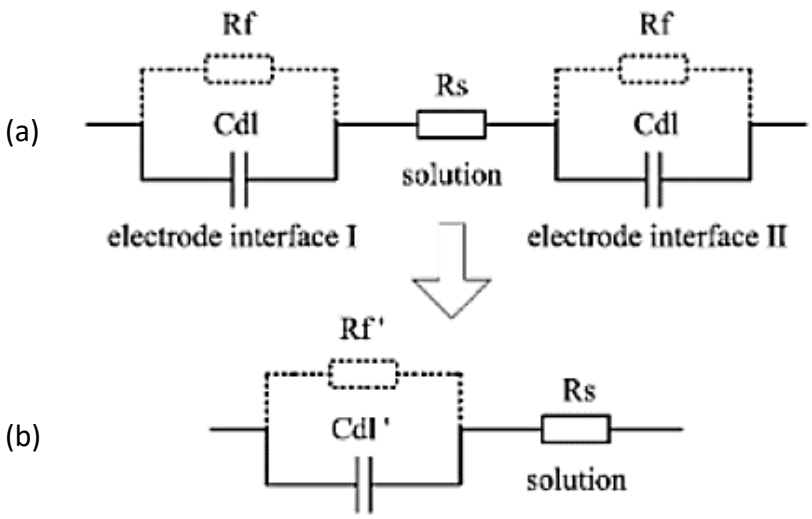

Figure 2-26: Equivalent circuit diagram representations of a two identical electrodes inside an electrolyte solution (a) showing equivalent circuit where different electrode materials are used and (b) showing the equivalent circuit where the same material is used for both electrodes [117].

During the applied voltage pulse, the double layer voltage is charged past the threshold voltage and back down. The time taken to reach this threshold is described by the equation (2-12) where t_{th} is the threshold time and I is the current flowing through the chamber [119]. This equation shows that if the pulse width of the system is shorter than the threshold time, no electrochemical reactions will occur. As the pulse width is usually a fixed parameter during PEF treatment, Figure 2-27 is presented to show the threshold current density required for the range of pulse widths most commonly used in industry.

$$\boldsymbol{t_{th}} \frac{\boldsymbol{C'_{dl} U'_{th}}}{\boldsymbol{i}} \qquad (2\text{-}12)$$

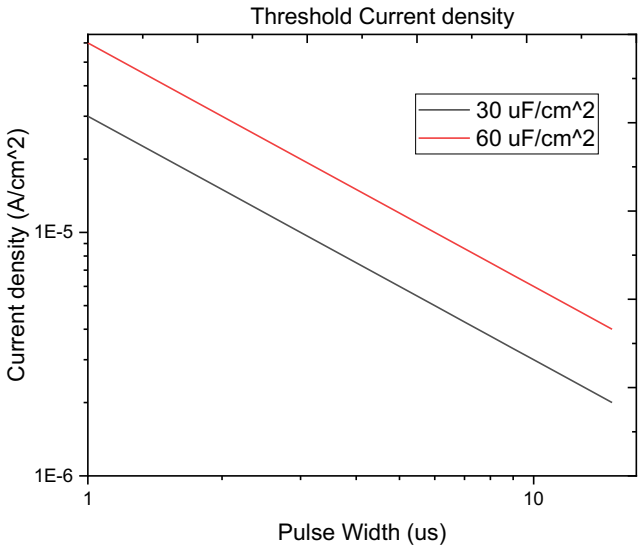

Figure 2-27: Threshold current density vs pulse width for 2 different electrode materials with double layer capacitance of 30 µF/cm^2 (Stainless steel) and 60 µF/cm^2 (Ti_6AL_4V) [119].

The electromotive series is used to determine the order in which oxidation and reduction reactions take place after the threshold voltage has been reached. Table 2-1 shows the electromotive series for stainless steel, which is the most commonly used PEF electrode. This table shows the possible half-cell reactions as well as the standard reduction potentials for stainless steel (E^0). In addition, the elements of the most commonly used electrolytes, NaCl and H_2O, are also shown in this table.

In most cases, the reaction with the more negative half-cell reduction potential takes place at the anode and is referred to as oxidation. The reaction with the more positive half-cell reduction potential takes place at the cathode and is referred to as a reduction reaction [118]

E^{o}_{RED}	Reactant		Product	Reaction #
1.36	$Cl_{2(g)}+2e$	⇔	$2Cl_{(aq)}$	1
1.23	$O_{2(g)}+4H^{+}_{(aq)}+4e$	⇔	$2H_2O_{(l)}$	2
0.77	$Fe^{3+}_{(aq)}+e$	⇔	$Fe^{2+}_{(aq)}$	3
0	$2H^{+}_{(aq)}+2e$	⇔	$H_{2(g)}$	4
−0.04	$Fe^{3+}_{(aq)}+3e$	⇔	$Fe_{(s)}$	5
−0.28	$Ni^{2+}_{(aq)}+2e$	⇔	$Ni_{(s)}$	6
−0.41	$Cr^{3+}_{(aq)}+e$	⇔	$Cr^{2+}_{(aq)}$	7
−0.44	$Fe^{2+}_{(aq)}+2e$	⇔	$Fe_{(s)}$	8
−0.74	$Cr^{3+}_{(aq)}+3e$	⇔	$Cr_{(s)}$	9
−0.83	$2H_2O_{(l)}+2e$	⇔	$H_{2(g)}+2OH_{(aq)}$	10
−0.91	$Cr^{2+}_{(aq)}+2e$	⇔	$Cr_{(s)}$	11
−2.71	$Na^{+}_{(aq)}+e$	⇔	$Na_{(s)}$	12

Table 2-1: The electromotive series for the most common stainless steel elements plus the electrolyte NaCl [118].

To look further into the reactions that occur during a single pulse, Figure 2-28 divides one bipolar (contains both positive and negative potion of the waveform) into 4 fragments.

Fragment 1

When no voltage is applied to the electrodes, the cell will behave as an electrolytic cell, and no current or voltage will flow through the system. If both electrodes are made of the same composition and the electrolyte is homogeneously distributed, the cell will behave as an electrolytic cell and no current or voltage will flow through the system.

Fragment 2

Electrode 1 is assumed to be the cathode and 2 is assumed to be anode. Thus, current flows from 2 to 1 and electrons flows from 1 to 2. As the voltage is increase in the cell the ionic species of the electrolyte Na^{+} and Cl^{-} will migrate toward the anode and cathode respectively. At the anode there are only two substances present that can be oxidized: Cl^{-} and H_2O. As water has a lower reduction potential than Cl- (at 1.23V and 1.36V, respectively), water should oxidize first; however, because the potentials are nearly identical and Cl- reactions kinetics are significantly faster than those of water, Cl- oxides first, followed by water. At the cathode two substance are also present that can be reduced: Na^{+} and H_2O. In this case water will reduce much easier than sodium ions due to their large reduction potential difference (-0.83V

and -2.71V respectfully). These reactions result in the formation of H_2 and OH^- at the cathode, as well as O_2, Cl_2 and H^+ ions in the vicinity of the anode.

The stainless steel electrode remains inert initial due to the present of the native oxide film that forms on the surface. This degradation of the film is greatly accelerated by the creation of secondary compounds, which are discussed in greater detail in section below. Once the film is damaged, the water and Cl^- ions will react with the iron present, oxidizing it at the anode. From the point of view of thermodynamic, the order of reactions at the anode will be reaction numbers, #5, #6, #8, #9 and finally #11 seen in Table 2-1.During the corrosion process, iron reacts first then nickel and finally chromium.

Fragment 3.

Once the pulse waveform transitions into the negative the anode and cathode are filled. Electrode 1 now becomes the anode and electrode 2 the cathode. This will cause migrations of the newly formed ions. There will be a high concentration of O_2, Cl_2, and H^+ at the cathode, and a high concentration of H_2, OH^- and Na^+ ions at the anode. The reaction order can be seen from Table 2-1. This Fragment seems to oxidize (partial) the reduced products from fragment 2 and reduced the oxidized produces from fragment 2.

Fragment 4

If there has been no damage to the electrode or changes in the chemical composition of the electrode, this fragment will behave in the same way as fragment 1. Depending on whether one of the electrodes has been damaged (corroded) or whether there is still an inhomogeneity in the reaction electrolyte, the cell can be converted from an electrolytic cell to a galvanic cell. This results in a voltage flowing through the cell without the need for an external source of power. This allows electrochemical reactions to continue to occur, which are referred to as galvanic corrosion. This can be minimized by draining the electrolyte from the system while it is not in use.

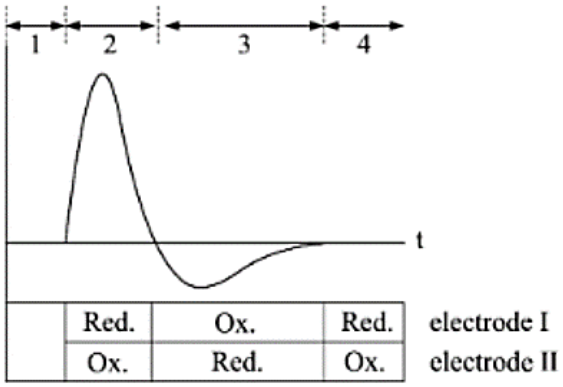

Figure 2-28: Four distinguishable fragments during a PEF pulse and for each interval of the reaction, noting the reactions per electrode [118].

2.3.5 Secondary chemical reactions

Alongside the primary electrochemical reactions that occur at the electrode electrolyte interface, secondary reactions can also take place inside the solution, these reactions are a lot more condition dependent then the primary as reacting media, pH, and chemical composition of the electrode will all change the route and type of the reactions that can occur. Here are some examples of common secondary chemical reactions seen [120].

The chloride gas (Cl_2) produced at the anode can react with the water molecules producing hypochloric acid.

$$Cl_2 + H_2O = HCLO + H^+ + Cl^- \quad (2\text{-}12)$$

Metal ions released from the electrodes can act as Lewis acid and spontaneous undergo hydrolysis reactions

$$Fe^{3+} + nH_2O = Fe(OH)_n^{3-2+} + nH^+ \quad (2\text{-}12)$$

Iron ions can also act as catalysts in the Fenton reaction

$$Fe^{3+}\, H_2O_2 = Fe^{2+} + \cdot OH + OH^- \quad (2\text{-}13)$$

$$Fe^{2+}\, H_2O_2 = Fe^{3+} + \cdot OOH + H^+ \quad (2\text{-}14)$$

These radicals are extremely reactive species and can interfere with possible food sources and react with the electrode leading to further corrosion. There metal ions can also react with

the food molecules themselves forming metal complexes or coagulant. Some work performed by [121] showed that small amounts of irons ions being released can slow down further reactions from occurring. These iron ions are hydrolyzed at the anode that can reduce the pH of the solution at that point.

2.3.6 Method to reduce metal released

Most methods in the literature for reducing metal release in PEF systems focus on optimizing processing parameters and selecting appropriate media, with limited research on modifying the electrodes themselves. Roodenburg et.al. introduced a proof-of-concept approach involving a conductive film overlay on electrodes [122]. FEA tests with a conductive copolymer film showed it could reduce *Lactobacillus plantarum* by up to 2.1 log at certain energy levels, although achieving full pasteurization remains challenging due to the need for lower energy inputs. Additionally, the disposable nature of these film electrodes may limit their application across various industries.

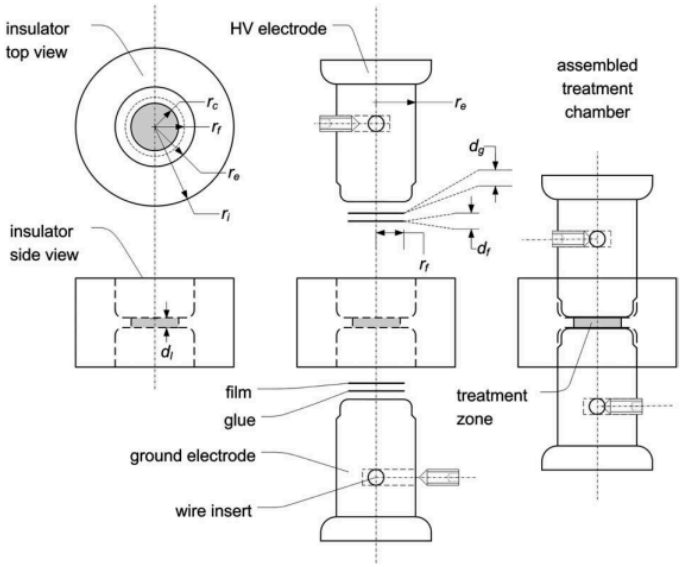

Figure 2-29: Construction drawing of the batch type treatment chamber, which can be equipped with any plastic electrode covering.[122]

2.4 Experimental Analysis

In this section, the primary analytical techniques employed in this study are outlined. These include surface chemical characterization via X-ray Photoelectron Spectroscopy (XPS), corrosion behaviour assessment through Linear Polarization and Electrochemical Impedance Spectroscopy (EIS), and statistical analysis using Design of Experiments (DOE) and Analysis of Variance (ANOVA).

2.4.1 XPS Spectroscopy

XPS is a powerful surface-sensitive analytical technique used to identify the elemental composition, chemical state, and electronic environment of atoms within the top ~1–10 nanometers of a material's surface. It works by irradiating a sample with monochromatic X-rays (typically Al Kα) which eject core-level electrons from atoms. The kinetic energy (KE) of these electrons is measured, and the binding energy (BE) is calculated using the photoelectric equation [123]:

$$BE = h\nu - KE - \phi \qquad (2\text{-}15)$$

With hν photon energy of the X-ray, and ϕ being the spectrometer work function.

Each element has characteristic binding energies, allowing for identification and quantification of elements present on the surface. XPS can also distinguish between different oxidation states (e.g., Cr^{3+} vs. Cr^{0}) based on small shifts in binding energy.

Raw peak areas from XPS spectra do not directly reflect the true atomic concentrations. Several correction factors must be applied for accurate quantitative analysis, these are Sensitivity Factors, Background Subtraction, Peak Overlap and Deconvolution, Charge Correction and Surface Contamination

Sensitivity Factors, Each element has a different photoionization cross-section, electron mean free path, and detector efficiency. To account for this, raw peak areas are divided by element-specific RSFs, The RSFs used where obtained from standard libraries and can be seen in Table 3-3 .

Background Subtraction, A background signal from inelastic scattering must be removed before integrating the peak area. For all samples in this work a Shirley background was used.

Peak Overlap and Deconvolution, Some peaks may overlap (e.g., Fe 2p with satellite peaks). Proper peak fitting and deconvolution is necessary to isolate the true signal from each element or oxidation state this as done using casa XPS software and can be seen in Figure **3-3**.

Charge Correction, Non-conductive samples can experience surface charging, which shifts the binding energy to combat this shift correction via aligning peaks is done. For this work C 1s from adventitious carbon was used as the correction peak as it has a standard reference value of 284.8 eV[124].

Surface contamination, such as adventitious carbon or oxygen can significantly affect the accuracy of elemental ratio calculations in XPS analysis. To mitigate this, sputtering was performed prior to depth profile XPS measurements to remove surface carbon contamination. Additionally, for the data referenced from Paper 3, the total carbon content in all samples remained below 2 at% and was therefore deemed acceptable for exclusion in the quantitative analysis presented in this report.

2.4.2 Potentiodynamic polarization

Potentiodynamic polarization is a widely used electrochemical method for evaluating the corrosion behaviour of metals by assessing their response to a broad range of applied potentials. It provides detailed insights into corrosion mechanisms, corrosion rate, passivation behaviour, and pitting susceptibility. In this technique, the sample is polarized (i.e., its potential is changed) in a controlled manner, typically starting from a value slightly below the open circuit potential (OCP) and sweeping in the anodic direction. During the sweep, the current response is measured, producing a polarization curve that plots current density (log scale) versus applied potential. The polarization curve can be used directly to obtain the corrosion potential (Ecorr), pitting potential (Epit) and to analysis the passivation region of the curve. With the use of Tafel interpolation the corrosion current (Icorr) can be obtained [125,126].

a) b)

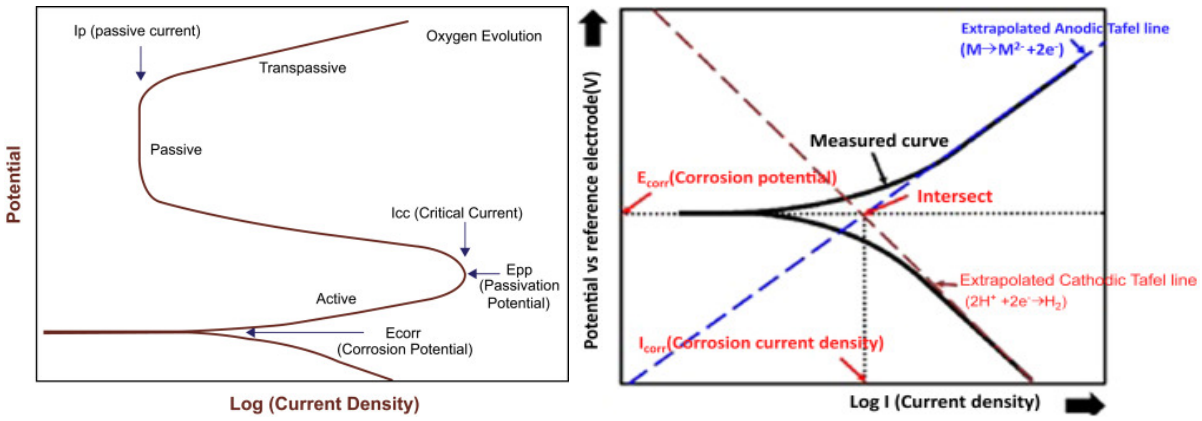

Figure 2-30:(a) Showing a potentiodynamic polarization plot of a material that is experiencing pitting corrosion, (b) Graphical demonstration on how the Tafel plot is preformed and analysed (corrosion nomenclature is not standardised full so you can see different name for the same terms) .

Pitting Potential

Epitt is the potential at which a sudden increase in anodic current occurs after the passive region, indicating localized breakdown of the protective oxide layer and the initiation of pitting. A higher Epitt value reflects greater resistance to pitting corrosion.

Corrosion Current Density

Icorr represents the rate of uniform corrosion and is determined through Tafel extrapolation. By extending the linear regions of the anodic and cathodic branches of the polarization curve back to their intersection at Ecorr, the corresponding current density is obtained. Lower Icorr values indicate lower corrosion rates.

Tafel Slopes

Tafel slopes characterize the kinetics of the anodic and cathodic reactions and are extracted from the linear (logarithmic) segments of the polarization curve. These slopes are essential for calculating Icorr using the Stern–Geary equation (equation 2-16) and provide insight into the reaction mechanisms at the interface.

$$I_{corr} = \frac{\beta_{anodic}\beta_{cathodic}}{R_{pol}2.3(\beta_{anodic} + \beta_{cathodic})} \quad (2\text{-}16)$$

Where β_{anodic}, $\beta_{cathodic}$ are the Tafel slopes, R_{pol} Represents the polarization resistance. [125,126]

2.4.3 Electrochemical Impedance Spectroscopy

Electrochemical Impedance Spectroscopy (EIS) is an advanced analytical technique used to study the electrochemical properties of materials and interfaces, particularly in corrosion science, and surface coating evaluation. EIS measures the impedance (resistance to alternating current) of an electrochemical system over a wide range of frequencies. A small AC voltage (typically 5–10 mV) is applied to the system, and the resulting current is measured. By analysing how the system responds to different frequencies, valuable information about electrochemical processes can be extracted. This is usually represented as 2 separate plots Being the Nyquist and Bode Plots. With the Nyquist plots graphing Imaginary impedance vs. real impedance useful for identifying resistive and capacitive behaviour. While the Bode plots Graph Impedance magnitude and phase angle vs. frequency used to analyse time constants and process kinetics.

The most valuable information comes from the Nyquist plots which can be analysis using an Equivalent Electrical Circuits (EECs), which model the electrochemical behaviour of a system through combinations of electrical elements such as resistors, capacitors, and constant phase elements. This method allows complex interfacial phenomena to be interpreted in terms of well-understood electrical analogy. A basic model, such as the Randles circuit, typically includes a solution resistance (Ru) in series with a parallel combination of charge transfer resistance (Rp) and double-layer capacitance (Cdl). For systems with non-ideal capacitive behaviour—often due to surface roughness or inhomogeneity—the Cdl is replaced with a constant phase element (CPE). More complex systems, such as those involving coated metals or duplex oxide layers, may require models with two time or more constants, represented by two CPEs combinations in series. By fitting the experimental EIS data (usually Nyquist and Bode plots) to an appropriate EEC model, values for Rp, Ru, CPE, and other parameters can

be extracted. These values provide quantitative insights into corrosion resistance and interfacial properties; for instance, a higher Rp suggests improved corrosion resistance, while the presence of Warburg impedance indicates diffusion-controlled processes. Selecting and validating the correct model is essential to accurately interpreting the electrochemical processes occurring at the material's surface [127] .

2.4.4 Design of Experiments (DOE)

Design of Experiments (DOE) is a structured methodology used to systematically investigate the relationships between multiple input factors and one or more response variables. In the context of laser surface modification, DOE allows researchers to vary parameters such as laser power, frequency, scan speed, and hatching distance in a controlled manner to evaluate their individual and combined effects on outcomes like surface chemistry, color, or corrosion resistance. This approach improves efficiency, reduces the number of required experiments, and enables the identification of optimal processing windows with high reproducibility. Two types of design where used they were full factorial designs and body centre cubic designs (BCC)

A full factorial design is a type of DOE in which all possible combinations of selected factor levels are tested. For example, a 3-factor, 3-level full factorial design would require 27 experiments (3^3). This design is highly effective for identifying not only the main effects of each factor but also all possible interactions between them. In your research, a full factorial approach was employed to explore how each laser processing parameter, as well as their interactions, affected oxide formation and corrosion behaviour, allowing for robust model development and precise optimization.

Body-Centred Cubic (BCC) Design

The Body-Centred Cubic (BCC) design is a type of response surface methodology used in DOE to model nonlinear relationships between multiple factors and a response. It includes experimental points at the centre and midpoints of the design space, forming a structure similar to a body-centred cube. BCC designs are efficient for fitting quadratic models while requiring fewer runs than full factorial designs. In this research, BCC was used to optimize the

effect of processing parameters inside the PEF system by capturing both linear and interaction effects with reduced experimental effort.

Analysis of Variance (ANOVA)

Analysis of Variance (ANOVA) is a statistical tool used alongside DOE to determine which factors and interactions significantly influence the response variable. It separates the total variance observed in the data into components associated with each factor and their interactions, and compares these against the residual error using F-tests. A low p-value (typically <0.05) indicates that the factor has a statistically significant effect. ANOVA calculates the percentage contribution of each factor to the total variation in the response. This helps rank the factors by importance and understand which variables have the strongest influence on performance. ANOVA analysis can also be used to produce models to describe the system where ANOVA outputs R^2 (coefficient of determination) and Adjusted R^2, which indicate how well the model explains the variability in the data. Higher values (close to 1) suggest a strong fit between the model and experimental results.

The results from ANOVA can be used to produce interaction plots or response surface plots which can visually show how two or more factors influence the response together, revealing synergistic or antagonistic effects [128].

2.5 Conclusion and Aims of work

The aim of this thesis was to generate a fundamental understanding of how the laser processing parameters can change the surface properties of stainless steel, including chemical and morphological properties. Pulsed electric field systems are used for the non-thermal pasteurisation of food products, but some drawbacks and challenges of the technology include low electrode lifetime and electrode fouling. The goal of this work is to identify the reasons for this short life time and come up with an approach to maximise the stainless steel life time. Most of the work in the area of PEF corrosion reduction has been focused on system process optimisation such as changing reaction media (pH and salt concentration), optimising processing parameter (voltage and frequency) and machine design (chamber shape, electrode spacing). The area that I have investigated is the modification of the electrode surface itself with a view to reduce corrosion. This was only minimally investigated previously

in the literature. In those past published works, the electrode was coated with ceramic or polymer, which can lead to the possible contamination of the reaction media.

The approach taken in this study involved the use of laser surface oxidation, as this method could reduce corrosion without introducing new compounds to the material's surface. Although laser surface oxidation has been previously explored, limited research has focused on the impact of processing parameters on corrosion outcomes. This thesis presents research to enhance the corrosion resistance of stainless steel by controlling the laser surface modification process parameters. This increase in electrode lifetime was specifically examined within the context of a pulsed electric field system.

This work was undertaken with three focus areas:

1, There has been limited past investigation into the mechanisms by which laser-induced oxidation affects the chemical composition and morphology of 316L stainless steel, with particular focus on how this process changes the Mo content, which can significantly impact the intergranular corrosion of stainless steel—an especially critical factor in acidic food environments. This research focus employed a full factorial DoE approach to modify the process parameters, including laser scan speed, laser power, and laser frequency. The results, analysed through XPS, were targeted to contribute to a deeper understanding and refinement of the existing thermokinetic model for laser surface oxidation.

2, Few studies have examined the effects of modifying individual laser processing parameters on the corrosion aspects of laser-induced oxidation. There has been a gap in the literature related to the understanding of how the laser surface oxidation of 316L can effect corrosion properties. Given the wide range of available processing parameters, it is crucial to identify the most impactful ones to modify. This research provides a comprehensive characterization of laser-induced oxides on 316L stainless steel, fabricated using a 3.5W Nd: YAG laser according to two full factorial DoEs, investigating laser power, laser frequency, hatching distance, and scan speed. The study analysed the impact of these parameters on corrosion properties, followed by detailed chemical analysis.

3, No studies have investigated the extent of metal release from PEF electrodes and its mitigation through laser surface modification, making this work the first practical application

of this approach. Initially, a body-centered cubic DoE design was used to identify the impact of altering PEF processing parameters on metal release, measured by ICP-MS. Following this, three laser-processed electrodes were incorporated into the PEF system and tested under the most extreme conditions over an extended testing period and there impact on the corrosion result were evaluated

Chapter 3 Mechanism for control of laser induced stainless steel oxidation

Publication Status: Published

Mark Swayne, Gopinath Perumal, Dermot Brabazon, Mechanism for Control of Laser-Induced Stainless-Steel Oxidation, Advanced Materials Interfaces. DOI:10.1002/admi.202300991

Abstract

This paper presents the development of a model for Nd:YAG laser surface oxidation of 316L stainless steel. Full factorial design of experiments were implemented to produce a model for the prediction of elemental composition and colour produced via laser surface oxidation. The elemental composition of the films produced where measured using X-ray photoelectron spectroscopic and the colour was measured using optical reflectance spectroscopy. Oxide layers produced were seen to have a Cr/Fe ratio in the range of 0.13 to 2.09, and highly controllable colour variation via single-pass laser process. The effect of the process parameters used such as power, frequency and scan speed on laser-induced oxides was examined with an aim to produce a model suitable for predictive control of the elemental composition and colour of the oxide film. Surface morphology control via alteration of the laser power was found to be an important factor for defining the resulting surface colouration. A new finding from this work is the discovery that within the range of laser surface processing parameters investigated, the molybdenum concentration is inversely proportional to the chromium concentration. This paper provides data required for control of 316L stainless steel surface chemistry, and for the expansion of the current thermokinetic model to incorporate the mechanistic effect of molybdenum.

3.1 Introduction

Stainless steels are among the most widely used alloys in a variety of applications such as the automobile, pharmaceuticals, food, marine, and architectural fields due to its low cost, excellent mechanical strength, ease of fabrication, surface lustre, and resistance to corrosion.[129,130] In particular, their use is increasing in architectural and decorative applications owing to its weathering, resistance to general corrosion and localized corrosion[131]. This originates from the protective passive Chromia layer formed on the steel surface. Thus, the production of a denser and thicker oxide films with appropriate colour and chemical composition is significant for controlling their corrosion resistance and aesthetics [132].

Traditionally, physical vapor deposition (PVD), thermal tinting, coatings, electrochemical methods were used as surface colouring techniques on stainless steel [94,133–136] However, these approaches often involve complex technology, difficulties in automation, environmental pollution, high lead time and high processing costs. Subsequently, a simplistic approach to produce surfaces with high corrosion resistance and control of the colour on stainless steel is indispensable to ensure their viability for a range of applications. Recently, pulsed lasers have attracted wide spread interest due to their ability to enhance control of the produced surface colour. These methods have included metal nanoparticle deposition[137,138], Laser induced periodic surface structure (LIPSS) [139–141], and the fabrication of thin film oxides via laser induced oxidation. Laser induced oxidation was chosen to investigate in this work as it is non-invasive, precise, and preserves the intrinsic qualities of the material while reducing the reliance on environmental harmful contaminants, making it a more sustainable approach [142].

Laser-induced oxidation is a rapid process where a material's surface oxidizes upon exposure to a laser beam, followed by rapid cooling. This non-equilibrium oxidation results in unique surface properties and surface modifications in the material [143]. This high precision of such laser processing allows for the modulation of the colour, morphology, thickness and chemical composition of the oxide film[144,145] Likewise, the resulting colour changes were attributed to thin film interference, a phenomenon in which the interference of reflected light waves generates varied colours with respect to the film thickness and refractive index [146,147]. Thus, colourimetric analysis of the oxide layer could be vital for future research in corrosion control and engineering [148].

Cui et. al. examined the formation of an oxide film on AISI 304 stainless steel using a 1064nm Nd:YAG pulsed laser and derived a thermokinetic model to help define the film's composition [149]. This model was used in this work to help define and understand the diffusion of elements. Due to the Gaussian energy distribution from a typical laser spot, a non-homogenous composition and morphology often result [34] The reason for this distribution is due to the relationship between the thermodynamic and kinetic reaction occurring in the process. Initial the formation of Cr_2O_3 oxide is preferred over the formation of Fe_2O_3 as chromium has a lot higher affinity for the chemisorbed oxygen than iron does, so is thermodynamically favorable. This causes an initial increase of chromium at the surface of the stainless steel. However, due to the higher temperature at the center of the laser spot and the higher diffusion rate of Fe inside the oxide layer, Fe_2O_3 appears on the stainless steel surface. This in turn, produces a duplex oxide at the center of the laser spot [149]. The results of Cui et al. where also consistent with the work reported from Li et al. and Yan Lu et al. who used this model to produce a variety of colours on stainless steel surface by varying laser parameters such as laser power, focal offset and scanning direction [131,150]. While laser-induced colouration has been extensively studied on stainless steel alloys like AISI 304 and titanium [71,151]. investigations to identify the effects of laser induced oxidation on stainless steel 316L, as well as its implications for optical and chemical compositional properties are not explored previously.

In this work, our goal is to systematically vary the laser parameters such as power, scan speed and frequency using a full factorial design of experiment (DOE) approach. This study aims to elucidate the relationships between color, composition, morphology and laser processing conditions. In addition, X-ray photoelectron spectroscopy (XPS) and scanning electron microscopy (SEM) techniques were used to characterize the composition of the oxide films and examine the distribution of key elements, particularly molybdenum which has been not well defined or understood in previous studies [70,152] Furthermore, colorimetric measurements were taken to quantitatively assess the alterations in color induced by laser processing. Additionally, this research establishes for the first time a correlation between laser morphology and the resultant coloration, giving further insight on how laser surface interaction mechanisms influence both brightness and hue perception. This correlation, in turn, facilitated the development of an expedited laser coloration method. Therefore, the findings of this investigation provide a new understanding on the fundamental mechanisms underlying the laser induced oxidation of SS316L

surfaces. Moreover, the results contribute to the development of methodology to achieve control of the surface colour, chemical composition and optical properties of metallic materials.

3.2 Experimental Methods

SS316L sheets of 1.7 mm thickness were purchased from Impact Ireland (Metals) Limited, Ireland. The composition of the sheet is given in Table 3-1 Composition of the SS316L sheet material utilised in this work.Disks of 100 mm diameter were sections from the sheet using an industrial used CO_2 (CW) laser. All samples were cleaned using deionized water and then ethanol. The surface of the steel was then uniformly sandblasted to increase surface roughness to 3.9 µm Sa to enhance laser absorption [18] .

Chemical	**Fe**	**C**	**Cr**	**Mn**	**Mo**	**Ni**	**N**	**P**	**Si**	**S**
Composition Content (wt. %)	Bal.	130 (ppm)	16.64%	1.41%	2.03%	10.0 %	400 (ppm)	200 (ppm)	4250 (ppm)	60 (ppm)

Table 3-1 Composition of the SS316L sheet material utilised in this work.

3.2.1 Laser processing of SS316L surface

The sand blasted samples were cleaned with acetone, ethanol and sonicated for 15 minutes to remove any contaminants or excess sand from the surface then allowed to dry for 5 minutes on the laser stage. The laser system used consisted of a 3.5 W maximum power 1064 nm Q-switched, diode-pumped solid-state neodymium-yttrium aluminium garnet laser (Bright Solutions 1064 WEDGE HF). A 2D scanning galvanometer (Raylase SS-12) was used to raster the beam in the xy-plane, and a movable z-stage (PI M-404 4PD) used to control the position of the sample. The beam was focused on the sample surfaces, which were placed 340.3 mm below the galvanometer lens at the focal plane to produce a spot diameter of 100 µm. The pulse width of the laser varying between 2-3 ns, with a peak pulse energy of 4 mJ. The laser processed sample can be seen in

Figure 3-1.

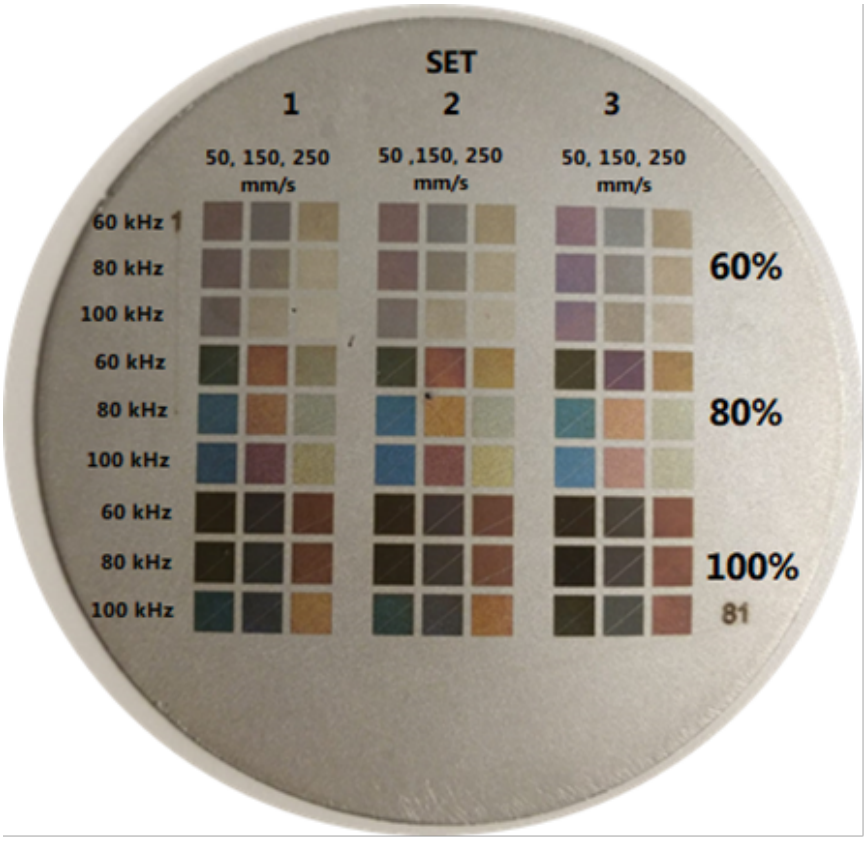

Figure 3-1: Photograph of 81 laser-processed areas of 5 by 5 mm produced on a stainless steel 316L disk.

Laser processed areas of 5mm X 5mm were processed using fixed parameters of a bidirectional hatching strategy with a hatching distance of 10 µm. A bidirectional hatch strategy provides a uniformly repeating heat flow during processing by means of the laser scanning in both directions (left-to-right and right-to-left) during the filling process of each layer, rather than resetting to one side after each pass. The laser processing parameters were altered using a 3 x 3 (81 samples) full factorial design of experiment (DoE) set up using Design Expert Version 13 software, resulting in 27 sets of process parameters. Parameters selected for examination were laser power, frequency, and scan speed. Three repeats of each set of parameters were prepared on the stainless steel disk and analysed this allows for the variance in each value to be obtained. The scan speeds examined were 50, 150, and 250 mm/s; frequencies were 60, 80, and 100 kHz; and laser powers were 2.1, 2.8 and 3.5 W (60, 80 and 100% of maximum power). These parameter ranges where selected after screening experiments in order to produce the widest range of colour oxide while keeping

the processing time low. The full factorial design of experiments with process parameter settings is shown in **Table 3-2**.

Run	Frequency (kHz)	Power (%)	Scan Speed (mm/s)
1	60	60	50
2	60	60	150
3	60	60	250
4	80	60	50
5	80	60	150
6	80	60	250
7	100	60	50
8	100	60	150
9	100	60	250
10	60	80	50
11	60	80	150
12	60	80	250
13	80	80	50
14	80	80	150
15	80	80	250
16	100	80	50
17	100	80	150
18	100	80	250
19	60	100	50
20	60	100	150
21	60	100	250
22	80	100	50
23	80	100	150
24	80	100	250
25	100	100	50
26	100	100	150
27	100	100	250

Table 3-2 Design of experiments (DOE) showing the investigated laser process parameters.

3.2.2 Surface characterization analysis

The surface chemistry of the steel substrates were examined using X-ray photoelectron spectroscopy (Scienta Omicron XPS, Monochromated Al Kα source 1486.74 eV, 6.5 x 10^{-7} Pa base

pressure) between the ranges of 0-800 eV binding energy. The sample were taken directly from laser processing into the XPS while been kept under vacuum to reduce the environmental effects on the surface. The surface was cleaned with acetone and ethanol before analysis. Casa XPS software (version 2.3.23) was used to analysis the results of surface chemistry of the four main compounds of interest iron, chromium, oxygen and molybdenum. A Shirley baseline was use for all compounds. For iron and chromium only the $2p_{3/2}$ peak was taken into account for the composition analysis while for oxygen the 2s singlet peak was used and for molybdenum both the $3p_{5/2}$ and $3p_{3/2}$ peaks where taking into account. Normalization was preformed using the Casa XPS software.

3.2.3 Optical analysis

Reflectance spectra were obtained using a 200-µm reflectance optical probe (ThorLabs fibre bundle, reflectance probe), a calibrated white light source (Ocean optics XG 35), 45^{o} optical fibre mount (ThorLabs RPS_SMA) and an optical spectrometer (Ocean optics Maya 2000 pro). The samples were placed at 45^{o} to the light source to minimize the spectral reflections and maximize the diffuse reflections to increase the accuracy of the result. A white spectral standard was measured with and without the calibrated white light source and was adjusted to 100% to use as a reference point and to obtain the background spectra. The reflectance's of each coloured sample were detected at each wavelength in steps of 10 nm. OceanView software converted the reflectance spectra into a CIE tristimulus value using a standard 2-degree observer angle and D65 illumination spectra, which mimics the colour at daytime exposure. Optical imaging was performed using a VHX-2000 (Keyence) 3D optical microscope. Scanning electron microscopy was conducted using JSM-IT 100 (Jeol) with an accelerating voltage of 2 kV and a probe current of 52 pA.

3.3 Results and discussion

Based on the Cabrera-Mott theory, the oxidation of thin oxide films is determined by the interstitial ions migration [153,154] Upon exposure to air, the steel substrate undergoes oxidation, resulting in the formation of a few angstrom-thick passive layer. For further oxidation, electrons transfer from the steel substrate to the oxide surface. This leads to the ionization of adsorbed oxygen molecules through tunnelling and thermionic emission effects. Consequently, electron transfer continues until an equilibrium Fermi level is established among the steel layer and the

passive film surface. As a result, a uniform electric field develops within the passive layer, driving the migration of oxygen ions and causing an increase in the thickness of the passive layer. However, as the oxide layer grows, the natural oxidation rate diminishes significantly due to the rapidly declining electric field. The oxide thickness no longer increases once it reaches a threshold and the Mott potential will disappear [153,155] During laser irradiation, the outer layer of the oxide film absorbs light through inverse Bremsstrahlung absorption. The absorbed energy propagates into the subsurface atoms exciting the electrons to higher energy levels and become more energetic. In addition, the surface-adsorbed oxygen molecules have a higher probability of decomposing into oxygen ions [155]. Thus, this regeneration of the Mott potential facilitates the continued growth of the oxide layer [156] .

To be able to normalize the process parameter into a single parameter, the areal energy equation was adapted from the paper by Pacquentin et al [157]. It takes into account the total number of laser impacts times the laser fluence of an individual pulse. Since the horizontal and vertical overlap are different in the parameters examined, the equation 3.1 becomes:

$$\#\ laser\ \text{pulses}(N_p) = \frac{1}{(d^2 * (1 - Hatching\ overlap)(1 - Pulse\ overlap))} \quad \text{Eq. 3.1}$$

Hatching overlap correlates to the overlap in the perpendicular of the direction of laser travel, given by equation 3.2 where h is the hatching distance (10µm) and d is the spot diameter at the focal length (100µm).

$$Hatching\ overlap = \frac{1 - h}{d} \quad \text{Eq. 3.2}$$

whereas the pulse overlap corresponds to the overlap parallel to the direction of travel of the laser, with V being the scan speed (mm/s) and f being the frequency (Hz).

$$Pulsed\ overlap = 1 - \frac{V}{d \times f} \quad \text{Eq. 3.3}$$

The total areal energy is given by multiplying the total number of pulses by the fluence per laser spot which is giving by equation 3.4.

$$Areal\ energy\ =\ Np\ \times\ Pulse\ Fluence \quad \text{Eq. 3.4}$$

3.3.1 Morphology analysis

In **Figure 3-2**, three laser-processed samples (Run 9, Run 18, and Run 27) are shown highlighting the impact of altering process parameters on surface morphology and colour. The morphology of Run 9 **(Figure 3-2a, d**), resembles that of the unprocessed samples, suggesting minimal alterations in the surface structure. However, a noticeable change in colour occurs due to the formation of an oxide film. This suggests that the laser processing at lower power primarily affects the surface properties without significantly modifying the underlying morphology. In contrast, Run 18 **(Figure 3-2b, e**) reveals intriguing phenomena of surface remelting and subsequent solidification. As a result, the material from the peaks of the surface roughness flows into the adjacent valleys that lead to an enhanced homogeneous surface and a reduction in surface roughness. The cracks and holes that are present on the surface are shallow and can be explained due to the initial high surface roughness from the sandblasting surface. Run 27 **(Figure 3-2 c** and **f**) was conducted at the highest power level. The images from this run demonstrate substantial material removal, indicating the ablation threshold has been surpassed. The visible laser track lines serve as tangible evidence of this ablation. Interestingly, as the scan speed decreases, the laser track lines become more pronounced, indicating an accumulation effect of the laser pulses [15] This sub sequential scanning results in a surface heating effect. Such preheating the surface facilitates a reduced ablation threshold, resulting in more efficient material removal. Furthermore, by decreasing the frequency, the peak pulse power increases, further enhancing the removal of material.

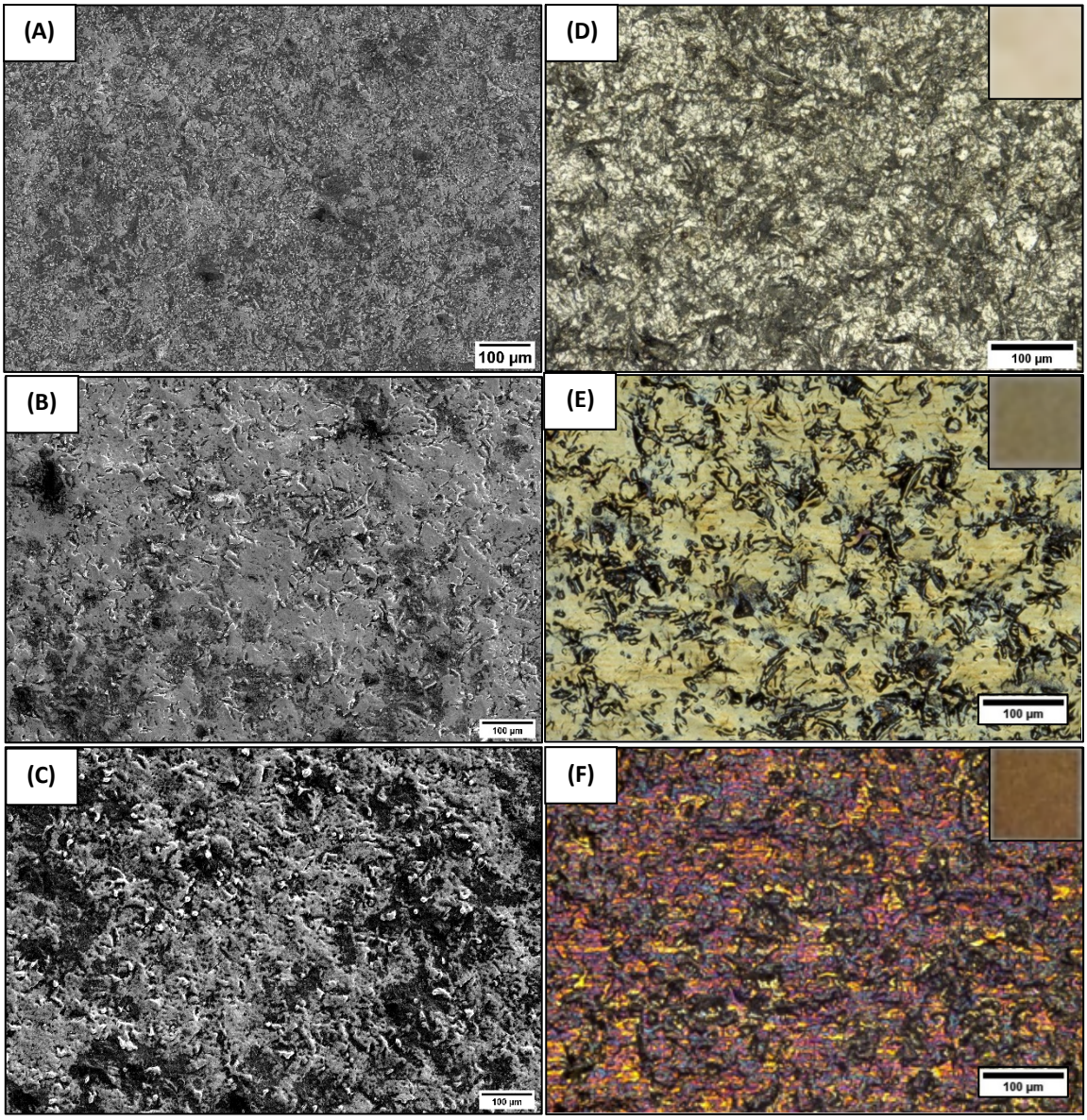

Figure 3-2: SEM of the laser induced oxide for (a) Run 9, (b) Run 18, and (c) Run 27 and the corresponding optical images for (d) Run 9, (e) Run 18 and (f) Run 27; inserts show visual representation of the colour taken under a white light.

The laser track lines observed in the **Figure 3-2 e** are smaller than the laser beam diameter of 100 µm. This occurrence can be attributed to the Gaussian distribution of the laser beam and the high overlap rate employed during the laser processing [34]. An interesting observation is the absence of laser-reassembled structures, such as LIPPS, on the surface. This absence is explained by the initial high surface roughness, which acts as a masking effect, hindering the formation of these structures. The initial surface roughness plays a crucial role in dictating the formation of laser-induced structures with a smoother surface being more conducive to their development [158].

3.3.2 Surface Concentration

XPS analysis was performed on all 81 samples to identify the surface chemistry of the four main elements of interest. These were iron, chromium, oxygen and molybdenum. To acquire the relative concentration of each, element the ratio of the peak areas where first measured using Casa XPS software. The peak intensities of Fe, O and Cr are quite high in all samples showing that the surface mainly consisted of iron and Chromia oxides. There is also a small amount of carbon present which can be due to either surface or XPS system contamination. The detailed high resolution XPS of seen in **Figure 32.** The corresponding used sensitivity factor, reference peaks and experimentally recorded peak positions are shown in **Table 3-3**

O1s Spectra: For all runs, the shape of the O1s peak was very similar. The peak forms an O_{2-} metal oxide singlet at binding energy 530.4 eV; this indicates that the laser processing has oxidized the steel surface. Shoulder peaks are also present with a binding energy of 532.1 eV due to the presents of OH- O1s, Fe2p, Cr2p and Mo3d are metal hydroxides. XPS quantitative analysis revealed that the O_{2-} / OH- ratio varies throughout the samples, with run 1 having an O_{2-} / OH- ratio of 2.78 with run 27 having a ratio of 1.10. These both show higher oxide ratios than the unprocessed sandblasted sample at a ratio of 0.61. Hydroxides film are more defect prone than oxide film so this increase in the ratio can positively impact the density of the passive film present on the steel surface [159].

Mo3d Spectra: The Mo3d spectra displayed two major peaks at binding energies of 232.36 and 235.42 eV, corresponding to Mo_{6+} $3d_{5/2}$. Due to the low concentration of Mo at the lower energy density run the resolution of the peaks are quite low leading to a low signal to noise ratio. XPS quantitative analysis reveals that Mo concentration varies a lot through the runs with run 15 having the maximum concentration at 14.15% to no molybdenum being present such as in run 10.

Fe 2p Spectra: From the Fe 2p spectra it can be seen that four major peaks have formed at binding energy values of 710-711, 724-725, 715-716, and 729 eV. These peaks correspond to the Fe $2p_{3/2}$ and Fe $2p_{½}$. With the peak at 716 and 729 being, a satellite peaks. These peak can correspond to the Fe(III) oxides of Fe_2O_3. Due to Fe_2O_3 being a high spin compound it produces more complex spectra containing satellite peaks that can overlap with each other making it more difficult to identify the exact oxide. In lower energy density runs there is a peak present at ~706 eV this shows that the surface has not completely oxidized and metallic Fe in present on the surface.

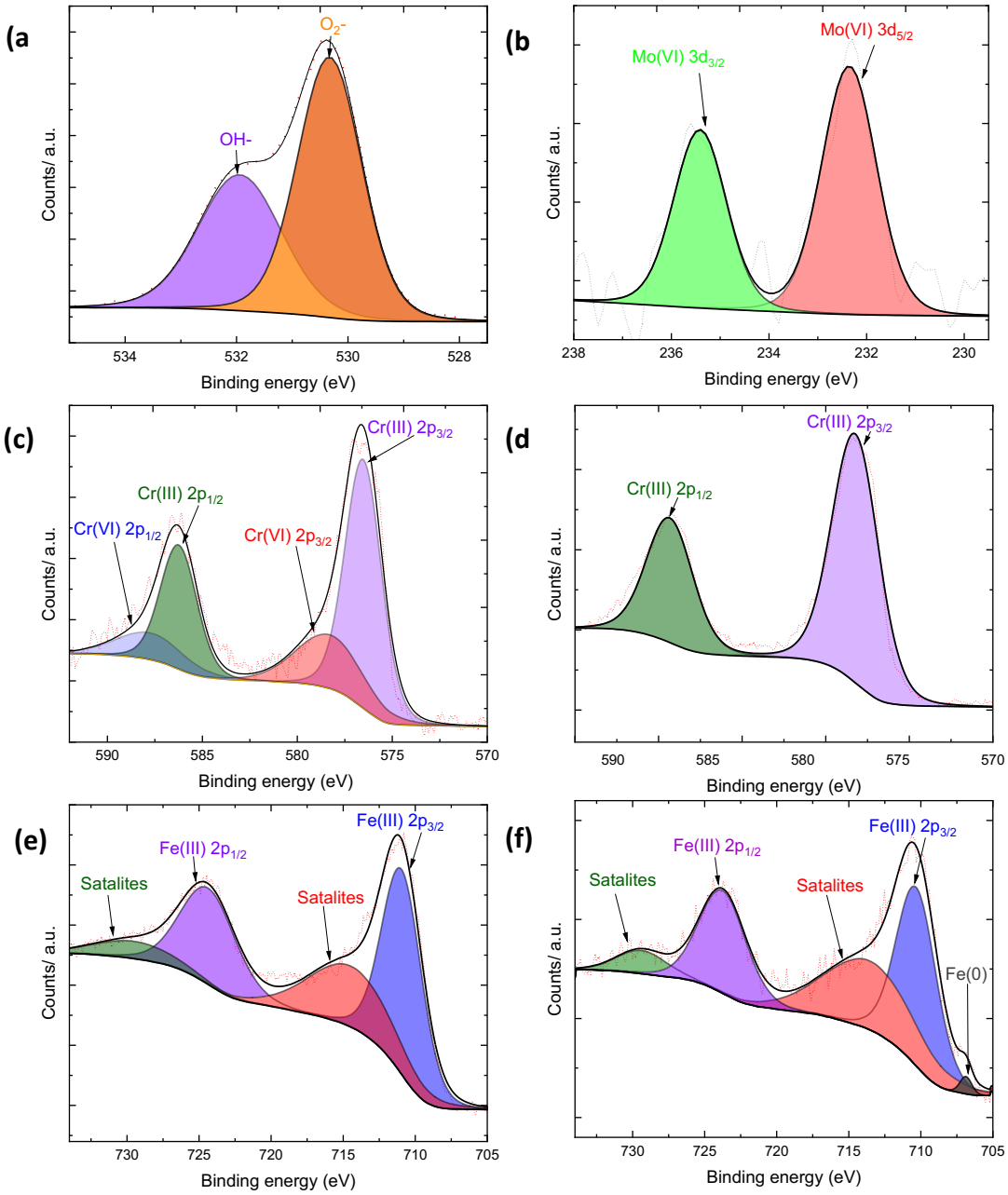

Figure 3-3: High resolution XPS spectra of (a) O1s spectra, (b) Mo 3d spectra, (c) Cr 2p spectra of run 27, (d) Cr 2p spectra of run 9, (e) Fe 2p spectra of run 27, (f) Fe 2p spectra of run 9

Cr 2p Spectra: The Cr 2p spectra exhibited three major peaks at binding energies of approximately 577, 580, and 587 eV, corresponding to Cr 2p $_{3/2}$ for Cr(III) oxide, Cr 2p $_{3/2}$ for Cr(VI) oxide, and Cr ½$_{1/2}$ for both oxides, respectively. The identified oxides were Cr_2O_3 and CrO_3. Although satellite peaks were present, they did not provide additional information and were not considered in the results. The analysis revealed the formation of three different oxide combinations on the laser processed surface: Cr_2O_3 alone, CrO_3 alone, and a combination of both. The oxide combinations

closely followed the areal energy density, With the lower energy densities Run 9 favouring Cr_2O_3 comprising of a oxide ratio Cr(III)/Cr(VI) of 100%/0%. Higher energy densities Run 22 favouring CrO_3, having a ratio of 0%/100% and intermediate energy densities Run 26 and run 27 resulting in a combination of both 73.2/26.8% and 65.8/34.2% respectfully. At the lowest energy densities, a small peak at 575 eV representing metallic Cr (0) was observed, indicating incomplete oxidation. This finding shows that higher power processing is not ideal for any use in where the surface comes in contact with a food or pharmaceutical product as Cr(VI) is classified as carcinogenic category 1A [160]. In supplementary information (S3) a full table showing the XPS results and standard error is presented along with the high resolution XPS of the unprocessed sample (S4).

Peaks	Compounds	Binding Energies (eV)		Sensitivity Factor	FWHM
		Experimental	Reference		
Fe 2p 3/2	Fe (metal)	706.8	706.5		1.04
	Fe_2O_3	710.9	710.8	10.82	3.29
Cr 2p 3/2	Cr (metal)	574.8	574.3		0.53
	CrO_3	580	580	7.69	1.79
	Cr_2O_3	577	576	7.69	2.87
O 1s	O_2 -	530.1	529-530	2.93	1.24
	OH-	532.0	531.5-532		1.92
Mo 3d 5/2	MoO_3	231.5	232	5.62	1.32
Mo 3d 3/2	MoO_3	236.1	235.6	3.88	1.28

Table 3-3 Binding energies and sensitivity of the compounds used in this study. *[123,161]*

3.3.3 ANOVA analysis of XPS

Table 3-4 presents the primary analysis of Variance (ANOVA) parameters derived from the three-element iron, chromium and molybdenum. Each of the developed models exhibited an R-squared value exceeding 0.69, demonstrating their satisfactory fit. The considerable adequate precision of the three responses implies that the error has an insignificant impact on the model. Furthermore, the large F-value, which compares parameter variance to residual variance again indicating strong model significance. All modules are three-factor modules, indicating that the initial parameters exert a significant influence on the model. With 7 degrees of freedom for both Cr and Mo models and 8 degrees of freedom for Fe model. All the models incorporate nonlinear and higher-order terms, such as the P^2 term. These terms capture the saturation of the response variables as the factors increase, providing valuable insights into the behaviour of the system being

studied. By including these nonlinear terms, the models account for complex interactions and nonlinearity in the relationship between the predictors and the responses, resulting in more accurate and comprehensive representations [162], the model formulas and full ANOVA information is given in supplementary information S1.

Response	Degrees of freedom	R-Squared	Adjusted R-Squared	Adequate Precision	F-value
Fe	8	0.6919	0.6576	18.085	20.21
Cr	7	0.836	0.8203	28.01	53.17
Mo	7	0.7131	0.6852	17.1972	25.57

Table 3-4 Primary analysis of variance (ANOVA) parameters for iron, chromium and, molybdenum models.

All three models contain strong power-scan speed and power-frequency two factor interactions (see Figure 3-4). The chromium peak is maximums at the initial parameters of 100kHz, 60% power and 250mm/s this will produce the lowest overall areal energy density with a value of 69.82% Cr, there is a secondary peak that occurs at 100% power used, this is due to the formation of a CrO_3 which occurs due to its higher Gibbs free energy. This graphs also shows that in medial areal energy densities the chromium content is at its lowest, showing that the transitions stage where both Cr(III) and Cr(VI) are present the overall concentration is lower. The maximum value lies at the limits of the process parameter examined showing that the model could be expanded to find a turning point in this concentration. As for most practical application of stainless steel, a minimal iron content is desirable. The minimal value of Iron corresponds with the maximum Cr content at the lower areal energy density at an iron content of 27.3%. The molybdenum content shows an inverse trend to the chromium with the maximum concentration occurring at maximum frequency (100 kHz) lower scan speed (50mm/s) and a power of 75%. With the higher and lower powers showing a dip in Mo concentration. These models show the intrinsic relationship between the elemental compositions allowing for the production of oxides that can be precisely altered to suit a variety of applications.

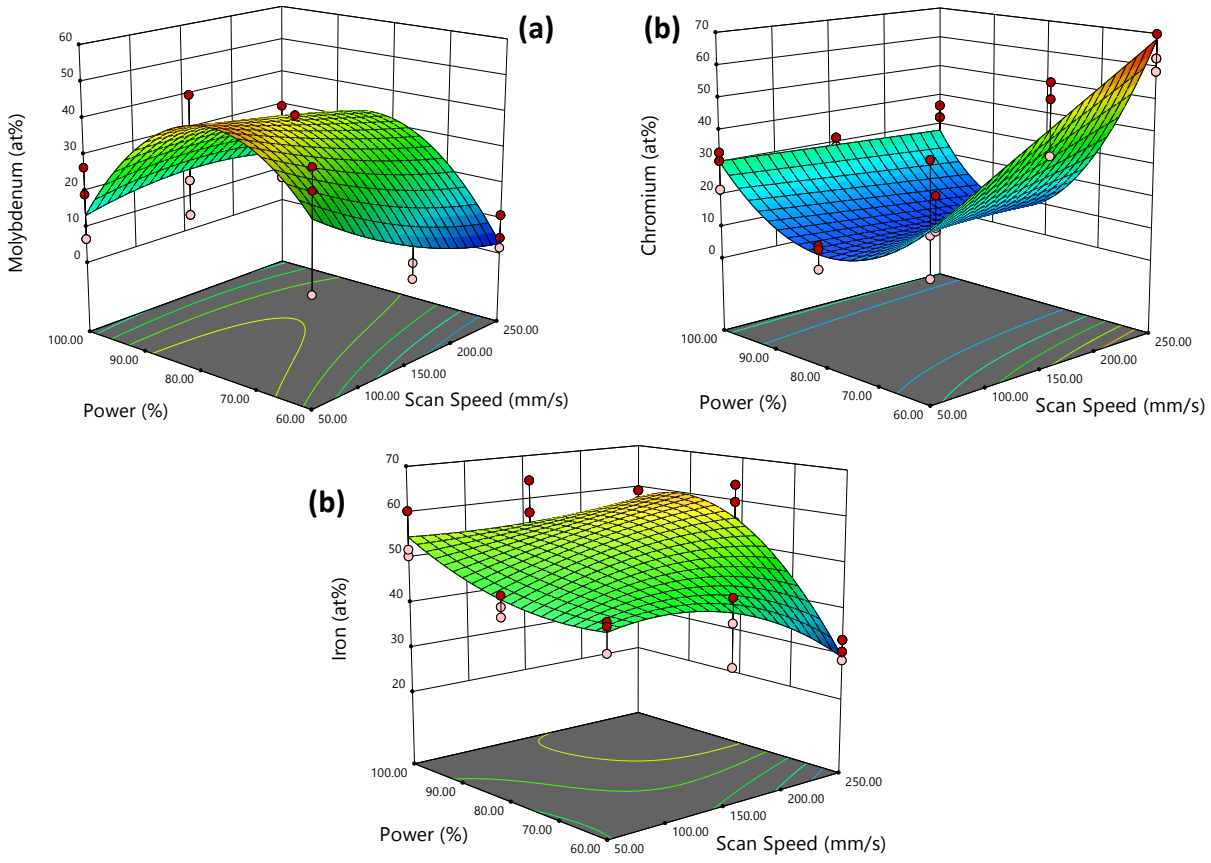

Figure 3-4: Response surface of power vs scan speed at 100 kHz frequency for, (a) molybdenum, (b) chromium, and (c) iron.

Two noteworthy results emerged across the entire parameter range, providing valuable insights into the surface properties of the steel surface. The first observation pertains to the relationship between the chromium concentration and the molybdenum concentration (Figure 3-5b). A highly correlated inverse 2nd order polynomial relationship was observed between these two elements. This finding poses challenges in achieving maximum corrosion resistance for the steel surface since an enrichment of the oxide film with both chromium and molybdenum is ideal. However, due to this inverse relationship, maximizing one element's concentration would hinder the other. This observation has not been reported previously in the literature.

The second observation pertains to the relationship between the chromium-to-iron ratio and the applied areal energy density (Figure 3-5a). Initially, the ratio increases sharply from the

unprocessed samples, reaching a maximum value of 2.09 at the lowest applied energy density. Subsequently, a significant decrease occurs, dropping below the ratio of the unprocessed sample (0.67). From the ANOVA analysis of the Cr/ Fe ratio, it can be seen that the power term considerable influences the model. At higher powers, the Cr/Fe ratio is decreased below the value of unprocessed steel. Frequency was found to have a similar trend on the measured output ratio but at a much smaller overall influence. This shows the peak pulse power is less influential then the areal energy density for the Cr/Fe ratio. The analysis also shows that the strong two factor interaction between power and scan speed also exists having an even high significance than either one of the original parameters. This shows that when lower power is used the effect of changing scan speed becomes more influential. This result corresponds well with that presented in the work of Lecka et al.[163].

These results can be explained the thermo-kinetic model developed by Cui Yi *et. al*. [149] As the surface oxygen content is quite high, preferential oxidation of chromium takes place first due to chromium's extremely high affinity for the chemisorbed oxygen compared to iron. Due to the rapid heating and cooling dynamics of laser processing diffusion is unable to occur allowing for the Chromia oxides to accumulate on the surface increasing their concentration. As more energy density is applied, the sub surface atoms gain energy, facilitating easier movement of atoms throughout the newly created passive layer. As the iron, concentration is higher and the ion mobility through the oxide layer is more favourable than chromium, iron oxides start to form on the surface which reduces the Chromia oxide present on the surface of the steel.

The ratio of Mo to Cr is low at lower areal energy densities due to the higher metal bond strength seen for Mo-Mo over Cr-Cr, as the formation of an oxide nucleation site requires the initial disruption of the metal-metal bond [164] As more energy is applied, the Mo metal-metal bond can be disrupted and free Mo (unoxidized) can diffuse through the oxide layer along with Fe and begin to oxidise. Once the high Mo concentration oxide layer is formed, it will depress the concentration of Cr_2O_3 layer pushing it into the subsurface oxide layer, the further formation of Cr_2O_3 is reduced due to the reduced concentration of free Cr present in the layer.

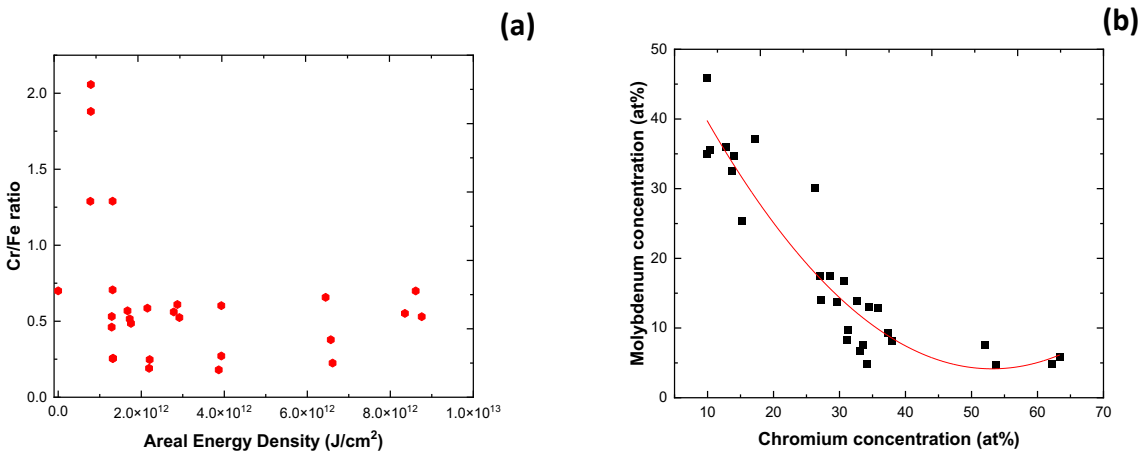

Figure 3-5: Graph of (a) Cr/Fe ratio vs the areal energy density, and (b) atomic concentration of molybdenum vs atomic concentration of chromium.

3.3.4 Colourimetry analysis of the samples

The CIE (*Commission Internationale de l'éclairage)* 1931 chromatometry system was used to describe the colour, hue and brightness of the laser coloured samples [165]Colour spaces defined by CIE 1931 were employed to establish a quantitative relationship between the spectral distributions of colours seen by the human eye and the electromagnetic visible spectrum. The dominant wavelength, tristimulus value and colour gamut are all obtained from the reflectance spectra of the coloured sample.

The tristimulus values: X,Y,Z are the tristimulus values at a given reflection and are used as a primary value for colour (similar to RGB) but can be used for a wider range of colours and can be easily visualized in two dimensional coordination curve. These XYZ values are obtained from the interaction of the reflectance spectra with the standard tristimulus values $\bar{y}(\lambda)$,ẍ(λ), $\hat{z}(\lambda)$ which are spectral representation of how the human eye preserves each colour at the white light standard E. X, Y, Z are needed to acquire the chromaticity coordinate are calculated using the equations [166] .

$$X = k \sum_{\lambda} R(\lambda) S(\lambda) \bar{x}(\lambda) \Delta\lambda \quad \text{Eq. 3.5}$$

$$Y = k \sum_{\lambda} R(\lambda) S(\lambda) \bar{y}(\lambda) \Delta\lambda \quad \text{Eq. 3.6}$$

$$Z = k \sum_{\lambda} R(\lambda) S(\lambda) \bar{z}(\lambda) \Delta\lambda \quad \text{Eq. 3.7}$$

were X, Y , Z are the tristimulus values, S(λ) is the D65 spectral power distribution, R(λ) is the obtained reflectance spectra, x,y,z bar are the tristimulus values at white light(E), Δλ is the wavelength interval set at 10 nm and k is an adjustment factor obtain by setting Y = 100 [167].

The brightness of the sample is described by the tristimulus value Y with 100 being a fully bright sample and 0 being completely dark. From ANOVA analysis, it can be seen that all three starting parameter have an influence over the brightness of the sample. With scan speed and frequency both have a positive influence over the brightness and power having a negative influence. Scan speed has the greatest influence over the brightness followed by power then frequency. This variation in brightness can mainly be described by the power density used to produce each colour mark. As the power density increase, more heat input is being applied to the surface. This causes a thickening of the oxide film decreasing the reflectivity darkening the sample. As can be seen in both runs 19 and 22 a dark black colour mark was seen with the 2 lowest brightness values of 5.92 and 4.82 respectfully these 2 also correlate the second and third highest power density. Another factor effecting their darker appearance is due to the higher pulse energy experienced at lower frequencies this higher pulse energy allowed for ablation to occurring along with oxide formation. This causes a topological change to the surface forming visible laser tracks on the surface seen in **Figure 3-2e**. The brightest sample Run 18 had a Y value of 99.37 and produced a bright yellow colour. As can be seen from morphology analysis the slightly higher power allowed for a surface re-melting and solidification process to occur this can cause a reduction in surface roughness allowing for a laser polishing effect increase the reflectivity / brightness of the surface. The concept of combining laser polishing with laser coloration has not evidently been explored. This novel approach holds the potential to reduce lead times in the surface treatment and marking processes.

Specifically, it offers the exciting prospect of minimizing or even eliminating the necessity for pre-surface polishing procedures prior to laser colour-marking applications.

From the ANOVA analysis, quadratic models were designed to describe the relationship between the 3 starting parameters and the response X,Y,Z of possible samples. All modules are highly correlated three-factor modules with R^2 values in excess of 0.8. Analysis of the results from repeated runs showed a standard error between 0.6-6.2%. With 6 degrees of freedom for both X and Y models and 5 degrees of freedom for Z model. The designed models can described by the equations:

$$\mathbf{X} = -225.76 + 0.21V + 0.011F + 6.38P + 0.0023VF - 0.0024VP - 0.042P^2 \quad \text{Eq. 3.8}$$

$$\mathbf{Y} = -260.81 + 0.34V + 0.099F + 6.99P + 0.0021VF - 0.0036\,VP - 0.045P^2 \quad \text{Eq. 3.9}$$

$$\mathbf{Z} = -111.34 + 0.28V + 0.27F + 2.69P - 0.0024VP - 0.017P^2 \quad \text{Eq. 3.10}$$

With V being Voltage, P representing Power and F representing frequency. Visual representations of the model are shown in **Figure 3-6**. From the model, maximum brightness will be seen at the highest frequency and scan speed possible. To maximize the brightness power parameter, the scan speed will also needs to be taken into account as the maximum brightness alters with scan speed moving from 80% power at lowest scan speed towards 70% power at higher scan speeds. Scan speed and power were found to have the highest two-way factor interaction.

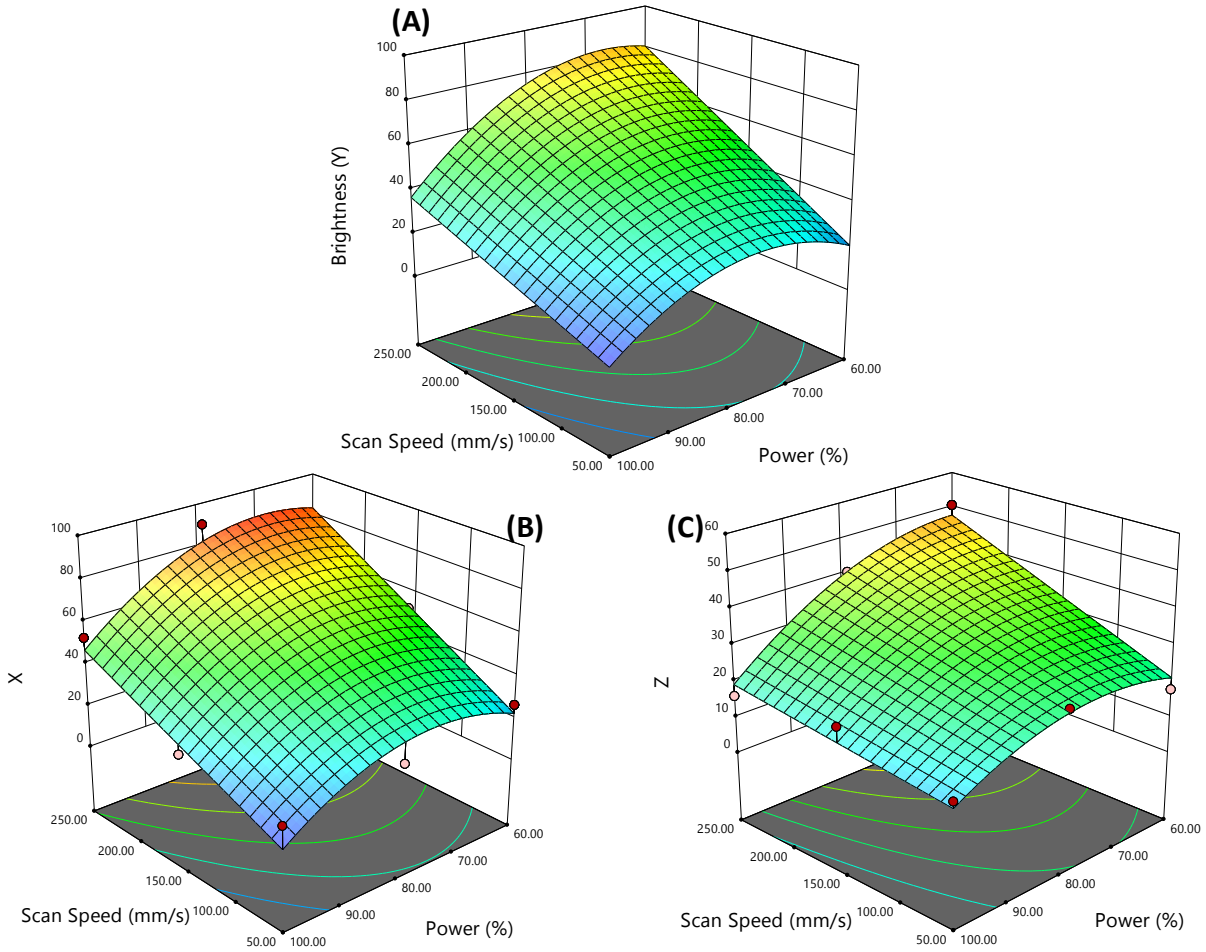

Figure 3-6: Response surface of power vs scan speed at 100 kHz frequency for brightness (a) Y, (b) X, and (c) Z.

To be able to produce a colour gamut the X, Y, Z trismulus values need to be converted into a two dimensional coordinate system. This was preformed using the CIE 1931 equations: [168].

$$x = \frac{X}{X+Y+Z} \qquad \text{Eq. 3.11}$$

$$y = \frac{Y}{X+Y+Z} \qquad \text{Eq. 3.12}$$

These values can then be seen on the CIE Chromaticity diagram **Figure 3-7**. The point E on each diagram represents the equal point energy, representing the white light colour. The black circle on each diagram represents the colour gamut at each power level. 60%, 80% and 100% with the larger circle representing a larger colour gamut. As can be seen from the diagrams the largest

gamut is present at 80% power this shows that under the parameter used the widest range of colour can be seen using 80% power. In **Figure 3-2e** the colour varies from inside the track to outside showing the sensitivity of the colour formation around that range of colours. Moving from 60% to 80% the black circle elongate along the x-axis more than the y-axis forming an oval shape this show that with altering processing parameter the hue/dominate wavelength of the colour mark changes while the saturation stays quite similar. The colour distance (ΔE_{ab*}) is a numerical measure of the variation between two colours. Taking into account the largest distance for each set, 80% power showed the largest variation of 12.14 ΔE_{ab*}, followed by 60% at 7.39 ΔE_{ab*}, with the lowest colour change of 6.85 ΔE_{ab*} seen for 100% power. As evident from the observation, the coloration of the oxide film is not solely dependent on its thickness. Instead, the colour is the result of a complex interplay involving thin film interference, the inherent hues of the native oxides contained within the film, and the surface morphology generated. Thus, this work contributes to understand the intricate interplay among thin film interference, intrinsic oxide colours, and surface morphology, which are crucial for precise control over oxide film coloration.

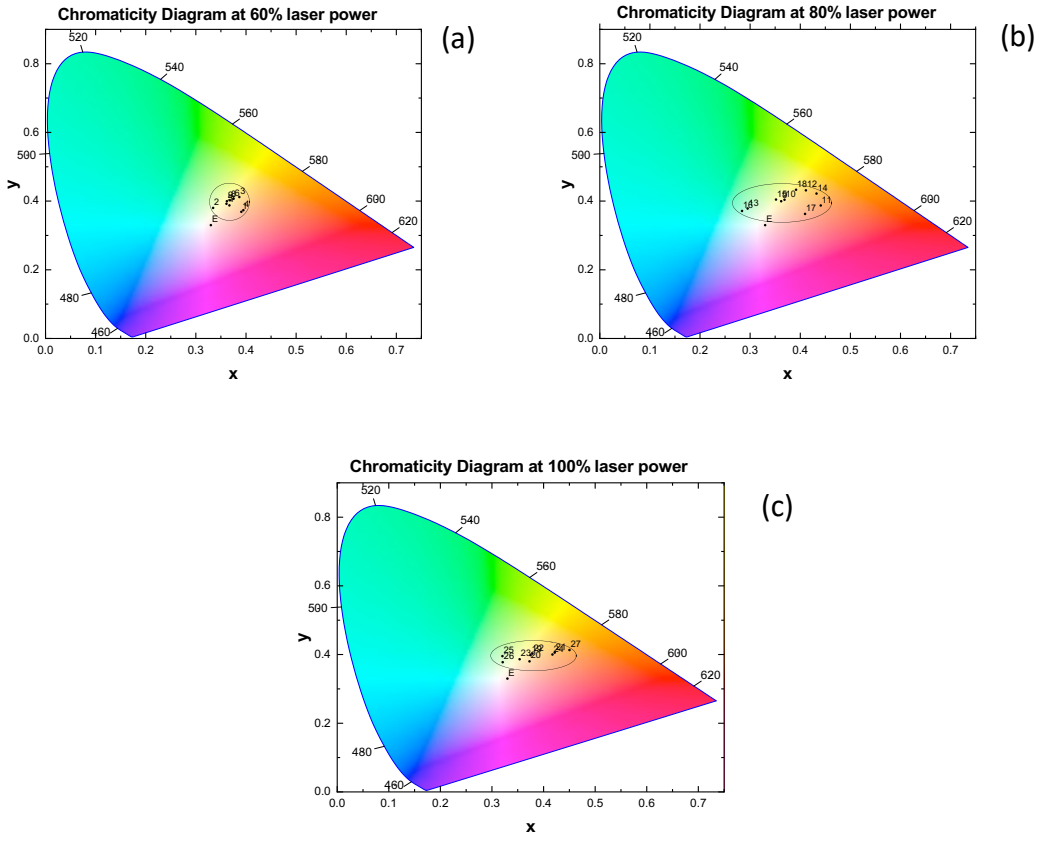

Figure 3-7: Chromaticity diagram at powers of (a) 60%, (b) 80%, and (c) 100%.

3.4 Conclusion

In this work, the effect of altering laser processing parameters on the composition and optical properties of laser-induced oxidation on 316L stainless steel surfaces, has been investigated. By using a full factorial design of experiment approach, the relationships between colour, composition, and laser parameters were revealed, and the following conclusions were obtained. The surface morphology was significantly impacted by altering laser processing parameters. Different process conditions led to distinct surface structures, ranging from pure oxide growth at lower laser powers to surface remelting and solidification and mid-range powers, and to material ablation at higher laser powers.

Laser-coloured samples were analysed using the CIE 1931 chromaticity system, providing a valuable method to correlate laser process parameters with surface colour, hue, and brightness. Tristimulus values (X, Y, Z) allowed for quantitative colour characterization, revealing that sample brightness (Y) correlated with scan speed, frequency, and power parameters. The colour distance varied with changing laser power, with 80% power exhibiting a colour distance of 12.14 ΔE_{ab*} and 100% power showing the smallest colour distance of 6.85 ΔE_{ab*}.

Surface chemistry, analysed using X-ray photoelectron spectroscopy (XPS), showed that the surface was mainly comprised of iron, chromium, and molybdenum oxides. Cr2p spectra indicated chromium oxide formations are linked to the areal energy density, favouring Cr_2O_3 at lower energies and CrO_3 at higher energies. A surface response model was generated which defines well the relationship between the chromium-to-iron ratio and applied areal energy density, showing a maximum peak at the lowest applied energy density. While plain stainless steel has a Cr/Fe ratio of 0.67, a maximum value of Cr/Fe of 2.09 was found in this work which can lead to advantageous surface properties such corrosive resistant over conventional stainless steel. The models can therefore be used to selectively alter the composition of the oxide films or surface colour for varying applications.

A new finding from this work is the quantified inverse relationship determined between chromium and molybdenum concentrations. These findings allow for the expansion of thermokinetic models to incorporate molybdenum for the laser surface oxidation of 316L stainless steel.

Chapter 4 - Exploring the impact of laser surface oxidation parameters on surface chemistry and corrosion behaviour of AISI 316L stainless steel

Publication Status: Published

Mark Swayne, Gopinath Perumal, Dilli Babu Padmanaban, Davide Mariotti, Dermot Brabazon, **Exploring the Impact of Laser Surface Oxidation Process Parameters on XPS Elemental Depth Profiling and the Related Corrosion Resistance of 316L Stainless Steel**, Applied surface science advances (2024). DOI:10.1016/j.apsadv.2024.100622

.

Abstract

This study delves into the corrosion resistance enhancement of stainless steel through laser processing, focusing on the interplay between surface chemistry, morphology, and electrochemical properties. Two sets of 3x3 full factorial design of experiment (DoE) designs were employed to explore the influence of laser process parameters, including power, scan speed, frequency, and hatching distance. The findings underscore the superiority of reduced areal energy in producing optimal corrosion resistance 10 times better then unprocessed stainless steel, demonstrating the best results under optimized conditions of a 15 µm hatching distance, 250 mm/s scan speed, 100 kHz frequency, and 80% power. X-ray Photoelectron Spectroscopy (XPS) analysis reveals the predominant surface composition of iron and chromium oxides, with variations in the oxide combinations correlating closely with areal energy. Depth profiling revealed the transformation of oxide layers and highlights the importance of chromium-to-iron ratio in surface corrosion behaviour. Cyclic polarisation results demonstrate the formation of passive, transpassive, and pitting domains, with metastable pitting observed in some samples. The direct positive correlation recorded between corrosion current and Cr/Fe ratio underscores the significance of oxide composition in corrosion resistance. Electrochemical impedance spectroscopy (EIS) further confirmed the superior corrosion resistance of laser-processed samples to non-laser processed samples, with lower areal energy exhibiting higher resistance compared to higher areal energy. SEM morphology analysis revealed the removal of surface defects and the formation of a protective oxide layer in laser-processed samples, with lower areal energy samples exhibiting the lowest level of surface defects. The 3D optical profilometer measurements of corrosion pits corroborate these findings, with lower areal energy samples demonstrating the lowest pit depth and area, indicating superior corrosion resistance. Overall, this study provides comprehensive insights into optimizing laser processing parameters to enhance the corrosion resistance of stainless steel, offering valuable understanding and strategy for improving the metal surface corrosion resistance.

4.1 Introduction

Stainless steels especially 316L have increasingly been used in the pharma and food industries because of its high mechanical strength, good surface gloss, as well as high resistance to both general and localized corrosion. The excellent corrosion resistance originates from the native Cr oxide protective layer on the stainless steel surface, which can act as a barrier against the intrusion of the corrosive media. Therefore, the production of a denser and thicker oxide film with appropriate chemical composition on the stainless steel surface is of importance and significance for further improving their corrosion resistance [169].

In recent years, laser processing techniques have emerged as promising methods for modifying the surface properties of metallic materials, offering precise control over surface characteristics such as roughness, microstructure, and composition [170–172] . These techniques, including laser surface melting, laser surface alloying, and laser surface cladding [54,173,174], enable tailored modifications that can potentially enhance the corrosion resistance of stainless steel. In this work we look into the effect of altering laser processing parameters on the modification of the native oxide film present through a process called laser induced oxidation.

Laser induced oxidation is an almost instantaneous process due to the rapid heating and cooling of the laser modification this causes a non-equilibrium oxidation process to occur. This highly precise processing method allows for the fine-tuning of the thickness and chemical composition of the oxide film. Cui et. al. examined the formation of an oxide film on AISI 304 stainless steel using a 1064 nm Nd:YAG pulsed laser and derived a thermokinetic model to help define the film's composition [73]. This model was used in this work to help define and understand the diffusion of elements. Due to the Gaussian energy distribution the energy decaying radial outwards from a typical laser spot, a non-homogenous composition and morphology often result [175]. The results from this past work show a 2-fold increase in the concentration of Cr on the surface over that of the original sample. The reason for this is due to the relationship between the thermodynamic and kinetic reaction occurring in the process. Initially the formation of Cr_2O_3 oxide is preferred over the formation of Fe_2O_3 as chromium has a lot higher affinity for the chemisorbed oxygen than iron does, so it is thermodynamically

favorable. This causes an initial increase of chromium at the surface of the stainless steel, However, due to the higher temperature at the center of the laser spot and the higher diffusion rate of Fe inside the oxide layer, Fe_2O_3 appears on the stainless steel surface. This in turn, produces a duplex oxide at the center of the laser spot [73]. Secondary compounds also become present in the surface layer such as spinel $FeFe_2$-$xCrxO_4$. These results were consistent with the work done Li et al. and Lu et al. [75,76].

Li et al. used this model to produce a variety of thickness levels of the oxide film on the stainless steel surface by varying the laser power, focal offset and scanning direction [76]. In the study by Lecka et al., the corrosion resistance in 3% sodium chloride solution and sulphuric acid of the laser induced oxides produced on the AISI 304 stainless steel was investigated [77]. Quite similar results were seen for both the testing environments with an initial large increase in corrosion resistance up to a maximum with a lower fluences of 50 -70 J/cm^2 then a sharp decrease back down to a minimum. These results almost perfectly match the work done by Li et al. and Cui et al. with respect to the chromium to iron ratio produced on the surface [73,76]. At higher fluence, temperature of the surface is increased allowing more time for the diffusion of iron through the oxide layer. This decreases the Cr/Fe ratio on the surface of the metal which in turn decreases the effect of the passivation layer causing a lower corrosion resistance [176]. Zhu et al. investigated the effect of laser processing on the microstructure of 304ss. The laser processing altered the microstructure of the top most surface to be composed of ultrafine grains with dislocation in the sublayer. This grain refinement allowed for the production of a more homogenous oxide layer which increased the pitting resistance of the surface [177].

Laser induced oxide formation and its effect on corrosion properties has been studied for a variety of different materials such as 304 stainless steel and Ti_4Al_4V but there are fewer publications on 316 stainless steel [55,76,79] and much less on The effect of the individual laser processing parameters. To fill this gap in this paper, the effect of altering the laser processing parameters on the laser surface oxidation on 316L stainless steel and its effect on its corrosion properties have been studies in this work and are presented herein. For the first time in the literature this paper presents the use of long term EIS and depth profiling XPS to elude and compare the long term behaviour of the samples and to identify how the surface and subsurface oxides influence the corrosion results.

4.2 Materials and Methods

SS316L sheets of 1.7 mm thickness were purchased from Impact Ireland (Metals) Limited, Ireland. The composition of the sheet is given in Figure **4-1**. Disks of 100 mm diameter was sectioned from the sheet using an industrial CO2 (CW) laser. All samples were cleaned using deionized water and then ethanol. The surface of the steel was then uniformly sandblasted to increase surface roughness to 3.9 µm Sa to enhance the laser wavelength absorption [170].

Chemical	**Fe**	**C**	**Cr**	**Mn**	**Mo**	**Ni**	**N**	**P**	**Si**	**S**
Composition Content (wt. %)	Bal.	130 (ppm)	16.64%	1.41%	2.03%	10.0%	400 (ppm)	200 (ppm)	4250 (ppm)	60 (ppm)

Table 4-1 Composition of the SS316L sheet material utilised in this work.

4.2.1 Laser processing

The sand blasted samples were cleaned with acetone, ethanol and sonicated for 15 minutes to remove any contaminants or excess sand from the surface then allowed to dry for 5 minutes on the laser stage. The laser system used consisted of a 3.5 W maximum power 1064 nm Q-switched, diode-pumped solid-state neodymium-yttrium aluminium garnet laser (Bright Solutions 1064 WEDGE HF). A 2D scanning galvanometer (Raylase SS-12) was used to raster the beam in the xy-plane, and a movable z-stage (PI M-404 4PD) used to control the position of the sample. The beam was focused on the sample surfaces, which were placed 340.3 mm below the galvanometer lens at the focal plane to produce a spot diameter of 100 µm. Laser areas of 5 mm X 5 mm were processed using fixed parameters of a bidirectional hatching strategy with a hatching distance of 10 µm. Compared to more complicate scanning strategies, a bidirectional hatch strategy provides a more uniformly repeating heat flow during processing.

4.2.2 Surface characterization analysis

X-ray photoelectron spectroscopy (XPS) was performed on laser processed 316L SS samples using an ESCALAB Xi+ spectrometer microprobe (Thermo Fisher Scientific) with a focussed monochromatic Al Kα X-ray source (*hv* = 1486.6 eV, spot area of 650 µm x 650 µm) operating at a power of 225 W (15 kV and 15 mA) and the photoelectrons were collected using a 180° double-focusing hemispherical analyser with a dual detector system. The base pressure of analysis chamber was always maintained < 5 x 10^{-9} mbar, which increased up to ~5 x 10^{-7} mbar during measurement along with charge neutraliser (flood gun) operated at 100 µA emission current. XPS sub-surface chemical composition analysis was performed using a soft cluster clean and monoatomic depth profiling using Ar gas. In the cluster clean, the sample surface of raster size 3.25 mm were exposed to Ar clusters of 1000 atoms, energy at 4 keV for 30 s. XPS depth profiling was performed using 4keV Ar+ monoatomic beam on a raster area of 1.5 mm on the sample. The sputter rate at 4keV energy for the sample is referenced to Ta_2O_5 sample (BCR −261T standard) to 0.96 nm/s as given by Advantage operation software. Further relationship between sputter rates of different compounds to standard Ta_2O_5 can be understand from references [178,179]. In all these cases, survey scan spectra were recorded with parameters of step size 1 eV, pass energy 150 eV and narrow core shell high resolutions scans were taken at step size of 0.1 eV, pass energy of 20 eV. Casa XPS software was used to analysis the results for elemental and chemical oxidations states of all elements of interest. The $2p_{3/2}$ peak was taken into account for the composition analysis of chromium, and Iron while for oxygen the 2s singlet peak was used and for molybdenum both the $3p_{5/2}$ and $3p_{3/2}$ peaks were taken into account. The sensitivity factor and peak position can be seen in Table **4-3** below.

4.2.3 Electrochemical Corrosion Test

For the characterization of corrosion behaviour electrochemical measurements were performed using the Potentiostat (Gamry, interface 1000E) with an open beaker 3 electrode cell with an Ag/AgCl reference electrode, graphite rod counter electrode and the working electrode being the laser processed samples. To isolate the samples, they were first cut into individual pieces using a precision saw. The edges of the samples where then ground using a low grit paper to remove any burs or blemishes. A 3D printed isolation holder was used to just expose the surface. An open circuit potential (OCP) was first carried out on the sample in

0.5 M NaCl for 10,800 s to obtain the OCP. Electrochemical impendence spectroscopy (EIS) was then carried out with Impedance data collected at OCP over a frequency range from 10 mHz to 10 MHz with peak to peak amplitude of 10 mV. Circuit models were designed using Gamry Echem analyst software. A second OCP was then measured for 3600 s to act as a reference point for the cyclic polarization (CP). Cyclic polarization was then preformed on the sample with a forward scan rate of 0.1667 mV/s between -0.3 V to 1.5 V against the OCP. Once the maximum voltage was achieved the reverse scan started with a scan rate of 0.1667 mV/s down to -0.3 mV/s of the OCP. Tafel plot interpolation was used to extract the corrosion data for the cyclic polarization curve.

4.2.4 Morphology analysis

Optical imaging was performed using a VHX-2000 (Keyence) 3D optical microscope. Scanning electron microscopy was conducted using JSM-IT 100 (Jeol).

4.3 Results

Two distinct full factorial design of experiment (DoE) designs (3x3) were conducted to examine the effect of the laser process parameters. The process factors examined in the first model were laser power (W), scan speed (mm/s), and laser frequency (kHz). The processing factors and their levels examined are listed in supplementary information. The optimal values of the laser frequency (100 kHz) from the first DoE were used in the second model. The findings from the first DoE showed that reduced areal energy produced superior corrosion results, so the scan speed and laser power were also investigated in the second DoE. To further investigate the effect of laser processing on the corrosion, five samples were selected from the two DOEs with varying corrosion results the samples and parameter can be seen in Table **4-2**

Sample	Power (W)	Frequency (kHz)	Scan-Speed (mm/s)	Hatching Distance (μm)	Time (s/m^2)
1 (S1)	1.52	60	50	10	20,000
2 (L24)	2.60	100	450	8	2,778
3 (L25)	2.60	100	250	15	2,667
4 (L21)	3.44	100	250	10	4,000
5 (S27)	2.60	100	450	1	22,222

Table 4-2 Selected samples and laser process parameters for production of the laser surface oxidised samples.

To be able to normalize the process parameters into a single parameter, the areal energy equation was calculated. It takes into account the total number of laser impacts, the laser fluence of an individual pulse, and the pulse overlap with the Pulse fluence being defined as the laser power divided by the laser spot area and d being the spot size area:

$$Areal\ energy\ = \frac{Pulse\ Fluence}{(d^2 * (1 - Hatching\ overlap)(1 - Pulse\ overlap))} \qquad \text{Eq. 1}$$

4.3.1 Surface Concentration

X-ray Photoelectron Spectroscopy (XPS) was conducted on the five laser-processed samples to analyse the surface chemistry of four key compounds: iron, chromium, oxygen, and molybdenum. Casa XPS software was initially used to determine the relative concentrations of these compounds by measuring the ratio of peak areas. Notably high peak intensities of iron, oxygen, and chromium were observed in all samples, suggesting a predominant surface composition of iron and chromium oxides. For detailed analysis, refer to the high-resolution XPS data in Figure **4-1** and Table **4-3** provides information on sensitivity factors, reference peaks, and experimentally recorded peak positions.

Fe 2p Spectra (Figure 4-1 e-f): Examining the Fe 2p spectra reveals the presence of four prominent peaks at binding energy values of 710-711 eV, 724-725 eV, 715-716 eV, and 729 eV, corresponding to Fe $2p_{3/2}$ and Fe $2p_{½}$. Notably, the peaks at 716 eV and 729 eV are

identified as satellite peaks, indicative of Fe (III) oxides, specifically Fe_2O_3. In the case of lower areal energy runs, such as S3, an additional peak at ~706 eV is observed, signifying incomplete oxidation and the presence of metallic Fe on the surface. O1s Spectra (Figure **4-1**c): For all runs, the shape of the O1s peak was very similar. This peak forms at binding energy 530.4 eV and with a full width half max (FWHM) of 1.5 eV indicating an O_{2-} metal oxide; this indicates that the laser processing has oxidized the steel surface. Shoulder peaks are also present with a binding energy of 532.1 eV due to the presence of OH- in part due to metal hydroxides. The O_{2-} / OH- ratio in the oxide film was calculated from the O 1s spectra, with a larger variation in ratios throughout the processed samples with S3 having an O_{2-} / OH- ratio of 8.01 and with S4 having a ratio of 1.11. These both show higher oxide ratios than the unprocessed sandblasted sample at a ratio of 0.61. This ratio plays an important role in the pitting corrosion as hydroxides film are more defect prone than oxide film so this increase in the ratio can positively impact the density of the passive film present on the steel surface [180]. The amount of oxygen present on the surface is a lot higher in S4, which is explained by the higher content of hydroxides present compared to the other processed samples. Mo 3d Spectra (Figure **4-1**d): The Mo3d spectra displayed two major peaks at binding energies of 232.36 eV and 235.42 eV, corresponding to Mo^{6+} $3d_{5/2}$. The concentration of Mo is only detectable in samples 1 and 5, due to the higher power used allowing longer diffusion times, but the concentration is still extremely low at under 1%. Cr 2p Spectra (Figure **4-1** a-b): The Cr 2p spectra reveal three primary peaks at binding energies around 577 eV, 580 eV and 587 eV, corresponding to Cr $2p_{3/2}$ for Cr(iii) oxide, Cr $2p_{3/2}$ for Cr(vi) oxide, and $Cr_{½}$ for both oxides, respectively. The identified oxides include Cr_2O_3 and CrO_3. Analysis discloses the formation of three distinct oxide combinations on the laser-processed surface: Notably, these oxide combinations closely correlate with areal energy, with lower areal energy in S3 favouring Cr_2O_3 with 100% of the Cr(iii) peak against 0% of CrO_3. In contrast, higher areal energy in S5 favours CrO_3, with the Cr(vi) peak at 89% vs. 11% of the Cr(iii) peaks corresponding to Cr_2O_3.

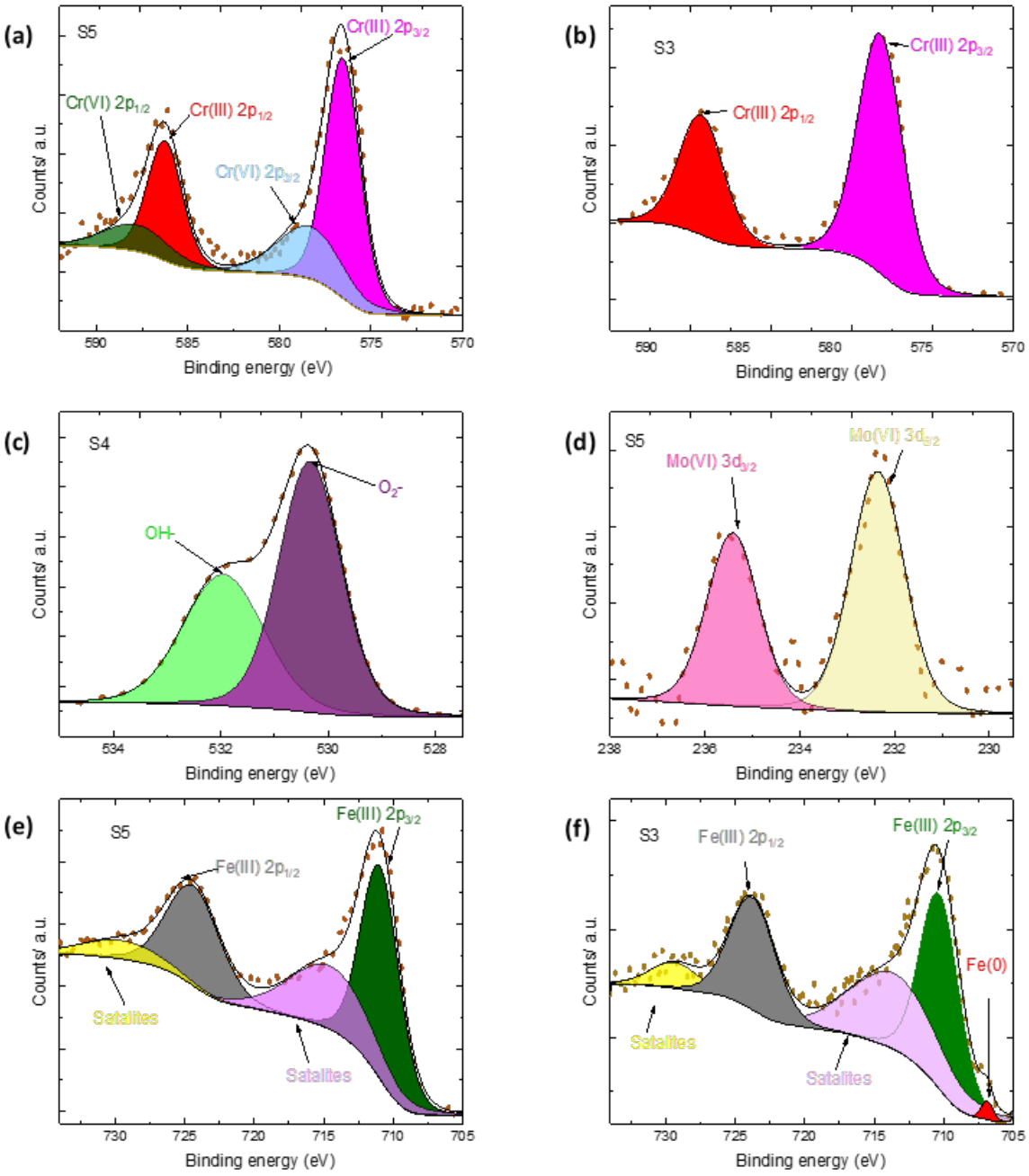

Figure 4-1: High resolution XPS spectra of (a) Cr 2p for S3 (low areal energy), (b) Cr 2p for S (high areal energy), (c) O1s spectra of S4 (middle areal energy) , (d) Mo 3d of S5 (high areal energy) , (e) Fe 2p for S5, (f) Fe 2p of S3 (low areal energy).

Peaks	Compounds	Binding Energies (eV)		Sensitivity Factor
		Experimental	Reference	
Fe 2p 3/2	Fe (metal)	706.8	706.5	
	Fe_2O_3	710.9	710.8	10.82
Cr 2p 3/2	Cr (metal)	574.8	574.3	
	CrO_3	580	580	7.69
	Cr_2O_3	577	576	7.69
O 1s	O_2 -	530.1	529-530	2.93
	OH-	532.0	531.5-532	
Mo 3d 5/2	MoO_3	231.5	232	5.62
Mo 3d 3/2	MoO_3	236.1	235.6	3.88

Table 4-3 Binding energies and sensitivity of the compounds used in this study [20–22].

4.3.2 Depth profile

Figure **4-2** shows the XPS depth profiles of the five selected laser processed samples (See Table **4-2**) and the unprocessed blank samples. These profiles show that the individual elements vary quite drastically through the depth of the oxide layer; the oxygen content of the laser processed samples is elevated compared to the blank samples further into the depth profile showing an expansion of the oxide layer. An interesting observation is the variation in nickel content between samples 2 and 3 where the chromium content varies similarly throughout the profile but S2 has an increase in nickel content further into the profile while S3 has an increase in Fe. All other samples have a relatively constant oxide layer composition after 20-40nm vs Ta_2O_5 into the depth profile, while samples 2 and 3 vary throughout the entire profile. The oxide layer thickness was measured using a O 50% method, where the concentration of the oxygen drops below 50 % of its original value [181,182]. Table **4-4** shows the results, samples 1 and 5, have a very larger oxide layer present greater than the depth profiled. Samples 2 and 3 show similar oxide behaviour at values in the 75-85 nm range, samples 4 and the blank also show similar results.

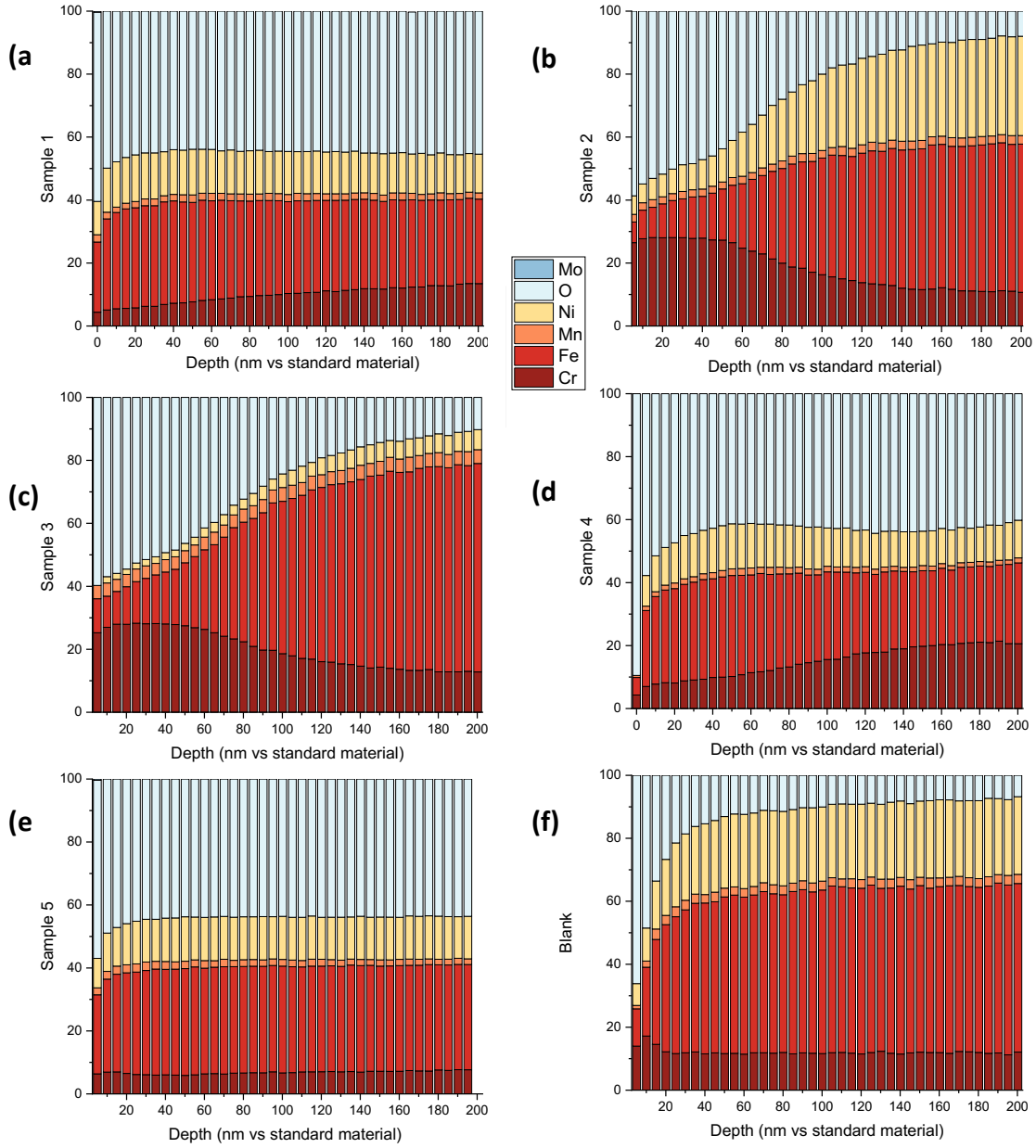

Figure 4-2: XPS depth profile of laser-processed vs Ta_2O_5 standard material (a) S1, (b) S2, (c) S3, (d) S4, (e) S5, and (f) blank sample.

The analysis of Mo into the depth profile was hindered due to the argon etchant used which can cause the Mo oxide to be reduced to a mixture of lower oxide states and can cause them to not be detected at the low concentrations.

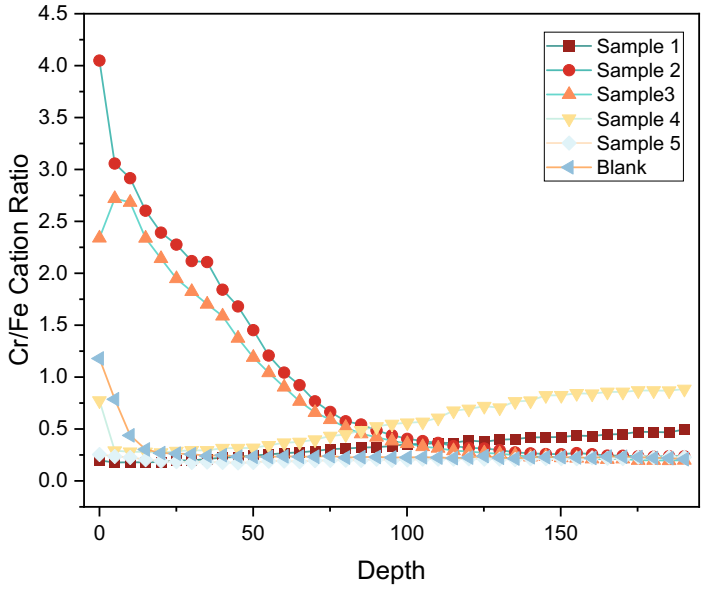

Figure 4-3: Cr/Fe ratio throughout the depth profile for all tested samples.

Examining the variation in the Cr/Fe ratio throughout the depth profile provides insights into the transformation of oxide layers. The blank sample exhibits a consistent decrease in the Cr/Fe ratio up to 20 nm, levelling off into the bulk stainless steel, indicating the presence of a single-layer oxide. Samples 4 had a similar Cr/Fe ratio starting behaviour as the blank sample but this started to increase further into the depth profile. This shows that it had a thin outer passive layer but a larger oxide layer depth in total compared to other samples.

Samples 1 and 5 show similar behaviour with an almost constant Cr/Fe ratio throughout the entire depth profile, with a ratio very similar to that of bulk stainless steel. This shows that for the higher areal energy runs the protective passive layer seems to almost be fully removed after processing.

S2 shows the highest initial Cr/Fe ratio, being over 4.0. The ratio sharply drops over the first few nm. Where it meets a turning point in the results, these inflection points could be indicative of a multilayer oxide forming on the surface, which has been seen previously in the literature. S2 has two discrete turning points one at 5 nm and one at 35 nm.

S3 shows a slightly different behaviour to the rest if the oxides where the Cr/Fe ratio increase over the initial few nm of the passive film going from 2.3 to 2.6 over the first 5 nm showing that there is a chromium enriched inner oxide layer. It meets an inflection point and starts to decrease in value again. This indicates that the lower areal energy does not allow for full diffusion causing a smaller altered layer thickness.

Sample	Fe (at%)	Cr (at%)	Mn (at%)	Ni (at%)	Mo (at%)	O (at%)	Cr/Fe	Oxide Depth
Sample 1	23.38	4.33	1.92	12.00	0.34	58.03	0.19	>200
Sample 2	6.01	21.67	3.04	4.75	0.00	64.52	3.61	75
Sample 3	9.24	21.17	4.38	0.00	0.00	65.21	2.63	85
Sample 4	7.33	5.90	0.22	0.00	0.00	86.55	0.80	25
Sample 5	23.12	5.85	2.29	9.79	0.32	58.63	0.25	>200
Blank	14.01	9.92	0.61	6.37	0.00	69.09	0.71	15

Table 4-4 Surface (Depth = 0) composition of the laser processed samples, including the Cr/Fe ratio and the oxide layer depth.

4.3.3 Cyclic polarisation results

Figure **4-4** depicts the potentiodynamic polarization curves of 316L stainless steel with the five varying laser-processing conditions in a 0.5M NaCl solution at room temperature. As increasing polarization potentials, the curves of all steels contain the active, passive, transpassive and oxygen evolution process regions. The first passive domain is associated with the presence of a Chromia oxide based passive layer. The magnitude and occurrence of this layer is driven by the oxidation processing and is therefore directly related to the chemical composition of the passive oxide layer.

Sample	S1	S2	S3	S4	S5	Blank
Icorr (nA/cm^2)	730.40	49.53	51.50	69.65	301.75	502.00
Ecorr ($mV_{Ag/AgCl}$)	-87.22	-60.30	-66.50	-70.75	-170.00	-125.00
E_{corr}- E_{pit} ($mV_{Ag/AgCl}$)	133.50	395.90	509.15	168.28	105.39	160.80

Table 4-5 Electrochemical parameters of corrosion current, corrosion potential and pitting resistance (E_{corr} – E_{pit}) measured for laser processed samples.

When the electrical potential exceeds a critical threshold, chloride ions migrate toward the interface between the metal and oxide layers, resulting in the creation of a metal chloride phase. This phase cracks the overlying oxide because of its large specific volume. Consequently, the chloride phase becomes a readily available source of chloride ions that foster the initiation and stabilization of pit growth. After pitting nucleation, these pits continue to expand, forming microscale cavities before eventually undergoing repassivation. This ongoing cycle of breaking down and restoring the thin passive film is termed metastable pitting and is a crucial stage. Only the pits that survive this stage have the potential to develop into stable, growing pits [183]. The presence of this metastable pitting phenomenon can be observed in samples 2 and 4.

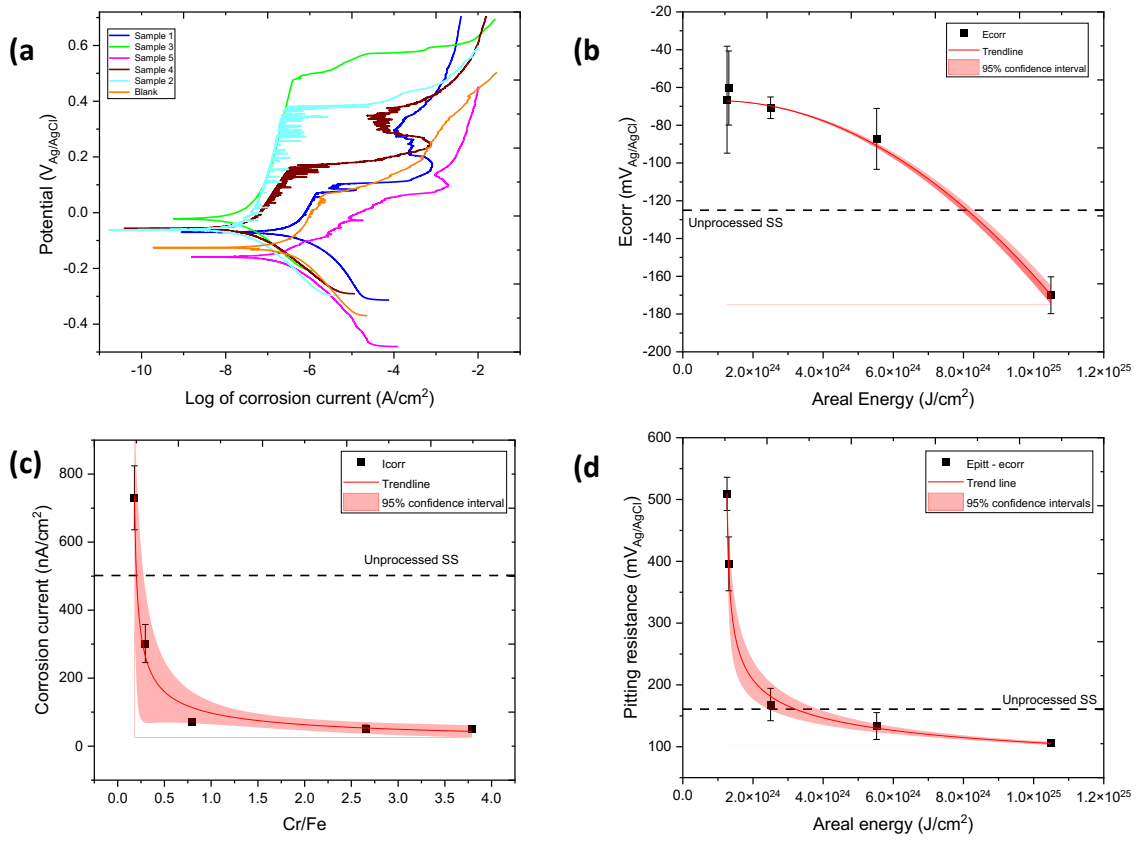

Figure 4-4: (a) Cyclic polarization graph of the 5 laser processed samples vs Ag/AgCl, (b) Ecorr vs areal energy, (c) Corrosion current vs Cr/Fe ratio, (d) Pitting resistance vs areal energy.

Ultimately, the dynamic balance between the rupture and repair of the passive film at local defects is disrupted, leading to the formation of stable pits, which is known as the pitting resistance for the given sample. Within these pits, those in a locally activated state (characterized by low potential) serve as the anode, while the majority of the surrounding surface remains passivated (exhibiting high potential) and serves as the cathode. Consequently, an electrochemical corrosion cell with an "big cathode and small anode" is established both inside and outside the pit [184,185]. As the anodic reaction progresses, the concentration of metal cations, such as Fe^{2+}, within the pit increases. To maintain charge neutrality within the pit and balance the charge associated with these cations, chloride anions electro-migrate into the pit. Cation hydrolysis and the absence of a localized cathodic reaction contribute to a decrease in pH within the pits. Once an acidic chloride-rich environment is

established within the pits, it facilitates pit growth through an autocatalytic pitting mechanism.

It can also be seen that in samples 1, 4 and 5 that a second zone of repassivation has occurred after the pitting resistance has been surpassed. This is evident by the increase in anodic current density at potential above the pitting resistance. These samples are all associated with a smaller first passive domain than samples 2 and 3, this second repassified layer can be associated with the change of oxidation state of chromium due to the applied electrochemical potential, referred to as Cr transpassivation. This causes a thickening of the surface film and causes a depletion in the Cr content in the oxide due to rapid dissolution of chromium in this domain, making the layer more susceptible to further electrochemical breakdown [186]. This does not occur in samples 2 and 3 due to there more favourable passive layer that does not break down until above the second passive domain of +0.4 V vs SHE.

To further assess the effect of laser processing on the corrosion resistance of the samples, the key electrochemical parameters, namely the pitting resistance, free corrosion potential (Ecorr) and free corrosion current density (Icorr), are determined using the Tafel extrapolation method [187]. Table **4-5** lists these electrochemical values for all samples.

It can be seen that the Ecorr trends to more noble values with a decrease in the applied areal energy, this higher Ecorr value corresponds to a more compact and protective passive film, being less susceptible to corrosion attack. The two noblest Ecorr values correspond to samples 2 and 3 at -60.3 and -66.5 mV respectfully with the Ecorr value dropping exponentially with an increase areal energy until it reaches the lowest value of -170 mV for S5. This shows that S5 has the least compact passive film, which is evident by the cracks and defects in its passive film.

The pitting resistance ($E_{corr} - E_{pit}$) can also be seen to follow a similar trend where the lower the applied areal energy corresponds to the higher pitting resistance with S3 having the highest pitting resistance at 509.15 mV which is 8 fold increase compared to the unprocessed value of 60.9 mV. It is also seen in Figure **4-4** (c) that the corrosion current followed closely the Cr/Fe ratio with a sharp drop off once the Fe content surpasses the Cr in the passive oxide layer, increasing from 49.5 nA/cm^2 to 730.4 nA/cm^2 with an increase in Cr/Fe ratio of 0.179 to 3.61.

These results show that the composition has a strong influence over the general corrosion of the surface while the surface morphology has more of an influence over the localised corrosion. Lower hatching distances result in an increased amount of heating and cooling cycles and thermal stresses inside the layer allowing for more surface defects to be present.

4.3.4 Electrochemical impedance spectroscopy

EIS test is a common method for evaluating the properties of the passive film on stainless steel surfaces. The Bode and Nyquist plots measured in 0.5 M NaCl solution at OCP of S2,5 and unprocessed are seen in Figure **4-5** As the passive film on stainless steel is not always perfectly stable, and its resistance can change with time and exposure conditions. Therefore, the Rp value measured at a specific point in time may not represent the long-term stability of the passive film for this reason we have preformed a long exposure examination with EIS measurement taken over a 10 day period under the same conditions as above. The Nyquist plots of the three samples over the 10-day period are shown in Figure 4-6.

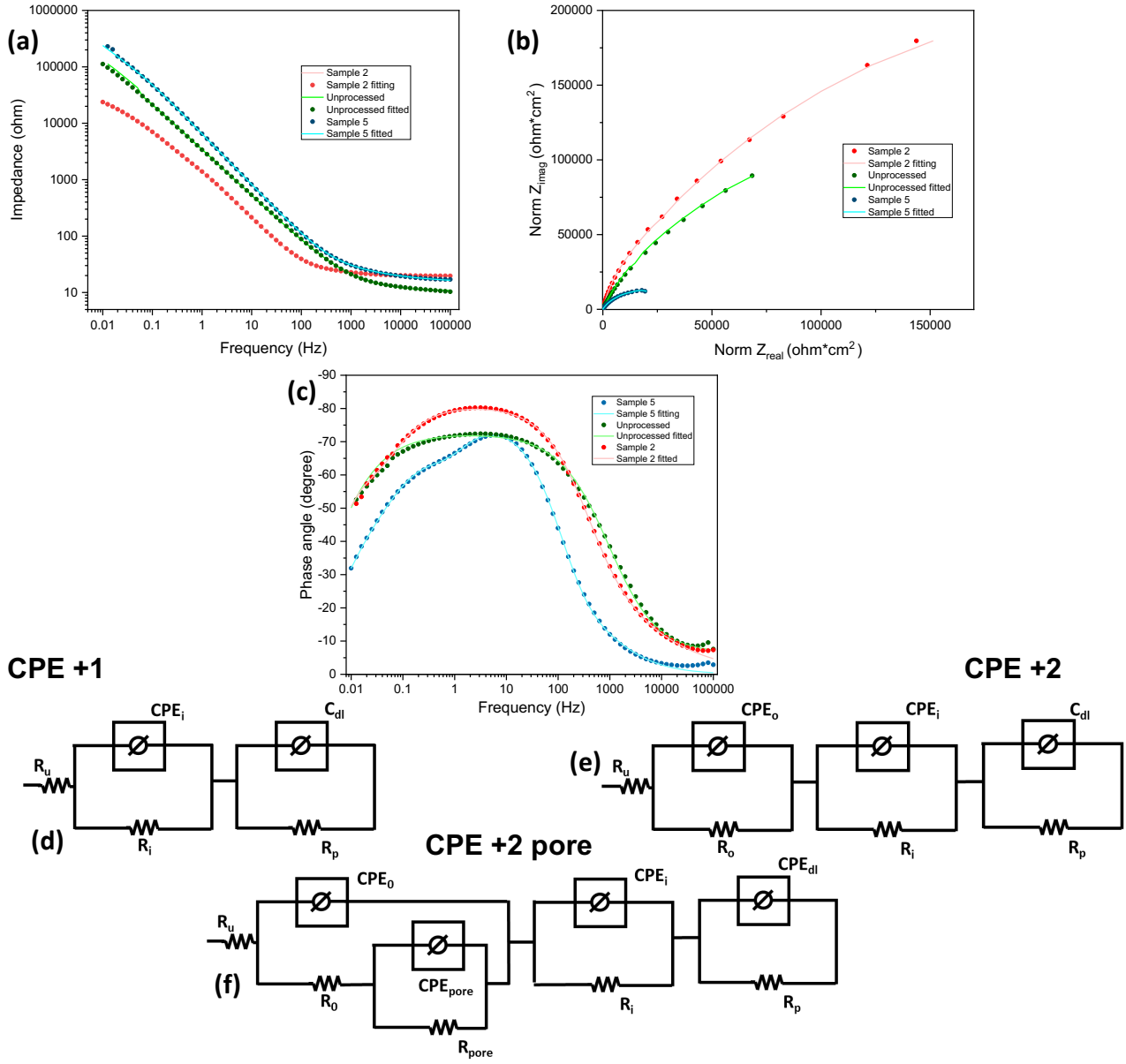

Figure 4-5: Electrochemical impedance plots for laser processed samples (a) Bode impedance plot (b) Bode phase plot, (c) Nyquist plot, (d) EEC for Blank (CPE + 1), (e) EEC for S2 (CPE + 2), and (f) EEC for S5 (CPE + 2 pore).

The impedance was significantly higher for S2 compared to the unprocessed samples with S5 being significantly smaller then both Figure **4-5**. The phase angle vs frequency plots for all samples in Figure **4-5** show a broad peak in the mid-frequency range which is indicative of the capacitive characteristic of the system. The capacitive characteristic is the result of charge transfer and formation of double layer capacitance at metal/electrolyte interface where, the

diameter of the capacitive loop indicates the charge transfer resistance (Rp). Higher Rp signifies lower dissolution rate and correspondingly higher corrosion resistance.

The Nyquist plot for the S2 showed the largest radius signifying highest corrosion resistance amongst all samples. The Bode plot for each of the three samples are unique and show different surface properties, with all samples having multiple time constants. The unprocessed sample is fitted with a circuit with two time constant connected in series; this is due to the oxide layer acting as one time constant and the sandblasted surface roughness acting as the other. S2 then expands the equivalent circuit to include a third time constant due to the formation of a multilayer oxide being produced. Samples 5 has the same three-time constants in series but also include a fourth time constant in parallel to incorporate the effect of the porosity/cracked outer passive film produced. Therefore, a two-time-constant EEC for the as-received alloy and a three and four-time-constant EEC for both the processed specimens 2 and 5 respectfully were used to model the electrochemical system. The EEC for as-received steel and both the processed specimens are shown as insets in Fig. 8(c) and (d) respectively.

Here, Ru is the solution or electrolyte resistance, Cdl and Rp are the electrochemical double layer capacitance and charge transfer resistance, respectively, for the high frequency part of the spectrum, whereas CPEi and Ri are the corresponding elements inner oxide layer properties. With CPEo and Ro resenting the outer oxide layer and CPEpore and Rpore representing the pore capacitance and resistance. CPE, a frequency dependent constant phase element with exponent α, was used instead of pure capacitance to account for surface in-homogeneities, such as roughness, adsorption, and diffusion. The values of different elements of the electrochemical equivalent circuit are summarized in Table **4-6** with the more detailed results seen in supplementary information 3.

Table 4-6 Electrochemical impedance spectroscopy results for samples 2, 5 and unprocessed

Sample	**Rtotal (k ohm/cm)**	**Rp**	**Cdl** ($\mu S\ s^a/cm^2$)	**Ru**	**Ri**	**CPEi**	**Ro**	**CPEo**	**Rpore**	**CPEpore**
Blank	384736	375800	757.5	11.18	8936	5475	-	-	-	-
Sample 2	586015	547200	473.4	15.61	15	3592	38800	773.2	-	-
Sample 5	37362.85	7639	3599	19.68	6.75	2604	417.1	4355	29300	1337

Rtotal gives the total resistance for the processed and unprocessed specimen (Table **4-6**). The total resistance was found to be highest for S2 followed by unprocessed and then S5. Charge transfer resistance shown by S2 was noticeably higher compared to other two specimens. This is in line with Tafel results, supporting highest corrosion resistance for S2 followed by unprocessed and them S5. In addition, the α value for both the processed samples was higher, indicating better homogeneity of the passive layer. The likely cause of superior pitting corrosion behaviour of processed samples.

Figure 4-6 shows the time dependent EIS profiles for samples 2, 5 and Blank, The EIS results all show multiple time constants and the equivalent circuit alters over time, showing a variation in the RP values and EEC. The Nyquist plots of all the samples display a similar semicircle feature under different condition, but at different diameters.

During S5 initial experiences of exposure, a CPE+2 pore equivalent electrical circuit (EEC) develops due to imperfections in the passive film. In the early stages of exposure, the metal surface undergoes passivation, as evidenced by an enlargement of the semicircle feature in the Nyquist plot, see Figure 4-6. This results in the formation of a passive film that contributes to the increase in Rp, reflecting the resistance to corrosion. The initial rise in Rp is linked to the growth and stabilization of the passive film. As the passive film thickens and becomes more protective, Rp continues to increase, transforming the EEC into a CPE+2 configuration. This change is indicative of the evolving electrochemical behaviour as the metal surface interacts with its environment. The enhanced Rp signifies a more robust protective layer, indicating the progression of passivation. The impedance steadily rises until reaching a peak on day 4, after which it starts to decline. This decline is attributed to the degradation of the passive film, signifying reduced protection and heightened susceptibility to corrosion. By day 6, localized corrosion initiates, leading to a transition in the EEC to CPE+2, with pores now forming due to pitting corrosion of the passive film. This shift in the electrochemical response is a critical point, highlighting the initiation of a corrosive process that compromises the integrity of the passive film. The formation of pores introduces new pathways for corrosive agents, further accelerating the corrosion process. The overall resistance (Rtotal) continues to decrease throughout the remaining 4-day period, indicating an ongoing deterioration of the metal's corrosion resistance. The detailed understanding of these electrochemical

changes can inform strategies for corrosion prevention and mitigation in practical applications.

S2 exhibits distinct mechanistic effects compared to S5. Initially, S2 starts with an EEC of a CPE+2, a configuration that remains consistent as the surface undergoes passivation processes, leading to an increase in impedance. This impedance steadily rises until day 2, reaching its peak, after which it stabilizes, indicating the establishment of steady-state conditions as the passive film attains a stable state.

Rp, representing the passive film resistance, reaches a plateau during this period, suggesting the formation of a relatively constant and well-developed passive film. Over the subsequent 8 days, there were minor fluctuations in impedance, followed by prompt re-establishment of the passive film. These fluctuations may indicate evidence of metastable pitting occurring during electrochemical impedance spectroscopy (EIS) [188].

On day 7, the EEC undergoes a transition, increasing the number of time constants to CPE+3. This change signifies the formation of a multilayer oxide, indicating a complex evolution of the passive film structure. This shift in the EEC configuration provides insights into the ongoing processes of oxide layer formation and the dynamic nature of corrosion resistance mechanisms within S2.

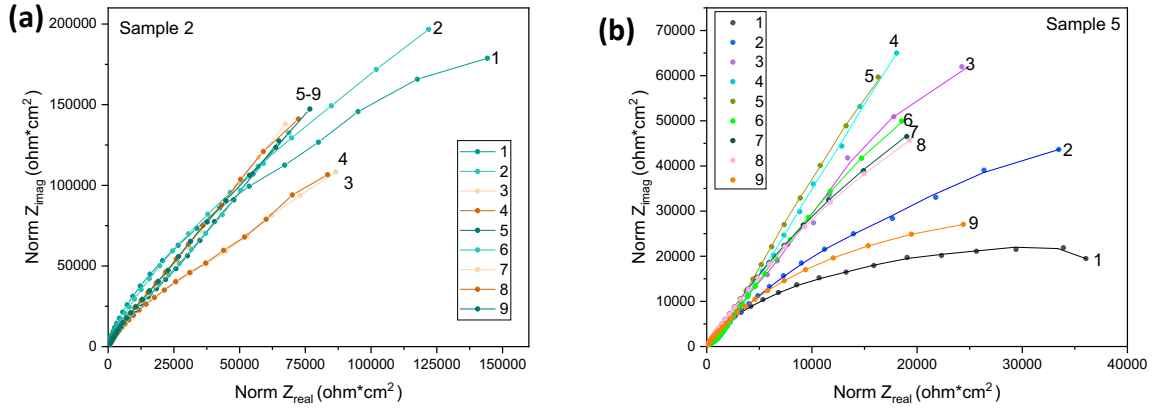

Figure 4-6: Long-term electrochemical impedance spectroscopy for laser processed samples (a) S2, (b) S5.

In S3, additional information from the supplementary data 4 reveals an intriguing pattern in the total resistance. Initially, there is a gradual increase in total resistance over the first four runs. However, from runs five to ten, there is a notable and abrupt decrease in resistance. Followed by a sudden and substantial increase where it stabilizes. This fluctuation in resistance dynamics may be linked to the formation of a multilayer oxide. As evident from the depth profile the outer oxide layer formed contains lower chromium content. However, as this outer layer undergoes breakdown, the underlying layer with higher chromium content becomes exposed, leading to an enhanced passivation effect.

4.3.5 Morphology analysis

SEM images of the laser processed samples 2, 5 and unprocessed are seen in Figure **4-7** . These two samples experience the lowest and highest areal energy between them. It is evident from Figure **4-7** b that the laser processing removes many of the surface defects due to the process of oxide growth and laser remelting and solidification. The oxide growth causes a change in the optical properties of the surface changing the colour of the surface due to the process of thin film interference caused by the production of a thin film oxide. It can be seen for the higher areal energy processed samples (Figure **4-7**a) that defects start to occur in the oxide film with oxide cracks and a very porous oxide film being produced.

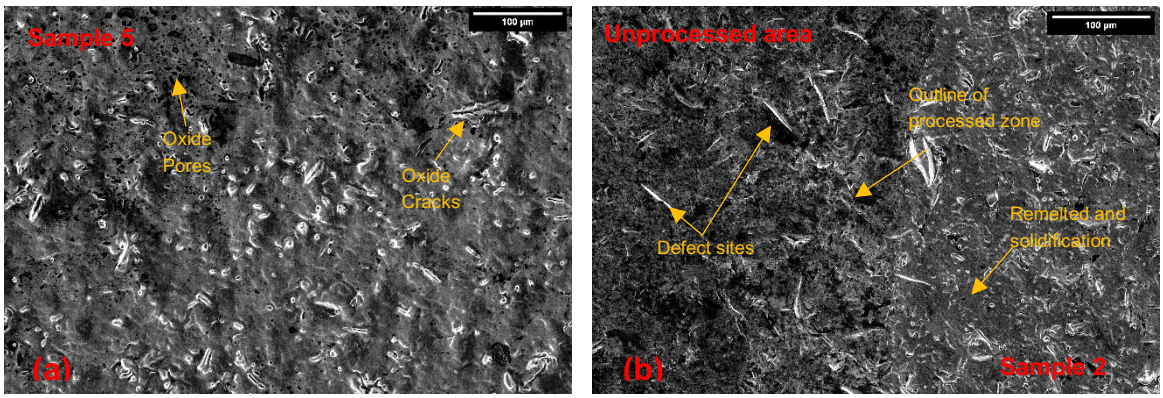

Figure 4-7: SEM images of (a) S5 and (b) S2 and unprocessed sample.

Scanning electron microscope (SEM) image of the corroded surfaces for all cases are shown in Figure **4-8**. Both unprocessed and S5 showed extensive corrosion, in contrast S2 showed lower overall corrosion supporting its superior corrosion resistance. It was seen that samples 5 experienced a variety of difference corrosion fails; the surface oxide colour was fully stripped which a few very large pits formed, while also experienced delamination of the oxide

layer showing that the oxide is not strongly bonded to the substrate. The unprocessed sample experienced a higher pitting density with multiple larger pits on the surface with no evidence of delamination. S2 seem to perform the best with sight evidence of general corrosion seen by the discolouration of the oxide film at certain location, with only a singular pits present. The 3D optical profilometer measurements of the corrosion pits for all samples are shown in Figure **4-8**. The pit depth for the unprocessed samples shows a peak at 116 µm compared to the 61 µm for the optimised S2, S5 preformed the worst producing the largest and deepest pits with a peak depth of 354 µm and a pit area six times larger than unprocessed stainless steel. As the surface roughness was quite high in all samples, the peaks could mask the smaller pits and trough the pit density was quite low with larger spacing between each pit, this shows that the area surrounding each large pit became cathodically activated reducing it susceptible to pit initiation.

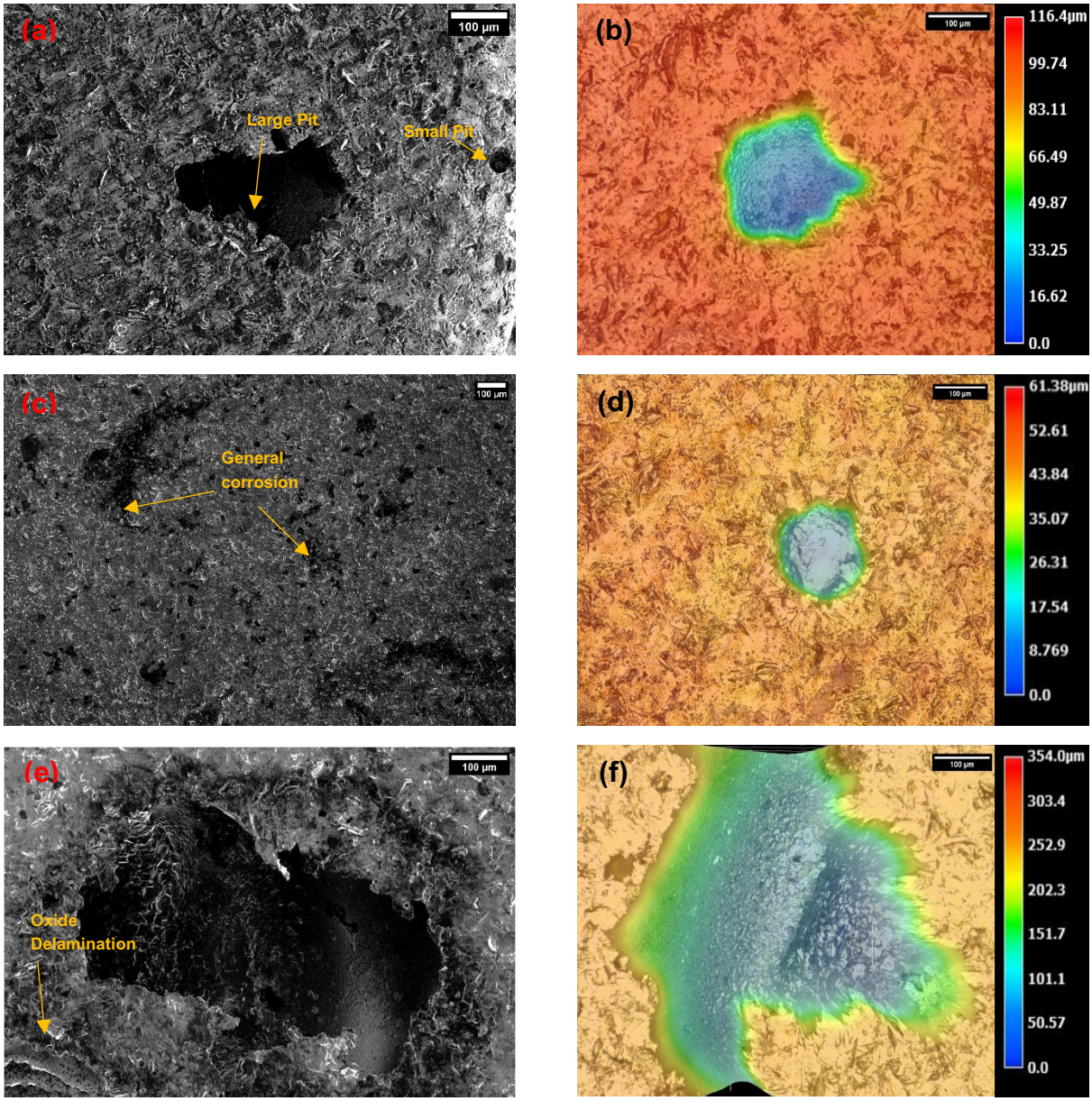

Figure 4-8: (a) SEM image of unprocessed showing corrosion morphology, (b) optical profilometer of unprocessed pitting corrosion, (c) SEM image of S2 showing corrosion morphology,(d) optical profilometer of S2 pitting corrosion (e) SEM image of sample of S5, and (f) optical profilometer of S2 pitting corrosion.

4.4 Discussion

The corrosion resistance of stainless steel is mainly attributed to the protective nature of the passive film and its self repairing ability [169,189], a three layer model has been suggested for the passive films on austenitic stainless steel [190,191]. The outmost layer has been shown to composed of a hydroxide film with an oxide layer beneath, this oxyhydroxy film, mainly enriched with Cr(III), is formed on top of a Ni(0) enriched layer in the metallic alloy region. This orientation of the oxide film is clearly seen from the depth profile Figure **4-3** (e). During laser irradiation, the outer layer of the oxide film absorbs light through inverse Bremsstrahlung absorption. The absorbed energy propagates into the subsurface atoms exciting the electrons to higher energy levels and become more energetic. In addition, the surface-adsorbed oxygen molecules have a higher probability of decomposing into oxygen ions [192]. Thus, this regeneration of the Mott potential facilitates the continued growth of the oxide layer [9]. The rapid heating and cooling caused by the laser processing allows for non-equilibrium oxidation of the surface, this gives the ability to fine-tune the oxide composition, which can heavily influence the corrosion properties of the surface.

The optimized laser processed sample was obtained by the ns-laser processing with S3 conditions of a 250 mm/s scan speed, 15 µm hatching distance, 100 kHz frequency and a 80% power. These conditions led to a peak pitting resistance of 509.15 mV vs Ag/AgCl and an Icorr value of 51.5 nA/cm^2. This shows that the optimal sample (S3) had a corrosion resistance 10 times better then unprocessed stainless steel,

As depicted in Figure **4-2**, the corrosion current closely correlates with the Cr/Fe ratio observed on the surfaces of laser processed samples, indicating that higher Cr/Fe ratios above 1.0 are associated with lower corrosion currents, indicative of a reduced corrosion rate. This observation highlights the significant influence of the chromium-to-iron ratio on the corrosion behaviour of the samples. Interestingly, the trend of increasing Cr/Fe ratio being more proficient at lower areal energies is noteworthy. For instance, S3 demonstrates a notable Cr/Fe ratio of 3.61 at the lowest areal energy level, suggesting a robust resistance to corrosion. Conversely, S1 exhibits the highest corrosion current despite its longer processing time, which is intriguing considering its relatively low Cr/Fe ratio of only 0.19. This discrepancy

highlights the intricate interaction between processing parameters and resulting surface characteristics on corrosion resistance.

Furthermore, the variation in Cr/Fe ratio observed across samples can be explained by the thermokinetic model proposed by Cui et al. [73]. According to this model, during the initial stages of laser exposure, chromium ions are preferentially oxidized due to their higher affinity for oxygen, leading to the formation of a chromium-rich oxide layer on the surface. This phenomenon accounts for the higher chromium-to-iron ratios observed in samples subjected to lower areal energy inputs.

As the energy input increases, the thermal environment becomes more conducive to the diffusion of iron atoms toward the surface. This is attributed to the higher mobility of iron ions through the oxide layer compared to chromium ions. The accumulation of iron at the surface results in the formation of an iron oxide layer, which gradually overlays and suppresses the underlying Chromia oxide. Consequently, a multilayer oxide structure develops, characterized by an inner chromium-rich layer and an outer iron-rich layer. This stratified oxide formation is evident in the depth profile presented in Figure **4-2**.

Importantly, Cui et al. highlight that laser-induced oxidation occurs under non-thermal equilibrium conditions, where extremely rapid heating and cooling rates cause deviations from conventional oxidation behaviour. Under these conditions, the oxidation process is governed not only by thermodynamic stability but also by kinetic factors such as ionic mobility and short-range diffusion. This non-equilibrium state enables selective oxidation and element redistribution that would not typically occur under slow or conventional thermal treatments. [73]

The pitting resistance results closely track the areal energy utilized for each sample produced. Notably, S3 exhibits a higher pitting resistance than S2 despite having a lower Cr/Fe ratio. This discrepancy in pitting resistance values, despite similar applied areal energies, can be elucidated by the increased hatching distance employed in producing S2. It is conceivable that the reduced laser overlap at greater hatching distances contributes to enhanced pitting resistance. This reduction potentially mitigates the thermal stress within the oxide film and

diminishes the formation of surface cracks and defects, which serve as primary sites for initial pitting formation and propagation. This also shows that the hatching distance is more influential than the scanning speed, showing that a reduced number of longer thermal cycles produces less thermal stresses and defects then multiple shorter thermal cycles [193]. The SEM images (Figure **4-8**) reveal disparities between samples 2 and 5, with S2 exhibiting fewer and smaller initial defects compared to S5, which employs a hatching distance of 1 µm. The presence of surface defects at higher areal energies has been documented in previous literature [194]. These defects intensify chloride attack and heighten the reactivity of the anions. Mechanical stresses at weak sites or flaws arising from electrostriction and surface tension effects may precipitate local breakdown events. In chloride-containing solutions, the hindrance to repassivation by chloride diminishes the likelihood of such breakdowns healing allowing for permanent pitting to be form [188].

Furthermore, samples 1, 4, and 5 possess a transpassivation zone where there is a sharp decrease in the anodic current density once the pitting resistance is surpassed. This phenomenon is attributed to the formation of a thicker oxide film with a lower chromium ion concentration, rendering further attacks more facile. However, samples 2 and 3 exhibit no such transpassive zone due to two reasons: first, the pitting resistance of their surfaces exceeds the transpassivation zone threshold of 0.4 V vs Ag/AgCl, and second, their favourable Chromia oxide composition, primarily comprising Cr (III), enhances resistance to transpassivation [186]. This further shows the favourable long-term corrosion resistance of the optimized laser processed samples.

Based on the XPS depth profile analysis, it is evident that in S5, the laser processing has effectively removed the oxide layer due to the removal of the chromium enriched outer layer. This consistent composition observed throughout the entire depth profile indicates the absence of a passive layer, which explains the nearly non-existent passive behaviour observed in this sample, leading to immediate pitting breakdown. The uniform oxide layer produced can be attributed to the extended duration of exposure to the laser source. This prolonged exposure provides ample time for elemental diffusion, enabling the complete suppression of the initially formed thin Chromia oxide layer by the subsequently produced iron oxide layer. This phenomenon underscores the critical role of time in the laser processing method, allowing for the formation of a uniform oxide layer on the surface and taking away the

removals the beneficial effects seen for the non equilibrium oxidation seen at shorter time scales. From the longer term EIS it is evident that change in the RP value is more pronounced in S5 compared to S2, indicating that S5 experiences more significant passivation upon immersion in the solution, whereas S2, being pre-passivated, undergoes a lesser increase in oxide layer growth.

The observed pitting morphology closely corresponds to the outcomes of the corrosion tests, indicating superior performance of S2 compared to S5 and the blank. S2 exhibits minimal pitting, primarily showcasing general corrosion, whereas the unprocessed samples and S5 display a higher quantity of larger pits, along with instances of oxide layer removal and delamination in S5. The heightened susceptibility to pitting in S5 can be attributed to the presence of cracks and pores in the oxide film post-processing, serving as initiation sites for pitting corrosion. Moreover, the Electrochemical Impedance Spectroscopy Equivalent Circuit (EIS EEC) employed to characterize the electrochemical behaviour supports this observation. The usage of a CPE+2 pore EEC for S5 indicates the presence of defects in the outer layer, consequently reducing the overall surface resistance. Conversely, SEM images of S2 reveal a smoother surface with evidence of surface remelting and solidification. The corresponding EEC of CPE + 2 suggests a more densely packed surface with fewer original defects. Further analysis of long-term EIS data highlights S2's enhanced corrosion resistance compared to S5. S5's Rp value sharply declines after day 5, accompanied by a change in EEC indicating the onset of pitting corrosion. In contrast, S2 exhibits a steady increase in resistance until day 2, maintaining this level throughout the 10-day test period without evident permanent surface breakdown.

Using the results from samples S2 and S3 specifically, it becomes evident how individual factors influence corrosion outcomes. Both samples share similar areal energies but differ in composition. S2 was produced with a high scan speed and low hatching distance, while S3 was prodices with a low scan speed and high hatching distance. These results highlight that hatching distance significantly affects pitting resistance due to its much lower impact on surface morphology. Conversely, lower areal energy plays a crucial role in corrosion currents, mainly influenced by the sensitive Cr/Fe ratio. S2, with slightly lower areal energy, demonstrated a 50% increase in the Cr/Fe ratio compared to S3, illustrating the substantial impact of individual processing parameters. These results highlight for the first time the long

term significant influence of laser processing parameters on the varying composition of elemental oxide layers on the surface and in the subsurface and in turn the corrosion performance of laser-processed SS316L stainless steel.

4.5 Conclusion

The optimization of laser processing parameters for stainless steel corrosion resistance was conducted using two full factorial designs of experiments (DoE), focusing on laser power, scan speed, frequency, and hatching distance. This study has revealed several key fundamental insights on how the laser surface modification affects the surface chemistry and corrosion properties.

Areal energy Influence: Samples processed with reduced areal energy of under $3x10^{24}$ J/cm^2 demonstrated superior corrosion resistance that surpass that of unprocessed SS. Optimal parameters resulted in a peak pitting resistance of 509.15 mV and an Icorr value of 51.5 nA/cm^2, indicating significantly improved corrosion resistance compared to unprocessed samples, which resulted in a pitting resistance of 160.8 mV and an Icorr value of 502 nA/cm^2

Surface Composition Analysis: X-ray Photoelectron Spectroscopy (XPS) analysis highlighted the predominant presence of iron and chromium oxides on the surface with a Cr/Fe ratio exceeding 3.5 for the optimised sample (S3), resulting in significantly improved corrosion resistance where noticeable increases in corrosion current once the Cr/Fe ratio surpassed 1.0 with minimally changes in Icorr below 1.0. Depth profiling indicated variations in oxide layer composition and thickness, providing valuable insights into corrosion behaviour.

Surface Morphology: Scanning Electron Microscope (SEM) imaging confirmed the efficacy of laser processing in reducing surface defects and enhancing resistance to localized corrosion. Samples with optimized processing parameters exhibited smoother surfaces with fewer defects, contributing to improved corrosion resistance.

Corrosion Behaviour: Cyclic polarization tests demonstrated a clear correlation between surface composition, morphology, and corrosion resistance. Samples with higher chromium content and smoother surfaces exhibited superior resistance to localized corrosion.

Electrochemical Impedance Spectroscopy (EIS): EIS revealed higher resistance and lower capacitance in optimally processed samples, indicative of enhanced corrosion protection. The long-term impedance spectra provided valuable information on the evolution of the passive film over time showing either the building or breaking down of the passive film highlighting there stability under corrosive conditions.

Overall, the findings underscored the importance of areal energy, composition, and morphology in tailoring stainless steel surfaces for improved corrosion resistance through laser processing. These results provide valuable insights for the development of corrosion-resistant materials and surface engineering techniques in various industrial applications. Further research could explore additional factors influencing corrosion behaviour such as other laser processing parameters, metal compositions and environmental conditions for specific applications.

Chapter 5 - Improved lifetime of a Pulsed Electric Field (PEF) system-using laser induced surface oxidation

Publication statues: Published

Mark Swayne, Gopinath Perumal, Dilli Babu Padmanaban, Davide Mariotti, Dermot Brabazon, **Improved lifetime of a Pulsed Electric Field (PEF) system-using laser induced surface oxidation,** Innovative Food Science and Emerging Technologies (2024). DOI:10.1016/j.ifset.2024.103789

Abstract

In this research, we explore the possibility and effectiveness of using laser-induced surface oxidation methods to enhance the durability and effectiveness of PEF (Pulsed Electric Field) systems. Despite advantages over thermal pasteurization, PEF faces challenges like electrode corrosion and biofouling, hindering its adoption. This research introduces laser-induced oxidation to mitigate metal ion release during PEF, directly targeting electrode alteration. Our examination adopts a comprehensive method, integrating Design of Experiments (DoE) parameter sets for PEF trials, morphological analysis, evaluation of metal ion release via Inductively Coupled Plasma Quadrupole Mass Spectrometry (ICP-QMS), waveform capture utilizing a Data Acquisition (DAQ) system, electrochemical assessment via impedance spectroscopy, and examination of oxide layer composition employing X-ray photoelectron spectroscopy. Pulse waveform characteristics shows the intricate relationship between PEF processing parameters with metal ion release, alongside XPS analysis providing insights into surface chemistry. Optimized results show a three-fold reduction in metal ion release post-PEF, with laser-treated samples outperforming untreated stainless steel due to selective surface chemistry alteration, notably an increased Cr/Fe ratio, reducing harmful elements. This study highlights laser-induced oxidation as a practical solution for enhancing PEF electrode performance and reducing metal ion release, addressing key challenges in PEF technology. It advances sustainable food processing, promising extended PEF system lifespan while maintaining efficiency and product quality.

5.1 Introduction

Concerns about the long-term viability of the world's food supply are nothing new for the food industries. It is critical for the food manufacturing industry to develop processing technologies that can maintain and improve the nutritional value of foods while also producing bio-accessible compounds. The food industry is investing more resources in nonthermal processing technologies such as pulsed electric fields (PEF), ultrasound, high hydrostatic pressure, pulsed light, and ultraviolet radiation [195–198]. Cohn and Mendelsohn published their findings on sterilisation by passing a DC-current through a nutrient solution in 1879. In recent decades, there has been a surge of interest in Pulsed Electric Field technology (PEF), which is a viable alternative for thermal food pasteurisation [199]. PEF is a method of food preservation that involves exposing the food to electric field pulses with typical field strengths of 2-5 kV/mm and pulse durations of 1-1000µs. The most significant advantages of PEF pasteurisation over thermal pasteurisation are the preservation of fresh-like characteristics and the reduction of processing energy required. By subjecting food products to short, high-voltage electrical pulses, PEF effectively deactivates microorganisms and enzymes while minimizing the detrimental effects on food quality. Under the influence of this external electrical field, biological membranes are punctured by the formation of hydrophilic pores and the forced opening of protein channels [200,201]. Once pores of 0.5 nm radius are formed, they may expand as a result of the applied electric field, disrupting the flow of material into and out of the cell [202]

The loss of membrane integrity causes cell contents to diffuse into their surroundings, resulting in the death of the living cell, a process known as irreversible electroporation [203]. Multiple studies have demonstrated that PEF successfully decreases the initial microbial load in liquid food products during pasteurisation, with minimal loss of nutrients and flavour [116,202–205]. Despite these promising results, a full transition from thermal to PEF has not occurred in industry due to some underlining issues experienced during the process. These are first, a short life span of the electrodes themselves, which must be replaced frequently due to the high corrosion that occurs; and second, biofouling caused by the food product inside the system [117]. Thus, the practical implementation of PEF systems faces challenges related to electrode durability and maintenance, particularly concerning electrode

degradation and fouling over prolonged usage. The electrode biofouling is due to be caused by the electrophoretic concentration of charged molecules within a boundary layer of food product that is adjacent to the treatment electrode. This agglomeration of the fouling agent on the electrode(s) during extended processing periods can result in arcing and reduced flow inside the system, further reducing the system's lifetime [206].

During food product treatment in a PEF system, the electrodes directly contact the liquid media, the current that flows in the electrode will consist of free electrons and in the liquid of charged particles. At the electrode-electrolyte interface, an electrical double layer forms, resembling a capacitor. Application of an external voltage increases this double layer's voltage until it reaches the threshold voltage (Uth), causing two independent electrochemical half-cell redox reactions occur in order to preserve charge conservations. This corrosion not only reduces electrode lifespan but also raises the risk of food contamination [118]. Hazardous byproducts can form inside the reaction chamber, such as chloride gas (Cl_2) which is produced at the anode and can react with the water molecules producing hypochloric acid [121]. Roodenburg et al. studied pulse shape effects on metal release from electrode surfaces in a NaCl solution, identifying three pulse topologies. [117]. Their findings showed a significant reduction in metal release when pulses contained both positive and negative waveform portions, with a notable 29-fold increase in iron concentration observed after switching from an exponential decaying pulse to an oscillatory decaying pulse. Various factors, including chamber design [207], and electrode material [208–211], electrical parameters such as peak voltage, total specific energy input, polarity, and pulse duration [208,212], as well as the composition and chemical– physical properties of the treated medium [117,208,213,214], have been studied for their influence on metal release from electrodes in PEF systems. While much research has focused on optimizing process conditions, little attention has been given to surface anticorrosion treatments. Although some studies have explored coating electrodes with conductive-plastic films [215] and ceramic-coatings [40], these methods may introduce new compounds into the solution, potentially disrupting industrial process conditions.

One promising approach to address these challenges is the utilization of laser-induced surface oxidation techniques to enhance the lifetime and performance of PEF systems. Laser induced oxidation is an almost instantaneous process due to the rapid heating and cooling causes a non-equilibrium oxidation process. By applying controlled laser energy to electrode surfaces,

surface properties can be modified to improve corrosion resistance, reduce fouling, and enhance electrical conductivity. This highly precise technique allows us to fine-tune the thickness and chemical composition of the oxide film, as observed in a study by C.Y. Cui. Where C.Y. Cui. derived a thermokinetic model to describe the composition of the film produced [73]. The Gaussian energy distribution of laser pulses leads to non-homogeneous morphology, with peak power concentrated at the center [74] . This results in a duplex oxide formation, with Chromia oxide (Cr_2O_3) concentration doubling on the surface due to its higher affinity for the chemisorbed oxygen [73]. Nevertheless, due to the higher temperature at the center and the higher diffusion rate of Fe inside the oxide layer, Fe_2O_3 becomes present at the surface of the stainless steel, altering the Cr/Fe ratio. These results were both consistent with previous literature results [75,76]. Lecka et al. found that varying surface energy affects corrosion resistance, with an initial large increase reaching a maximum at lower fluences, followed by a sharp decrease to the unprocessed value, correlating with changes in the Cr/Fe ratio [77]. These findings align with previous research by Li and Lu, indicating the critical role of surface chemistry in corrosion resistance [73,76].

In this research, we explore the possibility and effectiveness of using laser-induced surface oxidation methods to enhance the durability and effectiveness of PEF (Pulsed Electric Field) systems. Our investigation takes a thorough approach, incorporating Design of Experiments (DoE) parameter sets for PEF experiments, morphological analysis, assessment of metal ion release using Inductively Coupled Plasma Quadrupole Mass Spectrometry (ICP-QMS), waveform collection facilitated by a Data Acquisition (DAQ) system, electrochemical examination through impedance spectroscopy, and analysis of oxide layer composition using X-ray photoelectron spectroscopy (XPS). Our aim is to understand the mechanisms behind the observed improvements comprehensively. Additionally, we seek to assess the practical implications and relationships among parameters relevant to large-scale PEF processing. By clarifying the connection between laser-induced surface alterations and PEF system performance, this study contributes to the advancement and application of PEF technology in the food industry, ultimately aiding the development of more sustainable and efficient food processing methods.

5.2. Method:

5.2.1 Sample preparation

Sheets of stainless steel (316L) measuring 100 x 200 x 0.8mm were purchased from Impact Ireland (Metals) Limited, Ireland. All samples were cleaned using deionized water and then ethanol. The surface of the steel was then uniformly sandblasted to increase the average area surface roughness to 3.9 μm S_a to enhance laser absorption [170]. Table 5-1 depicts the list of parameters that were selected for laser processing and the total areal surface energy used to produce them [216]. These results performed the best and worst in terms of general and pitting corrosion performance evaluated using electrochemical cyclic polarization tests done on two preliminary design of experiment studies, P1 and P2. Afterwards, the bottom 25mm of each sample was laser processed in the same manner as described above; however, due to the larger size of the samples and the small processing area of the laser (75 x 75 mm), realignment and stitching of the laser processing were required. Figure **5-1** shows the PEF system (Elea pilot plant) used for the investigation.

Table 5-1: Parameter set for laser processed PEF electrodes.

Sample	Power (%)	Frequency (Hz)	Scan Speed (mm/s)	Hatching Distance (um)
S-A	80	100	450	8
S-B	80	100	250	15
S-C	80	100	450	1

Figure 5-1: Elea pulsed electric field system, with schematic of PEF test layout.

5.2.2 PEF processing

The PEF pilot plant was supplied by Elea technology, the system was set up in batch processing mode, using a 30 cm^3 chamber. To determine the effect of PEF parameters on the amount of metal released during pulsed processing, a central composite face-centered DOE design was utilized. A 20-run design with 15 distinct parameter sets and five repetitions of the central point are utilized. The investigated parameters included the pulse width, the frequency, and the voltage seen in Table **5-2**.

Table 5-2: Possible parameter for the commercial used Elea PEF pilot plant.

Parameter	Range	Intervals
Electrode Voltage	4-24 kV	1 kV
Pulse Count	1-10000 Pulses	1 Pulse
Frequency	1-500 Hz	1 Hz
Pulse Width	4-7 µs	1 µs

As the pilot plant is evaluating a low field strength system (1 kV/cm) due to its large electrode gap, the amount of material removed from the electrode surface is comparably low. Therefore, longer run times were required to bring the metal ion concentration above the detectable limit; therefore, a constant value of 10,000 pulses was used for each experimental run in the DOE 1

The system is equipped with additional safety features to protect both the machine and the user because they are designed for commercial use. This restricts the amount of current that can flow through the machine; as a result, we can only use a lower pulse count below 10,000 pulse range per run where multiple runs have to be used to increase pulse count, as higher frequencies will cause faster heating of the electrolyte, allowing the current to exceed the warning value and causing a voltage drop as a safety response. This consideration led to the selection of the maximum frequency of 35 Hz. For similar reasons, the conductivity of the electrolyte can also cause the current threshold to be reached; therefore, a 20 mM NaCl solution was selected for the experiment which has an electrical conductivity of 0.22 S/m. The DOE 1 parameters are displayed in **Table 5-3**.

Prior to PEF processing, the surface of the batch cell and unprocessed electrodes were cleaned with DI water and acetone to remove any contaminants. The electrode was attached to the batch cell using clamps. The batch cell was inserted into the PEF system and its electrical contact was attached. The cell was filled with 1 liter of electrolyte (NaCl), and the system was sealed. For DOE 1, a sample was collected every 10,000 pulses using a 10 mL pipette and a 50 mL sterilized solution holder from 5 fixed locations inside the reactor vessel, one in the center and four at each corner, in order to reduce the effect of solution inhomogeneity. After the

total number of pulses, the system was cleaned and each run utilized fresh electrodes and electrolyte. After each run, the maximum voltage, current, and total energy supplied to the system were recorded from the pilot plant display.

5.2.3 Laser processing

The sand blasted sample was cleaned with acetone and ethanol and sonicated for 15 minutes to remove any contaminants or excess sand from the surface then allowed to dry for 5 minutes on the laser stage. The laser system used consisted of a 3.5 W max power 1064 nm Q-switched, diode-pumped solid-state neodymium-yttrium aluminium garnet laser (BrightSolutions 1064 WEDGE HF). A 2D scanning galvanometer (Raylase SS-12) was used to raster the beam in the xy-plane, and a movable z-stage (PI M-404 4PD) was used to control the position of the sample. The beam was focused on the surface of the samples which lies 340.3 mm below the Galvo lens this produces a spot size of 100 µm. The samples where then processed using fixed parameters of a bidirectional hatching strategy.

Sample	Power (W)	Frequency (kHz)	Scan-Speed (mm/s)	Hatching Distance (µm)	Time (s/m^2)
S-A	2.60	100	450	8	2,778
S-B	2.60	100	250	15	2,667
S-C	2.60	100	450	1	22,222

Table 5-3 Selected samples and laser process parameters for production of the laser surface oxidised samples.

5.2.4 PEF processing of the laser processed electrodes.

The set of laser processed parameters used for PEF pulsed processing can be seen in Table 5-1. The laser processed electrode where PEF processed using fixed machine parameter of 24 kV, 5 Hz, 7 µs, 30,000 pulses and 1 litre solution. Each electrode was repeated three times with samples being collected every 10,000 pulses.

5.2.5 Metal Ion concentration measurements.

The elements of interest for this analysis where, Iron, Chromium, Nickel, Manganese and Molybdenum. Calibration standards were made volumetrically using a 100 mg/L TraceCERT® Sigma-Aldrich multi-element standard and a 0.3 M HNO_3 stock solution. The acid stock solution was made from Optima grade concentrated HNO_3 (68% w/w; Fisher Scientific trace metal grade acids) and purified water with a resistivity ≥18.2 MΩ cm from a Milli-Q system (Merck Millipore). The concentrations of the calibrants were between 0.1 and 500 µg/L. All calibration solutions and blanks were doped with a Leehman Labs (Teledyne) 100 ppm Gallium and a Perkin Elmer 1000 mg/L Yttrium standard solutions to obtain a consistent concentration of 50 µg/L (for both Ga and Y) for all solutions. Samples were diluted by a factor of 10 to lower the electrolyte (NaCl) concentration. All measurements were conducted using a Perkin Elmer NexION 350D Inductively Coupled Plasma Quadrupole Mass Spectrometer (ICP-QMS) under Kinetic Discriminator (KED) mode for the element masses 52Cr, 55Mn, 56Fe,60Ni and under Standard mode for the element mass 95Mo at the London Metallomics Facility, King's College London.

Table 5-4: DOE 1 parameter set for pulsed electric field experiment.

Run	Voltage (kV)	Frequency (Hz)	Pulse width (µs)
1	16	35	7
2	16	35	4
3	24	20	6
4	24	5	4
5	20	20	6
6	20	20	7
7	20	5	6
8	20	20	6
9	20	20	6
10	24	35	7
11	20	20	4
12	24	5	7
13	16	20	6
14	20	20	6
15	16	5	7
16	20	20	6
17	24	35	4
18	20	35	6
19	20	20	6
20	16	5	4
Pulses = 10000			
Solution = 20mM NaCl			
1 litre solution			

The introduction system to the instrument employed a Cetac ASX-100 auto sampler coupled to a SeaSpray glass nebulizer fitted to a quartz cyclonic spray chamber. Argon plasma flow and nebulizer gas flow rates were 18 L/min and 0.93 L/min, respectively. Quality control of ICP-QMS measurements was ensured through repeat measurements of blanks; a calibrant and a certified reference material (trace metal drinking water from High Purity Standards – CRM-TMDW-100). Sample measurements in counts per second (cps) were normalized to the Ga and the Y internal standards to account for both instrument drift and matrix effects. Sample and standard intensities were subsequently blank corrected by removing the average isotopic intensity (cps) of repeat blank measurements. The corrected isotopic intensity was converted to concentration measurements by applying a regression model from the calibration analysis.

5.2.6 Waveform acquisition

Waveform acquisition was performed using LabVIEW Software and the NI DAQ system. The voltage and current were directly measured from the output port on the pilot plant. Both the current and voltage signals were expressed as a damped voltage value, so a multiplier of 24000 and 1000 were applied to the recorded voltage and current values respectively to acquire the real values. An acquisition rate of 125000 was used for both input signals. The recorded data was then analyzed in python to acquire the voltage and current change during processing, and the effect of the parameters on the phases of the current and voltage to each other.

5.2.7 Surface characterization analysis

X-ray photoelectron spectroscopy (XPS) was performed on laser processed 316L SS samples using ESCALAB Xi+ spectrometer microprobe (Thermo Fisher Scientific) with a focussed monochromatic Al Kα X-ray source (hν = 1486.6 eV, spot area of 650 µm x 650 µm) operating at a power of 225 W (15 kV and 15 mA) and the photoelectrons were collected using a 180° double-focusing hemispherical analyser with a dual detector system. The spectrometer was prior calibrated with sputter cleaned references such as Au, Ag and Cu

supplied by Thermo Fisher scientific. The base pressure of analysis chamber was always maintained < 5 x 10^{-9} mbar, which increased up to ~5 x 10^{-7} mbar during measurement along with charge neutraliser (flood gun) operated at 100 μA emission current. XPS and sub-surface chemical composition were performed using soft cluster clean and monoatomic depth profiling using Ar gas. In cluster clean, sample surface of raster size 3.25 mm was exposed to Ar clusters of size 1000, energy at 4 keV for 30 s. In all these cases, survey scan spectra were recorded with parameters of step size 1 eV, pass energy 150 eV and narrow core shell high resolutions scans are done at step size of 0.1 eV, pass energy of 20 eV respectively. Casa XPS software was used to analyse the results for elemental composition and chemical oxidations states of all elements of interest. 2p 3/2 peak was taken into account for the composition analysis of chromium, and Iron while for oxygen the 2s singlet peak was used and for molybdenum both the 3p 5/2 and 3p 3/2 peaks were taken into account. The location of the peaks was identified with wide literature seen in supplementary S1. Further, the high-resolution spectra were analysed thoroughly by deconvoluting using asymmetric Lorentzian peak fitting function with Shirley background functions The sensitivity factor and peak position can be seen in supplementary S1.

5.3 Results

5.3.1 Effect of altering parameters on the metal ion concentration

The ANOVA analysis reveals that all three processing parameters exert influence over the iron ion concentration, demonstrating a quadratic relationship among them. Voltage and pulse width positively influence the concentration, whereas frequency has a negative impact. Frequency exerts the most significant effect on system corrosion, followed by voltage, with pulse width having the least impact. This is evident from the two highest results of 10.56 and 7.48 ppb, both associated with high voltage (24 kV) and the lowest frequency (5 Hz), whereas the three lowest results of 1.54, 2.00, and 2.04ppb are all associated to the highest frequency of 35Hz. These results indicate two significant two-factor interactions. Firstly, a negative relationship is observed between voltage and frequency, where at higher voltages, the impact of frequency on iron concentration becomes more pronounced. Specifically, with increasing voltage, the frequency-iron concentration graph exhibits a steeper trend. Secondly, a positive

two-factor interaction is noted between frequency and pulse width, albeit with less strength compared to the voltage-frequency interaction.

From the ANOVA analysis, a quadratic model was designed to describe the iron concentration of possible runs using the three starting parameter and can be described by the equation 1. With V being the voltage, W being the pulse width and F being the frequency:

$$Fe = 15.012 + 1.15V + 0.0325F - 9.33W - 0.0227VF - 0.0814VW + 0.058FW + 0.901W^2 \quad \text{Eq 5.1}$$

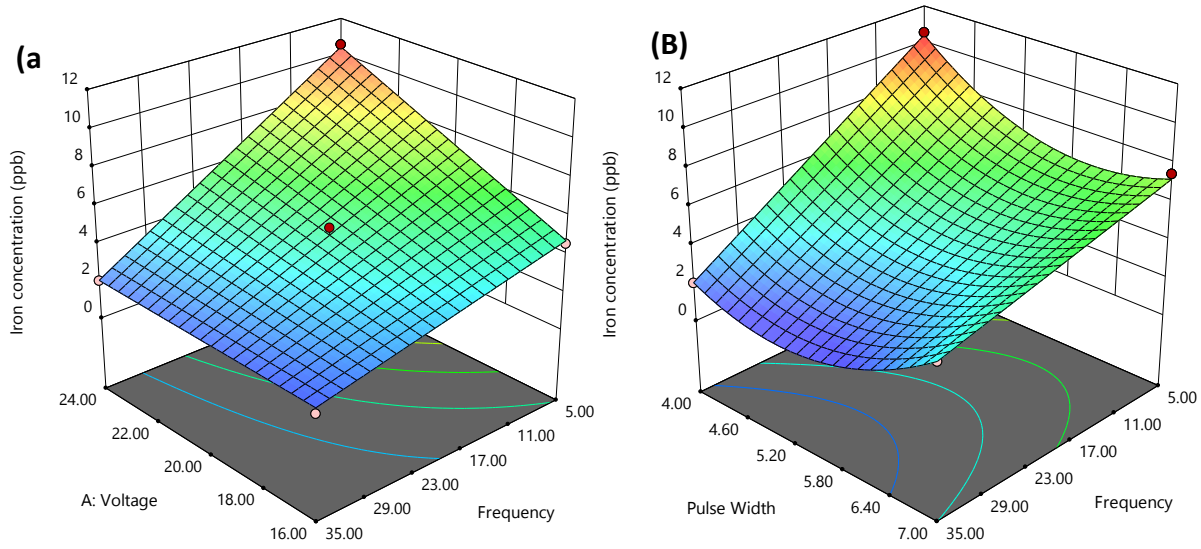

Figure 5-2: (A) Response surface for the iron corrosion inside a PEF system with constant pulse width of 4µs. (b) Response surface for the iron corrosion inside a PEF system with constant voltage of 24kv

Visual representation of the model can be seen in Figure **5-2**. To minimize the Fe concentration in the system the lowest pulse width and voltages should be used, alongside with the highest frequency, the model used to describe shows quite high correlation with an R^2 value of 0.8970.

5.3.2 Total energy input

The entire energy of each portion of the 10000-pulse run was recorded from the pilot plant's readout and summed together. Using Design Expert, the findings were analysed, and a model with a very high correlation coefficient (R^2) of 0.9973 was developed. When the Eq 5.2

voltage and pulse width are varied, this model exhibits a high positive dependence, whereas the applied frequency has a minor dependence. The results show that for when all other factors stay constant the total energy varies almost linearly with voltage. The equation derived from the ANOVA model is seen in equation 2.

$$\text{Total Energy} = 238100 + 119900V + 11767F + 103600W + 60831VW + 10639FW$$

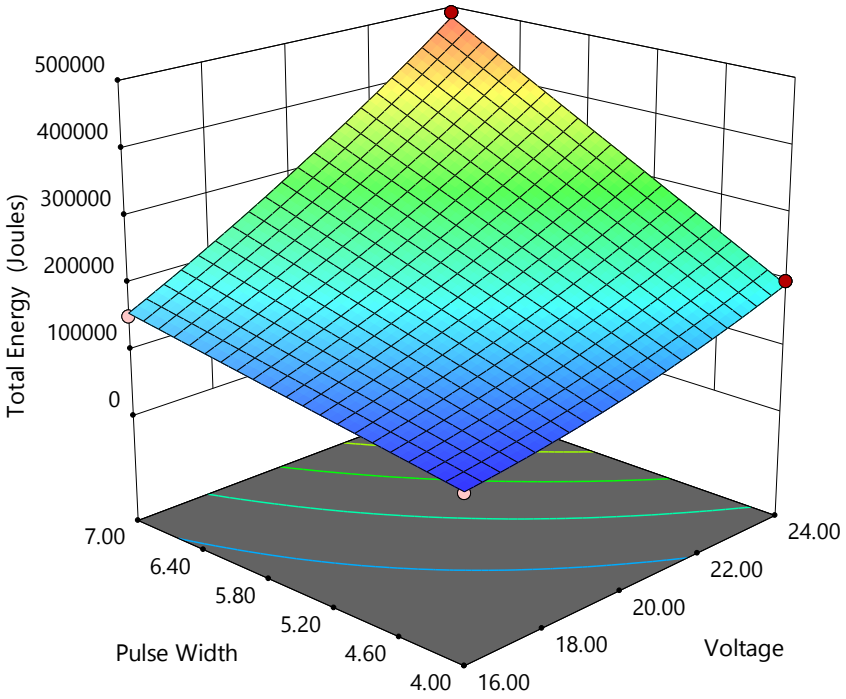

Figure 5-3: Response surface for the total energy inside a PEF at constant frequency of 35Hz.

5.3.3 Effect of processes parameters on the wave formation

Waveform graphs of the voltage and current were recorded using LabVIEW software. It can be seen that both the voltage and current form as mono-polar square wave pulses. It can be seen Figure **5-4** A that there is a linear increase in the current as the run continues, while the voltage stays relatively constant, this rise in current is due to the increase in solution temperature due to the applied energy from the pulses. A secondary reason for this increase is due to the segregation of ions in the solution due to their electrostatic interaction with the anode or cathode. The rate of increase of the current is heavily influenced by the frequency due to the high total energy applied.

Figure **5-4** C and D show the variation of the waveform with altering frequency, graph C is run at 100 Hz while D is running at 1 Hz. These graphs show that the phase of the current and

voltage to each other can alter with frequency from being completely in phase at low hertz and almost fully out of phase at higher hertz. This alters the power of each pulse being ~10 kW for high frequency and ~1500 kW for low frequency. This alteration in the peak pulse power can explain for high corrosion rate seen at the lower frequencies.

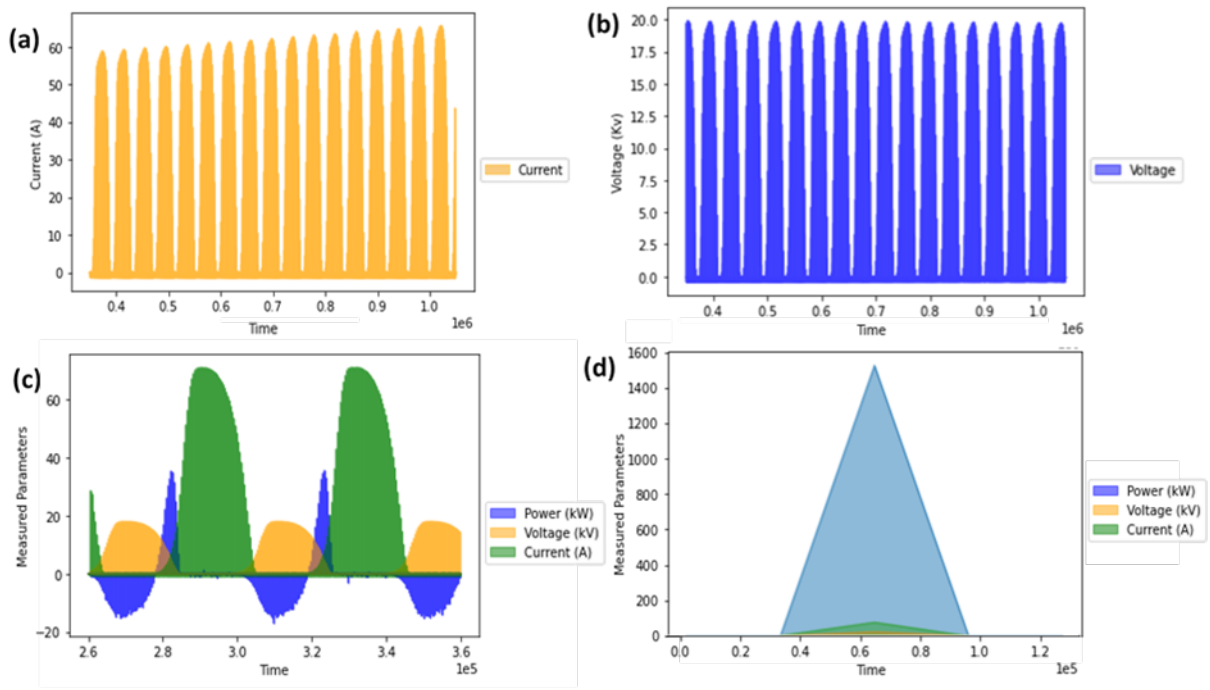

Figure 5-4: (A) the current waveform during a single PEF run. (B) the voltage waveform during a single PEF run. (C) the current, voltage and power waveform for a 100Hz run. (D) the current, voltage and power waveform for a 1Hz run

5.3.4 Electrochemical impedance spectroscopy (EIS)

Figure **5-5** depicts the Bode plots obtained from the EIS measurements conducted in a 0.5M NaCl solution at the Open Circuit Potential (OCP) for S-A, S-C, and an unprocessed sample S-B results were marginally different from S-A so where not included in this section. These measurements were conducted within the frequency range of 0-100 Hz, typical

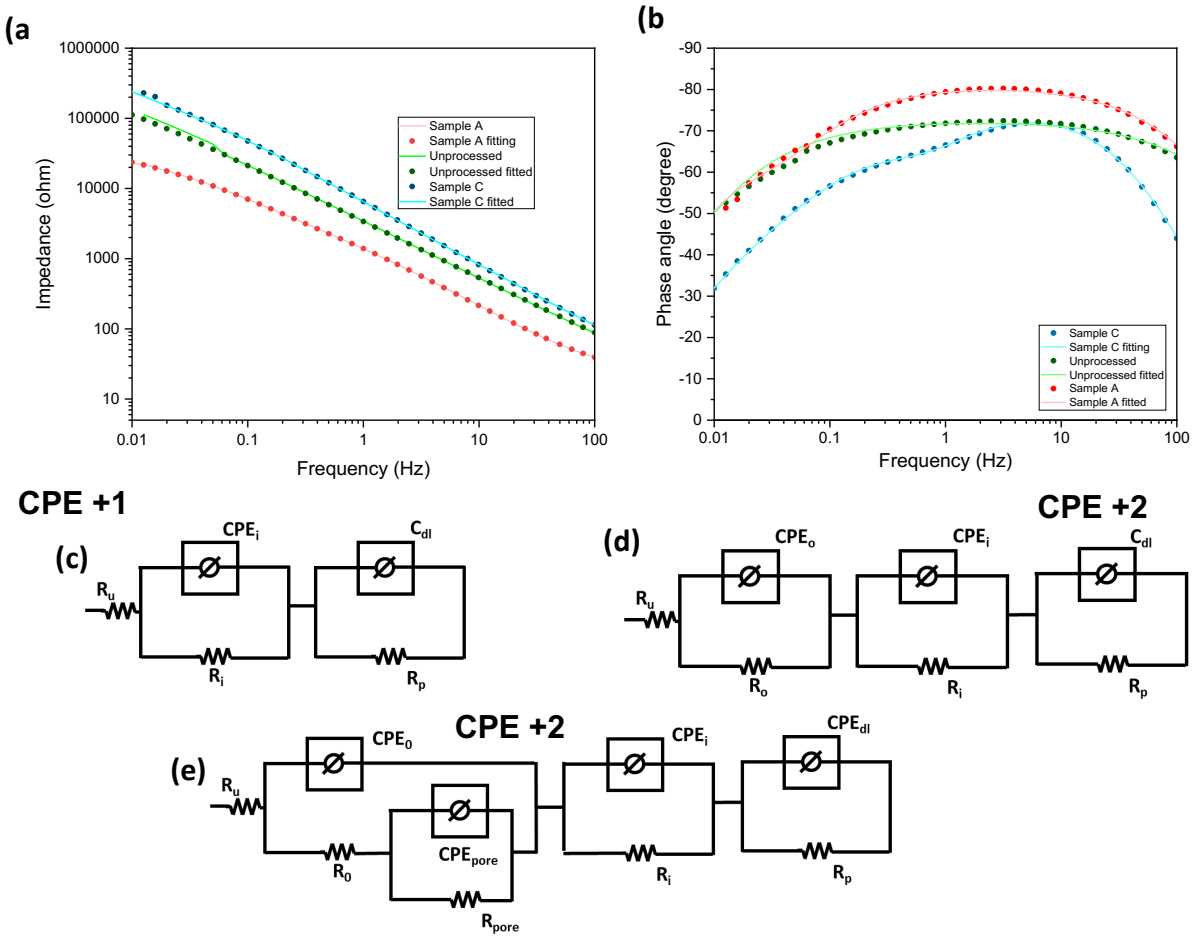

Figure 5-5: Electrochemical impedance plots for laser processed samples (a) Bode impedance plot (b) Bode phase plot, (c) EEC for unprocessed (CPE + 1), (d) EEC for S-A (CPE + 2), and (e) EEC for S-C (CPE + 2 pore).

for the PEF system. Upon comparison of impedance values, it was observed that S-A exhibited significantly lower impedance than the unprocessed sample, while S-C displayed notably higher impedance than both counterparts. This trend is graphically depicted in Figure **5-5**. The phase angle versus frequency plot for all samples, as shown in Figure **5-5**, revealed a broad peak within the mid-frequency range, indicating the capacitive behaviour of the system. This capacitive response originates from charge transfer phenomena and the formation of double-layer capacitance at the metal/electrolyte interface. The diameter of the capacitive loop correlates with the charge transfer resistance (R_p), where higher R_p values signify reduced dissolution rates and, consequently, heightened corrosion resistance. Notably, S-A exhibited

the most substantial phase shift across the entire frequency spectrum, indicating superior capacitive characteristics.

Each of the three samples depicted distinctive Bode plots, indicative of their respective surface characteristics. All samples manifested multiple time constants. Specifically, the unprocessed sample was modelled with an Equivalent Electrical Circuit (EEC) comprising two time constants in series, attributed to the oxide layer and surface roughness resulting from sandblasting. S-A extended this unprocessed specimen circuit to encompass a third time constant, reflecting the formation of a multilayer oxide. Similarly, S-C exhibited the same three time constants as S-A, with an additional fourth time constant in parallel to accommodate the influence of porosity/cracks in the outer passive film. The EECs representing the unprocessed steel and both processed samples are illustrated in Figure **5-5** as insets.

In this context, C_{dl} and R_p represent the electrochemical double-layer capacitance and charge transfer resistance, respectively, for the high-frequency portion of the spectrum. CPE_i and R_i represent the corresponding elements for the inner oxide layer properties, while CPE_o and R_o represent the outer oxide layer. CPE_{pore} and R_{pore} represent the pore capacitance and resistance, respectively. CPE, a frequency-dependent constant phase element with exponent α, was utilized instead of pure capacitance to accommodate surface in homogeneities. The values of different elements of the electrochemical equivalent circuit are summarized in

Table 5-5.

Table 5-5: Electrochemical impedance spectroscopy results for S-A, S-C and unprocessed

Sample	Rtotal (k ohm/cm)	Rp	Cdl (μS s^a/cm^2)	Ri	CPEi	Ro	CPEo	Rpore	CPEpore	α
Unprocessed	384736	375800	757.5	8936	5475	-	-	-	-	0.787
S-A	586015	547200	473.4	155	35592	38800	7773.2	–	-	0.921
S-C	37362.85	7639	3599	6.75	2604	417.1	4355	29300	1337	0.822

Furthermore, R_{total} represents the overall resistance for both processed and unprocessed specimens (refer to

Table 5-5). S-A demonstrated the highest total resistance, followed by the unprocessed sample, and then S-C. It is noteworthy that the charge transfer resistance exhibited by S-A was notably higher compared to the other two specimens. Additionally, the α value for both processed samples was higher, indicating a shift towards a more capacitive nature, rising from 0.787 for the unprocessed sample to 0.921 for S-A

5.3.5 X-ray photoelectron spectroscopy (XPS) analysis

Based on the XPS analysis of the laser-treated samples, it is apparent that the oxide film primarily consists of iron and chromium oxides, with minor traces of other alloying elements (Figure **5-6**). However, the composition of these films differs among the three treated electrodes. Particularly, S-A and S-B exhibit closely resembling compositions, characterized by notably high Cr/Fe ratios. In contrast, S-C displays elevated concentrations of additional alloying elements, predominantly nickel oxides.

Sample	**Rtotal (k ohm/cm)**	**Rp**	**Cdl** (µS sa/cm2)	**Ri**	**CPEi**	**Ro**	**CPEo**	**Rpore**	**CPEpore**	**α**
Unprocessed	384736	375800	757.5	8936	5475	-	-	-	-	0.787
S-A	586015	547200	473.4	15	3592	38800	773.2	-	-	0.921
S-C	37362.85	7639	3599	6.75	2604	417.1	4355	29300	1337	0.822

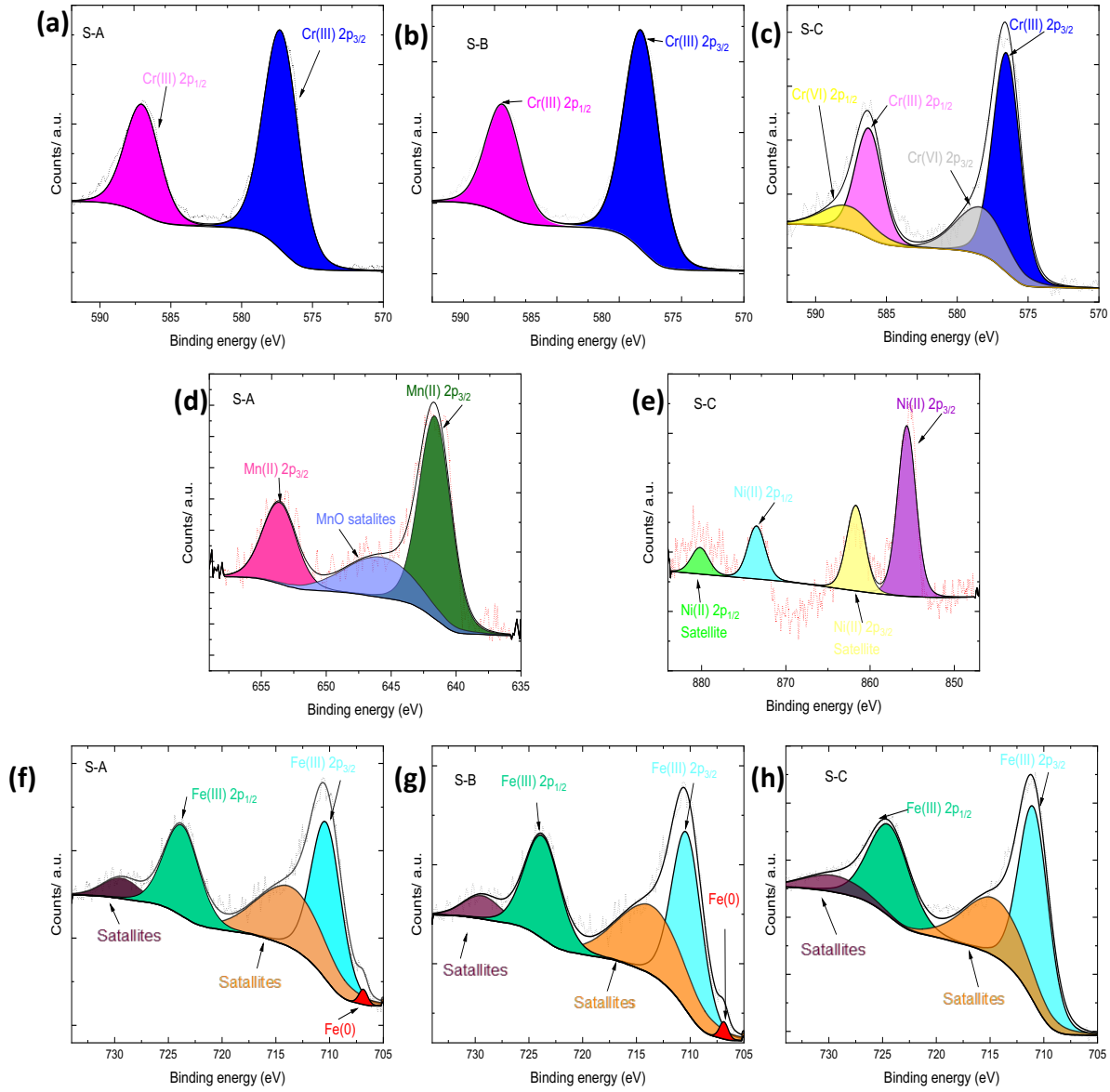

Figure 5-6: High-resolution XPS spectra of (a) Cr 2p for S-A, (b) Cr 2p for S-B, (c) Cr 2p for S-C, (d) Mn 2p for S-A, (e) Ni 2p for S-C, (f) Fe 2p for S-A, (g) Fe 2p for S-B, (h) Fe 2p for S-C.

Table 5-6: Surface composition of the laser processed samples, including the Cr/Fe ratio

Sample	Fe (at%)	Cr (at%)	Mn (at%)	Ni (at%)	O (at%)	Cr/Fe
S-A	6.01	21.67	3.04	4.75	64.52	3.61
S-B	9.24	21.17	4.38	0.00	65.21	2.63
S-C	23.12	5.85	2.29	9.79	58.95	0.25
Unprocessed	14.01	9.92	0.61	6.37	69.09	0.71

For a thorough analysis, please refer to the high-resolution XPS scans presented in Figure **5-6**. Additionally, supplementary information (S1) provides valuable insights into sensitivity factors, reference peaks, and experimentally captured peak positions.

Fe 2p Spectral Analysis: Upon examination of the Fe 2p spectra (Figure **5-6**g-i), four prominent peaks emerge at binding energy levels of 710-711, 724-725, 715-716, and 729 eV, corresponding to Fe 2p3/2 and Fe 2p1/2 states. Notably, the peaks at 716 eV and 729 eV are identified as satellite peaks, indicative of Fe (III) oxides, specifically Fe_2O_3. Additionally, in cases of lower energy runs, such as S-A and S-B, an additional peak at approximately 706 eV is discernible, signifying incomplete oxidation and the presence of metallic Fe on the surface. S-A and S-B exhibit a reduction in iron relative content, decreasing to 6.01% and 9.24% respectively from the unprocessed value of 14.01%, while S-C demonstrates an increase in Fe relative content up to 23.12%.

Cr 2p Spectral Analysis: The Cr 2p spectra (Figure **5-6**a-c) reveal three primary peaks at binding energies around 577 eV, 580 eV, and 587 eV corresponding to Cr 2p3/2 for Cr(III) oxide, Cr 2p3/2 for Cr(VI) oxide, and Cr 2p1/2 for both oxides, respectively. The lower areal energy samples S-A and S-B exhibit only the Cr(III) component while the S-C sample has both Cr(III) and Cr(VI) components in a ratio of 89% to 11% respectively. The total Cr content for S-A and S-C is significantly increased to 21.67 % for S-A and 21.17% for S-B, compared to the unprocessed value of 9.92% while S-C shows a decreased Cr content down to 5.85%.

Mn 2p Spectral Analysis: The spectrum (Figure **5-6**d) reveals the presence of 2 major peaks on at 641.5 eV and one at 653.4 eV with a satellite present at 645.5 eV these peaks correspond

to the Mn 2p3/2 and Mn 2p1/2 for Mn(0) respectfully. All 3 processed samples experience the same oxide type, with MnO being the main oxide produced this is evented by the satellite peak present and the delta E gap of 5.8 eV seen in the Mn 3s peak. Furthermore, all three laser-processed samples demonstrate elevated relative concentrations compared to the unprocessed sample, which stands at 0.61%. Among them, S-B experiences the most significant increase, reaching up to 4.38%.

Ni 2p Spectral Analysis: Examination of the Ni 2p spectra (Figure **5-6**f) unveils two prominent peaks at 855.4 eV, accompanied by a peak at 873.0 eV, with satellite peaks observed at 861.7 eV and 880 eV. These peaks correspond to the Ni(II) state, characteristic of the nickel hydroxide compound $Ni(OH)_2$. Notably, S-C exhibits an increased Ni content of 9.79% on the surface compared to the unprocessed steel, which stands at 6.37%. Conversely, S-A showcases a reduction in Ni content to 4.75%, while S-B demonstrates complete elimination of Ni content from the surface.

5.3.6 Effect of laser processing on the Metal realised

As can be seen in Figure **5-7**(a) the total metal released from the electrodes was reduced dramatically for the electrodes processed with lower number of pulses with respect to the unprocessed sample total ion released (dashed black line) the total elemental concentration only exceeding the unprocessed electrode after 3 times the pulse count on the electrodes. The total ion concentration is also similar for the three electrodes, with S-C ion total concentration being slightly higher. S-A shows a 4-fold decrease in total ion concentration after 10000 pulses. However, the make-up of the ion concentration from the different elements varies substantially from the general trend. It can be seen that for S-C, after 10,000 pulses, the individual elemental ion concentrations are all lower than the corresponding concentrations of the unprocessed stainless steel (SS) for any element after 10,000 pulses. While for S-A and S-B, the Cr concentration exceeds substantially the Cr concentration of unprocessed SS after 10,000 pulses. On the other hand, for S-A and S-B, the ion concentration of Ni has decreased drastically with respect to the unprocessed electrode, even after 30,000 pulses. Ni ion concentration for S-C however, exceeds the concentration of the unprocessed sample after 30,000 pulses. Iron and nickel make up the majority of the elements measured inside the solution.

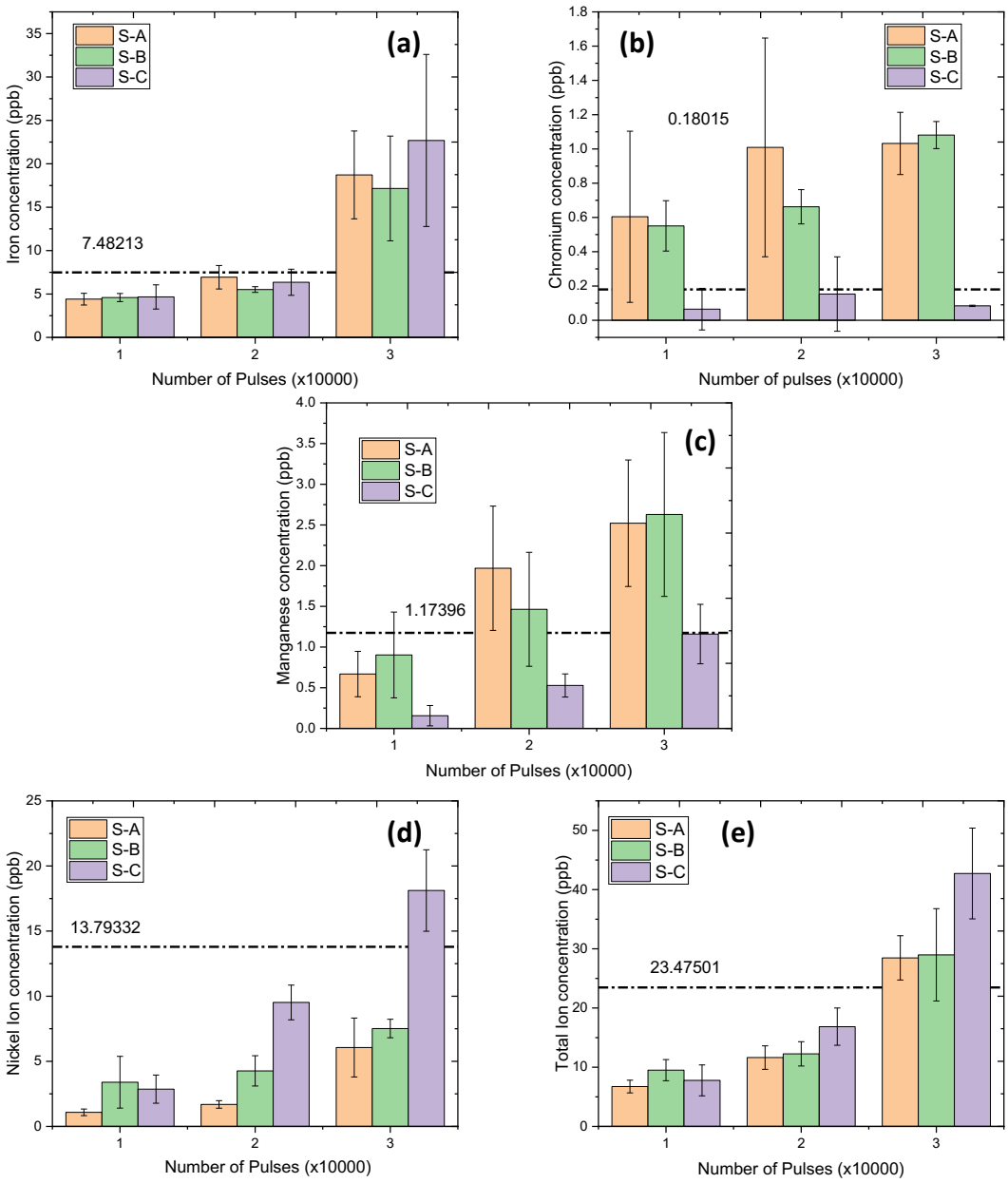

Figure 5-7: Metal ion concentration vs number of pulses for (a) Fe ion concentration, (b) Cr ion concentration, (c) Mn ion concentration, (d) Ni ion concentration, (e) Total ion concentration. With black line representing the ion concentration at 10000 pulses for unprocessed stainless steel.

5.3.7 Morphology analysis

SEM images of the unprocessed sample as well as the laser processed samples S-A and S-C are shown in Figure 5-8, providing a visual insight into the effects of laser processing on their surface morphology. Inspection of the unprocessed sample unveils an initial morphology

characterized by pronounced surface irregularities and a heterogeneous morphology characterised by the presence of an array of defects (cracks and pinholes). Delving into the morphology analysis depicted in Figure 5-8B, it becomes apparent that the lower areal energy laser processing methodology reduces a multitude of surface defects stemming from the intricate interplay of oxide growth, and the laser remelting and solidification process. Particularly noteworthy is the revelation within the higher areal energy processed samples (Figure 5-8c), where the emergence of defects within the oxide film, such as cracks and a markedly porous structure, due to the higher thermal stresses applied, underscores the important interplay between processing parameters and resultant surface characteristics. The phenomenon of oxide growth creates significant alterations in the optical properties of the surface, precipitating observable changes in surface colour owing to the intricate mechanism of thin film interference triggered by the growth of oxide thin films.

The examination of post-PEF processed electrodes unveils notable disparities, with conspicuous evidence of oxide removal evident across all electrodes although to varying degrees. S-A shows the least amount of oxide removal, surpassing both the blank and S-C counterparts. The blank sample, while exhibiting a reduced proportion of oxide removal compared to its S-C, displays individual spots characterized by larger and deeper impressions, indicative of the onset of localized corrosion phenomena. S-C experiences the most amount of oxide removal evident by the laser proportions of dark spots present on the surface. It is also event that the majority of oxide removal is seen in the troughs of the surface morphology. S-B experience similar morphology to samples S-A so wasn't discussed in this section.

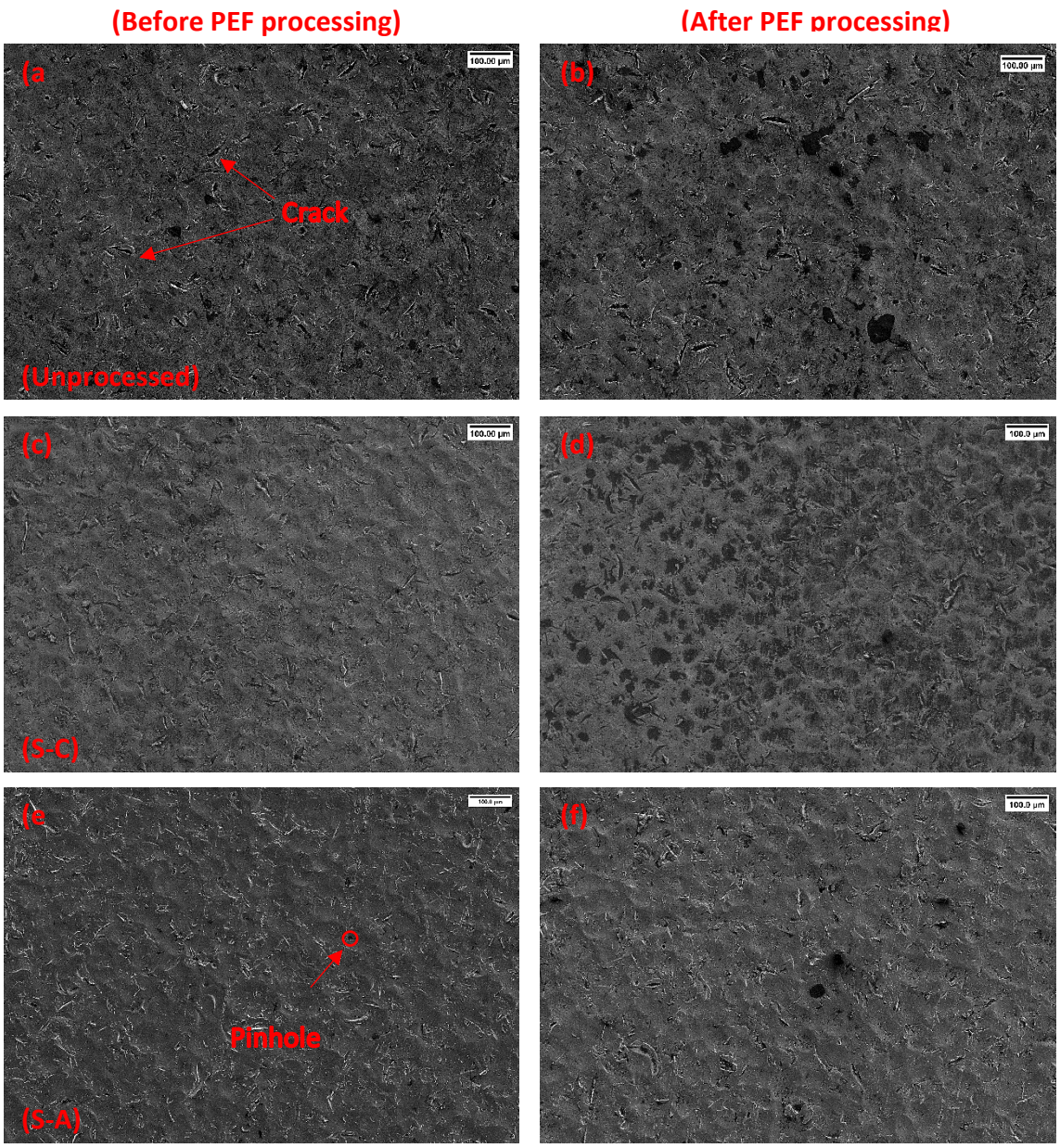

Figure 5-8**:** SEM images of 316L stainless steel under various conditions: (a) unprocessed before PEF treatment, (b) unprocessed after PEF treatment, (c) S-C condition before PEF treatment, (d) S-C condition after PEF treatment, (e) S-A condition before PEF treatment, and (f) S-A condition after PEF treatment.

5.4 Discussion

A variety of methodologies have been discussed in the literature that are capable of reducing metal ion release during the PEF process optimisation. However, we have proposed here the first practical implementation of a method that focused on diminishing ion release through the modification of the PEF electrode surface.

5.4.1 Iron concentration

Since the waveform used by the Elea PEF pilot plant is a monopolar square wave pulse, it causes a nearly instantaneous rise in voltage to its peak value, where it is held for an extended period of time above the threshold voltage, allowing for more electrochemical reactions to occur. The reason for the increase in Fe corrosion with increasing pulse width can be explained by the amount of time the electrode is exposed to voltages above the threshold voltage. As shown in Figure **5-3** the increased pulse width has a significant impact on the total energy applied to the system. Because the peak voltage remains relatively constant during the run, this total energy increase may be observed as an increase in current density (A/cm^2) across the system. In order to minimize the time that it takes to reach the threshold voltage, the current density must be increased. This will allow for a greater portion of the pulse length to be above the threshold voltage, increasing corrosion on the system. When the voltage is raised, the cause for increased corrosion is due to the larger applied over potential, which allows more voltage to be applied to the electrode, resulting in electrochemical reactions on the electrode surface.

Nickel follows the same trend as Iron for metal ions released, while chromium and manganese have been reduced to a two-factor model with an extremely small pulse width dependence compared to Iron, which could be explained by the lower concentration of both elements in solution and the lower range of values available for pulse width in the system.

5.4.2 Waveform

The current and voltage waveforms are in phase at low frequencies. This demonstrates that the interface impedance is essentially resistive. Hence, when the frequency is low, in the equivalent circuit model, the capacitor's impedance magnitude is high, so most current flows through the resistor. Lowering the frequency while maintaining

the same peak-to-peak voltage causes an increase in charge and thus an increase in voltage at the double layer, allowing more electrochemical reactions to occur [217].

When the waveforms are out of phase, the impedance is not purely resistive, causing the circuit to be dependent also on the capacitance of the double layer. Absolute dielectric constant and absolute dielectric loss would both be noticeable at higher frequencies. This modification causes in a similar way to an alternating current circuit. As the frequency rises, more current flows to the capacitor and less through the rest of the circuit, allowing for less charge build up on the capacitor and thus reducing electrochemical reactions [217]. The phase change observed at the two frequencies remains constant throughout the running process this was seen by the constant Lissojous curve.

From the EIS graphs this altering in phase shift and impendence is different for each sample will S-A having a lower impendence over the entire test range and unprocessed. This lower impendence with correlate to a larger phase shift in the circuit allowing the electrode to act more like a capacitor allowing more AC circuit behavior.

5.4.3 XPS

XPS analysis of the surfaces show that the laser areal energy plays a vital role in determining the surface chemistry. For instance, both S-A and S-B samples processed with a similar areal laser energy at ~1.25 x 10^{24} J/cm^2 exhibit an oxide layer with a high Cr/Fe ratio of 3.61 and 2.63 respectively. This is expected to increase the general corrosion observed for both samples. S-C was processed with a higher laser density of 8.39 x 10^{24} J/cm^2, which correlates with the lower Cr/Fe ratio of 0.25. These observations can be explained by the thermo-kinetic model developed by Cu *et al.*, 2014 where chromium is oxidized during the initial exposure to the laser source due to it higher oxygen affinity. This chromium rich layer is then preserved on the surface due to the non-equilibrium oxidation experience due to the rapid heating and cooling of laser processing which does not facilitate diffusion of other elements at lower areal energy . When higher energy is used, longer diffusion times increase the Fe concentration on the surface due to its higher bulk concentration and higher ion mobility inside the oxide film this intern suppresses the Cr concentration on the surface and increase Fe and other allowing elements.

5.4.4 Reduced metal released

It can be seen from Figure **5-2** that the concentration of elemental ions released after PEF processing is reduced for all the laser processed samples with all samples taking 3 times as many pulses to surpass the metals released from unprocessed after 10000 pulses. With S-A and S-B preforming slightly better than S-C after 30,000 pulses having 28.47, 28.98 and 42.73 ppb total ions respectively. This shows that all the laser processing conditions have a positive effect on the metal released. When you look into the individual elements you can see that the total metal released are made up of vastly different elemental composition. The S-C sample does not produce a concentration of ions higher than that of the unprocessed stainless steel sample for any of the elements after 10,000 pulses. While for S-A (0.60 ppb) and S-B (0.55 ppb) samples, the Cr concentration exceeds that of the unprocessed SS (0.18 ppb) after 10,000 pulses. While for nickel, S-C (18.12 ppb) experiences a lot higher Ni leaching than S-A (6.06 ppb) and S-B (7.52 ppb) after 30,000 pulses. This alteration in leaching concentrations can be explained by the respective surface compositions of the samples with S-A and S-B both exhibiting higher Cr and Mn concentrations, while S-C contains more Ni. The reason for a higher Ni concentration in solution compared to that of Cr, even with a lower surface composition, is due to Ni lower reaction potential compared to Cr, (-0.2 V and -0.41 V respectively, this allows for electrochemical reactions to take place at a lower potential for Ni than Cr [118]. This alteration in surface chemistry allows for the selective reduction of elements in the processing solution.

5.4.5 Selective reduction of elements

Excess amounts of nickel and chromium have been seen to cause negative health effects in humans such as in contact dermatitis, cardiovascular disease, asthma, lung fibrosis, and even respiratory system cancers which is especially seen for Cr(VI) exposure[218–220]. Human exposure to these elements has been seen to come from a variety of sources such as soils, water, plants and animals. While there is no known human enzymes or cofactors dependent on Ni for normal function, Cr(III) is essential for human health and metabolism of glucose, protein and fat; however, excess amounts of both can cause adverse effects [219,221]. Thus, the reduction of expose to these elements is important. With the US average daily exposure for Ni and Cr at 162 µg and 76 µg respectively [222]. With the FDAs advised Tolerable Upper Intake Level (UL) of 1000 µg and 120 µg for Ni and Cr respectively, this shows

that the Cr daily exposure is close to the UL and for people with metals sensitives these numbers are even closer [221]. Laser processing therefore can reduce the concentration of individual elements, while also reducing the overall corrosion of the electrodes. This can be particularly useful for food products such as peanuts, peas and chocolate milk which have a high nickel content already, close to the UL, at 956 µg/kg, 699 µg/kg and 871 µg/kg respectively [223]. Released metal ions can also produce secondary compounds that can have degradation effects on the food product themselves such as the production of OH and OOH radicals from the Fenton reaction of iron ions. These radicals can react with fatty acids and form lipid hydroperoxides and regeneration of another radical. Lipid peroxidised can then produce compounds such as malanoaldehyde and isoprotanes, which have been seen to cause diseases such as neuro generative diseases and diabetes [224].

5.5 Conclusion

The quest for sustainable food processing technologies that maintain and enhance food quality while preserving nutritional value has led to an increased interest in nonthermal methods like pulsed electric fields (PEF). While PEF offers significant advantages such as preserving freshness and reducing energy consumption compared to thermal pasteurization, it faces challenges like electrode corrosion and biofouling, hindering its widespread adoption in the food industry.

This study presents a novel approach to reducing metal ion release during pulsed electric field (PEF) processing, through the use of laser-induced oxidation of the electrodes. The implementation of this method marks a significant advancement in the field, as it addresses the issue of metal ion release at its source, offering a practical solution to mitigate environmental and health concerns associated with metal contamination.

Whilst the experimental conditions are not fully aligned with industrial PEF settings, e.g. lower field strength but higher total energy input have been applied, The findings reveal the intricate relationship between pulse waveform characteristics, such as frequency and pulse width, and the resulting metal ion release. Notably, the study demonstrates how variations in waveform parameters influence the electrochemical reactions at the electrode interface, affecting the corrosion behaviour of the system. Furthermore, X-ray photoelectron

spectroscopy (XPS) analysis provides valuable insights into the surface chemistry of the processed samples, shedding light on the mechanisms underlying the observed reduction in metal ion release. In the future, additional experiments should be conducted in real-time food processing environments to assess the potential for biofouling and corrosion.

The optimised results indicate a significant three-time reduction in metal ion release following PEF processing, with the laser-processed samples exhibiting improved performance compared to unprocessed stainless steel. This reduction in metal ion release is attributed to the selective alteration of the surface chemistry mainly through the increased Cr/Fe ratio on the surface, resulting in lower concentrations of harmful elements such as nickel and chromium. Given the adverse health effects associated with exposure to these elements, particularly in food products, the selective reduction achieved through PEF processing holds considerable promise for enhancing food safety and quality while also increasing the life time of the electrodes.

Overall, the findings highlight the potential of laser-induced oxidation as a practical solution for enhancing PEF electrode performance and reducing metal ion release in food processing applications. This method provides a solution for overcoming these obstacles and advancing the field of nonthermal food processing. By addressing key challenges in PEF technology, such as electrode corrosion and PEF parameter optimisation, this research contributes to the advancement of sustainable food processing methods with broader implications for food safety and human health. Thus, this innovative technique of laser surface oxidation presents an opportunity to extend the operational lifespan of PEF systems while maintaining or even enhancing processing efficiency and product quality.

Conclusion and Outlook

This study systematically examined the laser-induced oxidation on 316L stainless steel and it effect on the physical and chemical properties of the surface. The effect of the laser process parameters were explored for the potential to reduce metal ion release during the PEF processing. To achieve the research objectives, a comprehensive understanding was developed of how laser processing parameters impact the chemical, morphological, and corrosion properties of 316L stainless steel. The original contributions from each investigation are summarized below.

Chapter 3 presents the mechanisms of laser-induced oxidation on 316L stainless steel. This work investigated how varying laser processing parameters affect the composition and optical properties of oxidized 316L stainless steel surfaces. Using a full factorial design of experiments, the study revealed relationships between color, composition, and laser parameters, leading to the following conclusions. Surface morphology is significantly influenced by changes in laser processing parameters. Different processing conditions produced distinct surface structures: lower laser powers resulted in pure oxide growth, mid-range powers caused surface remelting and solidification, and higher powers led to material ablation.

Laser-colored samples were analyzed using the CIE 1931 chromaticity system, providing an effective method to link laser processing parameters with surface color, hue, and brightness. Tristimulus values (X, Y, Z) enabled quantitative color characterization, revealing that sample brightness (Y) was influenced by scan speed, frequency, and power settings. Color distance varied with laser power; 80% power yielded a color distance of 12.14 ΔEab*, while 100% power resulted in the smallest color distance of 6.85 ΔEab*. X-ray photoelectron spectroscopy (XPS) analysis showed that the surface was primarily composed of iron, chromium, and molybdenum oxides. Cr2p spectra indicated that Chromia oxide formation was tied to areal energy density, favouring Cr_2O_3 at lower energies and CrO_3 at higher energies. A surface response model was developed to describe the relationship between the chromium-to-iron ratio and areal energy density, showing a peak at the lowest energy density. While untreated stainless steel has a Cr/Fe ratio of 0.67, this study achieved a maximum Cr/Fe ratio of 2.09, potentially enhancing corrosion resistance over conventional

stainless steel. The models developed here can be used to tailor oxide film composition or surface color for various applications. A novel finding of this work is the quantified inverse relationship between chromium and molybdenum concentrations, allowing thermokinetic models of laser surface oxidation on 316L stainless steel to be expanded to include molybdenum

Chapter 4 presents a comprehensive study of the influence of laser process parameters, specifically laser power, laser scanning speed, laser frequency, and hatch distance, on the material properties of 316l fabricated by laser induced oxidation. Optimization of laser processing parameters for enhancing the corrosion resistance of stainless steel was conducted using two full factorial designs of experiments (DoE), with a focus on laser power, scan speed, frequency, and hatching distance. This study provided several key insights into the effects of laser surface modification on surface chemistry and corrosion properties. Samples processed with an areal energy below $3x10^{24}$ J/cm² demonstrated superior corrosion resistance, outperforming untreated stainless steel. Optimal parameters resulted in a peak pitting resistance of 509.15 mV and an Icorr of 51.5 nA/cm², a substantial improvement compared to untreated samples, which showed a pitting resistance of 160.8 mV and an Icorr of 502 nA/cm².

X-ray Photoelectron Spectroscopy (XPS) analysis revealed that the surface of the optimized sample (S3) was predominantly composed of iron and chromium oxides, with a Cr/Fe ratio exceeding 3.5. This high Cr/Fe ratio was associated with significantly improved corrosion resistance, as increases in corrosion current were observed once the Cr/Fe ratio surpassed 1.0, while minimal changes in Icorr occurred below this ratio. Depth profiling further indicated variations in oxide layer composition and thickness, providing insights into corrosion behavior.

Surface morphology analysis, performed using Scanning Electron Microscope (SEM) imaging, confirmed that laser processing reduced surface defects, thus enhancing resistance to localized corrosion. Optimally processed samples exhibited smoother surfaces with fewer defects, contributing to improved corrosion resistance. Cyclic polarization tests demonstrated a clear relationship between surface composition, morphology, and corrosion resistance, with

samples having higher chromium content and smoother surfaces showing superior resistance to localized corrosion.

Electrochemical Impedance Spectroscopy (EIS) results revealed that optimally processed samples exhibited higher resistance and lower capacitance, indicative of enhanced corrosion protection. Long-term impedance spectra provided valuable information on the evolution of the passive film over time, highlighting the stability of this protective layer under corrosive conditions.

These findings underscore the importance of areal energy, composition, and morphology in optimizing stainless steel surfaces for improved corrosion resistance through laser processing. The insights gained from this study contribute to the development of corrosion-resistant materials and surface engineering techniques for various industrial applications. Future research could explore additional factors influencing corrosion behavior, such as other laser processing parameters, metal compositions, and environmental conditions tailored for specific applications

Chapter 5 presents a comprehensive study into the effect of laser indued oxidation of stainless steel on electrodes operation in a Pulsed Electric Field system. This study introduced a novel approach to reducing metal ion release during pulsed electric field (PEF) processing by utilizing laser-induced oxidation of the electrodes. This method developed represents a significant advancement in the field, tackling the issue of metal ion release at its source and offering a practical solution to mitigate the environmental and health risks associated with metal contamination.

Although the experimental conditions differ from typical industrial PEF settings—such as using lower field strength but higher total energy input—the results reveal a complex relationship between pulse waveform characteristics (e.g., frequency and pulse width) and metal ion release. The study highlights how variations in waveform parameters influence electrochemical reactions at the electrode interface, affecting the corrosion behavior of the system. Additionally, X-ray photoelectron spectroscopy (XPS) analysis provides valuable insights into the surface chemistry of the processed samples, revealing the mechanisms behind the observed reduction in metal ion release. Future experiments should focus on real-time food processing environments to evaluate the potential for biofouling and corrosion.

The optimized results demonstrate a threefold reduction in metal ion release following PEF processing, with the laser-processed samples outperforming unprocessed stainless steel. This reduction is attributed to selective changes in the surface chemistry, notably an increased Cr/Fe ratio, which lowers the concentration of harmful elements like nickel and chromium. Given the negative health effects linked to exposure to these elements, particularly in food products, the selective reduction achieved through PEF processing holds significant promise for improving food safety and quality, as well as extending the lifespan of the electrodes.

Overall, the findings underscore the potential of laser-induced oxidation as a practical solution to enhance PEF electrode performance and reduce metal ion release in food processing applications. This approach addresses key challenges in PEF technology, such as electrode corrosion and PEF parameter optimization, contributing to the advancement of sustainable food processing methods with broader implications for food safety and human health. Consequently, this innovative technique of laser surface oxidation offers an opportunity to extend the operational lifespan of PEF systems while maintaining or even improving processing efficiency and product quality.

Future work

In PEF processing there can often be a flow of liquid during the processing. In future work, a flow mode of operation could be examined to understand the influence of the flow rate on the conventional and the laser surface oxidised electrode performance. This increased flow can cause biofouling to occur inside the electrode. The approach I proposed to reduce this is to introduce a laser surface texture on to the surface of the electrode. These textures have been shown to increase the wettability and anti-fouling properties of the surface. For this area of work, the effect of the different texture shapes could be examined. In such future work, how the laser process parameters can be used to produce hierarchical structures with increase hydrophobicity and anti-biofouling properties could be examined. I will utilize three distinct DOEs to optimise three distinct surface geometries, and then I will use several post-processing techniques to build the hierarchical structures required for super hydrophobic characteristics. For this work, multi-disciplinary collaboration is required, including with a biotechnology focus, to conduct a stationary and dynamic based biofouling test. Once antifouling surfaces are completely submerged in water, their antifouling qualities diminish, limiting their anticorrosion efficiency. Due to this, I plan to investigate the effect of the antifouling / water-repellent surface during flow corrosion, with parameters comparable to those encountered within a flow pulsed electric field system. To conduct this investigation, I have designed a flow corrosion vessel, with the 3D-printed prototype and schematic depicted in Figure 5-10. According to my knowledge, antifouling textures have never been utilized under flow corrosion, which will strengthen the originality of this work. Some of the premilitary work for this can be seen in supplementary information 1 below, where I conducted a 4 factor DOE to identify the ablation rated of Femtosecond texturing on stainless steel.

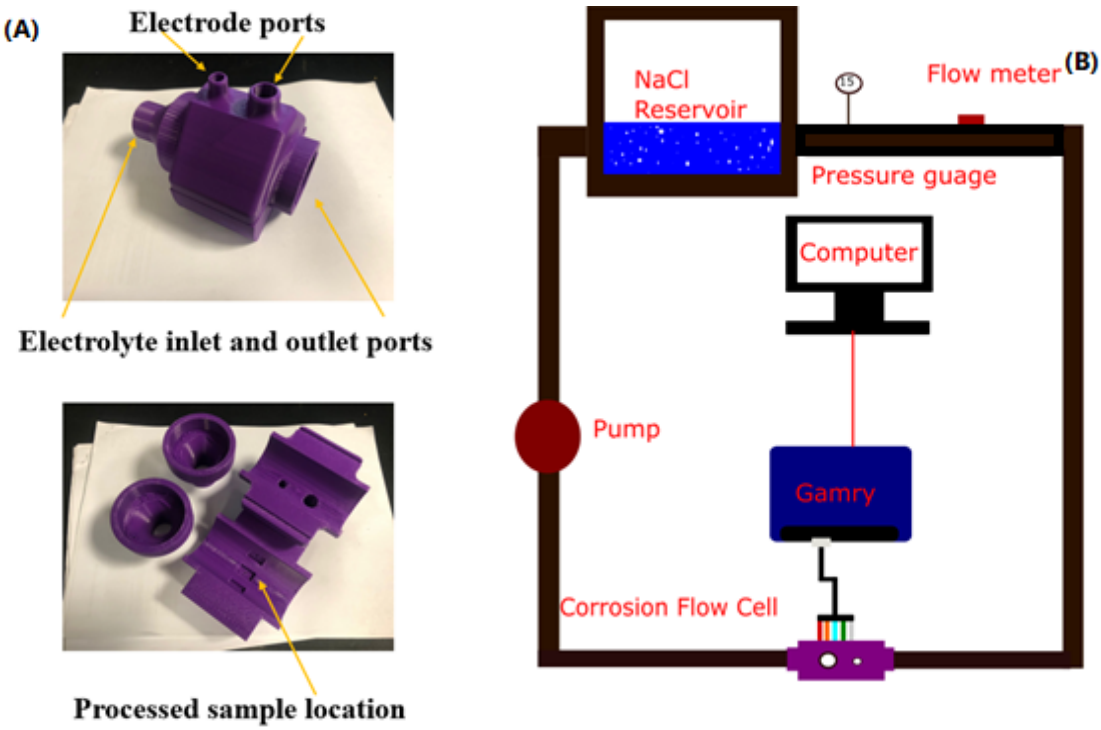

Figure 5-9: (A) 3D printed prototype of a flow cell and (B) schematic of the full flow corrosion system.

References

[1] S.O.Kasap, Optoelectronics. Prentice Hall, 1 edition., 1999.

[2] S.W.C.L.A. Coldren., Diode Lasers and Photonic Integrated Circuits. John Wiley & Sons, 3 edition., 1995.

[3] M. Fox., Optical Properties of solids. Oxford University Press, 2001, (2001).

[4] S.P.H. Narendra B. Dahotre, Laser Fabrication and Machining of Materials, Springer US, Boston, MA, 2008. https://doi.org/10.1007/978-0-387-72344-0.

[5] J.E. Geusic, H.M. Marcos, L.G. Van Uitert, LASER OSCILLATIONS IN Nd-DOPED YTTRIUM ALUMINUM, YTTRIUM GALLIUM AND GADOLINIUM GARNETS, Appl Phys Lett 4 (1964) 182–184. https://doi.org/10.1063/1.1753928.

[6] L. Nánai, R. Vajtai, T. F. George, Laser-induced oxidation of metals: state of the art, Thin Solid Films 298 (1997) 160–164. https://doi.org/10.1016/S0040-6090(96)09390-X.

[7] A. Atkinson, Transport processes during the growth of oxide films at elevated temperature, Rev Mod Phys 57 (1985) 437–470. https://doi.org/10.1103/RevModPhys.57.437.

[8] D.A. Jelski, L. Nánai, R. Vajtai, I. Hevesi, T.F. George, Kinetics of oxide crystal growth in the transition regime between Cabrera-Mott and Wagner thickness regions, Materials Science and Engineering: A 173 (1993) 193–195. https://doi.org/https://doi.org/10.1016/0921-5093(93)90214-Y.

[9] L. Nánai, R. Vajtai, I. Kovács, I. Hevesi, On the kinetics of laser-light-induced oxidation constants of vanadium, Journal of the Less Common Metals 152 (1989) L23–L26. https://doi.org/https://doi.org/10.1016/0022-5088(89)90104-5.

[10] J. Volpp, Laser beam absorption measurement at molten metal surfaces, Measurement 209 (2023) 112524. https://doi.org/https://doi.org/10.1016/j.measurement.2023.112524.

[11] P. Di Sia, Overview of Drude-Lorentz type models and their applications, Nanoscale Systems: Mathematical Modeling, Theory and Applications 3 (2014) 1–13. https://doi.org/10.2478/nsmmt-2014-0001.

[12] M.S. Brown, C.B. Arnold, Fundamentals of Laser-Material Interaction and Application to Multiscale Surface Modification, in: K. Sugioka, M. Meunier, A. Piqué (Eds.), Laser Precision Microfabrication, Springer Berlin Heidelberg, Berlin, Heidelberg, 2010: pp. 91–120. https://doi.org/10.1007/978-3-642-10523-4_4.

[13] T. Maeji, K. Ibano, S. Yoshikawa, D. Inoue, S. Kuroyanagi, K. Mori, E. Hoashi, K. Yamanoi, N. Sarukura, Y. Ueda, Laser energy absorption coefficient and in-situ temperature measurement of laser-melted tungsten, Fusion Engineering and Design 124 (2017) 287–291. https://doi.org/https://doi.org/10.1016/j.fusengdes.2017.04.025.

[14] J. Volpp, Laser light absorption of high-temperature metal surfaces, Heliyon 9 (2023) e21021. https://doi.org/https://doi.org/10.1016/j.heliyon.2023.e21021.

[15] F. Di Niso, C. Gaudiuso, T. Sibillano, F.P. Mezzapesa, A. Ancona, P.M. Lugarà, Role of heat accumulation on the incubation effect in multi-shot laser ablation of stainless steel at high repetition rates, Opt Express 22 (2014) 12200–12210. https://doi.org/10.1364/OE.22.012200.

[16] V. Gareyan, Zh. Gevorkian, Impact of surface roughness on light absorption, Phys Rev A (Coll Park) 109 (2024) 13515. https://doi.org/10.1103/PhysRevA.109.013515.

[17] A. Al-Mahdy, H.R. Kotadia, M.C. Sharp, T.T. Opoz, J. Mullett, J.I. Ahuir-Torres, Effect of Surface Roughness on the Surface Texturing of 316 l Stainless Steel by Nanosecond Pulsed Laser, Lasers in Manufacturing and Materials Processing 10 (2023) 141–164. https://doi.org/10.1007/s40516-022-00199-x.

[18] M. Ahmed Obeidi, E. McCarthy, S.I. Ubani, I. Ul Ahad, D. Brabazon, Effect of Surface Roughness on CO2 Laser Absorption by 316L Stainless Steel and Aluminum, Mater Perform Charact 8 (2019) 1167–1177. https://doi.org/10.1520/MPC20180091.

[19] P. Khan, T. Debroy, Absorption of CO2 laser beam by AISI 4340 steel, Metallurgical Transactions B 16 (1985) 853–856. https://doi.org/10.1007/BF02667524.

[20] C. Schaffer, A. Brodeur, E. Mazur, Laser-Induced Breakdown and Damage in Bulk Transparent Materials Induced by Tightly Focused Femtosecond Laser Pulses, Measurement Science & Technology - MEAS SCI TECHNOL 12 (2001). https://doi.org/10.1088/0957-0233/12/11/305.

[21] C.B. Schaffer, J.F. García, E. Mazur, Bulk heating of transparent materials using a high-repetition-rate femtosecond laser, Applied Physics A 76 (2003) 351–354. https://doi.org/10.1007/s00339-002-1819-4.

[22] S. Ma, J.P. McDonald, B. Tryon, S.M. Yalisove, T.M. Pollock, Femtosecond Laser Ablation Regimes in a Single-Crystal Superalloy, Metallurgical and Materials Transactions A 38 (2007) 2349–2357. https://doi.org/10.1007/s11661-007-9260-0.

[23] I. Etsion, Improving Tribological Performance of Mechanical Components by Laser Surface Texturing, Tribol Lett 17 (2004) 733–737. https://doi.org/10.1007/s11249-004-8081-1.

[24] J. Coroado, S. Ganguly, S. Williams, W. Suder, S. Meco, G. Pardal, Comparison of continuous and pulsed wave lasers in keyhole welding of stainless-steel to aluminium, The International Journal of Advanced Manufacturing Technology 119 (2022) 367–387. https://doi.org/10.1007/s00170-021-08226-5.

[25] E. Assuncao, S. Williams, Comparison of continuous wave and pulsed wave laser welding effects, Opt Lasers Eng 51 (2013) 674–680. https://doi.org/https://doi.org/10.1016/j.optlaseng.2013.01.007.

[26] R.(周锐) Zhou, Z.(张姿) Zhang, M.(洪明辉) Hong, The art of laser ablation in aeroengine: The crown jewel of modern industry, J Appl Phys 127 (2020) 80902. https://doi.org/10.1063/1.5134813.

[27] A. Dubey, V. Yadava, Laser beam machining—A review, Int J Mach Tools Manuf 48 (2008) 609–628. https://doi.org/10.1016/j.ijmachtools.2007.10.017.

[28] T. Aizawa, T. Inohara, Pico- and Femtosecond Laser Micromachining for Surface Texturing, in: Z. Stanimirović, I. Stanimirović (Eds.), Micromachining, IntechOpen, Rijeka, 2019. https://doi.org/10.5772/intechopen.83741.

[29] B.H. Christensen, K. Vestentoft, P. Balling, Short-pulse ablation rates and the two-temperature model, Appl Surf Sci 253 (2007) 6347–6352. https://doi.org/https://doi.org/10.1016/j.apsusc.2007.01.045.

[30] A. Miotello, R. Kelly, Laser-induced phase explosion: new physical problems when a condensed phase approaches the thermodynamic critical temperature, Applied Physics A 69 (1999) S67–S73. https://doi.org/10.1007/s003399900296.

[31] J. Zhang, D. Yang, A. Rosenkranz, J. Zhang, L. Zhao, C. Song, Y. Yan, T. Sun, Laser Surface Texturing of Stainless Steel − Effect of Pulse Duration on Texture’s

Morphology and Frictional Response, Adv Eng Mater 21 (2019) 1801016. https://doi.org/https://doi.org/10.1002/adem.201801016.

[32] K.-H. Leitz, B. Redlingshöfer, Y. Reg, A. Otto, M. Schmidt, Metal Ablation with Short and Ultrashort Laser Pulses, Phys Procedia 12 (2011) 230–238. https://doi.org/https://doi.org/10.1016/j.phpro.2011.03.128.

[33] W. Xiaofa, 康治军 Zhijun, 樊仲维 Zhongwei, 连富强 Fuqiang, 黄科 Ke, J. Yu, Beam Shaping of TEM00 Gaussian Beam by Using Diffraction Theory, Chinese Journal of Lasers 38 (2011) 402006. https://doi.org/10.3788/CJL20113804.402006.

[34] J. Alda, Laser and Gaussian Beam Propagation and Transformation, Encyclopedia of Optical Engineering (2003). https://doi.org/10.1081/E-EOE 120009751.

[35] O. Homburg, T. Mitra, L.L. Mikrooptik, Gaussian-to-top-hat beam shaping: an overview of parameters, methods, and applications, in: LASE, 2012. https://api.semanticscholar.org/CorpusID:121459716.

[36] X.L. Huang, J. Martinez-Vega, D. Malec, Morphological evolution of polytetrafluoroethylene in extreme temperature conditions for aerospace applications, J Appl Polym Sci 131 (2014). https://doi.org/https://doi.org/10.1002/app.39841.

[37] J. Blumm, A. Lindemann, M. Meyer, C. Strasser, Characterization of PTFE Using Advanced Thermal Analysis Techniques, Int J Thermophys 31 (2010) 1919–1927. https://doi.org/10.1007/s10765-008-0512-z.

[38] V.N. Aderikha, V.A. Shapovalov, Effect of filler surface properties on structure, mechanical and tribological behavior of PTFE-carbon black composites, Wear 268 (2010) 1455–1464. https://doi.org/https://doi.org/10.1016/j.wear.2010.02.022.

[39] M. Conte, A. Igartua, Study of PTFE composites tribological behavior, Wear 296 (2012) 568–574. https://doi.org/https://doi.org/10.1016/j.wear.2012.08.015.

[40] S. Ashokkumar, J. Adler-Nissen, Evaluating non-stick properties of different surface materials for contact frying, J Food Eng 105 (2011) 537–544. https://doi.org/https://doi.org/10.1016/j.jfoodeng.2011.03.018.

[41] F. Andreatta, A. Lanzutti, E. Aneggi, A. Gagliardi, A. Rondinella, M. Simonato, L. Fedrizzi, Degradation of PTFE non-stick coatings for application in the food

service industry, Eng Fail Anal 115 (2020) 104652. https://doi.org/https://doi.org/10.1016/j.engfailanal.2020.104652.

[42] Y. Liu, Modification of stainless steel surfaces by electroless Ni-P and small amount of PTFE to minimize bacterial adhesion, J Food Eng 72 (2006) 266–272. https://doi.org/10.1016/j.jfoodeng.2004.12.006.

[43] V.B. Damodaran, N.S. Murthy, Bio-inspired strategies for designing antifouling biomaterials, Biomater Res 20 (2016) 18. https://doi.org/10.1186/s40824-016-0064-4.

[44] T.M. Gilmore, R.R. Maller, V. Mills, Protecting stainless steel dairy equipment from corrosion, Dairy, Food and Environmental Sanitation: A Publication of the International Association of Milk, Food and Environmental Sanitarians (USA) (1998).

[45] D. AD, Stainless Steel for Dairy and Food Industry: A Review, Journal of Material Science & Engineering 04 (2015). https://doi.org/10.4172/2169-0022.1000191.

[46] Corrigendum to Regulation (EC) No 852/2004, 2004.

[47] J.W. Arnold, O. Suzuki, Effects of corrosive treatment on stainless steel surface finishes and bacterial attachment, Transactions of the ASAE 46 (2003) 1595.

[48] N. Benbettaïeb, R. Mahfoudh, S. Moundanga, C.-H. Brachais, O. Chambin, F. Debeaufort, Modeling of the release kinetics of phenolic acids embedded in gelatin/chitosan bioactive-packaging films: Influence of both water activity and viscosity of the food simulant on the film structure and antioxidant activity, Int J Biol Macromol 160 (2020) 780–794. https://doi.org/https://doi.org/10.1016/j.ijbiomac.2020.05.199.

[49] E. Fortunati, F. Luzi, L. Dugo, C. Fanali, G. Tripodo, L. Santi, J.M. Kenny, L. Torre, R. Bernini, Effect of hydroxytyrosol methyl carbonate on the thermal, migration and antioxidant properties of PVA-based films for active food packaging, Polym Int 65 (2016) 872–882. https://doi.org/https://doi.org/10.1002/pi.5090.

[50] A. Bahrami, R. Rezaei Mokarram, M. Sowti Khiabani, B. Ghanbarzadeh, R. Salehi, Physico-mechanical and antimicrobial properties of tragacanth/hydroxypropyl methylcellulose/beeswax edible films reinforced with silver nanoparticles, Int J Biol Macromol 129 (2019) 1103–1112. https://doi.org/https://doi.org/10.1016/j.ijbiomac.2018.09.045.

[51] H.-J. Park, J.Y. Kim, J. Kim, J.-H. Lee, J.-S. Hahn, M.B. Gu, J. Yoon, Silver-ion-mediated reactive oxygen species generation affecting bactericidal activity, Water Res 43 (2009) 1027–1032. https://doi.org/https://doi.org/10.1016/j.watres.2008.12.002.

[52] N. Durán, M. Durán, M.B. de Jesus, A.B. Seabra, W.J. Fávaro, G. Nakazato, Silver nanoparticles: A new view on mechanistic aspects on antimicrobial activity, Nanomedicine 12 (2016) 789–799. https://doi.org/https://doi.org/10.1016/j.nano.2015.11.016.

[53] A. Griffith, S. Neethirajan, K. Warriner, Development and Evaluation of Silver Zeolite Antifouling Coatings on Stainless Steel for Food Contact Surfaces, J Food Saf 35 (2015) 345–354. https://doi.org/https://doi.org/10.1111/jfs.12181.

[54] E.R.I. Mahmoud, S.Z. Khan, M. Ejaz, Laser surface cladding of mild steel with 316L stainless steel for anti-corrosion applications, Mater Today Proc 39 (2021) 1029–1033. https://doi.org/https://doi.org/10.1016/j.matpr.2020.04.763.

[55] T. Jwad, S. Deng, H. Butt, S. Dimov, Laser induced single spot oxidation of titanium, Appl Surf Sci 387 (2016) 617–624. https://doi.org/https://doi.org/10.1016/j.apsusc.2016.06.136.

[56] Y. Evren, D. Jan, K. Jean-Pierre, The investigation of the influence of laser re-melting on density, surface quality and microstructure of selective laser melting parts, Rapid Prototyp J 17 (2011) 312–327. https://doi.org/10.1108/13552541111156450.

[57] H.M. Alojaly, K.Y. Benyounis, K.A. Eldressi, 11.07 - Laser surface treatment of steels, in: S. Hashmi (Ed.), Comprehensive Materials Processing (Second Edition), Elsevier, Oxford, 2024: pp. 110–134. https://doi.org/https://doi.org/10.1016/B978-0-323-96020-5.00252-1.

[58] Q. Wu, W. Long, L. Zhang, H. Zhao, A review on ceramic coatings prepared by laser cladding technology, Opt Laser Technol 176 (2024) 110993. https://doi.org/https://doi.org/10.1016/j.optlastec.2024.110993.

[59] Y. Huang, Z. Wang, Z. Xu, X. Zang, X. Chen, Microstructure and properties of TiNbZrMo high entropy alloy coating, Mater Lett 285 (2021) 129004. https://doi.org/https://doi.org/10.1016/j.matlet.2020.129004.

[60] Y. He, M. Cong, W. Lei, Y. Ding, T. Xv, Z. Han, Microstructure, mechanical and corrosion properties of FeCrNiCoMnSi0.1 high-entropy alloy coating via TIG arc melting technology and high-frequency ultrasonic impact with welding, Mater

Today Adv 20 (2023) 100443.
https://doi.org/https://doi.org/10.1016/j.mtadv.2023.100443.

[61] E. Chen, K. Zhang, J. Zou, Laser cladding of a Mg based Mg–Gd–Y–Zr alloy with Al–Si powders, Appl Surf Sci 367 (2016) 11–18.
https://doi.org/https://doi.org/10.1016/j.apsusc.2016.01.124.

[62] A.A. Wang, S. Sircar, J. Mazumder, Laser cladding of Mg-Al alloys, J Mater Sci 28 (1993) 5113–5122. https://doi.org/10.1007/BF00570050.

[63] B.P. Fairand, A.H. Clauer, R.G. Jung, B.A. Wilcox, Quantitative assessment of laser-induced stress waves generated at confined surfaces, Appl Phys Lett 25 (1974) 431–433. https://doi.org/10.1063/1.1655536.

[64] A. Clauer, B. Fairand, B. Wilcox, Pulsed laser induced deformation in an Fe-3 Wt Pct Si alloy, Metallurgical Transactions 8 (1977) 119–125.
https://doi.org/10.1007/BF02677273.

[65] A. Clauer, B. Fairand, B. Wilcox, Laser shock hardening of weld zones in aluminum alloys, Metallurgical Transactions 8 (1977) 1871–1876.
https://doi.org/10.1007/BF02646559.

[66] R.K. Gupta, B. Sunil Kumar, R. Sundar, P. Ram Sankar, P. Ganesh, R. Kaul, V. Kain, K. Ranganathan, K.S. Bindra, B. Singh, Enhancement of intergranular corrosion resistance of type 304 stainless steel through laser shock peening, Corrosion Engineering, Science and Technology 52 (2017) 220–225.
https://doi.org/10.1080/1478422X.2016.1254422.

[67] A.K. Gujba, M. Medraj, Laser Peening Process and Its Impact on Materials Properties in Comparison with Shot Peening and Ultrasonic Impact Peening, Materials 7 (2014) 7925–7974. https://doi.org/10.3390/ma7127925.

[68] V. Kain, 5 - Stress corrosion cracking (SCC) in stainless steels, in: V.S. Raja, T. Shoji (Eds.), Stress Corrosion Cracking, Woodhead Publishing, 2011: pp. 199–244. https://doi.org/https://doi.org/10.1533/9780857093769.3.199.

[69] L. Hackel, J.R. Rankin, A. Rubenchik, W.E. King, M. Matthews, Laser peening: A tool for additive manufacturing post-processing, Addit Manuf 24 (2018) 67–75.
https://doi.org/https://doi.org/10.1016/j.addma.2018.09.013.

[70] K.M. Łęcka, A.J. Antończak, P. Kowalewski, M. Trzcinski, Wear resistance of laser-induced annealing of AISI 316 (EN 1.4401) stainless steel, Laser Phys 28 (2018) 96005. https://doi.org/10.1088/1555-6611/aac507.

[71] K.M. Łęcka, M.R. Wójcik, A.J. Antończak, Laser-Induced Color Marking of Titanium: A Modeling Study of the Interference Effect and the Impact of Protective Coating, Math Probl Eng 2017 (2017) 3425108. https://doi.org/10.1155/2017/3425108.

[72] S.L. Zhang, C. Suebka, H. Liu, Y.X. Liu, Z. Liu, W. Guo, Y.M. Cheng, F.D. Zhang, Y.D. Peng, L. Li, Mechanisms of laser cleaning induced oxidation and corrosion property changes in AA5083 aluminum alloy, J Laser Appl 31 (2019) 012001. https://doi.org/10.2351/1.5046470.

[73] C.Y. Cui, X.G. Cui, X.D. Ren, M.J. Qi, J.D. Hu, Y.M. Wang, Surface oxidation phenomenon and mechanism of AISI 304 stainless steel induced by Nd:YAG pulsed laser, Appl Surf Sci 305 (2014) 817–824. https://doi.org/https://doi.org/10.1016/j.apsusc.2014.04.025.

[74] J. Alda, Laser and Gaussian Beam Propagation and Transformation, Encyclopedia of Optical Engineering (2003). https://doi.org/10.1081/E-EOE 120009751.

[75] Y. Lu, X. Shi, Z. Huang, T. Li, M. Zhang, J. Czajkowski, T. Fabritius, M. Huttula, W. Cao, Nanosecond laser coloration on stainless steel surface, Sci Rep 7 (2017) 7092. https://doi.org/10.1038/s41598-017-07373-8.

[76] Z.L. Li, H.Y. Zheng, K.M. Teh, Y.C. Liu, G.C. Lim, H.L. Seng, N.L. Yakovlev, Analysis of oxide formation induced by UV laser coloration of stainless steel, Appl Surf Sci 256 (2009) 1582–1588. https://doi.org/https://doi.org/10.1016/j.apsusc.2009.09.025.

[77] K.M. Łęcka, A.J. Antończak, B. Szubzda, M.R. Wójcik, B.D. Stępak, P. Szymczyk, M. Trzciński, M. Ozimek, K.M. Abramski, Effects of laser-induced oxidation on the corrosion resistance of AISI 304 stainless steel, J Laser Appl 28 (2016) 32009. https://doi.org/10.2351/1.4948726.

[78] R. Davalos Monteiro, J. van de Wetering, B. Krawczyk, D.L. Engelberg, Corrosion Behaviour of Type 316L Stainless Steel in Hot Caustic Aqueous Environments, Metals and Materials International 26 (2020) 630–640. https://doi.org/10.1007/s12540-019-00403-2.

[79] S.K. Lawrence, D.P. Adams, D.F. Bahr, N.R. Moody, Environmental resistance of oxide tags fabricated on 304L stainless steel via nanosecond pulsed laser irradiation, Surf Coat Technol 285 (2016) 87–97. https://doi.org/https://doi.org/10.1016/j.surfcoat.2015.11.021.

[80] M. Svantner, M. Kučera, E. Smazalová, Š. Houdková, R. Čerstvý, Evaluation of Laser Marking Influence on Stainless Steel Corrosion Properties, 2014.

[81] Ya.M. Andreeva, V.C. Luong, D.S. Lutoshina, O.S. Medvedev, V.Yu. Mikhailovskii, M.K. Moskvin, G. V Odintsova, V. V Romanov, N.N. Shchedrina, V.P. Veiko, Laser coloration of metals in visual art and design, Opt. Mater. Express 9 (2019) 1310–1319. https://doi.org/10.1364/OME.9.001310.

[82] L. Liz-Marzán, ed., Colloidal Synthesis of Plasmonic Nanometals, Jenny Stanford Publishing, 2020. https://doi.org/10.1201/9780429295188.

[83] M.A. Rahman, S.M.K. Vivek, S.H. Kim, J.Y. Byun, Polarizonic-interference colouration of stainless steel surfaces by Au-Al2O3 nanocomposite thin film coating, Appl Surf Sci 505 (2020) 144428. https://doi.org/https://doi.org/10.1016/j.apsusc.2019.144428.

[84] F.Y. Alzoubi, A.A. Ahmad, I.A. Aljarrah, A.B. Migdadi, Q.M. Al-Bataineh, Localize surface plasmon resonance of silver nanoparticles using Mie theory, Journal of Materials Science: Materials in Electronics 34 (2023) 2128. https://doi.org/10.1007/s10854-023-11304-x.

[85] E. Chikarakara, P. Fitzpatrick, E. Moore, T. Levingstone, L. Grehan, C. Higginbotham, M. Vazquez, K. Bagga, S. Naher, D. Brabazon, In vitro fibroblast and pre-osteoblastic cellular responses on laser surface modified Ti–6Al–4V, Biomed Mater 10 (2014) 15007. https://doi.org/10.1088/1748-6041/10/1/015007.

[86] M. Gaidys, A. Selskis, P. Gečys, M. Gedvilas, Stainless steel colouring using burst and biburst mode ultrafast laser irradiation, Opt Laser Technol 174 (2024) 110561. https://doi.org/https://doi.org/10.1016/j.optlastec.2024.110561.

[87] Y. Tamamura, G. Miyaji, Structural coloration of a stainless steel surface with homogeneous nanograting formed by femtosecond laser ablation, Opt. Mater. Express 9 (2019) 2902–2909. https://doi.org/10.1364/OME.9.002902.

[88] J. Geng, L. Xu, W. Yan, L. Shi, M. Qiu, High-speed laser writing of structural colors for full-color inkless printing, Nat Commun 14 (2023) 565. https://doi.org/10.1038/s41467-023-36275-9.

[89] H. Liu, W. Lin, M. Hong, Surface coloring by laser irradiation of solid substrates, APL Photonics 4 (2019) 51101. https://doi.org/10.1063/1.5089778.

[90] D.N. Antonov, A.A. Burtsev, O.Ya. Butkovskii, Coloration of a metal surface under pulsed laser irradiation, Technical Physics 59 (2014) 1503–1505. https://doi.org/10.1134/S1063784214100077.

[91] H. Zhao, Q. Zhang, Y. Hou, Z. Cheng, T. Xia, S. Cao, P. Wang, Color visual art creation on metals via multifunctional laser paintbrush, Opt Laser Technol 159 (2023) 109040. https://doi.org/https://doi.org/10.1016/j.optlastec.2022.109040.

[92] M.A. Kats, R. Blanchard, S. Ramanathan, F. Capasso, Thin-Film Interference in Lossy, Ultra-Thin Layers, Opt. Photon. News 25 (2014) 40–47. https://doi.org/10.1364/OPN.25.1.000040.

[93] D. Austin, B. Everhart, F. Khurshid, J. Muthu, A. Pelton, M. Altvater, M. Smith, S. Post, P. Miesle, C. Muratore, R. Rao, M. Hofmann, P. Amama, N. Glavin, Exploiting Laser-Induced Oxidation Phase Diagrams for Multifunctional Titania Thin Films, Adv Funct Mater 34 (2024) 2310469. https://doi.org/https://doi.org/10.1002/adfm.202310469.

[94] G.T. Alliott, R.L. Higginson, G.D. Wilcox, Producing a thin coloured film on stainless steels – a review. Part 2: non-electrochemical and laser processes, Transactions of the IMF 101 (2023) 72–78. https://doi.org/10.1080/00202967.2022.2154495.

[95] A.J. Antończak, B. Stępak, P.E. Kozioł, K.M. Abramski, The influence of process parameters on the laser-induced coloring of titanium, Applied Physics A 115 (2014) 1003–1013. https://doi.org/10.1007/s00339-013-7932-8.

[96] F. Xia, L. Jiao, D. Wu, S. Li, K. Zhang, W. Kong, M. Yun, Q. Liu, X. Zhang, Mechanism of pulsed-laser-induced oxidation of titanium films, Opt Mater Express 9 (2019) 4097–4103. https://doi.org/10.1364/OME.9.004097.

[97] N.B. Dahotre, L.R. Katipelli, Oxidation Kinetics and Morphology of Laser Surface Engineered Hard Coating on Aluminum, in: Elevated Temperature Coatings, 2001: pp. 219–231. https://doi.org/https://doi.org/10.1002/9781118787694.ch17.

[98] Y. Cai, W. Chang, X. Luo, A.M.L. Sousa, K.H.A. Lau, Y. Qin, Superhydrophobic structures on 316L stainless steel surfaces machined by nanosecond pulsed laser, Precis Eng 52 (2018) 266–275. https://doi.org/https://doi.org/10.1016/j.precisioneng.2018.01.004.

[99] S. Milles, M. Soldera, T. Kuntze, A.F. Lasagni, Characterization of self-cleaning properties on superhydrophobic aluminum surfaces fabricated by direct laser writing and direct laser interference patterning, Appl Surf Sci 525 (2020) 146518. https://doi.org/https://doi.org/10.1016/j.apsusc.2020.146518.

[100] G. Li, Direct laser writing of graphene electrodes, J Appl Phys 127 (2020) 10901. https://doi.org/10.1063/1.5120056.

[101] D. Huerta-Murillo, A.I. Aguilar-Morales, S. Alamri, J.T. Cardoso, R. Jagdheesh, A.F. Lasagni, J.L. Ocaña, Fabrication of multi-scale periodic surface structures on Ti-6Al-4V by direct laser writing and direct laser interference patterning for modified wettability applications, Opt Lasers Eng 98 (2017) 134–142. https://doi.org/https://doi.org/10.1016/j.optlaseng.2017.06.017.

[102] A. Samanta, Q. Wang, S.K. Shaw, H. Ding, Nanostructuring of laser textured surface to achieve superhydrophobicity on engineering metal surface, J Laser Appl 31 (2019) 22515. https://doi.org/10.2351/1.5096148.

[103] L. Wang, Q.-D. Chen, X.-W. Cao, R. Buividas, X. Wang, S. Juodkazis, H.-B. Sun, Plasmonic nano-printing: large-area nanoscale energy deposition for efficient surface texturing, Light Sci Appl 6 (2017) e17112–e17112. https://doi.org/10.1038/lsa.2017.112.

[104] J. Bonse, S. Gräf, Maxwell Meets Marangoni—A Review of Theories on Laser-Induced Periodic Surface Structures, Laser Photon Rev 14 (2020) 2000215. https://doi.org/https://doi.org/10.1002/lpor.202000215.

[105] J.E. Sipe, J.F. Young, J.S. Preston, H.M. van Driel, Laser-induced periodic surface structure. I. Theory, Phys Rev B 27 (1983) 1141–1154. https://doi.org/10.1103/PhysRevB.27.1141.

[106] G. Giannuzzi, C. Gaudiuso, R. Di Mundo, L. Mirenghi, F. Fraggelakis, R. Kling, P.M. Lugarà, A. Ancona, Short and long term surface chemistry and wetting behaviour of stainless steel with 1D and 2D periodic structures induced by bursts of femtosecond laser pulses, Appl Surf Sci 494 (2019) 1055–1065. https://doi.org/https://doi.org/10.1016/j.apsusc.2019.07.126.

[107] Y. Zabila, M. Perzanowski, A. Dobrowolska, M. Kac, A. Polit, M. Marszalek, Direct Laser Interference Patterning: Theory and Application, Acta Physica Polonica Series a 115 (2009) 591–593. https://doi.org/10.12693/APhysPolA.115.591.

[108] A.I. Aguilar-Morales, S. Alamri, T. Kunze, A.F. Lasagni, Influence of processing parameters on surface texture homogeneity using Direct Laser Interference Patterning, Opt Laser Technol 107 (2018) 216–227. https://doi.org/https://doi.org/10.1016/j.optlastec.2018.05.044.

[109] B. Voisiat, C. Zwahr, A.F. Lasagni, Growth of regular micro-pillar arrays on steel by polarization-controlled laser interference patterning, Appl Surf Sci 471 (2019) 1065–1071. https://doi.org/https://doi.org/10.1016/j.apsusc.2018.12.083.

[110] V. Lang, T. Roch, A.F. Lasagni, High-Speed Surface Structuring of Polycarbonate Using Direct Laser Interference Patterning: Toward 1 m2 min−1 Fabrication Speed Barrier , Adv Eng Mater 18 (2016) 1342–1348. https://doi.org/https://doi.org/10.1002/adem.201600173.

[111] V. Vercillo, S. Tonnicchia, J.-M. Romano, A. García-Girón, A.I. Aguilar-Morales, S. Alamri, S.S. Dimov, T. Kunze, A.F. Lasagni, E. Bonaccurso, Design Rules for Laser-Treated Icephobic Metallic Surfaces for Aeronautic Applications, Adv Funct Mater 30 (2020) 1910268. https://doi.org/https://doi.org/10.1002/adfm.201910268.

[112] M.E.A. Mohamed, Pulsed Electric Fields for Food Processing Technology, in: A.H.A.E.E.-A.A. Eissa (Ed.), IntechOpen, Rijeka, 2012: p. Ch. 11. https://doi.org/10.5772/48678.

[113] Z. Liu, E. Esveld, J.-P. Vincken, M.E. Bruins, Pulsed Electric Field as an Alternative Pre-treatment for Drying to Enhance Polyphenol Extraction from Fresh Tea Leaves, Food Bioproc Tech 12 (2019) 183–192. https://doi.org/10.1007/s11947-018-2199-x.

[114] Q. Zhang, G. V Barbosa-Cánovas, B.G. Swanson, Engineering aspects of pulsed electric field pasteurization, J Food Eng 25 (1995) 261–281. https://doi.org/https://doi.org/10.1016/0260-8774(94)00030-D.

[115] T.J. Lewis, The electric conduction and strenth of pure liquids, High Voltage Technology, Alston LL (Ed), Oxford University Press, London, UK (1968) 111–120.

[116] K. Yogesh, Pulsed electric field processing of egg products: a review, J Food Sci Technol 53 (2016) 934–945. https://doi.org/10.1007/s13197-015-2061-3.

[117] B. Roodenburg, J. Morren, H.E. (Iekje) Berg, S.W.H. de Haan, Metal release in a stainless steel pulsed electric field (PEF) system: Part II. The treatment of

orange juice; related to legislation and treatment chamber lifetime, Innovative Food Science & Emerging Technologies 6 (2005) 337–345. https://doi.org/https://doi.org/10.1016/j.ifset.2005.04.004.

[118] B. Roodenburg, J. Morren, H.E. (Iekje) Berg, S.W.H. de Haan, Metal release in a stainless steel Pulsed Electric Field (PEF) system: Part I. Effect of different pulse shapes; theory and experimental method, Innovative Food Science & Emerging Technologies 6 (2005) 327–336. https://doi.org/https://doi.org/10.1016/j.ifset.2005.04.006.

[119] J. Morren, B. Roodenburg, S.W.H. de Haan, Electrochemical reactions and electrode corrosion in pulsed electric field (PEF) treatment chambers, Innovative Food Science & Emerging Technologies 4 (2003) 285–295. https://doi.org/https://doi.org/10.1016/S1466-8564(03)00041-9.

[120] G. Saulis, R. Rodaitė-Riševičienė, V.S. Dainauskaitė, R. Saulė, Electrochemical Processes During High-Voltage Electric Pulses and their Importance in Food Processing Technology, Advances in Food Biotechnology (2015) 575–592. https://doi.org/https://doi.org/10.1002/9781118864463.ch35.

[121] R. Rodaitė-Riševičienė, R. Saulė, V. Snitka, G. Saulis, Release of Iron Ions From the Stainless Steel Anode Occurring During High-Voltage Pulses and Its Consequences for Cell Electroporation Technology, IEEE Transactions on Plasma Science 42 (2014) 249–254. https://doi.org/10.1109/TPS.2013.2287499.

[122] B. Roodenburg, S.W.H. de Haan, L.B.J. van Boxtel, V. Hatt, P.C. Wouters, P. Coronel, J.A. Ferreira, Conductive plastic film electrodes for Pulsed Electric Field (PEF) treatment—A proof of principle, Innovative Food Science & Emerging Technologies 11 (2010) 274–282. https://doi.org/10.1016/j.ifset.2010.01.005.

[123] R.-H. Jung, H. Tsuchiya, S. Fujimoto, XPS characterization of passive films formed on Type 304 stainless steel in humid atmosphere, Corros Sci 58 (2012) 62–68. https://doi.org/https://doi.org/10.1016/j.corsci.2012.01.006.

[124] J.W. Pinder, G.H. Major, D.R. Baer, J. Terry, J.E. Whitten, J. Čechal, J.D. Crossman, A.J. Lizarbe, S. Jafari, C.D. Easton, J. Baltrusaitis, M.A. van Spronsen, M.R. Linford, Avoiding common errors in X-ray photoelectron spectroscopy data collection and analysis, and properly reporting instrument parameters, Applied Surface Science Advances 19 (2024) 100534. https://doi.org/https://doi.org/10.1016/j.apsadv.2023.100534.

[125] R. Keshavamurthy, C.S. Ramesh, G.S. Pradeep Kumar, V. Tambrallimath, Chapter 2 - Experimental investigation of tribocorrosion, in: A. Siddaiah, R. Ramachandran, P.L. Menezes (Eds.), Tribocorrosion, Academic Press, 2021: pp. 17–42. https://doi.org/https://doi.org/10.1016/B978-0-12-818916-0.00001-8.

[126] S.B. Arya, F.J. Joseph, Chapter 3 - Electrochemical methods in tribocorrosion, in: A. Siddaiah, R. Ramachandran, P.L. Menezes (Eds.), Tribocorrosion, Academic Press, 2021: pp. 43–77. https://doi.org/https://doi.org/10.1016/B978-0-12-818916-0.00003-1.

[127] S. Wang, J. Zhang, O. Gharbi, V. Vivier, M. Gao, M.E. Orazem, Electrochemical impedance spectroscopy, Nature Reviews Methods Primers 1 (2021) 41. https://doi.org/10.1038/s43586-021-00039-w.

[128] S.A. Weissman, N.G. Anderson, Design of Experiments (DoE) and Process Optimization. A Review of Recent Publications, Org Process Res Dev 19 (2015) 1605–1633. https://doi.org/10.1021/op500169m.

[129] H. Hermawan, D. Ramdan, J.R.P. Djuansjah, Metals for Biomedical Applications, in: R. Fazel-Rezai (Ed.), IntechOpen, Rijeka, 2011: p. Ch. 17. https://doi.org/10.5772/19033.

[130] Z. Cheng, Y. Xue, H. Ju, Chemical coloring on stainless steel by ultrasonic irradiation., Ultrason Sonochem 40 (2018) 558–566. https://doi.org/10.1016/j.ultsonch.2017.07.049.

[131] Y. Lu, X. Shi, Z. Huang, T. Li, M. Zhang, J. Czajkowski, T. Fabritius, M. Huttula, W. Cao, Nanosecond laser coloration on stainless steel surface, Sci Rep 7 (2017) 7092. https://doi.org/10.1038/s41598-017-07373-8.

[132] T. Hanawa, S. Hiromoto, A. Yamamoto, D. Kuroda, K. Asami, XPS Characterization of the Surface Oxide Film of 316L Stainless Steel Samples that were Located in Quasi-Biological Environments, Mater Trans 43 (2002) 3088–3092. https://doi.org/10.2320/matertrans.43.3088.

[133] G.T. Alliott, R.L. Higginson, G.D. Wilcox, Producing a thin coloured film on stainless steels – a review. Part 1: electrochemical processes, Transactions of the IMF 100 (2022) 128–137. https://doi.org/10.1080/00202967.2022.2035499.

[134] G.T. Alliott, R.L. Higginson, G.D. Wilcox, Producing a thin coloured film on stainless steels – a review. Part 2: non-electrochemical and laser processes,

Transactions of the IMF 101 (2023) 72–78. https://doi.org/10.1080/00202967.2022.2154495.

[135] R. Higginson, C. Jackson, E. Murrell, P. Exworthy, R. Mortimer, D. Worrall, G.D. Wilcox, Effect of thermally grown oxides on colour development of stainless steel, Materials at High Temperatures 32 (2015) 113–117. https://doi.org/10.1179/0960340914Z.00000000083.

[136] C. Esparza-Contro, G. Berthomé, G. Renou, F. Robaut, S. Coindeau, C. Vachey, J. Cambin, M. Mantel, L. Latu-Romain, Microstructures of titanium oxide thin films grown continuously on stainless steel wires by PVD in an inverted cylindrical magnetron: Towards an industrial process, Surf Coat Technol 389 (2020) 125643. https://doi.org/https://doi.org/10.1016/j.surfcoat.2020.125643.

[137] Ya.M. Andreeva, V.C. Luong, D.S. Lutoshina, O.S. Medvedev, V.Yu. Mikhailovskii, M.K. Moskvin, G. V Odintsova, V. V Romanov, N.N. Shchedrina, V.P. Veiko, Laser coloration of metals in visual art and design, Opt. Mater. Express 9 (2019) 1310–1319. https://doi.org/10.1364/OME.9.001310.

[138] A. Kristensen, J.K.W. Yang, S.I. Bozhevolnyi, S. Link, P. Nordlander, N.J. Halas, N.A. Mortensen, Plasmonic colour generation, Nat Rev Mater 2 (2016). https://doi.org/10.1038/natrevmats.2016.88.

[139] Y. Tamamura, G. Miyaji, Structural coloration of a stainless steel surface with homogeneous nanograting formed by femtosecond laser ablation, Opt. Mater. Express 9 (2019) 2902–2909. https://doi.org/10.1364/OME.9.002902.

[140] A.H.A. Lutey, L. Gemini, L. Romoli, G. Lazzini, F. Fuso, M. Faucon, R. Kling, Towards Laser-Textured Antibacterial Surfaces, Sci Rep 8 (2018) 10112. https://doi.org/10.1038/s41598-018-28454-2.

[141] S. Zhang, Y. Wang, H. Wang, L. Zhong, X. Zhu, G. Zhu, J. Qiu, X. Zeng, Laser Writing of Multilayer Structural Colors for Full-Color Marking on Steel, Adv Photonics Res 5 (2024) 2300157. https://doi.org/https://doi.org/10.1002/adpr.202300157.

[142] E. Chikarakara, P. Fitzpatrick, E. Moore, T. Levingstone, L. Grehan, C. Higginbotham, M. Vazquez, K. Bagga, S. Naher, D. Brabazon, In vitro fibroblast and pre-osteoblastic cellular responses on laser surface modified Ti–6Al–4V, Biomed Mater 10 (2014) 15007. https://doi.org/10.1088/1748-6041/10/1/015007.

[143] X. Li, Y. Guan, Theoretical fundamentals of short pulse laser–metal interaction: A review, Nanotechnology and Precision Engineering 3 (2020) 105–125. https://doi.org/https://doi.org/10.1016/j.npe.2020.08.001.

[144] A. Awasthi, D. Kumar, D. Marla, Understanding the role of oxide layers on color generation and surface characteristics in nanosecond laser color marking of stainless steel, Opt Laser Technol 171 (2024) 110469. https://doi.org/https://doi.org/10.1016/j.optlastec.2023.110469.

[145] F. Brihmat-Hamadi, E.H. Amara, L. Lavisse, J.M. Jouvard, E. Cicala, H. Kellou, Surface laser marking optimization using an experimental design approach, Applied Physics A 123 (2017) 230. https://doi.org/10.1007/s00339-017-0802-z.

[146] D.N. Antonov, A.A. Burtsev, O.Ya. Butkovskii, Coloration of a metal surface under pulsed laser irradiation, Technical Physics 59 (2014) 1503–1505. https://doi.org/10.1134/S1063784214100077.

[147] M.A. Kats, R. Blanchard, S. Ramanathan, F. Capasso, Thin-Film Interference in Lossy, Ultra-Thin Layers, Opt. Photon. News 25 (2014) 40–47. https://doi.org/10.1364/OPN.25.1.000040.

[148] H. Roozbahani, M. Alizadeh, H. Handroos, A. Salminen, Color Laser Marking: Repeatability, Stability and Resistance Against Mechanical, Chemical and Environmental Effects, IEEE Access 8 (2020) 214196–214208. https://doi.org/10.1109/ACCESS.2020.3040744.

[149] C.Y. Cui, X.G. Cui, X.D. Ren, M.J. Qi, J.D. Hu, Y.M. Wang, Surface oxidation phenomenon and mechanism of AISI 304 stainless steel induced by Nd:YAG pulsed laser, Appl Surf Sci 305 (2014) 817–824. https://doi.org/10.1016/j.apsusc.2014.04.025.

[150] Z.L. Li, H.Y. Zheng, K.M. Teh, Y.C. Liu, G.C. Lim, H.L. Seng, N.L. Yakovlev, Analysis of oxide formation induced by UV laser coloration of stainless steel, Appl Surf Sci 256 (2009) 1582–1588. https://doi.org/10.1016/j.apsusc.2009.09.025.

[151] R. Linggamm, M.M. Quazi, M. Ishak, M.H. Aiman, A.Q. Zafiuddin, A. Qaban, Formation of colours on SS304L stainless steel induced by laser colouring, IOP Conf Ser Mater Sci Eng 1078 (2021) 12015. https://doi.org/10.1088/1757-899X/1078/1/012015.

[152] A. Korakana, S. Korakana, N. Ulmek, A.K. Pagare, Analyzing the effect of the parameters of laser etching process influencing the corrosion resistance and

surface roughness of marine grade 316 stainless steel, Mater Today Proc 32 (2020) 452–462. https://doi.org/https://doi.org/10.1016/j.matpr.2020.02.130.

[153] N Cabrera, N F Mott, Theory of the oxidation of metals, Reports on Progress in Physics 12 (1949) 163. https://doi.org/10.1088/0034-4885/12/1/308.

[154] A. Atkinson, Transport processes during the growth of oxide films at elevated temperature, Rev Mod Phys 57 (1985) 437–470. https://doi.org/10.1103/RevModPhys.57.437.

[155] M. Tsuchiya, S.K.R.S. Sankaranarayanan, S. Ramanathan, Photon-assisted oxidation and oxide thin film synthesis: A review, Prog Mater Sci 54 (2009) 981–1057. https://doi.org/https://doi.org/10.1016/j.pmatsci.2009.04.003.

[156] L. Nánai, R. Vajtai, I. Kovács, I. Hevesi, On the kinetics of laser-light-induced oxidation constants of vanadium, Journal of the Less Common Metals 152 (1989) L23–L26. https://doi.org/https://doi.org/10.1016/0022-5088(89)90104-5.

[157] W. Pacquentin, N. Caron, R. Oltra, Nanosecond laser surface modification of AISI 304L stainless steel: Influence the beam overlap on pitting corrosion resistance, Appl Surf Sci 288 (2014) 34–39. https://doi.org/https://doi.org/10.1016/j.apsusc.2013.09.086.

[158] J. Bonse, S. Gräf, Maxwell Meets Marangoni—A Review of Theories on Laser-Induced Periodic Surface Structures, Laser Photon Rev 14 (2020) 2000215. https://doi.org/10.1002/lpor.202000215.

[159] Q. Yang, J.L. Luo, Effects of Hydrogen on Disorder of Passive Films and Pitting Susceptibility of Type 310 Stainless Steel, J Electrochem Soc 148 (2001) B29. https://doi.org/10.1149/1.1344529.

[160] Y. Deng, M. Wang, T. Tian, S. Lin, P. Xu, L. Zhou, C. Dai, Q. Hao, Y. Wu, Z. Zhai, Y. Zhu, G. Zhuang, Z. Dai, The Effect of Hexavalent Chromium on the Incidence and Mortality of Human Cancers: A Meta-Analysis Based on Published Epidemiological Cohort Studies., Front Oncol 9 (2019) 24. https://doi.org/10.3389/fonc.2019.00024.

[161] J.-G. Choi, L.T. Thompson, XPS study of as-prepared and reduced molybdenum oxides, Appl Surf Sci 93 (1996) 143–149. https://doi.org/https://doi.org/10.1016/0169-4332(95)00317-7.

[162] G. Savriama, F. Baillet, L. Barreau, C. Boulmer-Leborgne, N. Semmar, Optimization of diode pumped solid state ultraviolet laser dicing of silicon

carbide chips using design of experiment methodology, J Laser Appl 27 (2015) 32009. https://doi.org/10.2351/1.4919886.

[163] K.M. Łęcka, A.J. Antończak, B. Szubzda, M.R. Wójcik, B.D. Stępak, P. Szymczyk, M. Trzciński, M. Ozimek, K.M. Abramski, Effects of laser-induced oxidation on the corrosion resistance of AISI 304 stainless steel, J Laser Appl 28 (2016) 32009. https://doi.org/10.2351/1.4948726.

[164] P. Marcus, On some fundamental factors in the effect of alloying elements on passivation of alloys, Corros Sci 36 (1994) 2155–2158. https://doi.org/https://doi.org/10.1016/0010-938X(94)90013-2.

[165] J. Schanda, Colorimetry: Understanding the CIE System, Wiley, 2007. https://books.google.ie/books?id=uZadszSGe9MC.

[166] G.G. Lister, J.F. Waymouth, Light Sources, in: R.A.B.T.-E. of P.S. and T. (Third E. Meyers (Ed.), Academic Press, New York, 2003: pp. 557–595. https://doi.org/https://doi.org/10.1016/B0-12-227410-5/00378-1.

[167] K. Ji, H. Ju, J. Xun, Y. Su, K. Zhang, P. Liu, Y. Xue, Effect of hardening and sealing on color of chemically colored stainless steel., Sci Rep 10 (2020) 13561. https://doi.org/10.1038/s41598-020-70359-6.

[168] T. Jwad, S. Deng, H. Butt, S. Dimov, Laser induced single spot oxidation of titanium, Appl Surf Sci 387 (2016) 617–624. https://doi.org/https://doi.org/10.1016/j.apsusc.2016.06.136.

[169] F.S. Shieu, M.J. Deng, S.H. Lin, Microstructure and corrosion resistance of a type 316l stainless steel, Corros Sci 40 (1998) 1267–1279. https://doi.org/https://doi.org/10.1016/S0010-938X(97)00143-1.

[170] M. Ahmed Obeidi, E. McCarthy, S.I. Ubani, I. Ul Ahad, D. Brabazon, Effect of Surface Roughness on CO2 Laser Absorption by 316L Stainless Steel and Aluminum, Mater Perform Charact 8 (2019) 1167–1177. https://doi.org/10.1520/MPC20180091.

[171] W. Pacquentin, N. Caron, R. Oltra, Nanosecond laser surface modification of AISI 304L stainless steel: Influence the beam overlap on pitting corrosion resistance, Appl Surf Sci 288 (2014) 34–39. https://doi.org/https://doi.org/10.1016/j.apsusc.2013.09.086.

[172] E. Chikarakara, S. Naher, D. Brabazon, Spinodal decomposition in AISI 316L stainless steel via high-speed laser remelting, Appl Surf Sci 302 (2014) 318–321. https://doi.org/https://doi.org/10.1016/j.apsusc.2013.10.099.

[173] A. Dudek, B. Lisiecka, N. Radek, Ł.J. Orman, J. Pietraszek, Laser Surface Alloying of Sintered Stainless Steel, Materials 15 (2022). https://doi.org/10.3390/ma15176061.

[174] J.D. Majumdar, A. Kumar, S. Pityana, I. Manna, Laser Surface Melting of AISI 316L Stainless Steel for Bio-implant Application, Proceedings of the National Academy of Sciences, India Section A: Physical Sciences 88 (2018) 387–403. https://doi.org/10.1007/s40010-018-0524-4.

[175] K. Kiasaleh, Gaussian beam characterization for laser beam propagation through translucent, multi-layer medium with random indices of refraction, in: 2015 IEEE International Conference on Space Optical Systems and Applications (ICSOS), 2015: pp. 1–6. https://doi.org/10.1109/ICSOS.2015.7425082.

[176] P. Marcus, On some fundamental factors in the effect of alloying elements on passivation of alloys, Corros Sci 36 (1994) 2155–2158. https://doi.org/https://doi.org/10.1016/0010-938X(94)90013-2.

[177] Q. Zhu, W. Sun, Y. Yoo, X. Zhang, N. Hunter, A. Mao, N. Li, X. Huang, P. Fan, X. Wang, B. Cui, Y. Lu, Enhance corrosion resistance of 304 stainless steel using nanosecond pulsed laser surface processing, Surfaces and Interfaces 42 (2023) 103479. https://doi.org/https://doi.org/10.1016/j.surfin.2023.103479.

[178] R.K. Wild, Ion sputter rates of Cr□Mn□Fe spinel oxides, Surface and Interface Analysis 14 (1989) 239–244. https://doi.org/https://doi.org/10.1002/sia.740140505.

[179] M.P. Seah, D. David, J.A. Davies, T.E. Jackman, C. Jeynes, C. Ortega, P.M. Read, C.J. Sofield, G. Weber, An intercomparison of absolute measurements of the oxygen and tantalum thickness of tantalum pentoxide reference materials, BCR 261, by six laboratories, Nucl Instrum Methods Phys Res B 30 (1988) 140–151. https://doi.org/https://doi.org/10.1016/0168-583X(88)90110-3.

[180] Q. Yang, J.L. Luo, Effects of Hydrogen on Disorder of Passive Films and Pitting Susceptibility of Type 310 Stainless Steel, J Electrochem Soc 148 (2001) B29. https://doi.org/10.1149/1.1344529.

[181] Y. Gui, X.B. Meng, Z.J. Zheng, Y. Gao, Critical temperature determination of detectable Cr diffusion enhancement by nanostructure through structural evolution analysis of the oxide films at 25–450°C on 304 stainless steel, Appl Surf Sci 419 (2017) 512–521. https://doi.org/https://doi.org/10.1016/j.apsusc.2017.04.133.

[182] R. Kirchheim, Growth kinetics of passive films, Electrochim Acta 32 (1987) 1619–1629. https://doi.org/https://doi.org/10.1016/0013-4686(87)90015-6.

[183] R. Ovarfort, Critical pitting temperature measurements of stainless steels with an improved electrochemical method, Corros Sci 29 (1989) 987–993. https://doi.org/https://doi.org/10.1016/0010-938X(89)90088-7.

[184] G.S. Frankel, Pitting Corrosion of Metals: A Review of the Critical Factors, J Electrochem Soc 145 (1998) 2186. https://doi.org/10.1149/1.1838615.

[185] R.C. Newman, 2001 W.R. Whitney Award Lecture: Understanding the Corrosion of Stainless Steel, Corrosion 57 (2001) 1030–1041. https://doi.org/10.5006/1.3281676.

[186] G. Song, Transpassivation of Fe–Cr–Ni stainless steels, Corros Sci 47 (2005) 1953–1987. https://doi.org/https://doi.org/10.1016/j.corsci.2004.09.007.

[187] R.A. Buchanan, E.E. Stansbury, 4 - Electrochemical Corrosion, in: M.B.T.-H. of E.D. of M. (Second E. Kutz (Ed.), William Andrew Publishing, Oxford, 2012: pp. 87–125. https://doi.org/https://doi.org/10.1016/B978-1-4377-3455-3.00004-3.

[188] K. Darowicki, S. Krakowiak, P. Ślepski, Evaluation of pitting corrosion by means of dynamic electrochemical impedance spectroscopy, Electrochim Acta 49 (2004) 2909–2918. https://doi.org/https://doi.org/10.1016/j.electacta.2004.01.070.

[189] C.-O.A. Olsson, The influence of nitrogen and molybdenum on passive films formed on the austenoferritic stainless steel 2205 studied by AES and XPS, Corros Sci 37 (1995) 467–479. https://doi.org/https://doi.org/10.1016/0010-938X(94)00148-Y.

[190] I. Olefjord, L. Wegrelius, Surface analysis of passive state, Corros Sci 31 (1990) 89–98. https://doi.org/https://doi.org/10.1016/0010-938X(90)90095-M.

[191] E. De Vito, P. Marcus, XPS study of passive films formed on molybdenum-implanted austenitic stainless steels, Surface and Interface Analysis 19 (1992) 403–408. https://doi.org/https://doi.org/10.1002/sia.740190175.

[192] M. Tsuchiya, S.K.R.S. Sankaranarayanan, S. Ramanathan, Photon-assisted oxidation and oxide thin film synthesis: A review, Prog Mater Sci 54 (2009) 981–1057. https://doi.org/https://doi.org/10.1016/j.pmatsci.2009.04.003.

[193] M.C.C. Monu, Y. Afkham, J.C. Chekotu, E.J. Ekoi, H. Gu, C. Teng, J. Ginn, J. Gaughran, D. Brabazon, Bi-directional Scan Pattern Effects on Residual Stresses

and Distortion in As-built Nitinol Parts: A Trend Analysis Simulation Study, Integr Mater Manuf Innov 12 (2023) 52–69. https://doi.org/10.1007/s40192-023-00292-9.

[194] B. Szubzda, A. Antończak, P. Kozioł, Ł. Łazarek, B. Stępak, K. Łęcka, A. Szmaja, M. Ozimek, Corrosion resistance of the AISI 304, 316 and 321 stainless steel surfaces modified by laser, IOP Conf Ser Mater Sci Eng 113 (2016) 12017. https://doi.org/10.1088/1757-899X/113/1/012017.

[195] R.M. Aadil, A.A. Khalil, A. Rehman, A. Khalid, M. Inam-ur-Raheem, A. Karim, A.A. Gill, M. Abid, M.T. Afraz, Assessing the impact of ultra-sonication and thermo-ultrasound on antioxidant indices and polyphenolic profile of apple-grape juice blend, J Food Process Preserv 44 (2020). https://doi.org/10.1111/jfpp.14406.

[196] R.M. Aadil, X. Zeng, Z. Han, A. Sahar, A.A. Khalil, U.U. Rahman, M. Khan, T. Mehmood, Combined effects of pulsed electric field and ultrasound on bioactive compounds and microbial quality of grapefruit juice, J Food Process Preserv 42 (2018) e13507. https://doi.org/10.1111/jfpp.13507.

[197] R.M. Aadil, X.-A. Zeng, A. Ali, F. Zeng, M.A. Farooq, Z. Han, S. Khalid, S. Jabbar, Influence of different pulsed electric field strengths on the quality of the grapefruit juice, Int J Food Sci Technol 50 (2015) 2290–2296. https://doi.org/10.1111/ijfs.12891.

[198] X. Li, M. Farid, A review on recent development in non-conventional food sterilization technologies, J Food Eng 182 (2016) 33–45. https://doi.org/10.1016/j.jfoodeng.2016.02.026.

[199] U. Tylewicz, How does pulsed electric field work?, in: Pulsed Electric Fields to Obtain Healthier and Sustainable Food for Tomorrow, Elsevier, 2020: pp. 3–21. https://doi.org/10.1016/B978-0-12-816402-0.00001-X.

[200] T.Y. Tsong, Electroporation of cell membranes, Biophys J 60 (1991) 297–306. https://doi.org/10.1016/S0006-3495(91)82054-9.

[201] D. Gášková, K. Sigler, B. Janderová, J. Plášek, Effect of high-voltage electric pulses on yeast cells: factors influencing the killing efficiency, Bioelectrochemistry and Bioenergetics 39 (1996) 195–202. https://doi.org/10.1016/0302-4598(95)01892-1.

[202] A. Sale, W. Hamilton, Effects of high electric fields on microorganismsI. Killing of bacteria and yeasts, Biochimica et Biophysica Acta (BBA) - General Subjects 148 (1967) 781–788. https://doi.org/10.1016/0304-4165(67)90052-9.

[203] M. Gavahian, Y.-H. Chu, S. Sastry, Extraction from Food and Natural Products by Moderate Electric Field: Mechanisms, Benefits, and Potential Industrial Applications, Compr Rev Food Sci Food Saf 17 (2018) 1040–1052. https://doi.org/10.1111/1541-4337.12362.

[204] W. Zhao, R. Yang, R. Lu, M. Wang, P. Qian, W. Yang, Effect of PEF on microbial inactivation and physical–chemical properties of green tea extracts, LWT - Food Science and Technology 41 (2008) 425–431. https://doi.org/10.1016/j.lwt.2007.03.020.

[205] C. Zhang, X. Lyu, R.N. Arshad, R.M. Aadil, Y. Tong, W. Zhao, R. Yang, Pulsed electric field as a promising technology for solid foods processing: A review, Food Chem 403 (2023) 134367. https://doi.org/10.1016/j.foodchem.2022.134367.

[206] G. Pataro, G. Ferrari, Electrochemical Reactions in Pulsed Electric Fields Treatment, in: 2022: pp. 143–166. https://doi.org/10.1007/978-3-030-70586-2_4.

[207] K. Matra, P. Buppan, B. Techaumnat, Analytical and Experimental Studies on the Application of a Series of Treatment Chambers for Escherichia coli Inactivation by Pulsed Electric Fields, Applied Sciences 10 (2020) 4071. https://doi.org/10.3390/app10124071.

[208] A. Gad, S.H. Jayaram, M. Pritzker, Performance of Electrode Materials During Food Processing by Pulsed Electric Fields, IEEE Transactions on Plasma Science 42 (2014) 3161–3166. https://doi.org/10.1109/TPS.2014.2312711.

[209] M.M. Góngora-Nieto, D.R. Sepúlveda, P. Pedrow, G.V. Barbosa-Cánovas, B.G. Swanson, Food Processing by Pulsed Electric Fields: Treatment Delivery, Inactivation Level, and Regulatory Aspects, LWT - Food Science and Technology 35 (2002) 375–388. https://doi.org/10.1006/fstl.2001.0880.

[210] T. Tanino, M. Hirosawa, R. Moteki, M. Matsui, T. Ohshima, Engineering of pulsed electric field treatment using carbon materials as electrode and application to pasteurization of sake, J Electrostat 104 (2020) 103424. https://doi.org/10.1016/j.elstat.2020.103424.

[211] C.P. Samaranayake, S.K. Sastry, Electrode and pH effects on electrochemical reactions during ohmic heating, Journal of Electroanalytical Chemistry 577 (2005) 125–135. https://doi.org/10.1016/j.jelechem.2004.11.026.

[212] T. Kotnik, D. Miklavčič, L.M. Mir, Cell membrane electropermeabilization by symmetrical bipolar rectangular pulses, Bioelectrochemistry 54 (2001) 91–95. https://doi.org/10.1016/S1567-5394(01)00115-3.

[213] K. Nowosad, M. Sujka, U. Pankiewicz, R. Kowalski, The application of PEF technology in food processing and human nutrition., J Food Sci Technol 58 (2021) 397–411. https://doi.org/10.1007/s13197-020-04512-4.

[214] N. Meneses, H. Jaeger, D. Knorr, pH-changes during pulsed electric field treatments — Numerical simulation and in situ impact on polyphenoloxidase inactivation, Innovative Food Science & Emerging Technologies 12 (2011) 499–504. https://doi.org/10.1016/j.ifset.2011.07.001.

[215] B. Roodenburg, S.W.H. de Haan, L.B.J. van Boxtel, V. Hatt, P.C. Wouters, P. Coronel, J.A. Ferreira, Conductive plastic film electrodes for Pulsed Electric Field (PEF) treatment—A proof of principle, Innovative Food Science & Emerging Technologies 11 (2010) 274–282. https://doi.org/10.1016/j.ifset.2010.01.005.

[216] M. Swayne, G. Perumal, D. Brabazon, Mechanism for Control of Laser-Induced Stainless Steel Oxidation, Adv Mater Interfaces 11 (2024) 2300991. https://doi.org/10.1002/admi.202300991.

[217] A.L. Schulz, Capacitors: Theory, Types and Applications, Nova Science Publishers, Incorporated, 2010.

[218] Q.Y. Chen, J. Brocato, F. Laulicht, M. Costa, Essential and Non-Essential Metals, Molecular and Integrative Toxicology, (2017).

[219] G. Genchi, A. Carocci, G. Lauria, M.S. Sinicropi, A. Catalano, Nickel: Human Health and Environmental Toxicology., Int J Environ Res Public Health 17 (2020). https://doi.org/10.3390/ijerph17030679.

[220] Y. Deng, M. Wang, T. Tian, S. Lin, P. Xu, L. Zhou, C. Dai, Q. Hao, Y. Wu, Z. Zhai, Y. Zhu, G. Zhuang, Z. Dai, The Effect of Hexavalent Chromium on the Incidence and Mortality of Human Cancers: A Meta-Analysis Based on Published Epidemiological Cohort Studies., Front Oncol 9 (2019) 24. https://doi.org/10.3389/fonc.2019.00024.

[221] S. Wilbur, H. Abadin, M. Fay, D. Yu, B. Tencza, L. Ingerman, J. Klotzbach, S. James, Toxicological Profile for Chromium, Atlanta (GA), 2012.

[222] P. Trumbo, A.A. Yates, S. Schlicker, M. Poos, Dietary reference intakes: vitamin A, vitamin K, arsenic, boron, chromium, copper, iodine, iron, manganese, molybdenum, nickel, silicon, vanadium, and zinc., J Am Diet Assoc 101 (2001) 294–301. https://doi.org/10.1016/S0002-8223(01)00078-5.

[223] S.G. Capar, W.C. Cunningham, Element and Radionuclide Concentrations in Food: FDA Total Diet Study 1991–1996, J AOAC Int 83 (2000) 157–177. https://doi.org/10.1093/jaoac/83.1.157.

[224] V. Lobo, A. Patil, A. Phatak, N. Chandra, Free radicals, antioxidants and functional foods: Impact on human health., Pharmacogn Rev 4 (2010) 118–126. https://doi.org/10.4103/0973-7847.70902.

[225] M.C. Biesinger, C. Brown, J.R. Mycroft, R.D. Davidson, N.S. McIntyre, X-ray photoelectron spectroscopy studies of chromium compounds, Surface and Interface Analysis 36 (2004) 1550–1563. https://doi.org/https://doi.org/10.1002/sia.1983.

Corrections

The peak initially labelled as chromium (VI) in the XPS data presented in Chapters 3 to 5 was incorrectly assigned. This feature should instead be attributed to a combination of $Cr(OH)_3$ and ferrite-type duplex oxides, most likely $FeCr_2O_4$, as evidenced by [225].

Chapter 6 Supplementary information – Femtosecond laser texturing.

S.1 Method

S.1.1 Sample Prep:

Commercial 316L type stainless steel was choosing due to its initial high corrosion potential and high use in industry. The steel sheets were cut into 100mm diameter disks using an industrial used CO2 CW laser. All burs were removed using a low grit grinding paper.

S.1.2 Laser processing:

The 316L sample was cleaned with acetone and ethanol and sonicated for 15 minutes to remove any contaminants from the surface then allowed to dry for 5 minutes on the laser stage. The laser system used consisted of a 5 W max power 1030 nm average wavelength, solid state diode laser > 400fs (Origami XP NKT photonics). A 3D scanning galvanometer (Raylase focus shifter 15) and the sample position was controlled by the (225 Areotech 4 axis stage).The beam was focused on the surface of the samples which lies 219 mm below the galvanometer leans this produces a spot size of 50 µm. Weld mark 4 software is used to control the galvanometer. A 3^4 factor design was used to then investigate the effect of laser processing parameter on the channel width, channel depth and channel area of single line ablation tracks. With the varying parameter being scans speed, power, frequency and # of passes. The full list of DOE parameters can be seen in Table 5-7.

Parameter	Level 1	Level 2	Level 3
Frequency (kHz)	100	200	300
Power (W)	3	3.5	4
# Passes	1	11	21
Scan Speed (mm/s)	0.5	2.75	5

Table 5-7 : Femtosecond DOE laser parameters

S.1.3 Optical measurements

After laser processing the samples where cross-sectioned along the laser track using a precision saw, following this the sample were ground with 2000 grit sand paper to expose the cross section of the laser track. The samples where then mounted on their side and optical images where taking using the Olympus BX43 microscope at 10, 20 and 50x zoom. The image data of channel depth, channel width and channel area where then extracted using image J software.

S.2 Results and discussion

S.2.1 Channel Depth

From ANOVA analysis the Channel depth is significant to all the initial parameters expect scan speed. The ANOVA results can be seen in Table 5-8. Some significant two-factor interactions also occur with a most influence being the strong negative influence of the frequency - #passes interaction. The large positive influence of the #of passes can be explained by the increases time for ablation to occur each pass allows for an increasing amount of material removal. As can be seen in **Figure 5-10** as the channel depth is increase the channel width starts to taper in this is due to the focus point position being fixed throughout the entire run. This would cause a broadening of the spot size at the impact point of the substrate as the depth increase reducing the peak power of the pulse decreasing the ablation spot size. The frequency has a negative influence on the channel depth; this is due to the lower frequencies having high pulse power allowing for increased ablation per pulse.

Source	Sum of Squares	df	Mean Square	F Value	p-value Prob > F
Model	1133.81	9	126.00	198.71	< 0.0001
A-Frequency	284.54	1	284.57	448.68	< 0.0001
B-Power	31.65	1	31.65	49.88	< 0.0001
C-#Passes	664.57	1	664.48	1048.09	< 0.0001
D-Scan Speed	0.94	1	0.94	1.48	0.2270
AC	103.43	1	103.43	163.14	< 0.0001
AD	4.78	1	4.79	7.55	0.0075
BC	6.18	1	6.19	9.75	0.0025
CD	12.71	1	12.72	20.06	< 0.0001
C^2	25.21	1	25.22	39.77	< 0.0001

Table 5-8: ANOVA model with the results and parametric terms for channel depth of DOE.

A stepwise quadratic model was used to describe the channel depth; this model has a high correlation with a R^2 value of 0.9587 with an adequacy precision of 55.769. Since this ration is > 4, this means that the current design can be used to navigate the design space. The equation was used to describe the model. Figure 5-10 represents the response surface plots for channel depth.

Sqrt(Channel Depth) = +4.84985
-8.76400E-003 * Frequency
+0.61853 *Power
+0.71636 * #Passes
-0.092269 * Scan Speed
-1.69502E-003 * Frequency * #Passes
+1.62096E-003 * Frequency * Scan Speed
+0.082907 * Power * #Passes
-0.026415 * #Passes * Scan Speed
-0.011095 * $\#Passes^2$ **(S-1)**

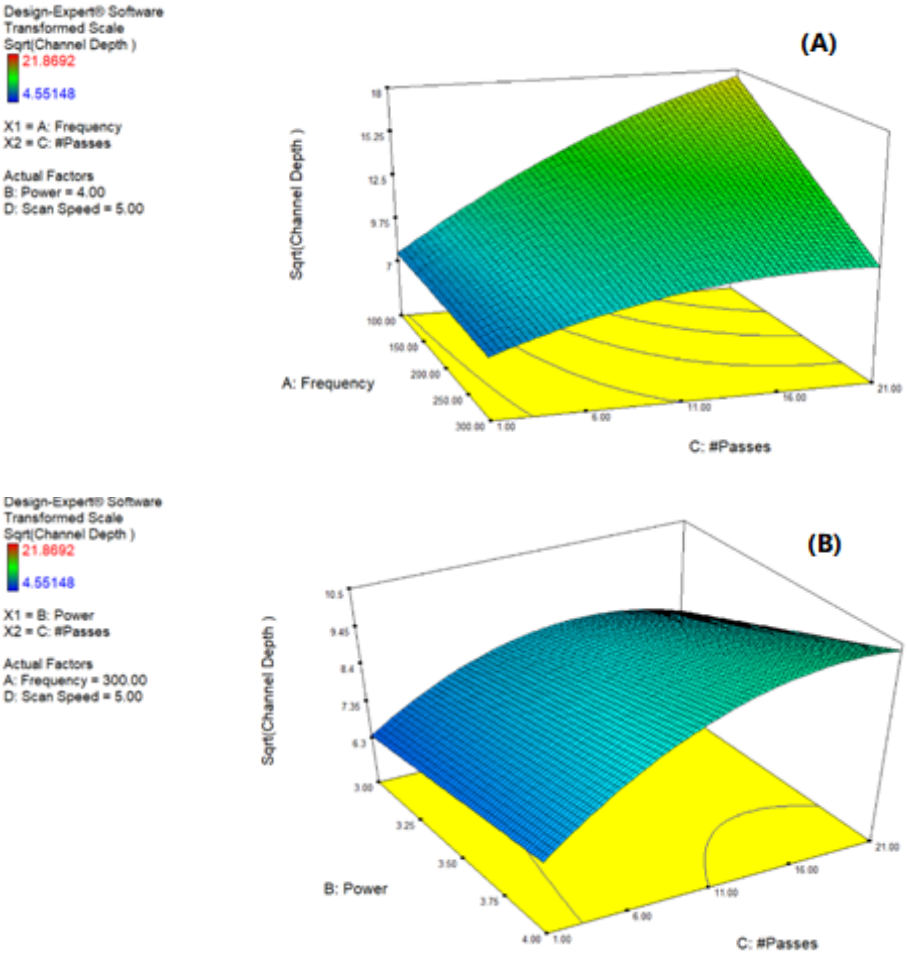

Figure 5-10: Response surfaces for channel area shown for (a) # Passes vs frequency and (b) Power vs #passes.

S.2.2 Channel width

The channel widths model has a lower correlation with a R^2 value of 0.5735 compared to channel depth. This is due to the fixed spot size of the laser at 50 microns. Also, at certain scan speed the laser track beings to wobble in a sine wave fashion this causes a broadening of the channel width and the formation of a W shaped channel. This can be seen in Figure 5-12 below. From the ANOVA analysis, it can be seen like the channel depth that all the individual factors are significant except scan speed. This is due to the wobble track seen at middle scan speeds.

Source	Sum of Squares	df	Mean Square	F Value	p-value Prob > F
Model	1.607E-07	7	2.29572E-08	15.30389884	< 0.0001
A-Frequency	1.06782E-07	1	1.06782E-07	71.18363781	< 0.0001
B-Power	2.3638E-08	1	2.3638E-08	15.75779498	0.0002
C-#Passes	5.02288E-09	1	5.02288E-09	3.348395004	0.0710
D-Scan Speed	2.64469E-09	1	2.64469E-09	1.763029036	0.1881
AB	8.43606E-09	1	8.43606E-09	5.623717322	0.0202
AD	5.26213E-09	1	5.26213E-09	3.507886258	0.0648
B^2	8.91475E-09	1	8.91475E-09	5.942831463	0.0170

Table 5-9: ANOVA model with the results and parametric terms for channel width of DOE.

An increase in both # passes and power causing a reduction in the channel width this could be cause but the effect of phase explosion at higher power. This can cause more of the ablated material to build up on the entrance to the channel narrowing the channel width. Frequency cause a slight positive influence, this is due to the reduced material ablation allowing less material to build to accumulate at the entrance. Equation (S-2) show the used to describe the relation.

$$\begin{aligned}(\text{Channel Width})^{-2.28} &= +1.01463\text{E-}003 \\ &+1.36848\text{E-}006 * \text{Frequency} \\ &-5.64755\text{E-}004 * \text{Power} \\ &-9.64449\text{E-}007 * \#\text{Passes} \\ &-7.63640\text{E-}006 * \text{Scan Speed} \\ &-3.06160\text{E-}007 * \text{Frequency} * \text{Power} \\ &+5.37337\text{E-}008 * \text{Frequency} * \text{Scan Speed} \\ &+8.34489\text{E-}005 * \text{Power}^2 \end{aligned} \quad \text{(S-2)}$$

S.2.3 Channel area

Channel Area reacts in a similar manner to channel depth, with only scan speed not being significant. In this case, frequency and number of passes are dominate factor with # of passes having a positive influence and frequency a negative. The R^2 value is 0.9163, which is slightly lower than channel depth.

Source	Sum of Squares	df	Mean Square	F Value	p-value Prob > F
Model	35.39017999	9	3.932242221	93.68384647	< 0.0001
A-Frequency	13.99004423	1	13.99004423	333.3063127	< 0.0001
B-Power	2.012122538	1	2.012122538	47.93788589	< 0.0001
C-#Passes	15.18986989	1	15.18986989	361.8916024	< 0.0001
D-Scan Speed	0.007453183	1	0.007453183	0.177568631	0.6746
AC	0.395341007	1	0.395341007	9.418816076	0.0030
CD	0.912790384	1	0.912790384	21.7468074	< 0.0001
B^2	0.215279798	1	0.215279798	5.12894131	0.0263
C^2	2.456362527	1	2.456362527	58.52169751	< 0.0001
D^2	0.149444403	1	0.149444403	3.56044357	0.0629

Table 5-10: ANOVA model with the results and parametric terms for channel area of DOE.

In some of the higher depth channel there is a recloser of the channel, this could be due to the ablated material being ejected into the channel and building up on the side of the channel causing a closer of the channel. The formula used to describe the model is seen in equation (S.3)

$$
\begin{aligned}
\ln(\text{Channel Area}) = {} & +1.16035 && -3.93721\text{E-}003 * \text{Frequency} \\
& +3.29499 && * \text{Power} \\
& +0.17066 && * \#\text{Passes} \\
& -0.021413 && * \text{Scan Speed} \\
& -1.04794\text{E-}004 && * \text{Frequency} * \#\text{Passes} \\
& -7.07704\text{E-}003 && * \#\text{Passes} * \text{Scan Speed} \\
& -0.41556 && * \text{Power}^2 \\
& -3.50929\text{E-}003 && * \#\text{Passes}^2 \\
& +0.017098 && * \text{Scan Speed}^2 \qquad \text{(S-3)}
\end{aligned}
$$

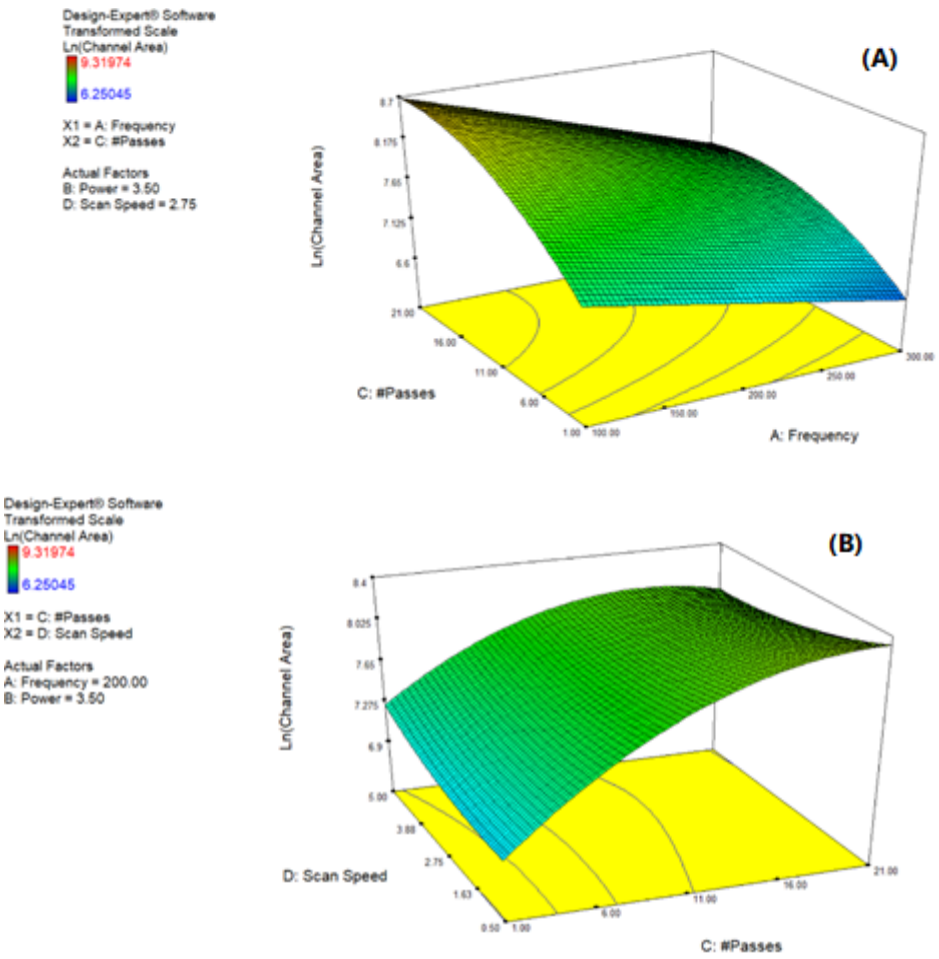

Figure 5-11: Response surfaces for channel area shown for (A) # passes vs Frequency and (B) Scan speed vs #Passes.

5.2.4 Optical Microscopy

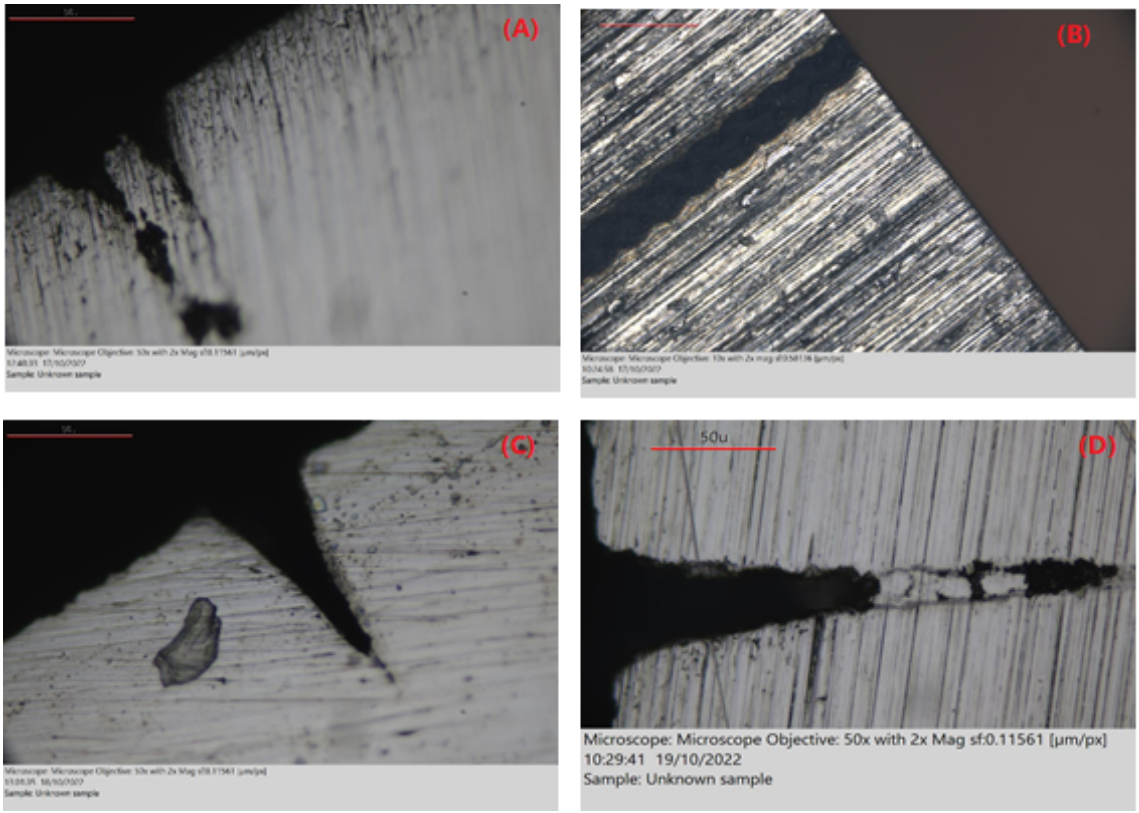

Figure 5-12: Laser ablated Tracks (a) w shape channel produced at 1 pass, 100Khz, 4w and 2.75mm/s. (b) Top View of W channel a, (C) V shaped channel produced at 11 passes, 300Khz, 4W and 2.75mm/s, (D) V shaped channel produced at 22 passes, 100kHz, 4W, 5mm/s.

Paper 1 Supplemental information

Molybdenum Final Equation in Terms of Actual Factors

Mo	=
+58.36	
-0.33	Scan Speed
-2.78	Repetition Rate
+0.0026	Scan Speed * Power
+0.071	Repetition Rate * Power
-0.0070	Power^2
+2.70E-06	Scan Speed^2 * Power
-0.00040	Repetition Rate * Power^2

ANOVA for Reduced Cubic model of Mo

Source	***Sum of Squares***	***df***	***Mean Square***	***F-value***	***p-value***	
Model	10568.89	7	1509.84	25.57	< 0.0001	significant
A-Scan Speed	1927.48	1	1927.48	32.64	< 0.0001	
B-Repetition Rate	2044.52	1	2044.52	34.62	< 0.0001	
AC	1694.02	1	1694.02	28.69	< 0.0001	
BC	330.74	1	330.74	5.60	0.0206	
C^2	3937.54	1	3937.54	66.67	< 0.0001	
A^2C	525.05	1	525.05	8.89	0.0039	
BC^2	938.20	1	938.20	15.89	0.0002	
Residual	4252.02	72	59.06			
Lack of Fit	1562.67	19	82.25	1.62	0.0851	not significant
Pure Error	2689.35	53	50.74			
Cor Total	14820.91	79				

Table 5-11: Molybdenum ANOVA analysis

Chromium

Final Equation in Terms of Actual Factors

Cr	=
-498.25	
+9.91	Repetition Rate
+11.90	Power
+0.0071	Scan Speed * Power
-0.25	Repetition Rate * Power
-0.064	Power^2
-0.000076	Scan Speed * Power^2
+0.0015	Repetition Rate * Power^2

ANOVA for Reduced Cubic model

Source	*Sum of Squares*	*df*	*Mean Square*	*F-value*	*p-value*	
Model	16386.02	7	2340.86	53.17	< 0.0001	significant
B-Repetition Rate	1454.17	1	1454.17	33.03	< 0.0001	
C-Power	706.83	1	706.83	16.06	0.0001	
AC	4578.26	1	4578.26	104.00	< 0.0001	
BC	1008.11	1	1008.11	22.90	< 0.0001	
C^2	4789.90	1	4789.90	108.81	< 0.0001	
AC^2	3597.88	1	3597.88	81.73	< 0.0001	
BC^2	1622.52	1	1622.52	36.86	< 0.0001	
Residual	3213.62	73	44.02			
Lack of Fit	833.75	19	43.88	0.9957	0.4804	not significant
Pure Error	2379.87	54	44.07			
Cor Total	19599.63	80				

Table 5-12: Chromium ANOVA analysis

Iron

Final Equation in Terms of Actual Factors

Fe	=
+84.38	
-0.32	Scan Speed
-0.27	Power
+0.015	Scan Speed * Power
-0.013	Repetition Rate * Power
-0.0019	Scan Speed²
+0.000020	Scan Speed² * Power
-0.00012	Scan Speed * Power²
+0.00012	Repetition Rate * Power²

ANOVA for Reduced Cubic model

Source	Sum of Squares	df	Mean Square	F-value	p-value	
Model	4619.95	8	577.49	20.21	< 0.0001	significant
A-Scan Speed	477.02	1	477.02	16.69	0.0001	
C-Power	178.69	1	178.69	6.25	0.0147	
AC	702.48	1	702.48	24.58	< 0.0001	
BC	186.20	1	186.20	6.52	0.0128	
A^2	128.22	1	128.22	4.49	0.0376	
A^2C	199.33	1	199.33	6.97	0.0101	
AC^2	818.26	1	818.26	28.63	< 0.0001	
BC^2	719.23	1	719.23	25.17	< 0.0001	
Residual	2057.70	72	28.58			
Lack of Fit	531.64	18	29.54	1.05	0.4291	not significant
Pure Error	1526.06	54	28.26			
Cor Total	6677.64	80				

Table 5-13 - Iron ANOVA analysis

RUN	Scan Speed	Frequency	Power	Fe	Fe (error)	Cr	Cr (error)	O	O (error)	Mo	Mo (error)
1	50	60	60	10.79	0.53	1.94	0.24	80.43	1.07	6.84	0.35
2	150	60	60	12.18	1.97	6.47	1.15	79.33	1.83	2.02	0.25
3	250	60	60	6.45	0.58	8.31	1.04	84.52	0.85	0.72	0.10
4	50	80	60	9.02	1.38	2.45	0.15	82.46	2.58	6.07	1.15
5	150	80	60	8.41	0.48	5.94	0.85	84.36	1.30	1.28	0.30
6	250	80	60	4.79	0.57	9.01	0.07	85.50	0.46	0.70	0.19
7	50	100	60	7.14	0.69	4.30	1.25	83.63	2.31	4.93	1.87
8	150	100	60	5.77	0.89	7.44	1.28	85.71	1.43	1.08	0.39
9	250	100	60	4.23	0.24	8.70	0.24	86.27	0.50	0.80	0.42
10	50	60	80	9.51	1.35	6.25	1.05	81.88	3.11	2.36	1.03
11	150	60	80	11.36	0.09	6.66	0.83	78.34	0.19	3.64	1.09
12	250	60	80	10.79	0.66	4.98	1.04	81.67	1.43	2.56	0.20
13	50	80	80	11.06	0.34	4.18	0.58	75.75	1.24	9.00	1.51
14	150	80	80	12.24	1.25	2.33	0.28	77.40	2.14	8.03	1.16
15	250	80	80	12.90	0.52	3.28	0.37	76.03	2.45	7.80	3.28
16	50	100	80	10.47	0.31	2.35	0.53	76.30	0.98	10.88	1.02
17	150	100	80	12.39	0.36	3.07	0.80	75.87	0.44	8.67	0.87
18	250	100	80	12.96	0.26	3.32	0.09	78.18	0.63	5.54	0.83
19	50	60	100	12.08	0.45	6.66	0.45	79.90	0.30	1.36	0.44
20	150	60	100	12.97	1.14	7.28	0.26	78.72	1.15	1.04	0.17
21	250	60	100	12.00	0.55	6.83	0.90	79.61	0.49	1.56	0.43
22	50	80	100	11.56	0.54	8.09	0.50	78.33	0.89	2.02	0.10
23	150	80	100	11.98	0.47	7.31	0.35	77.61	2.31	3.10	1.51
24	250	80	100	12.03	0.40	6.20	0.55	80.13	0.98	1.65	0.33
25	50	100	100	11.16	0.61	5.91	0.87	79.32	0.99	3.60	1.16
26	150	100	100	11.50	0.80	6.03	0.38	79.66	1.11	2.81	1.17
27	250	100	100	11.74	0.13	5.70	1.70	78.86	0.66	3.69	1.31

Table S.14 - XPS results table showing all compositions and error bars

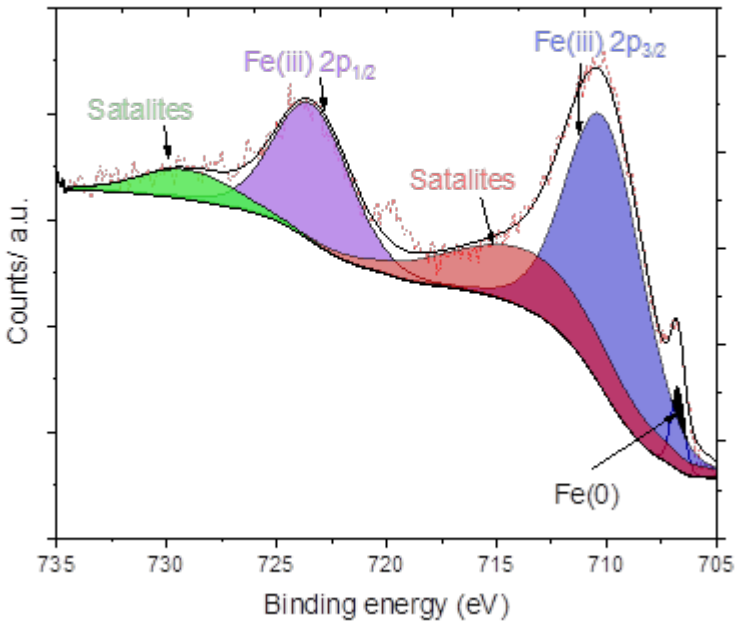

(a)

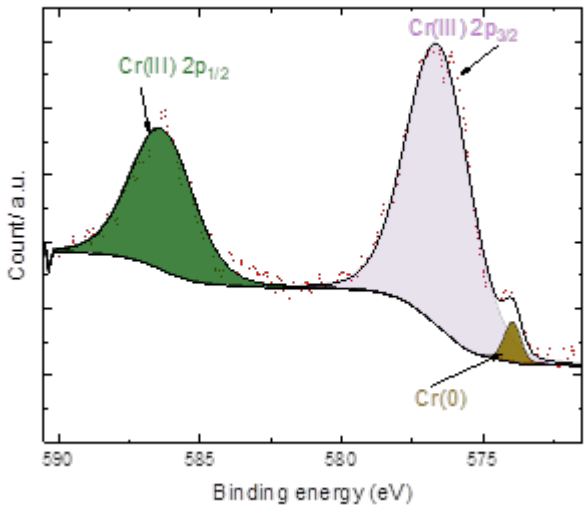

(b)

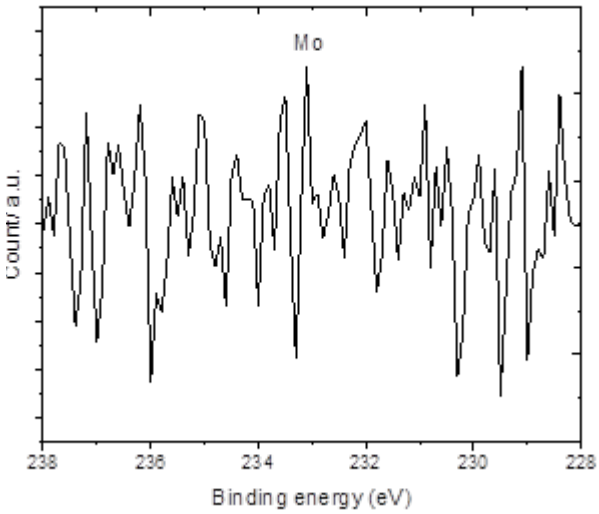

(c)

Figure 5-13: High resolution XPS spectra for unprocessed sample (a) Fe, (b) Cr, and (c) Mo.

Paper 2 Supplemental information

Experimental Methods

DOE 2 Laser processing

5mm X 5mm squares where then processed in the same way as DOE 1 using fixed parameters of a bidirectional hatching strategy and a 100kHz frequency. The laser processing parameter where altered using a 3 x 3 full factorial design of experiment set up with the altering parameter being power, hatching distance, and scan speed, this produced 27 samples which were repeated 3 times. The scan speed made discrete jumps between 250, 350, and 450 mm/s. The Hatching distance made discrete jumps between 1, 8, and 15 µm while the power made discrete jumps between 50, 65 and 80% of the maximum power. The single repeat full factorials design can be seen below.

Run	Frequency (kHz)	Power (%)	Scan Speed (mm/s)
S1	60	60	50
S2	60	60	150
S3	60	60	250
S4	80	60	50
S5	80	60	150
S6	80	60	250
S7	100	60	50
S8	100	60	150
S9	100	60	250
S10	60	80	50
S11	60	80	150
S12	60	80	250
S13	80	80	50
S14	80	80	150
S15	80	80	250
S16	100	80	50
S17	100	80	150
S18	100	80	250
S19	60	100	50
S20	60	100	150
S21	60	100	250
S22	80	100	50
S23	80	100	150
S24	80	100	250
S25	100	100	50
S26	100	100	150
S27	100	100	250
Focal offset = 0 Hatching Distance = 10 µm Hatching Stagey = Bidirectional			

Table 5-14: DOE 1 parameter set for laser colouration experiment.

This study was a continuation of DOE 1, which involved modifying the power, speed, and frequency. Because the lower surface energy findings from DOE 1 delivered the best results, the power and scan speed were both increased into new ranges in order to see if there was a maximum result in the lower range of surface energy. Due to the fact that frequency has the least impact on total corrosion, the hatching distance parameter is altered in this case.

Results and discussion

Electrochemical Results

From the cyclic polarization curves 3 different corrosion results where obtain these are the corrosion potential (Ecorr) the corrosion current (Icorr) and the corrosion per year (Mpy). The corrosion potential is obtained initial from the open circuit potential and is an indicator of the potential at which corrosion will start to occur. Icorr is highly related to the corrosion rate and is an indicator of the current needed for corrosion to being. The corrosion rate was then obtaining by using the tafel equation. Gamry Echem Analyst was used to applied this tafel equation and obtain the corrosion rate.

Cyclic polarization: As can be seen in both Run 9 and Run 11 in Figure **5-14**. Once the breakdown potential is reached the graph is still gaining potential instead of leveling off this shows that the passive film is not acting as an ideal protective film it is forming and breaking down simultaneously. This problem could be cause by the use of a sandblasted initial surface. This sandblasting increases the surface roughness of the sample which has been seen to have a huge negative effect on the overall corrosion properties of the material [113] and due to the thickness of the produced oxide film surface preparation post laser processing was not possible. This is also a factor in the formation of early crevice corrosion

Corrosion results: As can be seen in Figure **5-15**. The corrosion potential and corrosion current are graphed vs the surface energy. It can be seen that there is a slight trend that shows that the lower surface energies produce the best results for both the corrosion potential and current. With a minimum corrosion current seen at 7.87e13 J/m^3 with a value of 12nA, and a maximum corrosion potential see at -83.8 mV seen at 1.20e14 J/m^3. These two results can be explained by the ratio of Cr/Fe concentration on the surface. As seen above the ratio of Cr/Fe also say an initial increase at lower surface energies followed by a sharp decrease down to below that of unprocessed stainless steel. This increase chromium on the surface reduces the

availability of nucleation site to form on the surface. These results match quite similarly the results obtained by lecka *et al* [47]. Even with the Cr/Fe ratio dropping to or below that of unprocessed stainless steel at higher surface energies every single result shows a corrosion current lower than that experienced by the unprocessed sample of 148nA. For the corrosion potential surface energies of above 5e14 J/m^3 cause the potential to drop below that of the unprocessed sample.

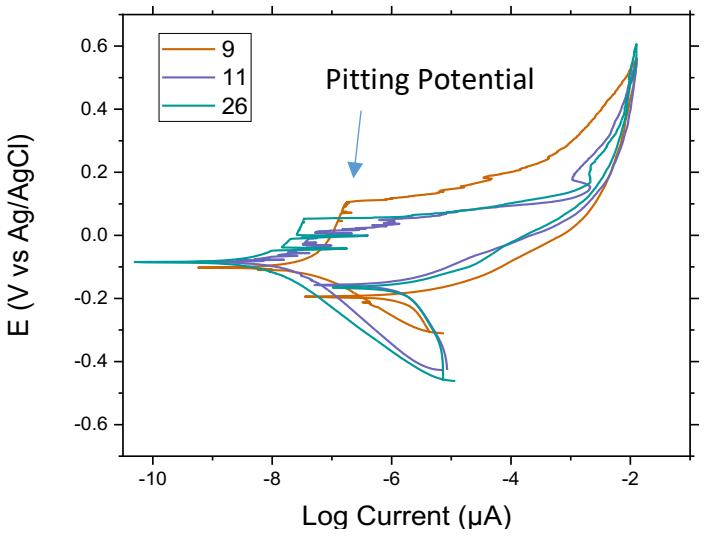

Figure 5-14: Cyclic polarization curve of Runs 9, 11 and 26.

By the use of the Tafel equation the corrosion rate of each sample was obtained. These results can be seen in Figure 5-16. It shows that the best result belongs to run 16. This run corresponds to the parameter 250 mm/s scan speed, 100 KHz frequency and an 100% power which produces a corrosion rate of 30.06 mpy. This result shows 9-fold increase in corrosion rate compared the unprocessed stainless steel sample.

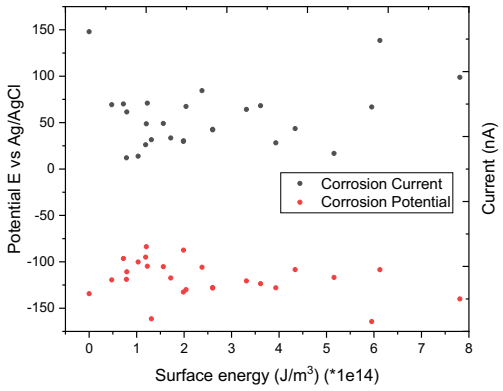

Figure 5-15: Graph of corrosion current and corrosion potential Vs the applied surface energy.

The worst result seen, and the only one that performed worse than unprocessed stainless steel, was produced by run 1, which had the parameters 50 mm/s speed, 60KHz frequency, and 60% power, resulting in a corrosion rate of 331.8 mpy. This low corrosion resistance can be explained by the fact that this run has the lowest Cr/Fe ratio of all the results, at 0.179, which is three times lower than the unprocessed steel. The relatively high surface energy used can explain the low Cr/Fe ratio. This higher energy increases the reaction time of the process this allows sufficient time for the diffusion of Fe ions through the produced oxide layer causing a accumulation of Fe oxide on the surface of the steel. This new formed layer will mask the Cr oxide layer reducing the total Cr on the surface. Due to the lower power of 60% both the CrO_3 and Cr_2O_3 are present on the surface so the full conversion of Cr(III) to Cr(IV) is not seen.

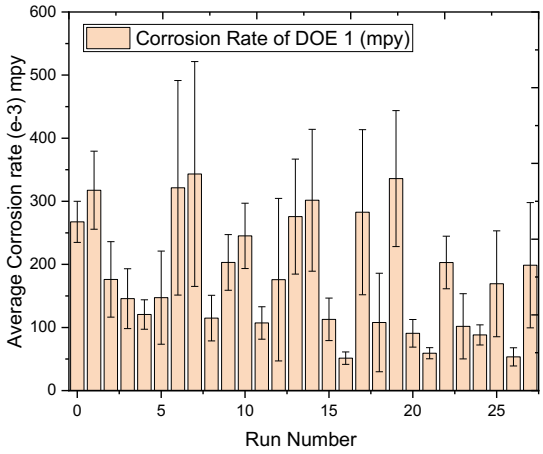

Figure 5-16**:** Bar graph of the corrosion rate vs the run number.

DOE 2 Results / Discussion

Figure 59 shows the 3 corrosion parameter of interest the corrosion potential (Ecorr) pitting potential (Epitt) and the Corrosion current (icorr). With the error bars representing the standard error of each run.

E_{pitt} analysis

According to the results of the ANOVA study, the hatching distance is the most critical factor influencing the pitting performance of the laser-processed specimens. This can be observed over the entire range of settings that have been employed. Changes in hatching distance at 80 percent power and 250 mm/s scan speed demonstrate this clearly, with the pitting resistance increasing from the second worst result of 35.3 mV to the best value of 419.3 mV as the hatching distance is increased from 1 to 15 microns. In addition, there is a two-factor interaction between the hatching distance and the power, which demonstrates that the pitting resistance changes more dramatically at higher powers. In this case, it is possible that the reduced laser overlap at higher hatching distances is responsible for the increased pitting resistance. By reducing the heating and cooling cycles that occur because of multiple overlaps, we can reduce thermal stress and the formation of surface cracks and defects, which are the primary areas for initial pitting formation and propagation.

Source	Sum of Squares	df	Mean Square	F Value	p-value Prob > F
Model	1200.227855	9	133.3586505	20.02239395	< 0.0001
A-Scan Speed	1.43658172	1	1.43658172	0.215687584	0.6438
B-Hatching Distance	850.2564515	1	850.2564515	127.6570328	< 0.0001
C-Power	5.085464211	1	5.085464211	0.763528781	0.3852
AB	10.1885591	1	10.1885591	1.529704622	0.2202
AC	25.50584642	1	25.50584642	3.829433659	0.0543
BC	181.9068854	1	181.9068854	27.31139905	< 0.0001
A^2	8.72076038	1	8.72076038	1.309330135	0.2564
B^2	86.64701165	1	86.64701165	13.00913435	0.0006
C^2	30.48029451	1	30.48029451	4.576294541	0.0359
R-Squared	0.717358427			**Pred R-Squared**	0.632905793
Adj R-Squared	0.681530622			**Adeq Precision**	15.20639358

Table 5.15: ANOVA model with the results and parametric terms for pitting potential of DOE 2.

A quadratic term was used to develop the ANOVA model with the results and parametric terms been seen in Table 5-15, the p-value of <0.0001 indicates that the model is significant, while only the significant individual factor being the hatching distance. With the combined effect of power and hatching distance also being significant. The model contains a reasonable R-square value of 0.7174. Finally, the adequacy precision of 15.206 indicates adequate model discrimination. Since this ration is >4, this means that the current design can be used to navigate the design space. The following equation S-4 was obtained from the model for the investigated range of the laser processing parameters and can be used to predict the pitting resistance of the stainless steel samples within this range.

Sqrt(Epitt + 78.76) =	-4.00385
0.016698	* Scan Speed
-0.37426	* Hatching Distance
+0.75653	* Power
+7.59989E-004	* Scan Speed * Hatching Distance
-5.61148E-004	* Scan Speed * Power
+0.021408	* Hatching Distance * Power
+6.96051E-005	* Scan Speed^2
-0.044776	* Hatching Distance ^{2}
-5.78350E-003	* Power^2

(S-4)

Figure 5-17 shows the 3D plots of the response surface method, RSM, for the pitting potential. In this figure, the effect of two factors on the response was examined while the third factor remains constant. Both the laser beam scan speed and hatching distance were changing at the time the laser power was fixed.

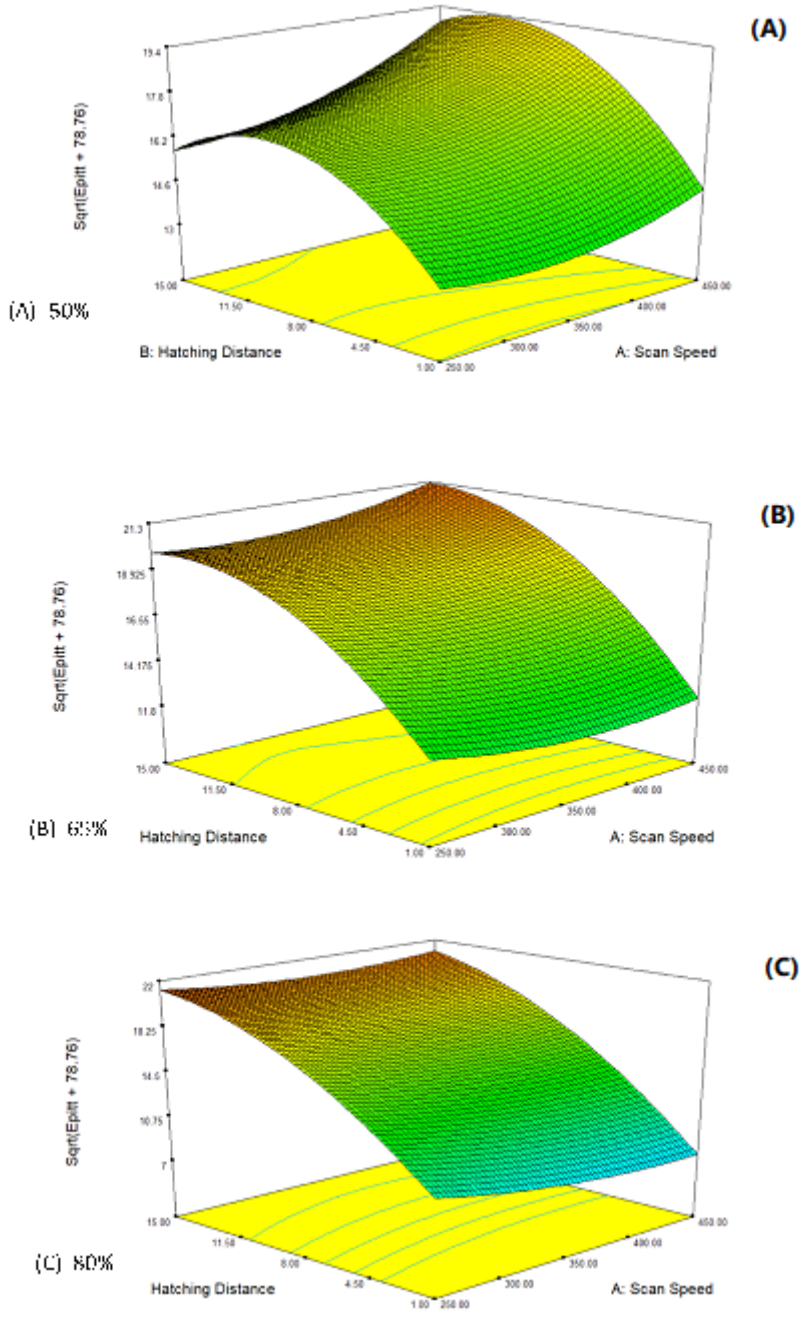

Figure 5-17**:** Response surface of sqrt(Epitt +78.76) at (a) 50% laser power, (b) 65% laser power, (c) 80% laser power.

Icorr analysis

The corrosion current of the laser processed samples can be seen to relate to the applied surface energy. They show a sharp decrease in the corrosion current up to the minimum followed by a slow increase up. As seen in Figure **5-18** c, the minimum corrosion current was seen at 7.211 J/mm^3 with a value of 73nA/cm^2, the second lowest value of 90.2nA/cm^2 appeared at 6.922J/mm^3 this results are valuable as it also belongs to the result with the maximum pitting corrosion resistance. This results can be explained by the thermoskinetic model developed by Cui *et.al* [43], where at the lowest surface energies the Chromia oxide will be oxides first due to its higher affinity for oxygen for a Chromia oxide layer on the surface. As more energy is, supplied iron oxide will then form, as the mobility of iron ions through the oxide is higher than chromium cause iron to then form over the chromium oxide. The surface energy equation used in this case is

$$\mathbf{E_s} = \frac{\mathbf{P}}{\mathbf{v\omega_o h}} \qquad \textbf{(5-5)}$$

where P is the average power of the pulse, ω_o is the spot size of the laser, h is the hatching distance and v is the scan speed.

This show that there is a maximum corrosion resistance peak occurs at ~7.0J/mm^2 with lower surface energies producing lower corrosion resistance. As can be seen in the graph a small change in surface energy form this point can see a large drop off in corrosion resistance. This show that the

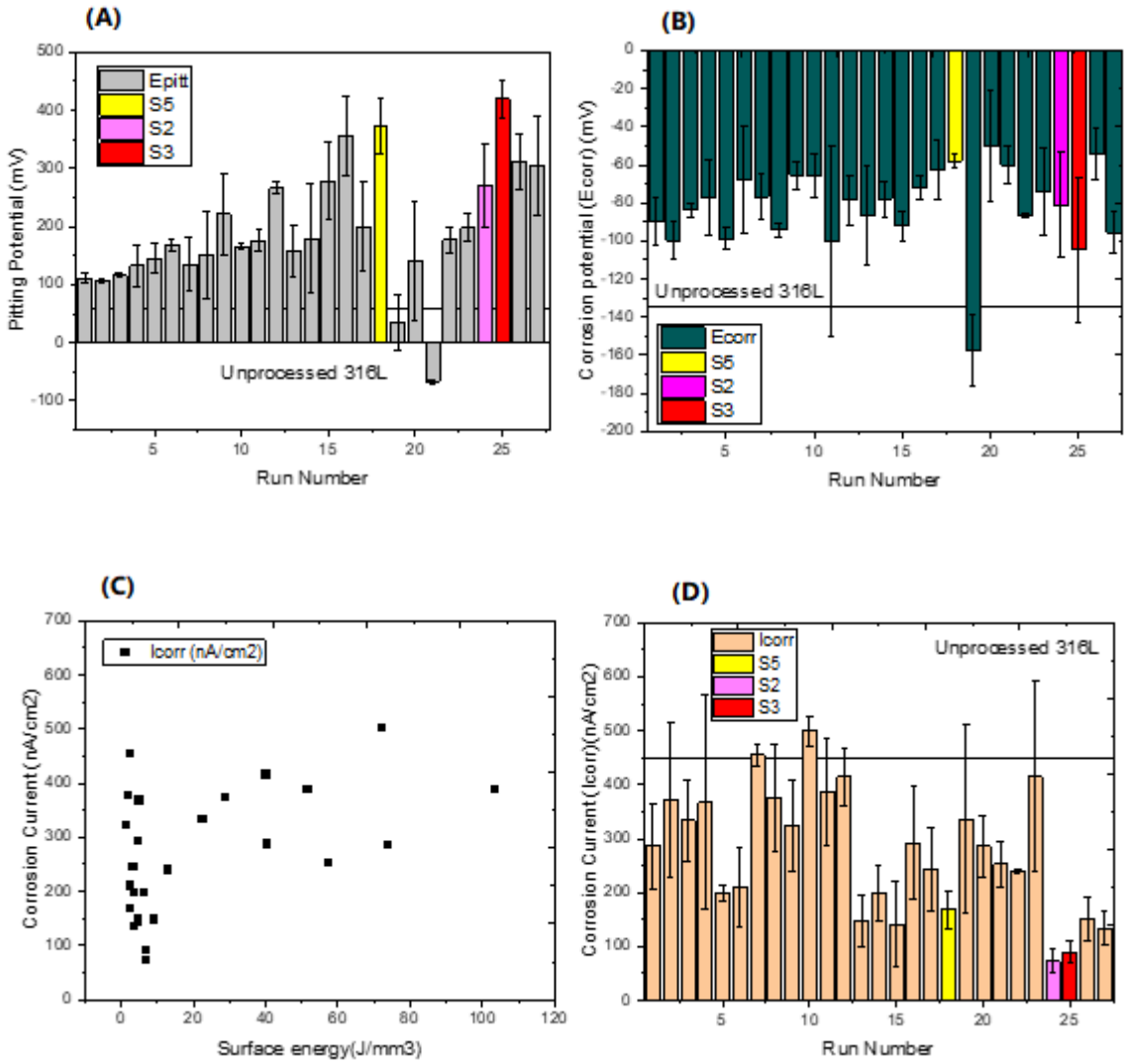

Figure 5-18**:** (A) Corrosion potential vs the run number for DOE 2. (B) Pitting potential vs the run number for DOE 2, (C) corrosion current vs applied surface energy for DOE 2, (D) corrosion current vs the run number for DOE 2, with standard Deviation shown for the error bars.

Run	Scan Speed (mm/s)	Hatching Distance (um)	Power (%)
L1	250	1	50
L2	350	1	50
L3	450	1	50
L4	250	8	50
L5	350	8	50
L6	450	8	50
L7	250	15	50
L8	350	15	50
L9	450	15	50
L10	250	1	65
L11	350	1	65
L12	450	1	65
L13	250	8	65
L14	350	8	65
L15	450	8	65
L16	250	15	65
L17	350	15	65
L18	450	15	65
L19	250	1	80
L20	350	1	80
L21	450	1	80
L22	250	8	80
L23	350	8	80
L24	450	8	80
L25	250	15	80
L26	350	15	80
L27	450	15	80
Focal offset = 0 Frequency = 100 kHz Hatching Stagey = Bidirectional			

Figure 5-19: Parameters used for second Design of Experiments.

Sample	Rp (k ohm/cm)	Cdl (µS s^a/cm^2)	α	Ru	Ri	CPEi	αi	Ro	CPEo	αo	Rpore	CPEpore	αpore
Blank	375800	757.5	0.787	11.18	8936	5475	0.9996	-	-	-	-	-	-
Sample 2	38800	773.2	0.921	15.61	14.96	3592	0.569	547200	473.4	0.889	-	-	-
Sample 5	7639	3599	0.822	19.68	6.75	2604	0.776	417.1	4355	0.958	29300	1337	0.962

Table 5-16: Electrochemical parameters of corrosion current, corrosion potential and pitting resistance measured for laser processed samples.

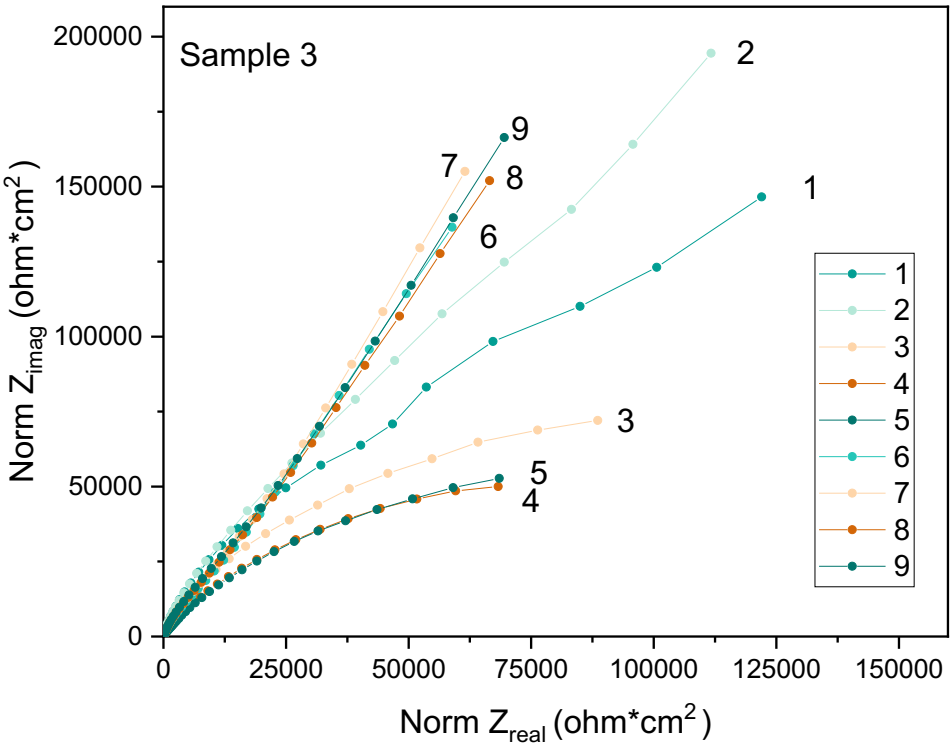

Figure 5-20: Long-term electrochemical impedance spectroscopy for laser processed sample 3.

Paper 3 Supplemental information

Peaks	Compounds	Binding Energies (eV)		Sensitivity Factor
		Experimental	Reference	
Fe 2p 3/2	Fe (metal)	706.8	706.5	
	Fe_2O_3	710.9	710.8	10.82
Cr 2p 3/2	Cr (metal)	574.8	574.3	
	CrO_3	580	580	7.69
	Cr_2O_3	577	576	7.69
O 1s	O_2 -	530.1	529-530	2.93
	OH-	532.0	531.5-532	
Ni 2p 3/2	$Ni(OH)_2$	855.4	855.6	22.18
Ni 2p 1/2		873	872.9	22.18
Mn 2p 3/2	MnO	641.5	641.4	9.17
Mn 2p 1/2	MnO	653.4	653.1	

Table 5-17 Binding energies and sensitivity of the compounds used in this study [123,132,161]